Dissertation
submitted to the
Combined Faculty of Natural Sciences and Mathematics
of the Ruperto Carola University Heidelberg, Germany
for the degree of
Doctor of Natural Sciences

Presented by

M.Sc. Robin Burk

born in: Heilbronn, Germany

Oral examination: 19th of November 2018

Visualization of the HIV-1 Nuclear Preintegration Complex Structure by High Precision Correlative Light - and Electron Microscopy and - Tomography

Referees: Prof. Dr. Hans-Georg Kräusslich

PD Dr. Jacomine Krijnse-Locker

Acknowledgement

This thesis was performed under supervision of Prof. Dr. Hans-Georg Kräusslich in the Department of Infectious Diseases, Virology, at the University Hospital of Heidelberg from August 2014 until September 2018.

First of all, I thank Prof. Hans-Georg Kräusslich for letting me follow up this special project. I enjoyed learning the manifold techniques and I also feel very privileged to have been able to follow up other interests and functions during my time as a Ph.D. student.

I also thank Prof. Barbara Müller and my TAC committee members, Dr. Jacomine Krijnse-Locker, Dr. John Briggs and Dr. Volker Lohmann for helpful input and fruitful discussions throughout my project.
Furthermore, I also thank the whole Virology department, friends and colleagues, fellow HBIGS students, Dr. Dr. Dr. Jens Kuhn and Dr. Sheli Radoshitzky for teaching me and providing material.

Special thanks go to Dr. Cecilia Bebeacua for introducing me patiently into Correlative Light- and Electron Microscopy. Along that line, I also thank Dr. Yura Bykov for support in the cryo-CLEM approach and sharing of tricks and knowledge. Dr. Martin Schorb was and is a huge support, without whom the analysis of the visualized structures might still be pending. Thanks to Dr. Vibor Laketa for excellent support and input on light microscopy.
I am also grateful for the experimental support and input from the EMCF Heidelberg Dr. Charlotta Funaya and Dr. Stefan Hillmer and EMCF users: Thanks to Niki Kolovou and Sebastian Wurzbacher for technical assistance and entertainment (respectively).
Thanks to you, Vojtech and Martin for always being available for data discussions, with or without additional beers. I feel sorry for my poor liver, but I am yet very grateful for your friendship. It wouldn't have been as much fun (or bearable) without you guys. The same holds true for so many other people: Ben, Annica, Thorsten, Magalie, Juliane, Shawon, Johnny, Pranav, Walther, Kathleen, Anke-Mareil, Tamtam and everyone else I had the pleasure to interact with, as well as my friends from Bachelor throughout Ph.D. and beyond: Lucas, Chrissy and Ann-Kathrin. It is always good to have co-sufferers.
Overall, I was very happy with my work environment and thank everyone for coping with me and my special humor.

Very special and warm thanks go to Frau Spätzle for supporting me throughout the main part of my experimental thesis and writing it up, for providing good levels of distraction by learning weird languages or swimming in the Neckar, for feeding me when I wouldn't have cared during my typing rages, for proofreading many parts of my PhD thesis, and a thousand other things, that help me being a generally satisfied and happy person. Thank you for your patience and endurance with me.

Last but not least, I thank my Family:
Auch wenn ich mich mit Anflügen hochdeutscher Abartigkeiten - wie etwa "viertel vor 12" - manchmal augenscheinlich Distanz von Daheim nehme, war ich immer (oder allermeistens) sehr froh im Ländle einen Ort zu haben an den ich zurückkehren kann, wenn mir die akademisch-theoretische Welt etwas zu nahe gerückt ist. Die Art wie ich aufgewachsen bin und erzogen wurde hat mich letztlich zu dem gemacht, der ich heute bin.

Summary

Upon fusion of the viral envelope with the host cell membrane, the capsid of the human immunodeficiency virus 1 (HIV-1) is released into the host cell cytoplasm. To productively infect a cell, the viral RNA genome needs to be reverse transcribed into viral DNA. This in turn needs to become integrated into the host cell genome. Integration can, however, only happen, after the viral genome is released from its capsid-container, in a process called uncoating.

This is a vital process and needs to be regulated and orchestrated in certain ways – which are still elusive and controversially discussed.

Some studies suggest that uncoating takes place soon after -, or concomitant with viral entry. Other researchers came to the result that the capsid needs to retain its structure to shield the viral components from being sensed by the innate cellular immune system. Both hypotheses, early uncoating and prolonged structural retention, are solidly supported by experimental data. Therefore, the timing and kinetics of uncoating remain unresolved. Based on previous results from our group, we had reason to believe that the capsid might indeed be retained, possibly even within the nucleus. A method was developed, that allows the detection of viral DNA. The presence of viral DNA was used as a criterion to discriminate between productive and nonproductive subviral particles in infected cells. Surprisingly, productive subviral particles displayed an intense, stable signal for capsid protein in immunofluorescence experiments, throughout the cytoplasm and even within the nuclei of infected cells. A strong signal is can be understood as a high concentration of labeled protein, which in turn might indicate the presence of a retained structure. However, intense immunofluorescence signals can also mean more efficient binding of antibodies due to structural rearrangements (such as uncoating), and a high spatial concentration of proteins cannot be directly interpreted as structure retention.

In this study, we present a unique way to address and solve this important question. We specifically focused on the small fraction of productive particles. Light Microscopy allows specific labeling but has low resolution. Electron Microscopy yields much higher resolution, but specific (immuno)labeling is difficult and often detrimental to ultrastructural retention. We overcame both limitations by correlative light – and electron microscopy: Regions of interest were identified by specific nuclear subviral particle surrogate markers in light microscopy. On these regions, tilt series electron tomography was performed, to visualize the subviral particles' structure, as well as the subcellular environment, around the region of interest.

Performing high resolution tilt series electron tomography, we could repeatedly and convincingly visualize a capsid-reminiscent structure that underlies HIV-1 nuclear preintegration complexes. This

apparent structure is very similar in shape, but smaller in size compared to capsids of virus particles of mostly identical preparations.

The discovery of a retained capsid structure in the nucleus of an infected cell will advance on our understanding of nuclear entry and provides whole new insights into the overall understanding of HIV-1 in early steps of infection.

Zusammenfassung

Während der Fusion zwischen der viralen und zellulären Membran der Wirtszelle wird das Kapsid des humanen Immundefizienzvirus 1 (HIV-1) in das Zytoplasma der Wirtszelle entlassen. Um eine Zelle produktiv zu infizieren muss das viral RNA Genom in virale DNA revers transkribiert werden. Die virale DNA wiederum muss in das zelluläre Wirtsgenom integriert werden. Die Integration kann jedoch erst stattfinden, nachdem das virale Genom aus seinem Kapsid-Container entlassen wird, in einem Prozess namens Freisetzung.

Dies ist ein unverzichtbarer Prozess und muss auf bestimmte Art und Weise – die noch nicht verstanden oder kontrovers diskutiert wird - reguliert und gesteuert werden.

Einige Studien legen nahe, dass das Freisetzen schnell nach -, oder gleichzeitig mit dem viralen Eintreten stattfindet. Andere Forscher kamen zu der Schlussfolgerung, dass das Kapsid in seiner Struktur erhalten bleiben muss um virale Komponenten vor der Erkennung durch zelluläre Immunsensoren zu schützen. Beide Hypothesen, baldiges Freisetzen und längere Erhaltung der Kapsid Struktur, werden durch fundierte experimentelle Daten gestützt. Der Zeitpunkt und die Kinetik der Freisetzung bleiben daher bisweilen ungeklärt.
Auf vorangehenden Ergebnissen aus unserer Arbeitsgruppe basierend hatten wir Grund zur Annahme, dass das Kapsid tatsächlich in seiner Struktur erhalten bleiben könnte, womöglich selbst im Zellkern.
Eine Methode wurde entwickelt, die es ermöglicht, virale DNA zu detektieren. Das Vorliegen viraler DNA wurde als Kriterium herangezogen um in infizierten Zellen zwischen produktiven und nichtproduktiven subviralen Partikeln zu unterscheiden. Unerwarteterweise wiesen produktive subvirale Partikel in Immunfluoreszenzexperimenten ein stabil intensives Kapsid Protein-Signal auf, nicht nur im Zytoplasma, sondern selbst im Zellkern infizierter Zellen. Ein intensives Signal kann als eine hohe Konzentration gefärbter Proteine verstanden werden, was wiederum auf das Vorliegen einer intakten Struktur verweisen könnte. Jedoch kann ein intensives Signal auch aufgrund ausgeprägterer Bindung von Antikörpern verstanden werden, bedingt durch strukturelle Umwandlungen (zum Beispiel: Freisetzung). Eine hohe lokale Konzentration von Proteinen kann also nicht direkt als der Erhalt einer Struktur interpretiert werden.

In dieser Arbeit präsentieren wir eine einzigartige Methode um diese wichtige Frage zu beantworten. Wir haben uns dabei speziell auf den kleinen Anteil produktiver Partikel fokussiert.

Lichtmikroskopie ermöglicht spezifische Färbungen, erlaubt jedoch nur eine geringe Auflösung. Die Elektronenmikroskopie erreicht eine sehr viel höhere Auflösung, wohingegen spezifische (Immun)Färbungen kompliziert sind und oft den Erhalt der Ultrastruktur negativ beeinflussen. Wir konnten beide Beschränkungen überwinden durch das Anwenden von korrelativer Licht- und Elektronenmikroskopie: Relevante Positionen wurden anhand eines indirekten spezifischen Markers mittels Lichtmikroskopie identifiziert. An diesen Positionen wurden Kippserien-Elektronentomogramme aufgenommen, um die Struktur des subviralen Partikels, sowie auch die subzelluläre Umgebung an dieser Position zu visualisieren.

Mittels hochauflösender Kippserien-Elektronentomographie konnten wir wiederholt und überzeugend Kapsid-ähnliche Strukturen visualisieren, die dem nukleären HIV-1 Präintegrationskomplex inne sind. Diese apparente Struktur hat in Bezug auf ihre Form große Ähnlichkeit mit den Kapsiden intakter Viruspartikel, unterscheidet sich jedoch markant in Bezug auf die Größe der Strukturen, obgleich die verglichenen Proben beinahe identisch angefertigt wurden.

Die Entdeckung einer erhaltenen Kapsidstruktur im Nucleus infizierter Zellen wird unser Verständnis für den viralen Eintritt in den Nucleus erweitern und erlaubt neue Einsichten in das generelle Verständnis von HIV-1 während frühen Stadien der Infektion.

Contents

List of Figures and Tables

List of Abbreviations

Abbreviation	Written-out
°C	degree Celsius
µ	micro
µg	microgram(s)
µL	microliter(s)
µM	micromolar
2A-PB	2A Peptide Bridge
AA	aminoacid(s)
AFS	Automated Freeze Substitution
Amp	ampicillin or ampere
APC	aphidicolin
APS	ammonium persulfate
b	base
bp	basepair(s)
BSA	bovine serum albumin
BSL3	Biosafety Laboratory Level 3
CA	Capsid protein
$CaCl_2$	calcium chloride
Caco	cacodylate
CC	cytochrome C
CCR5	C-C Motif Chemokine Receptor 5
CD4	Cluster of Differentiation 4
CLEM	correlative light and electron microscopy
cm	centimeter
CO_2	carbon dioxide
CPSF6	cleavage and polyadenylation specificity factor 6
CXCR4	C-X-C Motif Chemokine Receptor 4
Da	Dalton
DMEM	Dulbecco's Modified Eagle Medium
DMSO	Dimethyl sulfoxide
dNTP	deoxyribonucleoside triphosphate
DT	dual tilt

e.g.	exempli gratia
EDTA	ethylenediaminetetraacetic acid
EdU	5-Ethynyl-2’-deoxyuridine
eGFP	enhanced green fluorescent protein
EGTA	ethylene glycol-bis(ßaminoethyl ether) tetraacetic acid
EM	electron microscopy
EMCF	Electron Microscopy Core Facility
Env	Envelope protein
ET	electron tomography
EtOH	Ethanol
FCS	Fetal calf serum
FL	flexible linker
FS	Freeze Substitution
fwd	forward
GA	glutaraldehyde
Gag	group specific antigen
GFP	green fluorescent protein
GOI	gene of interest
h	hour
H_2O	water
HBS	HEPES buffered saline
HIV-1	human immunodeficiency virus type 1
HPF	High Pressure Freezing
hrs	hours
HyD	hybrid detector
i.e.	id est
IF	immunofluorescence
IN	Integrase
IN.eGFP	Vpr.Integrase.enhanced Green Fluorescent Protein-fusion
K	Kelvin
k	kilo (10^3)
Kan	kanamycin
kDa	kilodalton

Abbreviation	Written-out *continued*
KOH	potassium hydroxide
kV	kilovolts
L	liter
LB	lysogeny broth
LM	light microscopy
LN_2	liquid nitrogen
M	mega (10^6) or molar
m	milli (10^{-3}) or meter
MA	Matrix protein
mAmp	milliampere
mCh	mCherry
MeOH	methanol
min	minutes
mL	milliliter
mM	millimolar
MoMLV	moloney murine leukemia virus
MTOC	Microtubule organizing center
n	nano (10^{-9})
NaOH	sodium hydroxide
NC	nucleocapsid protein
nef	negative factor
NH_4Cl	ammonium chloride
nL	nanoliter
nm	nanometer
NPC	nuclear pore complex
Nup	nuclear pore protein
o/n	over night
OsO_4	osmium tetroxide
PAC	puromycin N-acetyl-transferase
PAG	protein A-gold colloidal gold
PbCi	lead citrate
PCR	polymerase chain reaction
PEI	polyethylenimine

Abbreviation	Written-out *continued*
PFA	paraformaldehyde
PIC	preintegration complex
PMT	photomultiplier tube
Pol	Polymerase polyprotein
PR	Protease
PuroR	Puromycin Resistance Gene (=PAC)
PVDF	polyvinylidene difluoride
Rb	rabbit
rCPSF6wt$_{AA}$.mCh	resistant CPSF6, silently mutated, fused to mCherry
rev	reverse (primer) or regulator of virion (accessory protein)
ROI	region of interest
rpm	revolutions per minute
RPMI-1640	Roswell Park Memorial Institute 1640
rsEGFP	reversibly switchable enhanced green fluorescent protein
RT	Reverse Transcriptase (enzyme) or Reverse Transcription (process) or Room Temperature
RTC	reverse transcription complex
SDS	sodium dodecyl sulfate
SDS-PAGE	SDS polyacrylamide gel electrophoresis
shRNA	short hairpin RNA
siRNA	small interfering RNA
SP1	spacer peptide 1
SP2	spacer peptide 2
ST	single tilt
T20	Enfuvirtide (Viral entry inhibitor)
TAMRA	5-Carboxytetramethylrhodamine Azide
tat	transactivator of transcription
TEM	transmission electron microscopy
TIA	TEM Imaging and Analysis
TOM20	transporter of outer mitochondrial membrane 20
UA	uranylacetate
V	volt(s)
vif	viral infectivity factor

Abbreviation	Written-out	*continued*
vpr	viral protein R	
vpu	viral protein U	
w/	with	
w/o	without	
WB	Western Blot	
wt	wildtype	

1 Introduction

1.1 HIV-1 Discovery

Before the actual virus, its caused disease, the acquired immunodeficiency syndrome (AIDS) was described in 1981 (Gottlieb et al., 1981). Immunocompromised patients were found to show drastically reduced counts of $CD4^+$ T lymphocytes, being the reason for the suffering of opportunistic infections (such as pneumonia and bronchial candidiasis) in AIDS. Moreover, these patients were often suffering from Kaposi's sarcomas. The causative agent, human immunodeficiency virus 1, was described only 2 years later, in 1983 (Barre-Sinoussi et al., 1983). Considering the at that time available methods and techniques, such a fast isolation and description can be considered an immense achievement. Furthermore, the route of transmission, horizontal human-to-human during sex, venous application of drugs with contaminated syringes and infected blood transfusions, was described.

HIV-1 is a bona fide example of a human epidemic originating from a zoonotic transmission: HIV-1, the major virus in the ongoing HIV/AIDS epidemics, is strongly suggested to have been introduced into humans by zoonotic transmission of a simian immunodeficiency virus from chimpanzees of the subspecies *Pan troglodytes troglodytes* (SIVcpz*Ptt)* (Gao et al., 1999; Jin et al., 1994; Keele, 2006; Sharp and Hahn, 2011).

HIV-1 is subdivided into 4 groups, M (major, responsible for the ongoing epidemics), N (non-M, non-O) (Simon et al., 1998), O (Outlier, largely restricted to equatorial western Africa) (De Leys et al., 1990; Gürtler et al., 1994; Peeters et al., 1997),summarized in (Gao et al., 1999)) and P (putative) (Plantier et al., 2009). Each of these groups is assumed to have originated in independent zoonotic transmission events (chimpanzees to humans). Phylogenetic modeling dates the estimated introduction for the M group back to the early 20^{th} century, ~1910-1930 (Korber et al., 2000; Lemey et al., 2004; Worobey et al., 2008).

HIV-2 (a related lentivirus) is assumed to have been introduced into humans from sooty mangabeys (species *Cercocebus atys)* (Sharp and Hahn, 2011).

In general, HIV-2 infected patients have better outcome chances, in comparison to HIV-1 patients, due to lower viral loads, accompanied with a reduced risk of virus transmission. Therefore, HIV-2 is considered less pathogenic, and so far remains largely restricted to western Africa (Ekouevi et al., 2013). As experiments in this study address HIV-1 only, more detailed descriptions solely cover HIV-1.

In 2017, 36.9 million people were estimated to live with an HIV infection. ~940,000 people succumbed to the virus (and its accompanied syndrome) while 1.8 million people got newly infected. A combination of 3 (or more) antiretroviral drugs (ARV) can efficiently suppress viral replication and thereby prevent the AIDS syndrome and considerably lower the risk of virus transmission. The combinatorial approach helps to restrict virus evolution to multi drug-resistant variants. It is estimated that a total of 70 million people got infected in the HIV/AIDS epidemic, of which ~35 million have died due to HIV related sickness (http://www.who.int/gho/hiv/en/).

The number of global new infections is steadily declining, thanks to efforts in education, antiretroviral therapy and research. Yet, the number of people living with an HIV-1 infection is still increasing annually. We therefore clearly need to understand the virus' biology in even more detail.

Education and antiretroviral therapy can be efficient to reduce human-to-human transmission. But without vaccines and cures available, it will hardly be possible to effectively reduce the number of patients and eventually eradicate HIV.

1.2 HIV-1 Classification and Morphology

HIV-1 is the sole member of the *Human immunodeficiency virus 1*, a lentivirus belonging to the *Retroviridae*. Morphologically, HIV-1 is an enveloped virus particle, measuring ~140 nm in diameter (Briggs, 2003). As for all retroviruses, its genome is organized in 4 main coding domains: gag-pro-pol (3 coding domains transcribed into 1 mRNA transcript, group-specific antigen, protease, polymerase), and *env* (envelope) (Petropoulos, 1997). Different from simple retroviruses, the complex HIV additionally encodes accessory proteins, discussed later.

Mainly, the Gag polyprotein is expressed from the *gag-pro-pol* coding domain. Gag-Pro-Pol can only be translated upon ribosomal frame shifting. In 5 % of the translations, the ribosome slips into the -1 reading frame. This happens at a slippery site in the p6-coding region (3' end of *gag*) of the *gag-pro-pol* mRNA. Once shifted into the -1 reading frame, the full Gag-Pro-Pol polyprotein is expressed (Hung et al., 1998; Jacks et al., 1988). The polyprotein Gag comprises the structural proteins (amino- to carboxyterminus) Matrix (MA), Capsid (CA), Spacer Peptide 1 (SP1), Nucleocapsid (NC), Spacer peptide 2 (SP2) and p6.

The 2 carboxyterminal domains of the Gag-Pro-Pol polyprotein, consist of the protease (PR, encoded by *pro*), the RNA-dependent DNA polymerase also called reverse transcriptase (RT, encoded by *pol*) and the Integrase (IN, encoded by *pol*). In HIV-1 research, Pro-Pol is mostly referred to as Pol.

Gag and Gag-Pro-Pol are translated as polyproteins and are proteolytically cleaved during the maturation step. During virus particle assembly at the plasma membrane, MA anchors Gag into the inner plasma membrane leaflet via its myristyl anchor (Bryant and Ratner, 1990; Kiernan et al., 1999; Paillart and Göttlinger, 1999). CA harbors the main Gag-multimerization domain and after maturation forms the cone-shaped capsid. Inside the capsid, NC, together with the 2 viral single stranded positive-sensed RNA copies, form the ribonucleoprotein particle. PR heterodimerizes, cleaves itself proteolytically first, and then the other polyproteins in an orchestrated fashion. Thereby, immature virus particles transform into mature, infectious virus particles. RT reverse transcribes the viral genomic RNA into viral (ds)DNA. Once completed, the viral DNA can be integrated into the host cell genome by IN.

The third coding domain *env* comprises the envelope glycoproteins gp120 and gp41. 7-14 Trimers of the gp41/gp120 heterodimer are inserted into the plasma membrane-derived envelope (Chertova et al., 2002; Zhu et al., 2003), defining the tropism and mediating entry into target cells. Furthermore, a set of viral accessory proteins is encoded: viral protein R (Vpr), viral protein U (Vpu), regulator of virion (Rev), negative factor (Nef), viral infectivity factor (Vif) and transactivator of transcription (Tat) (Coffin et al., 1997). The detailed genomic organization is represented in Figure 1 (Campbell and Hope, 2015; Freed, 2015; Sundquist and Kräusslich, 2012).

Ultrastructurally, HIV-1 particles can be observed in 2 different morphologies: Virus particles are released as immature particles from the producing host cell (panels C and E, Figure 1) (Fuller et al., 1997; Wilk et al., 2001). ~ 2500 Gag and Gag-Pro-Pol polyproteins form an electron dense layer attached to the membrane, ~140 nm in diameter (Briggs, 2003; Briggs et al., 2006). After maturation and proteolytic cleavage of the polyproteins into single, functional proteins, a major rearrangement takes place and the capsid is formed (panel D and F, Figure 1). The capsid consists of ~200-250 CA hexamers and 12 CA pentamers (Perilla and Schulten, 2017), meaning, only ~50 of the total CA make up the capsid. The mature capsid measures 120 nm in length and 60 nm in width, on average (Briggs, 2003).

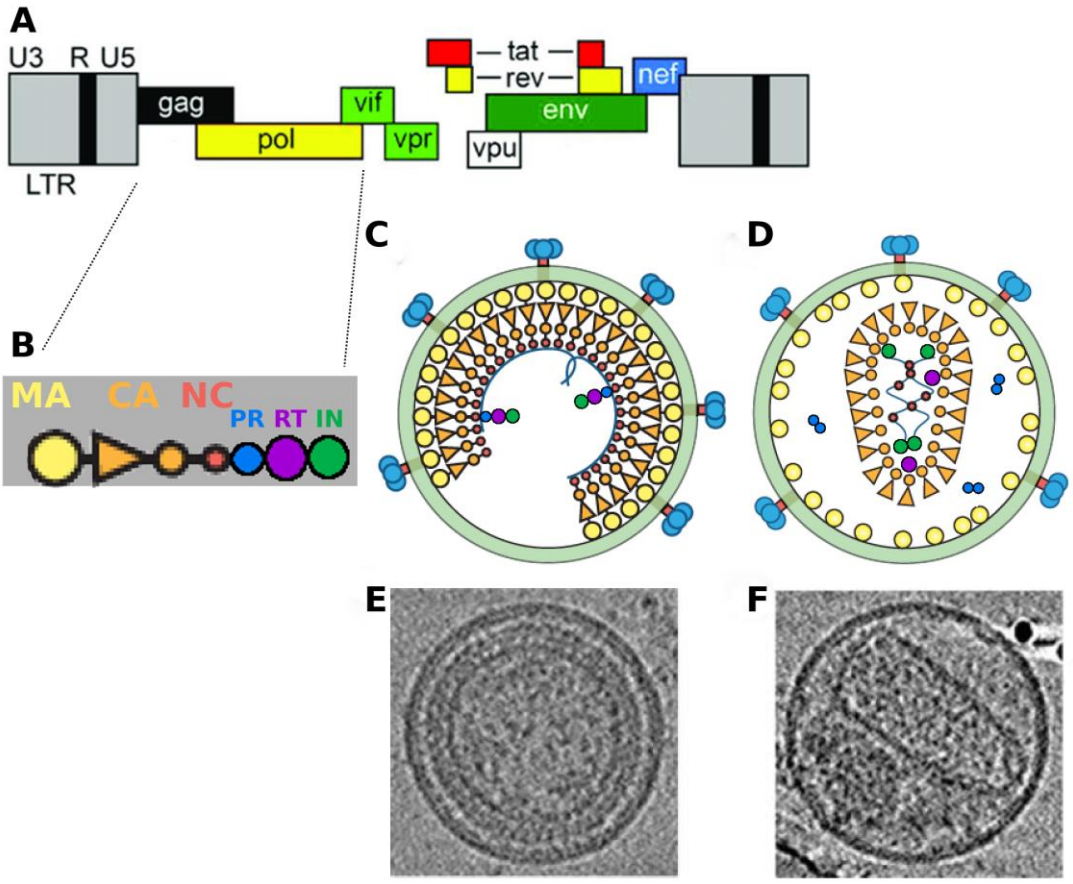

Figure 1: Schematic Genome Organization and Structural Organization of HIV-1

(A) schematically represents the genome organization of HIV-1. The coding regions are flanked by 2 long terminal repeats (LTR). Besides the 4 main reading frames, gag-pro-pol *(*pro-pol *is abbreviated as* pol*) and* env*, a set of accessory proteins is encoded (Vif, Vpr, Vpu, Tat, Rev and Nef). The GagPol polyprotein (B) is only expressed upon ribosomal frameshifting during translation, happening in ~ 5% of all translations. (B) The single proteins encoded by Gag-Pro-Pol are Matrix (MA), Capsid (CA), Nucleocapsid (NC), Protease (PR), Reverse transcriptase (RNA-dependent DNA polymerase, RT) and Integrase (IN). Spacer peptides 1 and 2 (SP1 and SP2) and p6 are graphically not represented. SP1 resides between CA and NC. Downstream of NC, SP2 and p6 are found.*

Gag and Gag-Pro-Pol assemble at the cytoplasmic side of the plasma membrane, forming viral budding sites. Eventually, progeny virus particles pinch off the host cell as immature virus particles (C – schematic, E – cryo-electron micrograph). During maturation, PR dimerizes and proteolytically cleaves Gag and Gag-Pro-Pol into single proteins. This allows major structural rearrangements, most prominently, the formation of the cone-shaped capsid, containing the viral ribonucleoprotein particle, IN and RT. The mature capsid is a hallmark of mature virus particles (D – schematic representation, F – cryo-electron micrograph). The Envelope glycoprotein (Env) resides at the outer surface of the plasma membrane, coordinating target cell binding and virus entry (blue trimers with red stems, panels C-D). Images adjusted from (Felli et al., 2017; Sundquist and Kräusslich, 2012).

1.3 HIV-1 Replication

Note: The main goal of this study was to structurally identify preintegration – and reverse transcription complexes (PIC and RTC). For the structural identification of nuclear PIC, cleavage and polyadenylation specificity factor 6 (CPSF6) was used as the main tool.
For better overview of their respective functions and interactions, CA and CPSF6 are separately discussed later in the introduction (Chapters 1.4 & 1.5).

1.3.1 Entry

HIV-1 is transmitted by mucosal contact with infected body fluids (during sexual intercourse or child birth), by blood transfusion or by reusing infected needles (e.g. in drug abuse) (Barre-Sinoussi et al., 1983). The tropism of HIV is defined by Env, which specifically binds the CD4 receptor and one of the coreceptors CXCR4 or CCR5 (Berger, 1997). Fusion of the viral and cellular membranes follows a defined sequence of events. Env trimers first bind to CD4. This binding leads to pronounced rearrangements in the gp120, a prerequisite for Env to further recognize and engage with coreceptors (Lu et al., 1997; McNicholl et al., 1997; Swanstrom and Coffin, 2012; Trkola et al., 1996). The coreceptor tropism is determined by the Env variable loop 3 (Huang et al., 2005; Liu et al., 2008). Upon binding of Env to its coreceptor, gp41 undergoes structural rearrangements: The fusion peptide, a functional region of the gp41 extracellular domain, inserts into the host cell membrane (Chan et al., 1997; Weissenhorn et al., 1997). A coiled-coil core, consisting of three helices from the aminoterminal gp41 heptad repeat, serves as a scaffold for the further binding of 3 helices from the carboxyterminal heptad repeat. Together, they form the six helix bundle, driving approximation between viral and cellular membrane (Caffrey, 2001; Chan et al., 1997; Weissenhorn et al., 1997). Putative further insertions into the host cell membrane by gp41 host membrane-proximal hydrohpobic residues, are suggested to support membrane fusion by increasing membrane curvature (Buzon et al., 2010). Structural changes are induced also in CD4 upon binding, bringing the viral envelope into closer proximity with the cellular membrane (Liu et al., 2008). Ultimately, the lipid bilayers of the cellular and viral membrane have to mix and fuse, requiring high membrane curvature, which is reported to strongly depend on the membranes' lipid compositions (Brügger et al., 2006; König et al., 2008).
Whether membrane fusion occurs at the plasma membrane (Felts et al., 2010) or after virus particle internalization/endocytosis (Daecke et al., 2005; Dale et al., 2011) was under debate for a long time. One study suggests fusion pore formation at the plasma membrane, while expansion of this fusion pore and viral entry eventually takes place in endosomes (Miyauchi et al., 2009). Meanwhile, it is common understanding that fusion takes place at the plasma membrane (Herold et al., 2014).

Upon fusion with the plasma membrane, the viral capsid needs to bypass a second physical barrier: The cortical actin cytoskeleton supports the plasma membrane in shape and is involved in e.g. cell motility (Hartwig and Yin, 1988; Salbreux et al., 2012). The HIV capsid can only fully access the cytoplasm, once the cortical actin is cleared (Vorster et al., 2011; Yoder et al., 2008). The subviral particle can then enter the cytoplasm unhampered and proceed to the next steps of infection to eventually integrate its genome into the host cell genome. Uptake in - and fusion from endosomes would bypass the cortical actin directly (reviewed in (Blumenthal et al., 2012; Spear et al., 2012; Wilen et al., 2012)).

1.3.2 Reverse Transcription and Transport to the Nucleus

The capsid is composed of ~1200-1500 capsid molecules (CA) and contains two copies of the positive-sense single stranded RNA genome with the attached integrase enzyme (IN), nucleocapsid protein (NC), the reserve transcriptase (RT), Vpr and protease (PR) (see Figure 1, (Ganser et al., 1999; Mattei et al., 2016)).

Before viral genome integration into the host cell genome, the viral RNA must be reverse transcribed into double stranded DNA. This functionality is provided in the RNA-dependent DNA polymerase (reverse transcriptase, RT). Reverse transcription takes place in the cytosol, in so-called reverse transcription complexes (RTC), mainly consisting of the ribonucleoproteins, IN and RT. CA has also been shown to be part of RTC, whether loosely attached, as cone-shaped shell or in another shape remains elusive.

Reverse Transcription follows a sequence of multiple consecutive, unique steps (Hu and Temin, 1990). In short, the negative strand synthesis is primed by a virion-packaged tRNA, positive strand synthesis starts at the nicked template RNA, and 2 DNA strand transfers take place to synthesize a double stranded DNA (described in more detail in Figure 2).

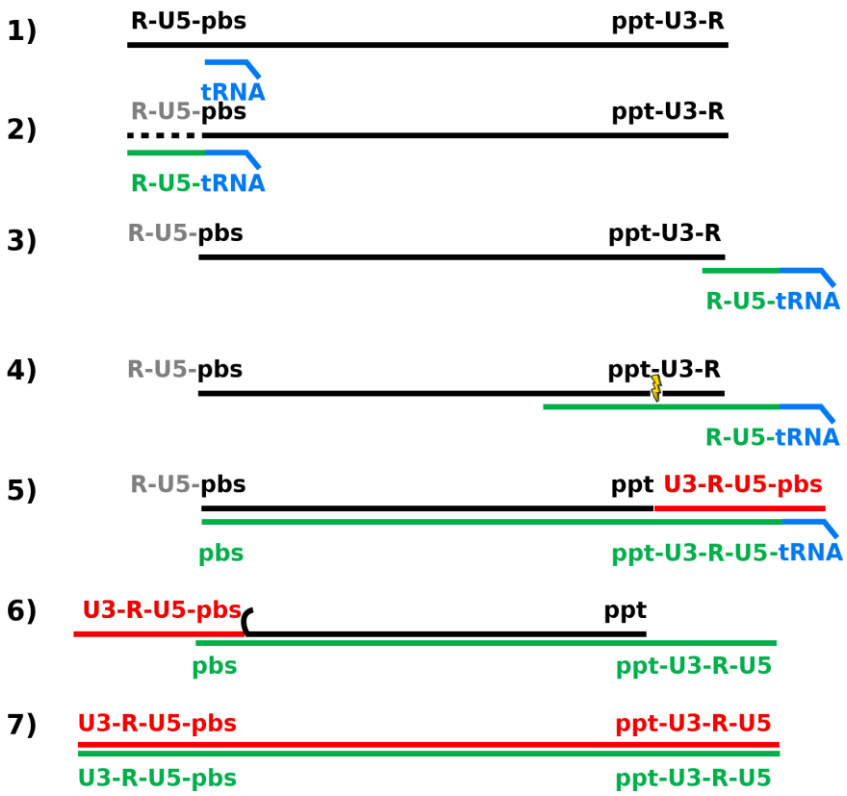

Figure 2: Schematic HIV Reverse Transcription

The viral RNA (black) needs to be reverse transcribed into dsDNA (red & green) for integration. A tRNA (blue) binds the primer binding site (pbs, 1), from where DNA synthesis of the minus strand (green) starts (2). While replicating, the RNAseH degrades the RNA template's 5' LTR (R-U5). After reaching the templates 5' end, the minus strand translocates and binds to the template 3' LTR (3) from where minus strand synthesis continues, while the RNAseH activity creates a single strand break (nick) between the polypurine track (ppt) and the U3 region (4). Plus strand (red) synthesis starts at the nick and replicates until the pbs (5). A second strand transfer takes place (6) and DNA synthesis continues at both strands to complete them.

For DNA synthesis, the host cells dNTP pool is employed. During reverse transcription, the RTC is actively transported to the host cell nucleus. Transport along microtubules, employing kinesins (towards plus-end) and dyneins (towards minus-end) has been reported. Furthermore, transport along actin microfilaments via myosin motors have been suggested (HIV intracellular trafficking is reviewed in (Gaudin et al., 2013)).

The viral DNA, together with cellular and viral proteins (e.g. IN and CA) forms the PIC. When and where exactly viral DNA synthesis is completed, so far remains elusive. At one point, the viral DNA gets transported into the nucleus, where it can get integrated into the host cell genome.

1.3.3 Nuclear Entry of HIV-1 and Subnuclear Localization

In contrast to ions and small molecules, the macromolecular PIC requires active transport to enter the nucleus (Kabachinski and Schwartz, 2015; Knockenhauer and Schwartz, 2016; Paine et al., 1975). Numerous viral factors are known to enable nuclear import in nondividing cells:

The HIV-1 PIC can interact with - and transit through nuclear pores, which is in contrast to other retroviruses, such as moloney murine leukemia virus (MoMLV, genus: *Gammaretrovirus*). MoMLV requires breakdown of the nuclear envelope during mitosis for nuclear entry (Emerman et al., 1994; Suzuki and Craigie, 2007).

Replacing the CA-encoding part of *gag* by the homologous MoMLV CA-encoding *gag* region was found to be sufficient to render the resulting HIV chimera noninfectious in postmitotic cells, and to depend on nuclear envelope breakdown. The chimera was apparently not anymore able to have its genome transported into the nucleus (Yamashita and Emerman, 2004).

Besides the nuclear localization signal in CA, further signals promote the import into the nucleus:

IN e.g. carries a noncanonical nuclear localization signal (NLS) (Bouyac-Bertoia et al., 2001). And a special DNA structure (DNA flap) in the polypurine tract (PPT) region of the viral DNA is also reported to strongly promote nuclear entry (Arhel et al., 2007; Sirven et al., 2000; Zennou et al., 2000).

The RTC has been shown to interact with a multitude of nuclear pore proteins (Nup): Nup153 is to date identified as the most important interaction partner (Brass et al., 2008). Knockdown of this protein results in strongly reduced HIV-1 subviral nuclear import and infectivity (Di Nunzio, 2013; Di Nunzio et al., 2012; Woodward et al., 2009). Nup153 resides at the nucleoplasmic side of the nuclear pore complex, where its FG-repeats interact with the incoming HIV-1 subviral particle via CA (Matreyek et al., 2013).

Knockdown of Nup358 (also called RanBP2) has also been shown to strongly impair nuclear entry of HIV-1 PIC (Zhang et al., 2010). Nup358, in contrast to Nup153, is located at the cytoplasmic side of the NPC and believed to be involved in PIC docking to the NPC (Di Nunzio et al., 2012). Furthermore, Nup98 and Nup214 are suspected to also affect nuclear entry (König et al., 2008).

CPSF6 and TNPO3 as host dependency factors will be discussed separately (chapter 1.5).

In addition to host dependency factors, there are also numerous host restriction factors. Those are often interacting with CA, where numerous resistance mutations can repeatedly be identified in. Some of the known cellular restriction factors are Cyclophillin A, MX2, SUN1 and SUN2 (reviewed in (Bhargava et al., 2018)).

These factors are described to reduce infectivity, while the exact mechanism of restriction remains largely elusive. PICs are considered to be displaced from preferred integration sites or to be hampered entering the nucleus. This clearly points out that we need to understand nuclear entry in more detail.

1.3.4 HIV-1 Integration

A hallmark of retroviruses is the integration of the viral genome into the host cell genome, where it resides either as latent provirus (forming an inactive, dormant reservoir that can be activated years later) - or as actively transcribing provirus. The central functionality of integration lies within IN. Still in the cytoplasm, IN dimers bind to each of the viral DNA long terminal repeats (LTR, (Krishnan et al., 2010)), forming the intasome (vDNA with IN tetramer). Of both viral DNA blunt ends at the LTRs, 2 nucleotides are removed from the 3' end (Hare et al., 2010; Maertens et al., 2010). The PIC (containing the intasome) is then transported into the nucleus, as described above. LEDGF and CPSF6 are currently understood to be the host factors with the most pronounced influence on integration site targeting. The current opinion is a 2-step mechanism: CPSF6 is supposed to first bind CA directly and to target the PIC to sites of high transcriptional activity (Sowd et al., 2016). In the second step, LEDGF, also interacting with CA, further directs the PIC towards gene bodies (Debyser et al., 2015; Singh et al., 2015). It has in fact been described repeatedly that HIV-1 does not integrate randomly into the host cell genome, but strongly prefers gene-rich regions.

Disruption of CPSF6 and LEDGF is reported to affect the integration site targeting (Lusic and Siliciano, 2017).

At the LTR, IN increases the electron-density of the 3' hydroxyl group oxygens at the shortened 3' ends and thereby renders them strongly nucleophilic. Those nucleophiles attack the host cell DNA and produce 1 nick each, usually in distance of 5 nucleotides. The viral DNA 3' end is ligated to the 5' phosphate of the host cell DNA (Vink et al., 1990). The 5' ends of the viral DNA first remain unligated and are sensed as single strand breaks by the host cell. In a process called "gap-repair", also the 5' ends of the viral DNA are connected to the host cell DNA. Thereby, the viral DNA is eventually fully integrated into the host cell genome, flanked by the duplicated pentanucleotide host DNA sequence (due to the 5 nucleotide-distance of the introduced nicks).

1.3.5 Viral Gene Expression, Particle Budding, Release and Maturation

This study aims to identify infectious RTC and PIC capsid structures. Progeny virus particle production, starting from viral gene expression, is not involved in the analyzed processes and are therefore described more concisely.

Gag and Gag-Pro-Pol polyproteins are translated and localize to the host cell plasma membrane, where they insert into the membrane via the myristoyl group attached to MA. Protein-protein interactions, mainly within Gag domains, mediate the formation of spherical particles. Env as a glycoprotein requires glycosylation and is therefore translated at rough endoplasmic reticulum (rER). During transport to the plasma membrane, Env trimers are cleaved into the gp41 and gp120 subunits. MA interactions with Env mediate the recruitment of Env trimers to the viral budding site. 2 copies of the genomic viral RNA are packaged into the nascent virus particle via interaction with the RNA packaging sequence. Furthermore, accessory proteins and the lysine-tRNA (necessary for reverse transcription priming) are packaged into the virus particle by different means. Gag and Gag-Pro-Pol multimerization is sufficient for particle formation, yet, the final scission from the plasma membrane is mediated by the host cell endosomal sorting complex required for transport (ESCRT) machinery. Members of the ESCRT complex are recruited by the Gag-carboxyterminal p6 peptide. After ESCRT mediated scission from the membrane, the virus particle is released in its immature form (see Figure 1, panels C and E).

In a process called maturation, the viral protease heterodimerizes and proteolytically cleaves the Gag and Gag-Pro-Pol polyproteins step wise into the single proteins (reviewed in (Freed, 2015)) as described in Chapter 1.2. Ultrastructurally, the final structural rearrangement can be best observed via electron microscopy (see Figure 1, panels D and F), but also superresolution microscopy allows to observe virus maturation (Hanne et al., 2016a). Virus assembly, budding and Maturation are reviewed in (Sundquist and Kräusslich, 2012).

1.4 HIV-1 CA

CA has been shown to interact with a multitude of cellular factors, being involved in steps during cytoplasmic trafficking, but also in nuclear steps of the viral replication cycle (see upper chapters 1.3.2, 1.3.3 & 1.3.4, reviewed in (Fassati, 2012)). To affect various steps in the viral life cycle, CA first of all needs to be present. However, detection of CA (e.g. by immunofluorescence) does not allow to draw conclusions about a potentially associated capsid structure. There might be a structure retained. Likewise, CA could rearrange into another structure, or could colocalize at RTC and PIC without occupying any distinct structure, while still mediating the reported functions. It was

therefore the main goal of this study to identify, whether productive RTC and PIC correlate with an apparent (capsid-derived) structure or not. In the following chapter, we want to illuminate why this question is debated highly controversial and of huge importance to answer.

An average virus particle contains roughly 2500 CA molecules. ~ 50% assembles into the capsid, the other half remains without apparent structure (Ganser et al., 1999; Mattei et al., 2016). The distinct structure of the HIV-1 capsid consists of ~ 250 CA hexamers and 12 so-called pentameric defects. The latter can be considered the corners of the structure, while hexamer arrays organize into honeycomb-like planar structures (see Figure 3). The unique capsid structure is achiever by interspersing 5 pentamers (or pentameric defects) into the narrow end and 7 pentamers into the wide end. This particular arrangement called fullerene architecture, due to its high similarity to elemental carbon structures (called fullerenes) (Ganser et al., 1999).

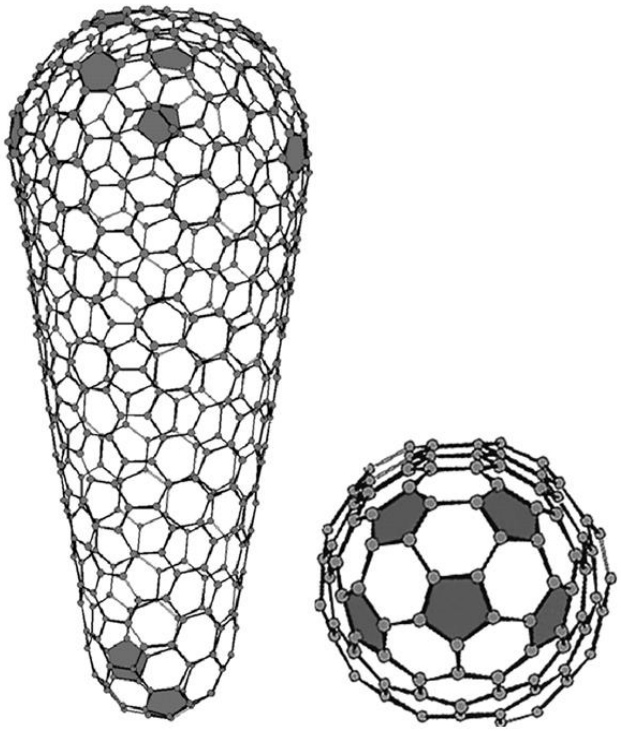

Figure 3: Fullerene HIV-1 Capsid Model

This model displays the fullerene-like arrangement of CA hexamers into the unique cone-shaped capsid. Pentameric defects, or CA pentamers, are shown as filled gray patches. 5 pentamers are located in the narrow end (better recognizable in the bottom view, left), 7 pentamers are located in the wide end of the structure. The majority of the capsid structure is made up of ~ 250 CA hexamers. Figure adjusted from (Ganser et al., 1999).

The capsid contains the viral RNA genome, IN, Vpr and NC (Bukrinsky et al., 1993; Miller et al., 1997). During entry, the capsid is released into the cytoplasm and at one point must undergo a process called “uncoating”. This process is necessary to release the viral DNA and IN from the capsid-enclosure, allowing them to access the host DNA for integration. Timing and kinetics of this process are still elusive.

The dimensions of an average capsid structure are 120 nm in length and 60 nm in width. The nuclear pore complex, however, has a central pore opening of merely ~ 40 nm nm (Bui et al., 2013). This means that the HIV-1 capsid is simply too big to enter the nucleus as such (Matreyek and Engelman, 2013; Whittaker, 2003).

If uncoating takes place before nuclear entry, it happens at some point after fusion, during (cytoplasmic) reverse transcription or at the nuclear envelope.

Biochemical assays were developed to elucidate the uncoating behavior of capsid, called “fate of capsid” assays. Permissive cells were infected and lysed after different time points. CA was then immunoprecipitated. In ultracentrifugation, particulate CA (arranged in capsids) would sediment much faster than soluble CA (Yang et al., 2014). In the afore-mentioned publication the majority of CA was found soluble quickly after infection and therefore suggests uncoating taking place soon after entry (Karageorgos et al., 1993), reviewed in (Arhel, 2010)). Also, reverse transcription has been reported to promote uncoating (Hulme et al., 2011; McDonald et al., 2002; Rankovic et al., 2017). The involvement of reverse transcription in uncoating is supported by calculations, saying that the viral DNA is too big and inflexible to fit into the capsid shell. This in turn is supported by fluorescence microscopy imaging of dual-labeled HIV particles: One fluorophore labels IN and a second fluorophore is used as marker for fluid capsid content, mixing with the cytoplasm upon (partial) capsid disassembly / uncoating. IN.eGFP positive viral particles where shown to lose the fluorescent fluid phase marker early after entry, which was interpreted as uncoating or loss of capsid integrity (e.g. (Francis et al., 2016)). Lastly, the HIV-1 capsid requires an optimal stability for infection: Both, hyper- and hypostabilization by introducing CA mutations, reduce the infectivity (Forshey et al., 2002). So far, it was only possible to visualize intracellular capsids upon introduction of hyperstabilizing CA mutations (Jun et al., 2011). If the capsid was retained in shape for prolonged periods of time, it should have been possible to also visualize metastable wildtype capsids.

Uncoating taking place in the cytoplasm poses the risk of HIV detection by cellular immune sensors (Santos et al., 2016). This would most likely lead to abrogation of infection (Lahaye et al., 2013;

Maelfait et al., 2014). In this regard, uncoating happening directly at the nuclear envelope would seem the ideal location for uncoating.

However, recent studies repeatedly detected CA in the nuclei of infected cells, arguing for at least a partial amount of CA to stay attached with the subviral particle (Francis et al., 2016; Hulme et al., 2015; Peng et al., 2014). It is worth mentioning that only a minor fraction of the HIV particles productively contribute to infection and progeny virus production (Marozsan et al., 2004; Vogt, 1997). Yet, this is also controversially discussed (Thomas et al., 2007). This means that bulk assays, such as the fate of capsid-assay cannot be extrapolated to the single infectious subviral particle. Also, when single particles are analyzed, it is necessary to regard the ones, which contribute to infection. These prerequisites are given in a study from our lab: the CA fluorescence intensities of viral particles was highly comparable to viral DNA-positive nuclear PIC, arguing for high CA amounts retained throughout the cytoplasmic stages and nuclear entry. As mentioned before, merely detecting CA cannot be extrapolated necessarily detecting an associated capsid structure, yet, it poses the possibility.

1.5 Cleavage and Polyadenylation Specificity Factor 6 - CPSF6

CPSF6 was first thought to be a cellular restriction factor for HIV-1: The expression of a truncated murine CPSF6, mCPSF6-358, has been shown to reduce viral infectivity (Lee et al., 2010). Truncated versions of CPSF6 can interact with CA but lack their serine-arginine-rich domain (SR-domain). This domain is necessary for CPSF6 to interact with the importin ß-like karyopherin TNPO3. TNPO3 is reported to mediate the nuclear import of SR proteins, such as the full-length CPSF6 (Brass et al., 2008; De Iaco et al., 2013; Gallay et al., 1997; Valle-Casuso et al., 2012). Truncated versions of CPSF6 (murine mCPSF6-358 or human hCPSF-375, (Hori et al., 2013; Lee et al., 2010)) are therefore not located to the nucleus, but primarily to the cytoplasm. The same holds true for full-length CPSF6 when its nuclear import-mediator TNPO3 is knocked out. Under native conditions, when CPSF6 is mainly located to the nucleus, it has been found to have key functions as a host dependency factor for HIV-1. CPSF6 has been shown to increase HIV-1 infectivity by supporting nuclear import of viral DNA (reviewed in (Lusic and Siliciano, 2017)).

Interestingly, it was found that CPSF6 shares its CA-interaction site with Nup153 (CA K70 and S102, as has been shown before ((Price et al., 2014), see Figure 4). This means that premature interaction of CPSF6 and CA in the cytoplasm, due to altered subcellular CPSF6 localization, would hamper Nup153 to interact with CA, thereby reducing nuclear import. Isothermal titration

calorimetry experiments with $Nup153_{1407-1423}$ and $CPSF6_{313-327}$ showed only marginal differences between Nup153 and CPSF6 binding affinities to CA hexamers (Price et al., 2014).

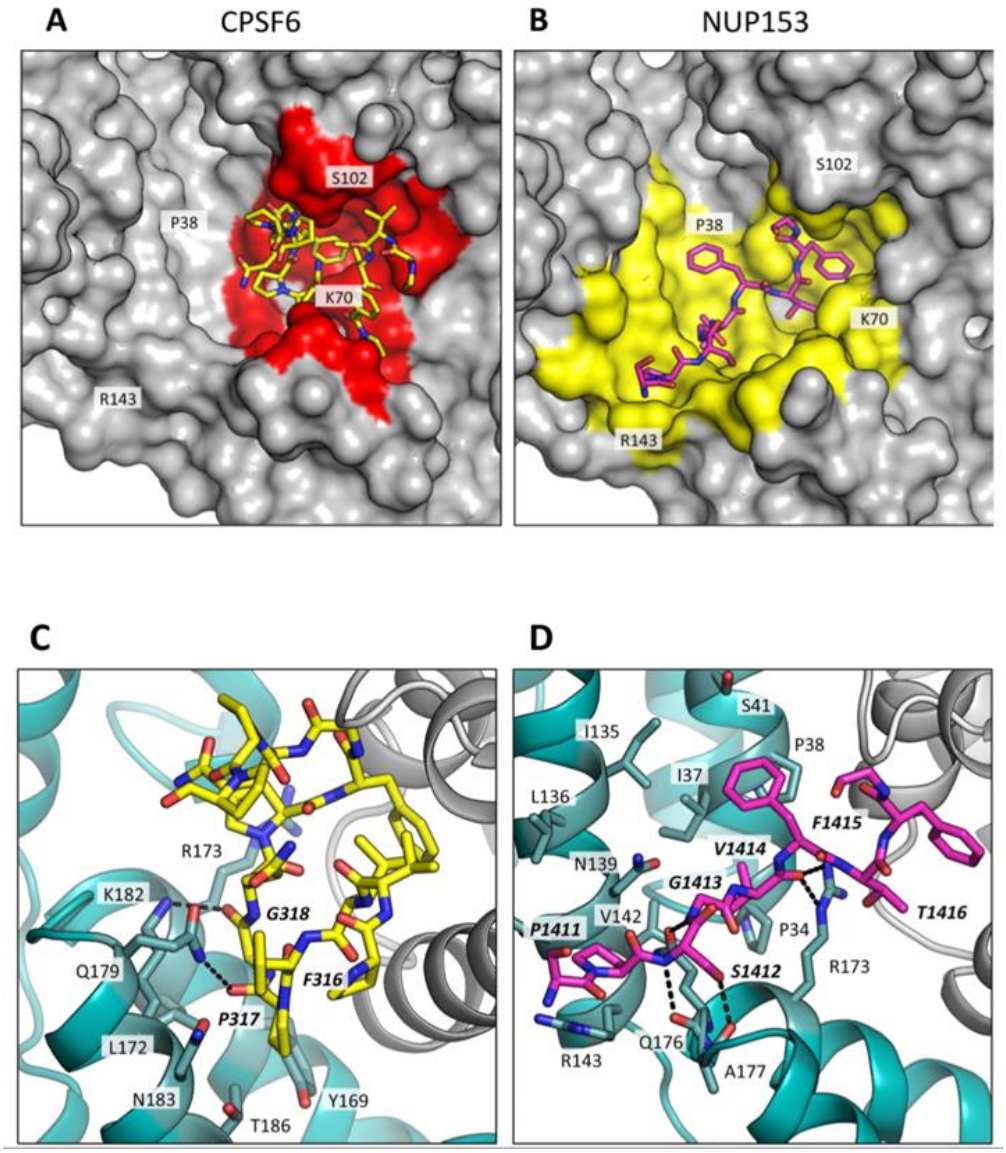

Figure 4: Binding Sites of CPSF6 and Nup153 at Hexameric CA

This figure illustrates the interaction of $CPSF6_{313-327}$ (yellow, A and C) and $Nup153_{1407-1423}$ (pink, B and D) with hexameric CA. Panels A and B show in gray the molecular surface of hexameric CA. The interaction footprint is shown in red (A) and yellow (B). Panel C and D show $CPSF6_{313-327}$ (C) and $Nup153_{1407-1423}$ (D) peptides bound to hexameric CA, one monomer shown in gray, and a second one shown in cyan. CA key residues are highlighted in panels A and B, CPSF6 and Nup153 residues in panels C and D. Figure adjusted from (Price et al., 2014). This illustration makes it obvious that the interaction sites of CPSF6 and Nup153 largely overlap.

Experimental data from our lab led to a working model hypothesis: After the incoming subviral particle engages with Nup358 at the cytoplasmic site of the NPC, it starts to translocate into the nucleus. Nup153, closer to the nucleoplasmic side, interacts with CA and thereby might promote its import. Within the nucleus, the CA-Nup153 interaction is competed off by CPSF6. Thereby, the Nup153 is free again to interact with other CA molecules, located closer to the cytoplasm. The cycle of CA interacting first with Nup153, then with CPSF6, might lead to a pulling force, into the nucleoplasm (manuscript in preparation, David Bejarano, Dr. Ke Peng).

Most importantly for this study, a published microscopy study from our lab (Peng et al., 2014), clearly showed a strong colocalization of nuclear PIC with CPSF6 cluster fluorescence signals.
Here, we employed CPSF6 as a surrogate marker to identify nuclear PIC, by expressing it as a fluorescence protein fusion (rCPSF6wt$_{AA}$.mCherry).

1.6 Technical Implementation: Correlative Light and Electron Microscopy (CLEM)

Light Microscopy was already invented in 1676 by Antoni van Leeuwenhoek (Khattab, 1995). He was the first person to build a microscope that would allow visualizing bacteria, a breakthrough in sciences. Ever since, this method was continuously advanced, in particular by 2 important inventions / discoveries:

Immunohistochemistry

In 1940, Albert Coons, was the first to develop the immunohistochemistry methodology (immunofluorescence labeling) (Coons et al., 1941). The possibility to specifically label antigens of interest and define localization and colocalization with other proteins and factors is invaluable. The restriction of this technique being limited to still images of fixed cells was then overcome by the second huge improvement:

Isolation and Implementation of Fluorescence Proteins

In 77 A.D. already, Pliny the Elder (Gaius Plinius Secundus) observed marine glowing animals. Two of his observations were the purple jellyfish (*Pelagia noctiluca*) and an edible clam, making his mouth glow (*Phalos dactylus*) (Pieribone and Gruber, 2005). Almost 2 millennia later, the Green Fluorescent Protein (GFP) was isolated from *Aequora victoria* jellyfish (Shimomura et al., 1962). Another 30 years later, the GFP coding sequence was solved (Prasher et al., 1992), and 2 more years later, the first fluorescence protein fusion was expressed and imaged (Chalfie et al., 1994).

(Osamu Shimomura, Martin Chalfie and Roger Tsien were awarded with the Nobel Prize in Chemistry for the discovery and development of GFP in 2008). Henceforth, it was possible to follow fluorescent fusion proteins over time in living organisms. Further fluorescence proteins were identified and developed, today offering a huge variety of more - or less stable, faster - and slower maturing and more – or less bleaching-resistant proteins (Day and Davidson, 2009; Miyawaki, 2011). Besides fluorescence protein fusions, a variety of other labeling methods has been developed and implemented for molecular research, e.g. also allowing to label lipids (e.g. TF-Chol, reviewed in (Klymchenko and Kreder, 2014), labeling techniques reviewed in (Hanne et al., 2016b; Sakin et al., 2016)). However, light microscopy also has its limitations: Ernst Abbe defined the resolution limit of lense-based systems with respect to the light's wavelength, suggesting the highest possible resolution to roughly equal half of the wavelength (Abbe, 1873). In other words, when working with visible light, the maximum resolution amounts to ~200-300 nm. Our structure of interest, the HIV capsid, measures merely 120 by 60 nm. Even though superresolution microscopy techniques, such as PALM/STORM and STED (Sahl et al., 2017; Sydor et al., 2015; Vicidomini et al., 2018) allow higher-resolution imaging, it would not be sufficient to undoubtedly answer the question about the putative shape underlying productive HIV-1 RTC and PIC. Additionally, fluorescent labeling allows to specifically label and image distinct structures / proteins, whereas the cellular environment remains mostly unknown, appearing simply dark (unlabeled).

Electron microscopy on the other hand allows to image at much higher resolution and without specific labeling. Therefore, it would not only allow to image putative RTC and PIC structures of, but also to visualize the complexes' subcellular environment.

The first electron microscope (the "Übermikroskop") was developed by Ernst Ruska and Max Knoll in March 1931 (Knoll and Ruska, 1932). Since an electron's wavelength is much shorter than a photon's, the achievable resolution is much higher (Abbe, 1873) in comparison to light microscopy (Ernst Ruska, Gerd Binning and Heinrich Rohrer were awarded with the Nobel Prize for Physics in 1986). In 1939, tobacco mosaic virus particles were imaged, the very first time, the elusive term "virus [particle]" could be linked to a visual representation (Kruger et al., 2000). Like in light microscopy, fascinating developments have been achieved, allowing researchers today to solve structures at few Å resolution (e.g. (Schur et al., 2016)).

In contrast to light microscopy, electron microscopy cannot be applied on living specimen. Specific labeling (using e.g. colloidal gold-coupled antibodies) can generally be performed. However, retaining the accessibility and antigenicity of antigens for detection by immunolabeling usually comes at the cost of e.g. low contrast or suboptimal ultrastructural preservation.

Both, light - and electron microscopy, offer powerful advantages but also have strong drawbacks. Correlative Light and Electron Microscopy (CLEM) combines the advantages of both techniques: Light microscopy allows to specifically label and image the event or structure of interest (in this study: RTC and PIC), while electron microscopy at the very same position yields high resolution images of the region of interest (ROI), including the surrounding environment. Fulfilling the requirements of both imaging methods, can be highly demanding, technically. However, the gained information is extremely valuable. The method and protocol of choice depend on a multitude of factors (e.g. nature of samples (cell layers or full organisms), expected size of observed structures, possibilities of fluorescent labeling, required correlation precision, etc), therefore, it is not surprising that the variety of applied protocols is overwhelming (e.g. On-section CLEM: (Kukulski et al., 2011), Live-cell imaging CLEM (Jun et al., 2011; Rijnsoever et al., 2008), reviewed in (de Boer et al., 2015; Bykov et al., 2016; Koistinen et al., 2016)). Identifying and adjusting a fitting method can be laborious, but, once it works, can yield unforeseen results - as presented in this study.

1.7 Aim and Relevance of This Study

The structure underlying the HIV-1 RTC and PIC is of immense interest. Whether fast uncoating occurs, or whether the HIV-1 capsid is retained in its shape for a prolonged time, is important to answer in order to provide more detailed insights into the HIV-1 biology, and maybe even to lay the foundation for rationally designed inhibitors: Is a capsid structure retained in RTC and PIC? If yes, is the retention of that structure important? Can the capsid be targeted for destabilization and can that way infection be reduced? Or, in the case of fast uncoating, should we aim stabilizing the structure to prevent infection?

Since these questions could not be answered to date, the final goal of this study was to shed light (and electrons) onto the presence or absence of a capsid structure in RTC and PIC.
Here, we present how we assessed the possibility to specifically identify cytoplasmic RTC and nuclear PIC complexes. While the technical problems did not allow to gain structural information on RTC, we developed and applied a protocol for high precision on-section correlation of light - and electron micrographs which allowed us to visualize the structure of the elusive HIV-1 nuclear PIC. We were able to repeatedly image nuclear PIC structures. These structures visually appear reminiscent of viral capsids. While fitting in shape, we observed considerable differences between cores of cell-surface bound virus particles and the uncovered nuclear PIC structures.

1.8 Term Definitions

Scientific exchange can only be effective when terms and definitions are clarified and used correctly. Minor differences in the interpretation of key terms can lead to misunderstandings and complicate scientific progress. To best convey the content of this, it is therefore my ambition to clearly state study-relevant definitions and to apply nomenclature correctly.

1.8.1 Virus, Virus Particle, Virion and Subviral Particle

The term *virus* has two distinct meanings, the italic written virus species (i.e. *Human immunodeficiency virus 1*) and the actual virus name (i.e. human immunodeficiency virus 1).
Virus in the sense of a species definition is nothing tangible, but a human understandable definition, allowing to assign an observed entity to phylogenetic classes (*Human immunodeficiency virus 1* belongs to the genus *Lentivirus*). The actual human immunodeficiency virus 1 (abbreviated as HIV-1) is the sole member of the species *Human immunodeficiency virus 1* (species names are not abbreviated). Such as humans being members of the species *Homo sapiens sapiens*.
The actual organism is referred to as *virus particle*. Virus particles can be isolated, injected and subjected to e.g. electron microscopy. A virus particle is the ultrastructural or functional representation of a virus. (Kuhn and Jahrling, 2010) It has been further suggested to name the productively infectious subpopulation of virus particles “virions”, which has so far not been officially implemented (Kuhn et al., 2013).
“Subviral particle” is defined as an incomplete virus particle. An enveloped virus particle that has fused with the plasma membrane at that moment separates into the fused membrane and the virus particle content, e.g. the core. The core, lacking its envelope to ultrastructurally represent the full virus particle, therefore represents a subviral particle.

1.8.2 Capsid Protein, Capsid and Core

Retrovirologists agreed on a definite nomenclature for retroviruses, coding domains and encoded (poly)proteins (Petropoulos, 1997). The relevant nomenclature is summarized here:
While “The capsid” defines the conically shaped, roughly 120 x 60 nm big structure observed in virus particles, “capsid” (without article) is defined as the capsid protein, also written as CA. Therefore, CA monomers make up the Capsid. “The core” is used interchangeably with “the capsid”. “Factor X interacts with CA” has therefore a very different meaning from “Factor X interacts with (the) capsid”.

2 Materials and Methods

2.1 Materials

2.1.1 Chemicals and Consumables

Chemical / Consumable	Supplier
0.45 µm sterile filter (Cat# KH55.1)	Carl Roth, Karlsruhe, Germany
6x agarose gel loading dye	New England Biolabs, Ipswitch, MA, USA
Acetone, dry (Cat# 481007.1611)	AppliChem, Darmstadt, Germany
Acrylamide 4K, 29:1 solution	AppliChem, Darmstadt, Germany
Agarose	Carl Roth, Karslruhe, Germany
Albumin Fraction V	Sigma-Aldrich, Steinheim, Germany
Ampicillin	Carl Roth, Karlsruhe, Germany
APS	Carl Roth, Karlsruhe, Germany
Bromophenolblue	Chroma, Fürstenfeldbruck, Germany
BSA Fraction V (Cat# A2153)	Sigma-Aldrich, Steinheim, Germany
$CaCl_2$	Merck (Sigma-Aldrich), Darmstadt, Germany
Cell Culture Material	
o 8 chamber microscopy slide	Nunc, Rochester, NY, USA
o 6 well plate (Cell Star, Cat# 657160)	Greiner bio-one, Frickenhausen, Germany
o 10 cm dish (Cell Star, Cat# 664160)	Greiner bio-one, Frickenhausen, Germany
o 15 cm dish (Cell Star, Cat# 639 160)	Greiner bio-one, Frickenhausen, Germany
o T25 (Cell Star, Cat# 690160)	Greiner bio-one, Frickenhausen, Germany
o T75 (Cell Star, Cat# 658170)	Greiner bio-one, Frickenhausen, Germany
o T175 (Cell Star, Cat# 660160)	Greiner bio-one, Frickenhausen, Germany
o Cell Scraper S	Techno Plastic Products, Trasadingen, Switzerland
Chloroform	VWR, Fontenay-Sous-Bois, France
Click-It EdU Detection Kit	Molecular Probes, Life Technologies, Eugene, OR, USA
DMSO	Merck, Darmstadt, Germany
dNTP mixture	Fermentas, Thermo Scientific, Schwerte, Germany

Chemical / Consumable	Supplier *continued*
Dulbecco's Modified Eagle's Medium, high glucose (4.5 g/l)	Gibco/Invitrogen, Karlsruhe, Germany
EDTA (Cat# 324503)	Merck, Darmstadt, Germany
EGTA (Cat# 324626)	Merck, Darmstadt, Germany
EndoFree Plasmid Maxi Kit	Qiagen, Hilden, Germany
Epon-812	Electron Microscopy Sciences, Hatfield, PA, USA
Ethanol	Merck (Sigma-Aldrich), Darmstadt, Germany
Fetal calf serum	Biochrom, Berlin, Germany
Filter Paper	VWR, Leuven, Belgium
Finder Grids	PLANO, Wetzlar, Germany
Fish skin gelatin (Cat# G7765)	Sigma-Aldrich, Steinheim, Germany
Gel Red Nucleic Acid Gel Stain	Biotium, Fremont, CA, USA
Gelatin	AppliChem GmbH, Darmstadt, Germany
GeneRuler 1kb Plus ladder	Fermentas, Thermo Scientific, Schwerte, Germany
Glass slides for Pioloform	Diagonal, Münster, Germany
Glass Vials (Cat# B793)	Agar Scientific, Essex, England
Glutaraldehyde, 25% solution	Electron Microscopy Sciences, Hatfield, PA, USA
Glycerol	AppliChem GmbH, Darmstadt, Germany
Glycine	Fisher Scientific, Loughborough, UK
HEPES (cell culture grade)	Carl Roth, Karlsruhe, Germany
Hexadecene (Cat# 8.22064.0500)	Merck, Darmstadt, Germany
Hoechst 33258	Sigma-Aldrich, Steinheim, Germany
Isopropanol	Sigma-Aldrich, Steinheim, Germany
Kanamycin	Carl Roth, Karlsruhe, Germany
LB Medium Powder	Carl Roth, Karlsruhe, Germany
Lead Nitrate (Cat# 1.07397.1000)	Merck, Darmstadt, Germany
LiCor blocking buffer	Licor Biosciences, Lincoln, USA
Lintfree tissues (Cat# 75512)	Kimberly-Clark, Reigate, UK
Lowicryl HM20	Polysciences, Warrington, PA, USA
LR Gold (Cat# 17412)	Polysciences, Warrington, PA, USA
Methanol	AppliChem, Darmstadt, Germany
Methylcellulose (Cat# M-6385)	Sigma-Aldrich, Steinheim, Germany
Methylene Blue (Cat# A514.1)	Carl Roth, Karlsruhe, Germany

Chemical / Consumable	Supplier *continued*
NH_4	Carl Roth, Karlsruhe, Germany
Nucleospin Gel and PCR Cleanup Kit	Macherey Nagel, Düren, Germany
Osmium tetroxide, 4%	Science Services, Munich, Germany
Paraformaldehyde, 16% solution	Electron Microscopy Sciences, Hatfield, PA, USA
Penicillin / Streptomycin	Invitrogen, Karlsruhe, Germany
Pioloform F	PLANO, Wetzlar, Germany
PIPES (Cat# 9156.3)	Carl Roth, Karlsruhe, Germany
Protein A-coupled colloidal gold	CMC, Utrecht, Netherlands
Protein marker (PageRuler Prestained)	Thermo Scientific, Schwerte, Germany
PVDF membrane (Immobilon-P)	Millipore, Billerica, MA, USA
Razor Blades (Cat# T 5016)	PLANO, Wetzlar, Germany
Restriction Enzymes	New England Biolabs, Ipswitch, MA, USA
RPMI-1640	Invitrogen, Karlsruhe, Germany
Sapphire Discs 50µm (Cat# 405)	Engineering Office Wohlwend, Sennwald, Switzerland
SDS	AppliChem, Darmstadt, Germany
Sodium Cacodylate	Serva Electrophoresis, Heidelberg, Germany
Sodium Citrate	Honeywell Riedel-de Haën, Seelze, Germany
Sodium Hydroxide Pellets	Merck (Sigma-Aldrich), Darmstadt, Germany
ß-mercaptoethanol	Sigma-Aldrich, Steinheim, Germany
Sucrose	AppliChem, Darmstadt, Germany
TAMRA (Cat# BCFA-008)	baseclick, Neuried, Germany
TEMED	Biomol, Hamburg, Germany
Tetrakis(acetonitrile)copper(I) Tetrafluoroborate	Sigma-Aldrich, Steinheim, Germany
TetraSpeck Fiducials (100 nm)	Sigma-Aldrich, Steinheim, Germany
Tris	Carl Roth, Karlsruhe, Germany
Triton X-100	Merck, Darmstadt, Germany
Trypsin	Biochrom, Berlin, Germany
Tween 20	Carl Roth, Karlsruhe, Germany
Uranyl Acetate (Cat# 22400)	Electron Microscopy Services, Hatfield, PA, USA
Western Blot blocking buffer concentrate	Li-Cor, Lincoln, NE, USA

2.1.2 Devices and Instruments

Device / Instrument	Supplier
AFS2	Leica Mikrosysteme, Vienna, Austria
o Binocular S6E	Leica Mikrosysteme, Vienna, Austria
o Robot EM FSP	Leica Mikrosysteme, Vienna, Austria
o 16707153 Filling Needles	Leica Mikrosysteme, Vienna, Austria
o 16707154 Reagent Bath	Leica Mikrosysteme, Vienna, Austria
o 16707157 Flowthrough Ring	Leica Mikrosysteme, Vienna, Austria
o 16707158 Reagent Container	Leica Mikrosysteme, Vienna, Austria
o Syringe, 10 mL Luer Lock	Braun Melsungen, Melsungen, Germany
Bacteria Incubator (IN75)	Memmert, Schwabach, Germany
Bacteria Shaker Multitron Pro	Infors, Bottmingen, Switzerland
Carbon Coater EMACE600	Leica Mikrosysteme, Vienna, Austria
o Carbon Thread BP2308	Baltic Präparation, Niesgrau, Germany
Cell Culture Centrifuge (MegaFuge 40R)	Heraeus, Hanau, Germany
CLEM sandwich holder (Cat# A7816)	Invitrogen, Karlsruhe, Germany
o 25 mm round glass (Cat# G31-0171)	VWR, Fontenay-Sous-Bois, France
Cover glasses 12 mm	Menzel Gläser, Thermo Scientific, Schwerte, Germany
DNA Electrophoresis Mini Sub Cell GT	Biorad (Hercules), CA, USA
Electrophoresis Power Supply - EPS 601	Amersham Pharmacia Biotech, Little Chalfont, UK
Tecnai F20 TEM	FEI, Eindhoven, The Netherlands
o 4k Eagle CCD camera (In-column)	FEI, Eindhoven, The Netherlands
o DT Holder (Model 2040)	Fischione, Export, PA, USA
Grid Box (Cat# G276N)	PLANO, Wetzlar, Germany
Heat Plate OTS 40.253	Medite Medizintechnik, Burgdorf, Germany
High Pressure Freezer HPM010	Abra Fluid, Widnau, Switzerland
o 0.1/0.2 mm planchettes (Cat# 241)	Engineering Office Wohlwend, Sennwald, Switzerland
o 0.0/0.3 mm planchettes (Cat# 242)	Engineering Office Wohlwend, Sennwald, Switzerland
Infrared Scanner (Odyssey)	Li-Cor, Lincoln, NE, USA
Laboratory centrifuge Avanti J-26 XP	Beckman Coulter, Krefeld, Germany
Leica TCS SP2 Laser Confocal Scanning Microscope	Leica Microsystems, Wetzlar, Germany
Leica TCS SP8 Laser Confocal Scanning Microscope	Leica Microsystems, Wetzlar, Germany

Device / Instrument	Supplier *continued*
Microwave (R-28SWT)	Sharp, Köln, Germany
Nanophotometer NP80 Touch	Implen, Munich, Germany
Neubauer Counting Chamber	Marienfeld, Lauda-Königshofen, Germany
Oven (Vacutherm)	Heraeus, Hanau, Germany
PCR cycler (Flex Cycler²)	Analytik Jena, Jena, Germany
Perfect Loop	Diatome, Bienne, Switzerland
pH-Meter (FiveEasy)	Mettler-Toledo, Columbus, OH, USA
Precision scale (Cat# EW220-3NM)	Kern, Balingen, Germany
Resin capsules	PLANO, Marburg, Germany
Rocker (for WB, Duomax 1030)	Heidolph Instruments, Schwabach, Germany
Rotation wheel mixer (Cat# SB1)	Stuart Scientific, Essex, United Kingdom
Scale (Cat# 650-2NM)	Kern, Balingen, Germany
SDS-PAGE System	Biometra, Göttingen, Germany
Spinning disc microscope	PerkinElmer, Rodgau, Germany
Sterile working bench Sterile Guard III Advance	The Baker Company, Sanford, ME, USA
Tabletop centrifuge 5417C	Eppendorf, Hamburg, Germany
Tabletop Ultracentrifuge TL-100	Beckman Coulter, Krefeld, Germany
TEM EM10	Zeiss, Oberkochen, Germany
Ultracentrifuge L8-M	Beckman Coulter, Krefeld, Germany
o Ultracentrifugation tubes (Cat# 7052)	Seton, Petaluma, CA, USA
Ultramicrotome EM UC6	Leica Mikrosysteme, Vienna, Austria
o Cryo-Chamber FC6	Leica Mikrosysteme, Vienna, Austria
o Cryo-Micromanipulators	Leica Mikrosysteme, Vienna, Austria
o Cryo-Aluminum pins (Cat# 16701950)	Leica Mikrosysteme, Vienna, Austria
o Ultramicrotome cryo-immuno knife	Diatome, Bienne, Switzerland
o Ultramicrotome ultra 35° knife	Diatome, Bienne, Switzerland
Vortexer Vortex Genie 2	Scientific Industries, Bohemia, NY, USA
Water bath Julabo UC	Julabo, Seelbach, Germany
WB semidry blotter (Transblot SD)	Biorad (Hercules), CA, USA
Wide field microscope Observer.Z1	Zeiss MikroImaging, Göttingen, Germany

2.1.3 Media and Buffers

Buffer / Medium	Contents
2x HBS	280 mM NaCl
	50 mM HEPES
	1.5 mM Na_2PO_4
	in H_2O, pH 7.10
4x PHEM	20 mM HEPES
	140 mM PIPES
	40mM EGTA
	8mM $MgCl_2$
	in H_2O, pH 6.9
6x WB sample buffer	10% sucrose
	0.1% Bromphenol blue
	5 mM EDTA (pH 8.0)
	200 mM Tris-HCl (pH 8.8)
	3.5% SDS
	0.35% ß-mercaptoethanol
$CaCl_2$	250 mM $CaCl_2$
	in H_2O
Caco buffer	50 mM sodium cacodylate
	in H_20, pH 7.2
Chelated-copper click mix	0.1 M HEPES pH 7.4 (KOH)
	20 µM azide dye
	2 mM Tetrakis(acetonitrile)copper(I) tetrafluoroborate
$DMEM_{complete}$	10% FCS
	100 units/mL penicillin
	100 µg/mL streptomycin
	in DMEM
Freeze Substitution Medium	94.6% dry Acetone
	3.0% H_2O
	0.1% UA
	2.3% MeOH
IF blocking buffer	2% BSA
	in PBS
LB Medium	1% tryptone
	0.5% yeast extract
	171 mM NaCl
	in H_2O

Buffer / Medium	Contents *continued*
LB agar	13% agarose in LB medium
Methylcellulose	2% methylcellulose in H_20
PBS	140 mM NaCl, 2.7 mM KCl 8mM Na_2HPO_4 1.8 mM KH_2PO_4 in H_2O, pH 7.4
PBST	0.1% Tween 20 In PBS
PHF	10% FCS 20 mM HEPES in PBS
$RPMI_{complete}$	10% FCS 100 units/mL penicillin 100 µg/mL streptomycin In RPMI-1640
SDS running buffer	25 mM Tris-HCl 200 mM glycine 1% SDS
$Sort_{10}$	1 µg/mL puromycin in $DMEM_{complete}$
$Sort_{50}$	50% DMEM 50% FCS 100 units/mL penicillin 100 µg/mL streptomycin 1 µg/mL puromycin
Tokuyasu blocking buffer	50 mM glycine 0.8 % BSA 0.1% fish skin gelatin in 1x PBS
WB blocking buffer	30% Western Blot blocking buffer concentrate In PBS

Buffer / Medium	Contents *continued*
WB blotting buffer	48 mM Tris-HCl 39 mM glycine 20% MeOH 1.3 mM SDS In H_2O

2.1.4 Primers

Name	Direction	Sequence (5' → 3')
delFLAG	fwd	GGGTTTGCCGCCAGAAC
	rev	TTGCGCCGGATCCTTACTCGAGTCCACTCCCACCACGATG
mChIns	fwd	GGGAGTGGACTCGAGGTGAGCAAGGGCGAGGAG
	rev	TTGCGCCGGATCCTTACTTGTACAGCTCGTCCATGC
SNAPIns	fwd	GGGAGTGGACTCGAGGACAAAGACTGCGAAATGAAGCG
	rev	TTGCGCCGGATCCTAAGCCCAGCCCAGGC
eGFPIns	fwd	GGGAGTGGACTCGAGGTGAGCAAGGGCGAGGAG
	rev	TTGCGCCGGATCCTTACTTGTACAGCTCGTCCATGC
AgeIrCPSF6	fwd	TAAGTGCAGTAGTCGCCG
mChNheI	rev	ATTGCTAGCCTTTACTTGTACAGCTCGTCCATG

2.1.5 Plasmids

Plasmid Name and Reference	Description
pLENTICRISPR-rCPSF6wt$_{AA}$.FLAG o Designed by David Bejarano & Dr. Ke Peng o Synthesized by Eurofins Genomic	Expression vector for rCPSF6wt$_{AA}$.FLAG
pLENTICRISPR-rCPSF6wt$_{AA}$.mCh o This thesis	Expression vector for rCPSF6wt$_{AA}$.mCh and shRNA$_{CPSF6}$
pNL4-3 o (Adachi et al., 1986)	Proviral full-length infectious HIV-1 Group M molecular clone for virus particle production.
vpr.IN.eGFP o (Albanese et al., 2008) o Anna Cereseto (CIBIO, Mattareo, Italy)	Expression vector for vpr.IN.eGFP fusion protein for fluorescent virus particle labeling
pMD2.G o Didier Trono, EPFL, Lausanne, Switzerland	Vesicular stomatitis indiana virus G protein (VSV-G) expression vector for pseudotyping

Plasmid Name and Reference	Description *continued*
pCHIV ○ (Lampe et al., 2007)	pcDNA3.1-based noninfectious molecular HIV-1 clone. Depleted of LTR and parts of nef.
pcHIV-mCh ○ (Eckhardt, 2010)	pCHIV-based. mCh gene fused to *gag* at MA carboxyterminus
pcHIV-SNAP ○ (Eckhardt et al., 2011)	pCHIV-based. SNAP gene fused to *gag* at MA carboxyterminus
pQE31-rsEGFP2 ○ Addgene #102879 ○ (Grotjohann et al., 2012)	Vector for rsEGFP2 expression
psPAX2 ○ Addgene #12260 ○ Didier Trono, EPFL, Lausanne, Switzerland	Packaging vector for lentiviral particle production
AAV helper ○ (Grosse et al., 2017; Matsushita et al., 1998)	Based on pVAE2AE4-5, AAP depleted. For AAV particle production
AAV6 Capsid ○ (Grosse et al., 2017)	Expression vector for AAV6 capsid protein For AAV particle production
AAVDJP2 Capsid ○ (Grimm et al., 2008)	Expression vector for AAVDJP2 capsid protein. For AAV particle production

2.1.6 Mammalian Cells

Cell Line	Origin
HEK 293T	(Sena-Esteves et al., 1999)
HeLa TZM-bl	(Wei et al., 2002)
U87$^{4/4}$	Modified from ATCC HTB-14, received from Caroline Goujon (King's College, London, United Kingdom)
MT-4	(Harada et al., 1985)
Monocyte-derived Macrophages	Extracted and differentiated from healthy blood donors' buffy coats prepared by Anke-Mareil Heuser (Riquelme and Hutchinson, 2018)

2.1.7 Antibodies

Target Protein	Species	Dilution	Supplier
CPSF6	rabbit	1:500	Sigma (Cat# HPA039973)
CA1	rabbit	1:1,000	inhouse
Cytochrome C	mouse	1:500	BD Pharmingen (Cat# 556432)
TOM20	rabbit	1:500	Santa Cruz (Cat# SC-11415)
α-tubulin	mouse	1:1,000	Sigma (Cat# T5168-2ML)
IRDye™ anti-mouse 700	donkey	1:10,000	Rockland
IRDye™ anti-rabbit 800	donkey	1:10,000	Rockland
Alexa Fluor anti-mouse IgG	goat	1:1,000	Invitrogen
Alexa Fluor anti-rabbit IgG	goat	1:1,000	Invitrogen

2.1.8 Programs, Plugins and Services

2.1.8.1 Image Analysis

Program	Application
FIJI / ImageJ	Image Analysis and Quantification
Icy	Image Analysis and Quantification
- ec-CLEM plugin	LM-EM Correlation

2.1.8.2 Electron Tomography and Modeling

Program	Application
IMOD package	
- eTomo	Tilt Series Reconstruction
- 3DMOD	Structure 3D Modeling
- SerialEM	Electron micrograph acquisition and microscope control
TIA	image acquisition F20 electron microscope
MatLab (with Dr. Martin Schorb)	
- correlation scripts	EM-EM Correlation
- custom scripts	3D model evaluation and measurement

2.1.8.3 Others

Program	Application
Ugene	DNA vector program
GIMP	Figure assembly
Microsoft Office	Document writing, presentations
LibreOffice	Document writing, presentations
Zotero	Reference manager

2.1.8.4 Services

Company	Service
GATC	Sequencing
Eurofins Genomics	Primers and DNA synthesis

2.2 Molecular Biology Techniques

2.2.1 Construct Cloning

2.2.1.1 rCPSF6wt$_{AA}$.GOI Constructs

PCRs were performed with the following reagents:

Amount	Reagent
100 ng	template DNA
1 µL	25 µM dNTPs
2.5 µL	10 µM forward primer
2.5 µL	10 µM reverse primer
10 µL	5x Phusion GC buffer (NEB)
0.5 µL	Phusion DNA Polymerase (NEB)
to 50µL	ddH2O

To replace the FLAG-Tag by an XhoI site for insertion of different genes of interest (GOI), a PCR was performed with pLENTICRISPR-rCPSF6wt$_{AA}$.FL.FLAG, using the XhoIns primers. Annealing temperature was 58°C, elongation time 2 min. The PCR product was purified with the PCR Cleanup & Gel Extraction Kit.

The purified PCR product and the parental plasmid were digested with BamHI and AgeI in CutSmart buffer according to the manufacturer's instructions. AgeI was heat-inactivated at 65°C for

5 minutes. The digestion reactions were then mixed with 6x agarose gel loading dye and separated on a 0.8% agarose gel at 85V for 50 minutes. The bands for the processed PCR product (~1.8 kb, insert) and the longer parental plasmid restriction product (~10 kb, backbone) were cut out of the gel and the DNA was purified using the PCR Cleanup & Gel Extraction Kit. 20 ng backbone DNA were mixed with the ~3-fold molar excess of insert DNA (10 ng) with 1 µL T4 DNA Ligase buffer, 1 µL T4 DNA Ligase, and H_2O to 10 µL. This ligation reaction was incubated for 1 hour at RT and transformed into competent DH5alpha bacteria as described below. The transformed bacteria were plated on ampicillin selective plates. In the produced plasmid, the FLAG-tag was hereby replaced by a unique XhoI restriction site and the plasmid then called pLENTICRISPR-rCPSF6wt_{AA}.XhoI.

This plasmid was then used to insert GOIs, i.e.: mCherry, SNAP, eGFP and rsEGFP2. mChIns primers were used with pCHIV-mCh, SNAPIns primers with pCHIV-SNAP plasmid, eGFPIns primers with vpr.IN.eGFP plasmid and also with the pQE31-rsEGFP2 plasmid, as eGFP and rsEGFP are mostly homologous. Those PCRs were performed as described above, annealing temperature set to 56°C, elongation time set to 2 minutes. As described for the deletion of the FLAG-tag above, purified PCR products and pLENTICRISPR-rCPSF6wt_{AA}.FL.XhoI were digested with XhoI and BamHI, GOI fragments and backbone DNA purified, ligated and plated as described above.

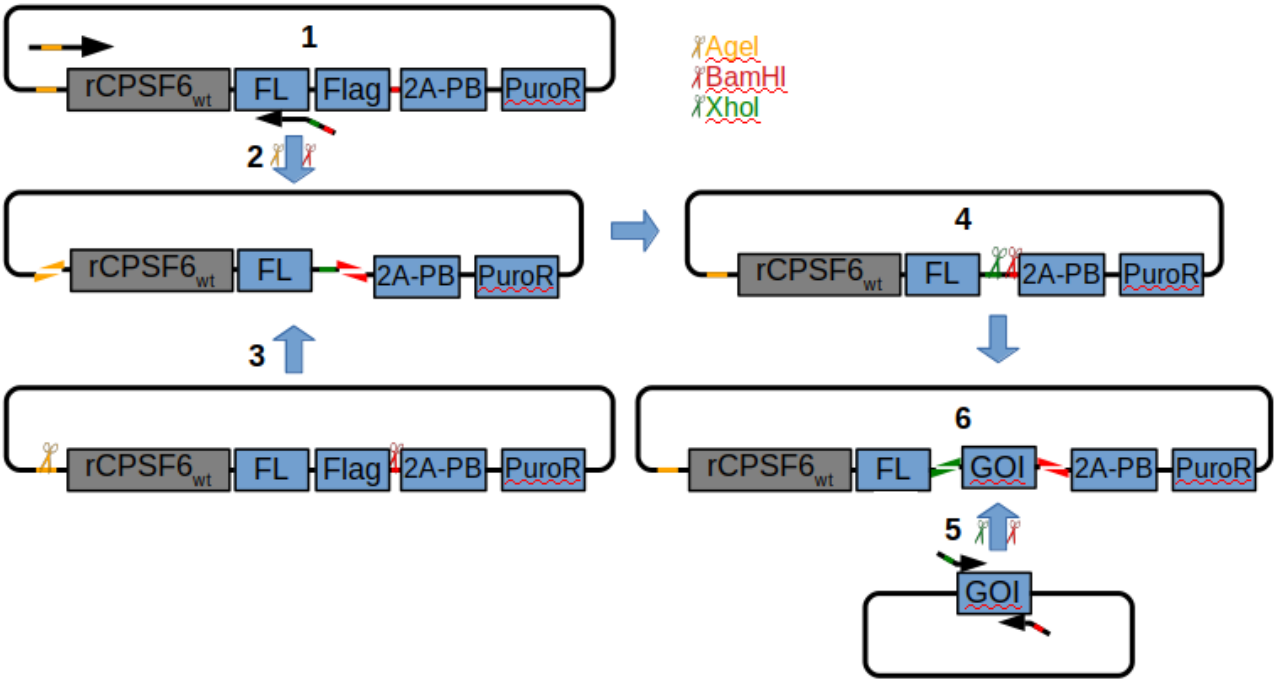

Figure 5: Schematic of Cloning pLENTICRISPR-rCPSF6wt$_{AA}$.GOI Constructs

Using the synthesized plasmid 1 (pLENTICRISPR-rCPSF6wt$_{AA}$.FLAG) as a template, a PCR was performed to add an XhoI site downstream of the flexible linker (FL, 1). The PCR fragment was digested (2) and inserted into the backbone of the AgeI/BamHI (scissors) digested plasmid 1 (3), yielding the pLENTICRISPR-rCPSF6wt$_{AA}$.FL.XhoI plasmid (4).

XhoI and BamHI sites were added to GOIs by PCR using mutagenic primers (5) and inserted into pLENTICRISPR-rCPSF6wt$_{AA}$.XhoI-shRNA^{-}, yielding pLENTICRISPR-rCPSF6wt$_{AA}$.FL.GOIshRNA^{-} (6). In a last step (not shown), an shRNA was inserted to be expressed under U6 promoter control.

2.2.1.2 shRNA insertion

The pLENTICRISPR-rCPSF6wt$_{AA}$.FL.GOI plasmids were restriction digested using KpnI and EcoRI, using CutSmart buffer according to the manufacturer's instructions, subjected to gel electrophoresis at 85V for 50 min and purified. An already digested DNA fragment encoding shRNA (provided by David Bejarano) was ligated into the excised and purified backbone DNA as described above and transformed into *E. coli* stable II bacteria. Plasmids were prepared and tested by restriction digest for the presence of the GOI and the shRNA. Once confirmed, the plasmids were also sequenced.

Like this, the following plasmids were produced:

pLENTICRISPR-rCPSF6wt$_{AA}$.mCh

pLENTICRISPR-rCPSF6wt$_{AA}$.eGFP

pLENTICRISPR-rCPSF6wt$_{AA}$.rsEGFP2

pLENTICRISPR-rCPSF6wt$_{AA}$.SNAP

In this study, we limited our work to the pLENTICRISPR-rCPSF6wt$_{AA}$.mCh, while cloning the other constructs for potential later uses in live cell- or superresolution microscopy.

2.2.2 AAV Construct Cloning

For the transduction of primary human macrophages, we transferred the rCPSF6wt$_{AA}$.mCh expression cassette from the pLENTICRISPR-rCPSF6wt$_{AA}$.mCh vector to a single-stranded AAV vector construct. The rCPSF6wt$_{AA}$.mCh cassette was amplified by PCR, using the primers AgeIrCPSF6 and mChNheI to add an AgeI site upstream of the 5’ end of the rCPSF6 and to add a stop codon and an NheI site to the 3’ end of mCh. The PCR product was digested with AgeI and NheI in Cutsmart buffer (according to the manufacturer’s instrictions), separated via agarose gel electrophoresis, the band cut out of the gel and purified (=insert). The AAV transduction vector was also AgeI and NheI digested and separated on an agarose gel. The backbone band was cut out of the gel an purified (=backbone). Backbone and insert were ligated using T4 DNA ligase and transformed into chemically competent bacteria. Single colonies were grown in 5 ml selective LB medium, plasmids purified and subjected to restriction digest to validate correct insertion of the rCPSF6wt$_{AA}$.mCh cassette.

2.3 Cellular Biology Techniques

2.3.1 Heat Shock Transformation

Chemically competent *E. coli* bacterial cells (Inoue et al., 1990), stored at -80°C, were thawed on ice. Once thawed, 1 ng (for retransformation of a plasmid preparation) or up to 100 ng (for transformation of ligations) were added to the cells and mixed. After 10 minutes incubation on ice, the cells were heat-shocked at 42°C in a water bath for 45 seconds, then returned to ice and mixed with 100 µL cool LB medium w/o antibiotics. After 2 minutes incubation on ice, the bacteria were shaken at 37°C for 1 hour to recover. For transformation of plasmids with ampicillin resistance, the

recovery step was skipped since ampicillin is not cytotoxic. Afterwards, the cells were plated onto selective LB-Agarose plates and incubated at 37°C o/n. Colonies were visible after 12 hours incubation.

2.3.2 Plasmid Preparations

To produce plasmid stocks, the desired plasmids were transformed into bacteria via heat shock transformation (see chapter 2.3.1). *E. coli* strain stable II cells were used for plasmids with repetitive elements prone to recombination (proretroviral - and AAV vector plasmids). *E. coli* strain DH5α cells were used for all other transformations.

A single cell clone colony was picked from the plate with a sterile plastic pipette tip, inoculated into selective LB medium and incubated for 2-16 hours in an incubator (37°C, shaking with 150 rpm). The medium was transferred into 2 mL reaction tubes (“MiniPrep”) or 50 mL conical tubes (“MidiPrep”). The cells were pelleted at 1400 rpm in a table top centrifuge (MiniPrep) or at 8000 rpm in a laboratory centrifuge (MidiPrep). Supernatant was discarded.

The bacteria pellets were further processed according to the manufacturer’s instructions.

For optimum yield, DNA was eluted in 2 steps, for each using 50% of the suggested H_2O volume. The plasmid preparations were vortexed prior to DNA concentration measurement using a Nanophotometer.

2.3.3 Mammalian Cell Culture

U87$^{4/4}$, 293T and Hela TZM-bl cells were maintained in $DMEM_{complete}$ medium at standard conditions, i.e. 37°C, 90% relative humidity and 5% CO_2 in incubators.

For cell splitting or seeding, the cell supernatant was removed, and cells once washed in PBS. Trypsin was added, spread over the complete surface and removed. Depending on the cell line, cells were then incubated 1-10 minutes in an incubator. Fresh $DMEM_{complete}$ medium was added to inactivate residual trypsin and to resuspend the loosened cells. Whenever necessary, cells were counted using a Neubauer Counting Chamber, diluted and seeded accordingly.

MT-4 cells were maintained in $RPMI\text{-}1640_{complete}$.

2.3.4 Virus Particle Production

Virus particles were mostly produced by transfecting proviral plasmids into producer cells (293T). HIV-1 virus particles were concentrated by ultracentrifugation through a 20% sucrose cushion and resuspended in PHF (PBS with 20 mM HEPES and 10% FCS). HEPES is used as a pH buffer, FCS prevents clustering of particles when thawed. Labeled aliquots were frozen at -80°C.

2.3.4.1 HIV-1 NL4-3 Preparation

At day 1, ~90% confluent 293T cells were split 1:6 (area wise) and seeded into 15 cm cell culture dishes. At day 2, 30 µg of pNL4-3 proviral plasmid DNA was diluted into 1 mL 2.5 M $CaCl_2$ solution in a 15 mL conical reaction tube. While vortexing, 1 mL HBS 2x was drop-wise added to the solution. This mixture was incubated for 30 minutes at RT to allow crystal formation. Afterwards, this transfection mixture was added to the 293T cells. After 8 hours incubation time, the cell supernatant was removed and replaced by fresh complete DMEM. Virus particles were harvested 48 hours and 72 hours after transfection: Cell supernatant was collected and centrifuged at 1500 rpm for 5 minutes (cell culture centrifuge) to pellet cell debris. The supernatant was 0.45 µm sterile filtered and in 40 mL ultracentrifuge tubes, 32 mL filtrate were layered over 6 mL 20% sucrose in PBS solution. Ultracentrifugation was performed at 28.000 rpm for 100 minutes. The supernatant was decanted, and residual supernatant wiped with tissue paper. 100µL PHF was added and incubated for 5 minutes. The virus particle pellet was resuspended, aliquoted and stored at -80°C.

2.3.4.2 MT-4 Coculture Virus Preparation for Virus Particle Pellet Tokuyasu Preparation

MT-4 cells were initially infected with NL4-3 virus preparation, produced by transfection of proviral pNL4-3 into 293T cells. Twice per week, when infected MT-4 cells showed signs of cytopathic effects, a 10-fold excess of uninfected MT-4 cells was added and mixed. Virus particles were harvested 1.5 days after addition of uninfected cells to the coculture.

Virus particles were harvested 30 hours after addition of uninfected cells to the coculture. Cell supernatant was collected and centrifuged at 1500 rpm for 5 minutes (cell culture centrifuge) to pellet cell debris. The supernatant was 0.45 µm sterile filtered and in 40 mL ultracentrifuge tubes, 32 mL filtrate were layered over 6 mL 20% sucrose in PBS solution. Ultracentrifugation was performed at 28.000 rpm for 100 minutes. The supernatant was decanted, and residual supernatant wiped with tissue paper. The virus particle pellet was incubated with 100 µL PHF per tube for 5

minutes at RT. Resuspension from the ultracentrifugation tubes was pooled and again layered over 200 µL 20% sucrose in PBS in a tabletop ultracentrifuge. Ultracentrifugation was performed 45 minutes at 44,000 rpm. The supernatant was carefully removed, and the virus particle pellet was fixed for 90 minutes at RT with 4% PFA and 0.2% GA in PBS. The fixed virus particle pellet was then processed according to the Tokuyasu technique (see Chapter 2.5.2).

2.3.4.3 Lentiviral Transduction Vector Preparation

At day 1, ~90% confluent 293T cells were split 1:6 (area-wise) and seeded into 6 well plate-wells in 2 mL $DMEM_{complete}$. At day 2, for each well 1.3 µg pLENTICRISPR, 0.24 µg psPAX2 and 0.6 µg VSV-G plasmids were mixed in 250 µL $CaCl_2$ added. 250 µL HBS 2x were added drop-wise while vortexing. The solution was incubated for 30 minutes at RT allowing crystals to form, and then drop-wise added to the cells. 8 hours after transfection, the cell supernatant was replaced by fresh $DMEM_{complete}$. Lentivirus particle-containing supernatant was harvested 48 and 72 hours after transfection and sterile filtered through a 0.45 µm filter.

2.3.4.4 AAV Transduction Vector Preparation

At day 1, ~90% confluent 293T cells were split 1:6 (area wise) and seeded into 6 well plate-wells in 4 mL $DMEM_{complete}$. At day 2, the cells were transfected with the following plasmids, 1.3 µg each (per 1 well): AdenoHelper, AAV Capsid (AAV6 or DJP2) and AAV-rCPSF6wt_{AA}.mCh plasmid. The plasmids were mixed in 400 µL DMEM complete. 8 µL Turbofect transfection reagent were added and the solution vortexed for 15 seconds. After 15 minutes incubation, the transfection mixture was added to the cells.

3 days after transfection, the cells' supernatant was removed, and cells were washed once with PBS. 1 mL PBS was added, and the cells were loosened by scraping. The cell suspension was collected in a 1.5 mL reaction tube and centrifuged for 10 minutes at 800 g. The supernatant was removed, and the pellet resuspended in 200 µL PBS. 5 freeze-thaw cycles were performed: First, flash freezing the reaction tubes in LN_2, then thawing them in a 37°C water bath followed by vortexing. Afterwards, the cell debris was pelleted at 8000 g for 10 minutes, the supernatant removed, aliquoted and frozen at -20°C until further use.

2.4 Virological Methods and Cell Line Characterization

Note: Many samples were initially treated similar, but later handled differently for different methods, e.g. for light – or electron microscopy, or for different EM techniques. To not be too repetitive, we describe e.g. fixation methods only once and refer to the according chapter.

2.4.1 Generation of the rCPSF6wt$_{AA}$.mCh U87$^{4/4}$ Stable Cell Line

150,000 U87$^{4/4}$ cells were seeded per well in a 6 well plate. While seeding, 2 mL lentivirus particle-containing supernatant (packaged pLENTICRISPR-rCPSF6.mCh) were added per well. 24 hours after incubation, the cell supernatant was removed and replaced with new lentivirus particle-containing supernatant (lentivirus particle production was synchronized). After another 24 hours of incubation, the supernatant was removed and replaced by fresh DMEM complete medium.

The cells were incubated for ~5 further days until a nuclear mCherry signal became visible. At that point, the cells were split 1:2 and seeded in a 6 well plate well in 2 mL Sort$_{50}$ Medium (50% FCS, 50% DMEM, Pen/Strep, 1 µg/ml Puromycin). The next day, the medium was replaced by fresh Sort$_{50}$ Medium to wash off dead cells. Once grown confluent again, the cells were split into a T25 bottle in Sort$_{50}$ Medium. Once the cells were confluent, medium was changed to Sort$_{10}$ medium (DMEM$_{complete}$ w/ 1 µg/ml Puromycin). Without selection pressure, the fluorescence was lost within 2-3 passages. Therefore, these U87 rCPSF6wt$_{AA}$.mCh cells were constantly kept in Sort$_{10}$ medium.

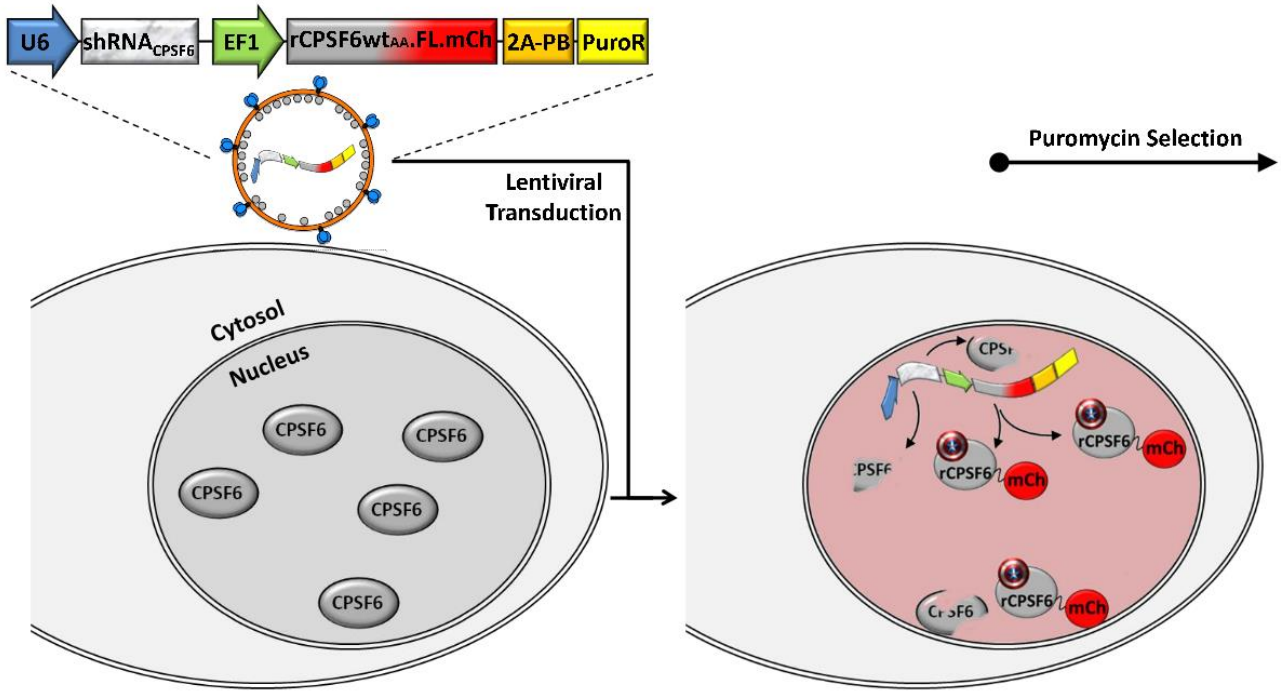

Figure 6: Schematic of the Generation of The U87$^{4/4}$ rCPSF6wt$_{AA}$.mCh

A lentiviral construct was packaged and used for transduction of U87 parental cells, encoding a short hairpin RNA targeting CPSF6 (shRNA$_{CPSF6}$) under U6 promoter control and a cassette under EF1 promoter control: Coding for a CPSF6, carrying silent mutations to confer resistance to shRNA driven degradation (rCPSF6wt$_{AA}$), fused to mCherry (mCh), followed by a 2A Peptide bridge linked to a Puromycin resistance gene. After successful lentiviral transduction, the encoded shRNA can degrade the endogenous nuclear CPSF6, while rCPSF6wt$_{AA}$.mCh is expressed and not degraded. Those cells' nuclei autofluoresce in red, due to mCherry.

2.4.2 Western Blot for CPSF6 Detection

For Western Blotting, proteins of sample lysates are separated according to their apparent molecular weight via SDS polyacrylamide gel electrophoresis (SDS-PAGE). SDS binds unspecifically to proteins and thereby provides them a negative charge relative to their number of amino acids. In gel electrophoresis, all proteins experience an electric force, relative to the bound SDS. Smaller proteins experience less resistance in the polymer gel and can therefore travel faster towards the anode. Larger proteins are more retained and therefore travel slower. This leads to a separation of proteins according to their molecular mass. Proteins are then transferred from the gel to a membrane (blotting) and immunolabeled with antibodies against proteins of interest. The amounf of protein that is initially loaded onto the gel can be normalized by so called house keeper proteins, such as GAPDH or (α-)tubulin. Such proteins are thought to be of constant concentration.

2.4.2.1 Cell Lysis

U87$^{4/4}$ rCPSF6wt$_{AA}$.mCh or wt cells were growing confluent in 6 well plates at 5 days after transduction (see Chapter 2.4.1). When these cells were split (see Chapter 2.3.3), 50% were further passaged and 50% were transferred into 2 mL reaction tubes and pelleted by centrifugation at 800 g for 10 minutes. The supernatant was mixed with 6x WB sample buffer and vigorously mixed using a vortexer. This cell lysate was incubated for 10 minutes at RT. Incubating the samples at 95°C for 10 minutes disrupts intra- and intermolecular bonds, like hydrogen bonds and salt bridges. Furthermore, disulfide bonds are reduced by the ß-mercaptoethanol in the 6x WB sample buffer.

2.4.2.2 Polyacrylamide Gel Preparation and Electrophoresis

Homemade SDS gels were prepared in 2 steps: A total of 10 mL solution was prepared for the separation gel: 12.5% acrylamide, 375 mM Tris-HCl (pH 8.8), 0.1% SDS, 0.1% APS, 0.0015% TEMED. This solution was filled in between glass slides to ¾ and overlayered with isopropanol to prevent surface drying. 4 mL of stacking gel solution was mixed: 4.5% acrylamide, 125 mM Tris-HCl (pH 6.0), 0.1% SDS, 0.06% APS and 0.3% TEMED. Isopropanol was removed from the polymerized separation gel and briefly blotted. The volume between the glass slides was filled with stacking gel solution and a comb was added to create sample pockets.

After polymerization, the glass slides were installed into the SDS-PAGE system, filled with SDS-PAGE running buffer and loaded with 20 µL cell lysate per lane and one pocket lane was filled with 10 µL protein size marker. Gel electrophoresis was performed at 160 V for 50 minutes. At this rather high voltage, the obtained bands did not show the typical smiley effect but remained well horizontally aligned (Most likely due to even heating, caused by the high voltage).

2.4.2.3 Membrane Blotting and Immunolabeling

The gel was removed from the system and the glass slides, briefly washed in blotting buffer and stacked for blotting as follows: 3 layers of blotting paper, 1 methanol-activated PVDF membrane, polyacrylamide gel, 3 layers of blotting paper (all layers soaked in blotting buffer). A semi-dry blot was performed, applying 25 V at a current of 3 mAmp/cm² for 50 min. The membrane was removed and incubated in WB blocking buffer, for 30 minutes rocking at RT (to sequester unoccupied protein binding sites and prevent antibodies from unspecific binding). Anti-CPSF6 (rabbit) and anti-α-tubulin (mouse) antibodies were mixed in 10 mL WB blocking buffer and incubated for 1 hour at RT. The membrane was washed 3 times 5 minutes in PBST (0.1% Tween in PBS) and incubated

with 10 mL WB blocking buffer with 1:10,000 IRDye™ anti-rabbit 800 and IRDye™ anti-mouse 700 secondary antibodies, each. Secondary antibodies were incubated for 1 hour at RT, rocking and washed 4 times in PBST for 5 minutes, and in PBS for 3 minutes.

The Western Blot membrane was imaged with an infrared scanner.

2.4.3 U87$^{4/4}$ Cell Infection for Cell Line Characterization and PIC Correlation

20,000 U87$^{4/4}$ rCPSF6wt$_{AA}$.mCh cells per chamber were seeded onto prepared sapphire discs (chapter 2.5.1.1) in 8 chamber microscopy slides, and transferred into the BSL3 laboratory. U87$^{4/4}$ cells were infected in a total volume of 100 µL, reduced to a minimum for maximal efficient infection. 5 µL virus particle preparation was added per well. We have identified 4 hours infection to be a good time point for the analysis of nuclear PIC (Peng et al., 2014).

Therefore, cells were further incubated for 4 hours at standard conditions before chemical fixation (described in chapter 2.4.5.3), then continued in chapter 2.5.4).

2.4.4 Virus Particle Arrest at the Cellular Plasma Membrane

To analyze core structures from surface-bound virus particles as a reference, it was necessary to prepare samples under identical conditions. Therefore, 20,000 HeLa TZM-bl cells per well were seeded onto prepared sapphire discs (chapter 2.5.1.1) in 8 chamber microscopy slides. HeLa TZM-bl cells were used preferentially due to better binding of virus particles to the plasma membrane (see Figure 35). 10 µL virus preparation in a total of 100 µL inoculum was added per chamber. To prevent entry and endocytosis of viral particles, the cells were incubated o/n at 16°C. To prevent cytotoxic pH changes, 20 mM HEPES was added to the cell culture medium. Virus inactivation was done as described above (chapter 2.4.5.3). Fixed samples were then processed as samples for PIC correlation (chapter 2.5.4)

2.4.5 Cell Fixation and Virus Inactivation

Samples were fixed according to the specific needs and downstream processing. When a specific kind of fixation was performed, it is either mentioned in the downstream chapter, or described separately.

2.4.5.1 Fixation for CA immunofluorescence labeling

Fixing for 90 minutes with aldehydes strongly reduces the signal obtained from CA immunofluorescence staining. Therefore, an alternative protocol was used for reliable inactivation of BSL3 HIV-1.

Infected cells' supernatant was removed, and cells were washed with warm PBS, before adding 4% PFA in PBS for 20 minutes at RT. The fixative was removed, and cells washed once in PBS. For permeabilization and full virus inactivation 0.5% Triton X-100 in PBS was added and incubated for 20 minutes at RT. The cells were then removed from BSL3. For samples that were directly immunofluorescence labeled, see Chapter 2.4.5.2. For samples, where EdU click labeling was performed in between, see Chapter 2.4.6.1.

2.4.5.2 Immunofluorescence Labeling (General)

In general, BSL3 samples for immunofluorescence labeling were fixed for 90 minutes at RT in 4% PFA in 1x PBS buffer, and removed from the BSL3 laboratory.

In contrast, when incubating cells on sapphire discs for high pressure freezing, these were typically fixed for 90 minutes in 4% PFA, 0.2% GA in PHEM buffer. After sapphire discs have been removed from the chambers, the residual cells were used as a phenotype control.

For samples, where CA was immunolabeled, cells were fixed as described in chapter 2.4.5.1.

The fixative was removed, cells washed once in PBS and permeabilized in 0.2% Triton in PBS for 20 minutes. After 2 times 3 minutes washing with PBS, residual aldehyde groups were inactivated in IF blocking buffer for 20 minutes. Primary antibodies were diluted accordingly into IF blocking buffer and incubated for 1 hour at RT. Samples were washed 5 times 3 minutes with PBS, before incubating secondary antibodies with Hoechst33258 (whenever enough channels were available), diluted in IF blocking buffer for 1 hour at RT. Samples were washed again 5 times 3 minutes and left in PBS for imaging and storage at 4°C.

2.4.5.3 Virus Inactivation for High Pressure Freezing by Chemical Fixation

For best possible retention of ultrastructure and fluorescence, we made use of published protocols and adjusted them to meet the needs of our cells and conditions (Kukulski et al., 2011). Throughout this protocol we used the less extracting PHEM buffer instead of PBS. Additionally, PHEM is devoid of phosphate ions, which precipitate easily with uranyl ions and thereby form electron-dense, insoluble crystals.

Before further processing, it was necessary to fully inactivate infectivity of cells and virus particles. Therefore, cell supernatant was removed, cells were once washed with 1x PHEM buffer and then fixed in 4% PFA and 0.2% GA in 1x PHEM buffer for 90 minutes at RT. The samples were then removed from the BSL3 laboratory. The Fixative was removed, and the cells washed and stored in PHEM buffer until further processing. Further preparation for EM was typically continued within 30 minutes (see Chapter 2.5.4.1) Samples for light microscopy were stored up to 1 day at 4°C before further processing.

After removing and processing the sapphire discs, some cells were remaining in the used well. Those that were growing directly on the well's plastic surface, in the space between sapphire discs. These cells were used as light microscopy samples to either directly confirm the presence of rCPSF6wt$_{AA}$.mCh clusters or for additional immunofluorescence stainings (see chapter 2.4.5.2).

2.4.6 EdU Click Labeling

The thymidine-analog EdU is readily taken up by living cells and incorporated into nascent DNA: In nuclei during S-Phase, in mitochondrial DNA (mtDNA) during replication and in viral DNA during reverse transcription (Salic and Mitchison, 2008). Click labeling is employed to label viral DNA, which is considered a sign for productive infection, or to label mtDNA, which was used as a model for viral DNA throughout protocol establishment. This application has been proven to faithfully identify viral DNA in subviral complexes (Peng et al., 2014).

2.4.6.1 EdU Click Labeling in Fixed Cells

For EdU click labeling, cells were incubated with 10 µM EdU during infection (i.e. for 4 hours). Cells were fixed as described above (see chapter 2.4.4) and permeabilized for 20 minutes with 0.2% Triton in PBS. Residual aldehydes were blocked with IF blocking buffer for 20 minutes at RT. The standard EdU click labeling mixture (clickIT kit) or the chelated-copper click mixture was incubated for 20 minutes at RT. Cells were washed with IF blocking buffer twice and IF blocking buffer was again incubated for 20 minutes. Afterwards, cells were stained by immunofluorescence as described below. The click reaction mixture was prepared and applied according to the manufacturer's instructions.

2.4.6.2 Live Cell Click labeling

Cells were grown on cover glasses, removed from their well and once washed with PBS. The cells were then incubated in 100 µL EdU click labeling mixture for indicated durations at RT.

Afterwards, they were washed with PBS 3 times for 2 minutes and then placed back into wells with fresh $DMEM_{complete}$ for recovery, or directly further prepared for epon flat embedding (see chapter 2.5.3) or cryo-CLEM approaches (see chapter 2.5.3). For live cell click labeling, we used the cell permeable TAMRA azide-dye.

2.4.7 HIV-1 Infectivity Titration by Wide Field Microscopy

20,000 $U87^{4/4}$ wt or $rCPSF6wt_{AA}$.mCh cells per chamber were seeded in 8-chamber slides. 1 day after seeding, cells were infected in 150 µL DMEM complete with 2, 0.5, or 0.125 µL NL4-3 virus particle preparation or left uninfected as controls. 4 hours after infection, the inoculum was removed and replaced with 200 µL fresh DMEM medium with 50 µM T20 entry inhibitor (Ding et al., 2017) to prevent second round infections. After 2 days, cells were washed in PBS, fixed with 4% PFA in PBS for 20 minutes at RT, and permeabilized with 0.5% Triton X-100 in PBS for 20 minutes at RT. The samples were then removed from BSL3. The permeabilizing solution was removed, cells were washed with PBS once and incubated with IF blocking buffer. After 20 minutes incubation at RT, the IF blocking buffer was removed and Rb anti-CA1 antibody (diluted 1:1000 in IF blocking buffer) was added to the cells. After one hour incubation, the antibody was removed and cells washed 4 times for 5 minutes with PBS. Alexa-488 goat anti rabbit IgG (diluted 1:1000 in IF blocking buffer with Hoechst 33258) was added and incubated for 1 hour at RT. Secondary antibody solution was removed, and cells washed again 4 times for 5 minutes with PBS at RT.
9 separate images were acquired using the cell culture wide field microscope. Images were analyzed using FIJI and infectivity was determined by automatically counting all (Hoechst) and only infected (CA-positive) cells.

2.5 EM Material and Sample Preparations

2.5.1 Material Preparation – Sapphire Discs and EM Grids

2.5.1.1 Sapphire Discs

50 µm sapphire discs were cleaned in 80% Ethanol and dried on filter paper. Once dry, the discs were placed into holders for carbon coating. A 15 nm carbon layer was coated onto the sapphire discs first. The discs were then removed from the coating chamber and an “F” was scratched into the carbon layer, using dentist tools. The discs were replaced into the holder and another carbon layer of 8 nm was coated on top of the first one. We found the second layer to improve the overall stability of the carbon coat, most likely by providing one continuous, closed surface. The carbon

coat allows easier separation of the sapphire disc from the embedding resin after polymerization, at the end of EM sample preparation. The scratched in “F” serves as a mark to discriminate the disc’s up – and down sides. Cells were grown on the carbon layer. To ensure seeding the cells on the right side of the sapphire disc, the F had to be readable as such, observed from above, and must not be inverted, meaning the carbon layer would be facing up.

To fix and stabilize the carbon layer, and for sterilization, the coated sapphire discs were incubated at 140°C for at least 3 hours in a closed glass Petri dish.

Sapphire discs were allowed to cool down to RT for at least one hour prior cell seeding.

They were then immersed in $DMEM_{complete}$ medium and transferred into 8 chamber microscopy slides’ wells prefilled with 200 µL $DMEM_{complete}$ medium, the carbon layer facing up. First immersing the disc in medium prevents floating of the discs and allows to place the sapphire discs in distinct positions within the well. Up to 6 sapphire discs were placed into one well. Into these prepared wells, 20,000 cells were seeded and allowed to attach and grow for one day before infection / treatment (see chapters 2.4.3 & 2.4.4).

2.5.1.2 EM Grids

A pioloform layer on the EM grid produces a closed surface. Pioloform itself is almost electron-transparent. When taking up sample sections on pioloform-coated grids, they are flatter and don’t hang into the mesh between grid bars. Adding a carbon layer increases the overall stability of the surface, and acts as a conductive layer, allowing local electric charges (due to the electron beam-exposure) to quickly discharge over the EM sample holder. Local charges can otherwise introduce artifacts by electrostatic interactions with the electron beam.

EM grids were briefly vortexed in acetone for cleaning, removed and allowed to air dry on filter paper. Glass slides were cleaned with lintfree tissues, before immersing the glass surface to 2/3 in 1% pioloform in chloroform solution.

The solution was steadily released through a nozzle, yielding a uniformly thin pioloform layer on the glass. The pioloform layer was allowed to dry for ~2 minutes. The layer’s sides were cut with a sharp razor blade close to the rim on all 4 sides. By gently immersing the coated cover glass in a ~45° angle into a water bath, the pioloform coat was loosened from the glass and floating on the water surface. Cleaned, dry EM grids were placed with the shiny side up, the dull side facing the floating pioloform film. Areas with impurities (like dust particles) were spared. Once completed, clean parafilm was placed on top of the grids, sandwiching them between the parafilm and the pioloform film. This sandwich was placed with the pioloform side facing upwards and allowed to

dry for 1 day at RT. The pioloform coated EM grids were then covered with a ~2.3 nm layer of carbon, using the carbon coater according to the manufacturer's instructions. Those grids were stored for up to 6 months in plastic containers to prevent the pioloform from becoming brittle.

2.5.2 Tokuyasu Sample Preparation

In the Tokuyasu sample preparation, cells are chemically fixed with aldehydes, pelleted, embedded in gelatin and infiltrated with sucrose o/n. The latter protects from ice crystal formation during the subsequent flash freezing in LN_2. Frozen pieces of cell pellets are cryo-thin sectioned and freed from gelatin. Since these samples are fully hydrated and only chemically fixed, not solid resin-embedded, immunofluorescence labeling usually works well because antigens are well retained and highly accessible (Slot and Geuze, 2007).

$1.2x10^6$ $U87^{4/4}$ or HeLa TZM-bl cells were seeded per 6 well plate-well. One day later, the cells were incubated with 10 µM EdU for 5 hours (see Chapter 2.4.6). Virus particle pellets (chapter 2.3.4.2) and cells were processed as follows:

The samples were washed in PBS and chemically fixed in 4% PFA and indicated concentrations of GA in PBS for 90 minutes, to mimic BSL3 requirements. The fixative was removed, the cells once washed in PBS and incubated for 20 minutes in 50 mM glycine and 1% gelatin in 1x PHEM at RT to sequester residual free aldehyde groups. The cells were scraped off in this buffer, transferred into a 2 ml reaction tube and centrifuged at 14000 rpm for 2 minutes at RT in a table top centrifuge. Supernatant was removed, and cells resuspended in 37°C warm 10% gelatin in PBS. After centrifugation at 14000 rpm for 30 seconds, most of the supernatant was removed. The gelatin holding the cell pellet was allowed to solidify on ice for 10 minutes. Using a tooth pick, the gelatin block was removed from the reaction tube and immersed in 2.3 M sucrose in PBS for further handling to prevent drying. Excess gelatin was removed, and the cell pellet cut into 6 pieces, which were transferred into 2 ml reaction tubes filled with 2.3 M sucrose for o/n sucrose infiltration at 4°C on a rotation wheel mixer. The next day, the surface of aluminum pins was roughened using sandpaper, to increase the surface are. Aluminum pins are used to mount the samples for cryo-sectioning. The pins were washed in 70% EtOH in H_2O and dried. One piece of a cell pellet was mounted onto one pin, excess sucrose solution removed, the pin flash frozen and stored in LN2.

The samples were cryo-sectioned using the ultramicrotome with the ultramicrotome cryo-chamber and a cryo-knife at -140°C. While milling a flat block surface, single sections were taken up using the perfect loop and checked for presence of cellular material using methylene blue. Therefore, the section was placed on a microscopy glass slide and dried at 90°C. One drop of methylene blue

solution was added and incubated at 90°C until the rim was starting to dry out. Excess solution was washed off, and the thawed cryo-thin section was visually analyzed for the presence of cell material using a standard wide field microscope.

The sides were trimmed (45° trim angle) to yield a block face rectangle of 150 µm x 100 µm, and serial section ribbons were produced using micromanipulators. The ribbon of serial sections was taken up in a drop of 2.3 M sucrose w/ or w/o methylcellulose using the perfect loop. This drop holding the section band was then transferred to a pioloform - and carbon coated EM grid on parafilm (see chapter 2.5.1.2). Grids with sections were incubated twice for 15 minutes at 37°C, first in 2% gelatin in PBS, then in 50 mM glycine in PBS to gently, step-wise remove the embedding gelatin from the sample. Before labeling, potential nonspecific protein binding sites were blocked using Tokuyasu blocking buffer for 10 minutes, followed by 2 washing steps in PBS for 2 minutes each.

For EdU click labeling, the sections were equilibrated in click reaction buffer without azide-coupled dye twice for 30 seconds, and then incubated for 30 minutes at RT in click reaction buffer with 2 µM azide-coupled dye, protected from light. The section was washed twice in PBS afterwards for 2 minutes each.

In order to stain and wash the sections they were placed on top of drops out of different solutions placed on hydrophobic parafilm. For antibody labeling, primary antibodies were diluted 1:200 in Tokuyasu blocking buffer. The sections were incubated at RT protected from light for 45 minutes and washed 4 times with PBS for 3 minutes each. The same was repeated for the secondary antibody. After washing the sections with PBS, they were washed with water at least 5 times for 2 minutes. The last 3 washing steps were performed on ice to precool the sample for the next step.

3 drops of 1.7% methylcellulose and 0.45% UA were prepared on ice, the sections briefly incubated on the first 2 drops, and then incubated for 7 minutes on the last drop. The EM grid was picked up with a perfect loop. Excess material was removed using filter paper, and the grid allowed to dry at RT. UA binds to phosphate groups of e.g. lipids, proteins and the chromatin backbone, providing contrast for electron microscopy. The methylcellulose acts as a kind of resin, replacing the water while keeping structures in shape. The grids were then ready for electron microscopy.

2.5.3 Epon Flat Embedding

Epon flat embedding is a fast technique, where sample cells are grown on cover glasses, harsh chemically fixed with aldehydes, UA and OsO_4, dehydrated and finally embedded in Epon resin. Epon polymerizes within several hours, so samples can be thin sectioned and imaged the next day already. With UA and OsO_4, a high contrast is usually yielded. Fluorescence on the other hand cannot be preserved, due to thermal requirements for polymerization of the resin (60°C) and OsO_4, reacting with C-C double bonds. Pi-electron systems, the basis of fluorescence, are thereby destroyed. Samples embedded this way typically retain HIV-1 capsid structures well (Bartonova et al., 2008).

50,000 $U87^{4/4}$ or HeLa TZM-bl cells were seeded onto round cover glasses in 24 well plate-wells, in 500 µL $DMEM_{complete}$. 1 day after seeding, the cells were incubated with 10 µM EdU for 5 hours.
Different fixatives and diluents were tested and compared in this study (see Results Figure 21). To mimic BSL3 requirements, cells were fixed for 90 minutes at RT and washed in PBS buffer. After removing the samples from BSL3, they were incubated with 2% OsO_4 in Caco buffer for 40 minutes on ice, washed 4 times 3 minutes at RT in Caco buffer and incubated with 0.5% UA in H_2O for 30 minutes at RT. The samples were washed 3 times 2 minutes in H_2O and dehydrated for 5 minutes each in increasing concentrations of EtOH in H_2O, starting from 30% followed by 40%, 50%, 60%, 70%, 80%, 90%, then 95%, followed by 2 times 10 minutes incubation in 100% EtOH. The cover glasses were then removed from the wells and mounted onto resin capsules prefilled (slightly overfilled) with Epon, cells facing the resin. Infiltration was done for 15 minutes at RT. The samples were then flipped upside down and placed onto the cover glass for solidification in an oven o/n at 60°C.
To remove the cover glasses, solid sample blocks were freed from the resin capsule using razor blades. The blocks were flash frozen in LN_2 and, once cold, transferred into hot water. Sudden temperature shifts lead to loosening of the cover glass from the resin surface. Once all the glass was removed, the big sample blocks were sawed into 2 halves. One half was stored for potential later use, the second half was mounted into a UC6 sample holder. The surface was trimmed in 45° angles to a trapezoid of roughly 0.8 x 0.5 mm. After aligning the trapezoid block face to the diamond knife, (ultra) thin sections were prepared and taken up onto prepared EM sample grids.

2.5.3.1 Addition of Colloidal Gold Fiducials to Sections

All following staining and washing steps were performed in 20 µL drops on clean parafilm at RT.

For later tilt series reconstruction, 15 nm PAG fiducials were added to the section surfaces. Therefore, grids were incubated first with the side not containing the sample section on 1:50 PAG in H_2O dilution for 10 minutes, 3 times washed for 10 seconds in H_20 and then blotted on filter paper. This was repeated for the sample section containing side without blotting at the end.

To increase contrast, sections were postcontrasted using established protocols for PbCi and UAc (Hall, 1995; Reynolds, 1963).

2.5.3.2 Postcontrasting of EM Thin Sections

Grids were calibrated twice for 5 seconds on 70% MeOH in H_2O, transferred onto 3% UAc in 70% MeOH solution and incubated another 5 minutes. The grids were washed twice for 5 seconds in 70% MeOH in H_2O and twice for 2 minutes in H_2O. Washing in MeOH is necessary to wash off excess UA but needs to be kept short to not wash out the contrast again. Drops of PbCi were surrounded by 5-10 KOH pellets to prevent CO_2 from reacting with the solution and forming insoluble $PbCO_3$ precipitates. Grids were equilibrated for 10 seconds on a fist drop and then incubated for 3 minutes on a second drop. 2 brief washing steps were performed within the CO_2 depleted area, then another 4 washes in H_2O were performed. Finally, the grid was blotted and stored in the grid box.

2.5.4 Sample Preparation for On-Section Correlative Light – and Electron Microscopy

2.5.4.1 High Pressure Freezing (HPF)

HPF is one way of cryo-immobilizing samples. A critical point is met at 2000 bars pressure and -200°C, where samples of up to 200 µm thickness can be frozen in a minimal time frame, preventing formation of crystalline ice (McDonald, 2009). This process is also called vitrification. Cell culture medium contains sugars and proteins (FCS), which also serve as cryo-protectants, counteracting crystal ice formation in samples that don’t require prefixation. Here, we have to chemically fix our sample cells before HPF using aldehydes in buffers (upstream sample preparation: Chapters 2.4.3, 2.4.4 and 2.4.5.3). Instead of vitrifying cells in plain PHEM, we add 100 mM sucrose to foster vitrification.

For HPF, planchettes are used to generate a volume over sample sapphire discs, in which the samples can be vitrified. 0.0/0.3 mm - and 0.1/0.2 planchettes were sorted and placed on filter paper soaked in hexadecene, which helps to exclude air from sample preparation. Air has a high thermal insulation capacity, and therefore would slow down the freezing process, thereby strongly promoting ice crystal formation. The first planchette was placed with the 0.0 mm (flat) side up into the sample holder. One sample sapphire disc was washed and immersed in PHEM with 100 mM sucrose and placed on top of the planchette. Using binoculars allows ensuring that the cells are facing up by reading the “F” in the carbon layer. A second planchette was placed on top of the sapphire disc as a lid, the 0.1 mm side facing the cells, thereby creating a chamber around the cells of 100 µm thickness (see Figure 7). Excess liquid was removed by plotting with filter paper and the sample holder closed. In an HPM010, the sample was high pressure frozen and quickly transferred into a reservoir of liquid nitrogen (LN_2), where the sample was stored, sandwiched between the planchettes until further processing. Keeping the planchettes sandwich as such, while storing the sample, reduces the risk of growing crystalline ice on the sample.

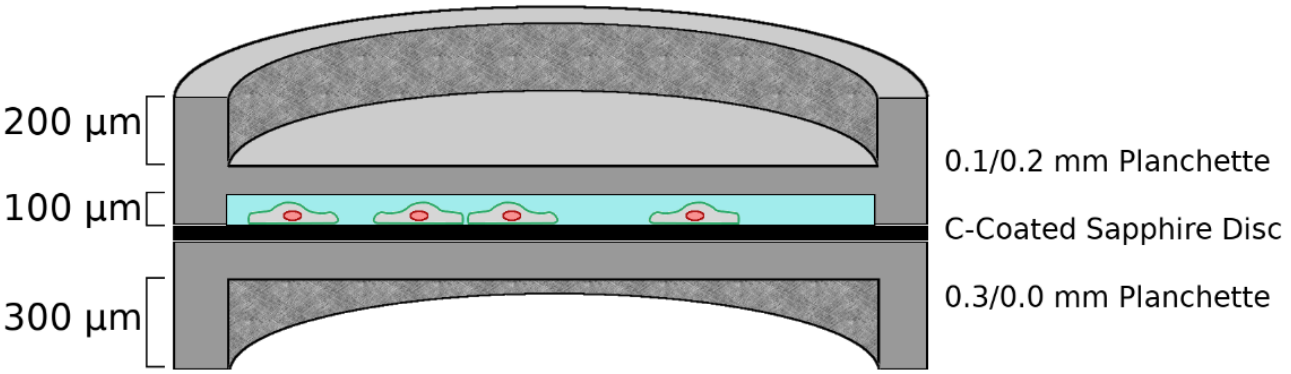

Figure 7: Schematic of a Cross Section Through an HPF Sample Sandwich

A carbon coated sapphire disc holding sample cells is placed on a 0.3/0.0 mm planchette as a carrier. A 0.1/0.2 mm planchette is placed on top of the sapphire disc, creating a 100 µm high sample chamber around the sample cells in cryo-protectant medium, e.g. 100 mM sucrose in 1x PHEM buffer. This sandwich is mounted into the HPF sample holder and vitrified.

2.5.4.2 Freeze Substitution (FS)

During FS, a sample's vitrified water is first replaced by a polar organic solvent (here acetone) at temperatures as low as -90°C, while mildly chemically fixing the sample using UA. The temperature can then be raised without crystal ice formation, and the acetone in turn is replaced by Lowicryl HM20 resin. The latter will infiltrate the sample, polymerize under UV light and allow sectioning of the sample at RT.

2.5.4.2.1 Freeze Substitution–Medium Preparation

To start the substitution run in an automated freeze substitution system (AFS), the AFS was filled to 75% with LN_2 and set to -90°C. Once this temperature was reached, the FS medium was prepared.
In the freeze substitution medium, the sample's H_2O is replaced by acetone.
A minimal percentage of water in the acetone is important: First, H_2O needs to be substituted as good as possible to prevent ice crystal formation, when rising the temperature. Second, the Lowicryl HM20 can only tolerate up to 4% H_2O (according to manufacturer's instructions) for infiltration and embedding. 3% UA stocks are prepared by dissolving UA powder in 70% methanol, 30% H_2O solution.
For one AFS run, 4 mL of dry acetone were pipetted into a 10 mL glass vial and cooled to -90°C in the AFS. Once this temperature has been reached, 134 µL 3% UA solution were added. Once mixed, 80 µL H_2O were added, immediately freezing in the solution. The glass container was removed from the AFS and warmed while shaking, until the water dissolved into the solution. The now ready FS medium was immediately placed back into the AFS and cooled down to -90°C.
If solutions are not cooled while mixing them, UA spontaneously precipitates. It remains insoluble, and the FS medium in that case is of no use.
The final concentrations of the FS medium are:

Acetone	94.6 %
H_2O	3.0 %
UAc	0.1 %
MeOH	2.3 %

2.5.4.2.2 Sample Loading Into the Automated Freeze Substitution System

The AFS2 incubation chamber was cooled down to -90°C with a metal holder for 2 sample processing holders. One sample wheel (holding up to 10 sapphire discs) was placed into the metal holder and a metal dish in the middle well was added for easy sapphire disc manipulation. 0.5 mL FS medium was filled into the metal dish, to directly immerse sapphire discs in FS medium upon transfer from LN_2.

After HPF, the sapphire discs were removed from the planchettes in LN_2. The sapphire discs were then transferred with a small LN_2 container to the AFS. Transfer of the discs from the LN_2 to the FS medium was performed within the AFS2 incubation chamber, usually in less than one second to ensure no sample thawing in between. The precooled tweezers serve as a cryogen during transfer. The discs were placed directly into the metal dish prepared with FS medium. Tweezers were used to prevent sample sapphire discs from floating on the FS medium. Ideally, the sapphire discs are instantly immersed in FS medium. The temperature in the sample chamber is only -90°C, where ice crystals could already grow. The discs were rotated and/or flipped, until the “F” in the carbon layer was readable. The sapphire discs were then transferred into the sample processing holder using tweezers, without further flipping. It was placed down on a rim in the bottom end of the sample processing holder. Correct horizontal positioning at the lower rim of the sample in the processing holder was ensured using manipulation tools. At the end of embedding, tilted sapphire discs eventually result in block faces not orthogonal to the resin block. Such samples cannot be sectioned due to their tilt angle.

When all samples were loaded, the AFS2 Robot was installed with a fresh filling needle. The settings of the AFS program are displayed in Figure 8 & Figure 9 for HM20. Modifications for embedding in LR Gold are described in chapter 2.5.4.2.4.

Once the program was finished, the sample processing holder with the embedded and polymerized samples was removed and wrapped in aluminum foil and stored in the dark, allowing residual polymerization and preventing bleaching of the retained fluorescence by surrounding light.

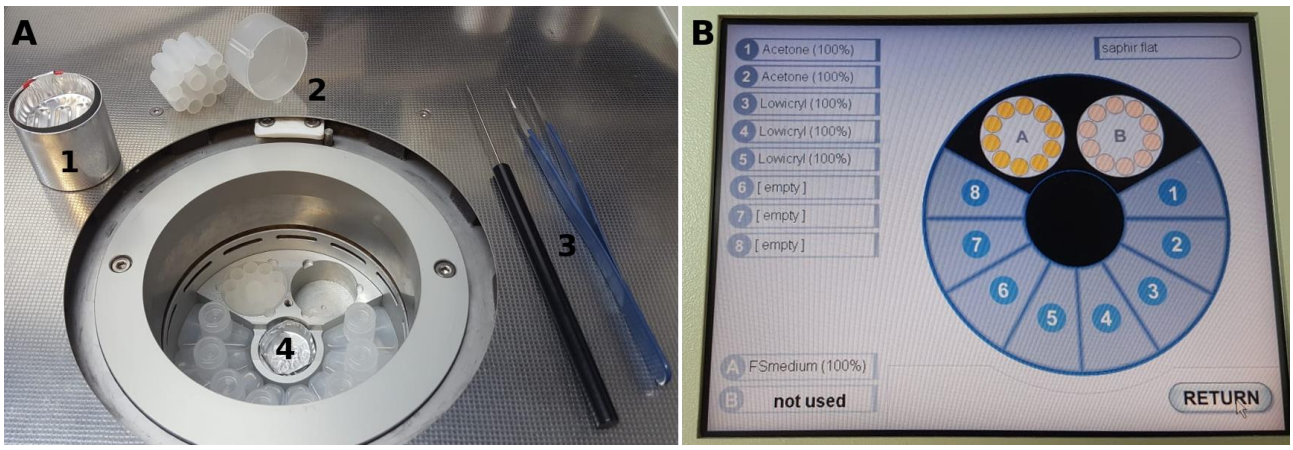

Figure 8: AFSII Sample Chamber and Reagent Loading

Panel A shows the sample chamber of an AFSII and tools, used for sample loading and freeze substitution: 1) Steel container with aluminum inset for quick and easy transfer of vitrified samples in LN_2 from the high pressure freezer to the AFSII. 2) Sample processing container: The inner part (left) can hold up to 10 sapphire discs. It has openings at the bottom of each compartment, allowing chemicals exchange. It is placed into the outer part (right) and then into the AFS sample chamber at the position indicated in panel B. 3) Tweezers and manipulation tool for disassembling the sample sandwich, and rotation and flipping of sapphire discs. 4) Aluminum inset: During sample loading, sapphire discs are first transferred here for immersion in FS medium and aligning, before transfer into the sample processing wheel.
Panel B shows the instructions for loading the reagents needed for freeze substitution. A and B correspond to sample processing containers (A is prefilled with FS medium, B unused). Numbers 1-8 correspond to reagent containers, filled or left empty accordingly.

2.5.4.2.3 Lowicryl HM20 Embedding

Lowicryl HM20 allows to retain ultrastructure as well as fluorescence in a sample (Kukulski et al., 2011). It was always freshly prepared, yielding the best embedding and polymerization results. To do so, 4.47 g Crosslinker D were first mixed with 25.53 g Monomer E. 150 mg Initiatior C was added and the solution mixed on a rotation wheel mixer for 5 minutes in the dark at 4°C, the wheel set very flat to introduce as little air as possible into the resin.

Once all solutions were prepared, they were placed into the AFS2 incubation chamber according to the scheme using AFS2 reagent containers.

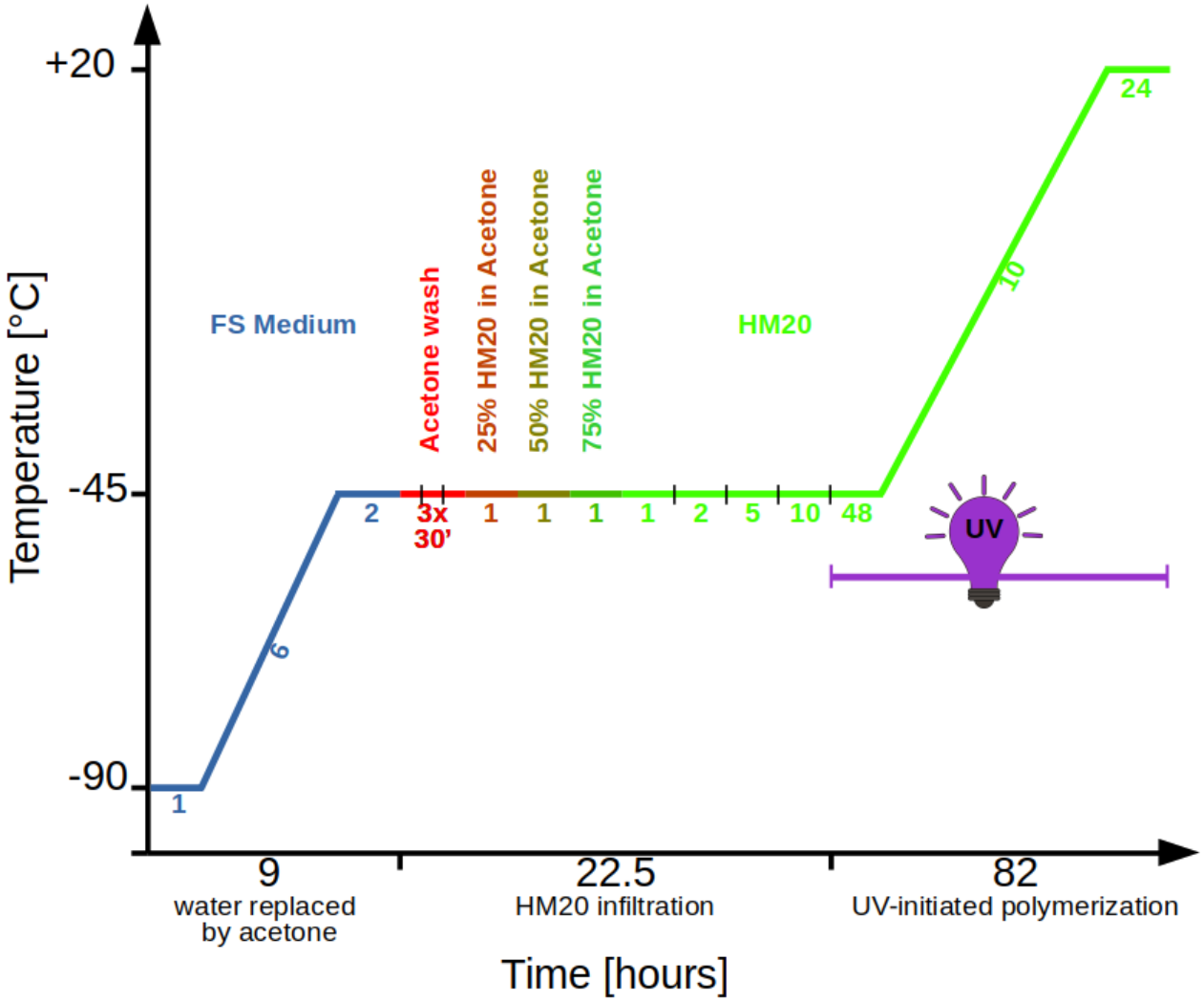

Figure 9: Freeze Substitution and Embedding Scheme for HM20 Embedding in an AFS2

This scheme represents duration (x axis, not drawn to scale), temperature (Y axis) and chemicals used for freeze substitution, and infiltration and embedding of samples in Lowicryl HM20. Chemical handling was performed by the AFS2 Robot. During the first step (9 hours in total), the vitrified water is replaced by acetone. In the next step, acetone in turn is replaced by HM20, the infiltrating and embedding resin (total of 22.5 hours). Once the infiltration is complete, the resin is polymerized by UV light. The sample chamber is still being cooled in the beginning, since polymerization creates a lot of heat that needs to be dissipated in order to not heat up and thereby deplete residual fluorsescence. After 82 hours, the samples are almost polymerized, after another 2-3 days storage in the dark, polymerization is considered complete.

2.5.4.2.4 LR Gold Embedding

Embedding samples in LR Gold is mostly homologous with HM20 embedding (chapter 2.5.4.2.3). LR Gold requires higher temperature for embedding, therefore the temperature is raised at the same

speed for 9 hours 20 minutes (instead of 6 hours), reaching -20°C. Otherwise, samples were also washed with dry acetone, embedded in increasing concentrations of LR Gold in acetone-dilutions and UV-polymerized.

2.5.5 Embedded Sample Processing and Sectioning

The outer plastic layer was removed from the sample processing holder. Razor blades were used to cut open the single wells. Sample blocks were only removed for direct processing. Keeping samples in the sample processing holder and therefore excluding air as much as possible helps retaining the fluorescence, as some fluorophores are susceptible to oxidation.

The removed block was installed in an ultramicrotome UC6 sample holder. With a razorblade, the excess resin, covering the bottom side of the sapphire disc, was removed. The block was removed from the holder and held into LN_2 atmosphere, to cool down the surface holding the sapphire disc. Once cold, the temperature was quickly raised by breathing onto the cold surface. This was repeated until the sapphire disc was easily removed from the resin block.

The block was installed into the ultramicrotome again. Using razor blades, cleaned in 80% Ethanol in water, a trapezoid of roughly 0.5 mm x 0.8 mm was introduced, by removing the residual surface resin. The sample was then aligned to the diamond knife according to the provider's instructions.

To ensure the presence of cellular material in 250 nm thin sections, 1-2 sections were taken up using the perfect loop and placed on a glass slide. By incubating the section(s) on a 90°C heat block, the sections were dried. One drop of methylene blue solution on the section was incubated at 90°C until the drop's rim was turning dry. Then, the methylene blue was washed off using distilled water, and dried again on the 90°C heat block. Once dry, the section was examined in a standard wide field microscope for the presence of cell sections, stained in blue.

When cells were present, further 250 nm sections were prepared. Sections were often compressed during sectioning, and therefore stretched with chloroform before taking them up onto prepared EM grids (see chapter 2.5.1.2).

The loaded grids were briefly dried (less than five minutes to prevent oxidation) on filter paper in a dark box to prevent bleaching. Leaving grids dry for longer time drastically reduces fluorescence. Those grids were then incubated on a 1:50 dilution of TetraSpeck Fiducials in 1x PHEM with Hoechst33258 for 10 minutes in the dark at RT, the thin section facing the dilution. Excess fiducials were washed off by briefly washing the grids twice on water, without any plotting of excess liquids. Grids were fully immersed in water and placed into a drop of water (~30 µL) on a 25 mm glass

cover slip. Immersing the grid in water completely before placing it, makes it easier to place the grid, thin section facing the glass, into, not onto, the drop of water. Placing it within the H_2O reduces the emergence of air bubbles between the cover slip and the section dramatically, which otherwise hampers LM acquisition.

Another 25 mm cover slip is placed onto the grid, and the now assembled sandwich placed into a CLEM sandwich holder.

This holder was then taken to a Leica SP8 for light microscopy.

2.6 Correlative Light – and Electron Microscopy

High precision on-section correlation is a lengthy method. For a better overview, we first show a schematic of the single steps.

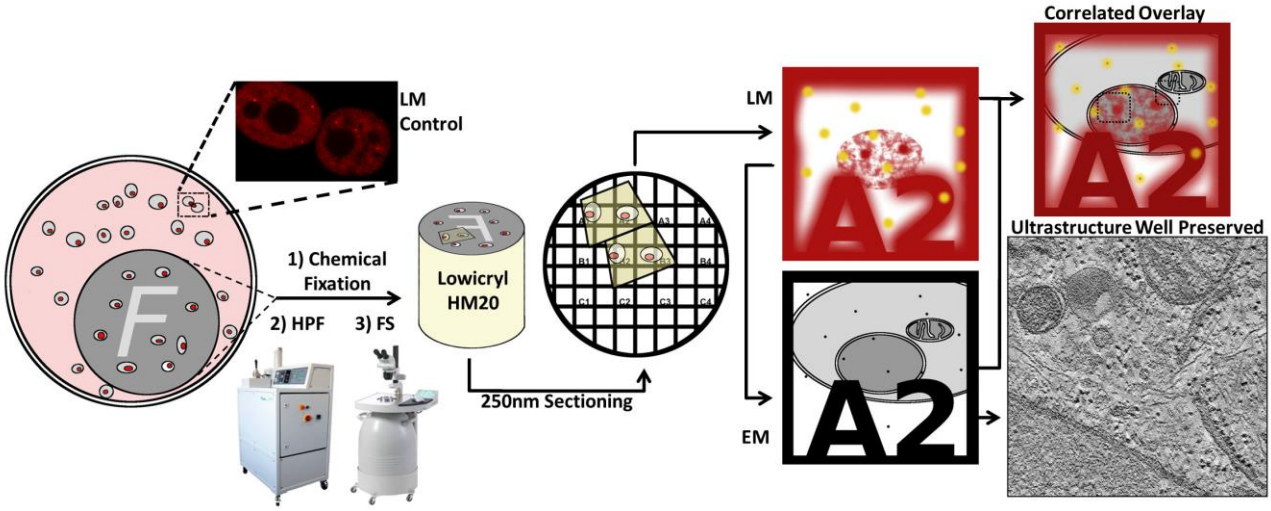

Figure 10: Correlative Light - and Electron Microscopy Workflow

Sample cells are seeded onto carbon coated sapphire discs (chapter 2.5.1.1) in 8 wells. 4 hours after infection (chapter 2.4.3), the samples are chemically fixed in aldehydes (chapter 2.4.5.3). The samples are high pressure frozen (HPF, chapter 2.5.4.1), freeze substituted and embedded in Lowicryl HM20 resin (chapter 2.5.4.2). 250 nm thin sections are prepared and incubated with TetraSpeck Fiducials. Light microscopy is performed in at least 2 channels to visualize rCPSF6wt$_{AA}$.mCh and TetraSpeck Fiducials in the red channel and TetraSpecks only in e.g. the green channel. Therefore, rCPSF6wt$_{AA}$.mCh are red only, while TetraSpeck Fiducials appear yellow (red and green, see chapter 2.6.1). The sections are then postcontrasted (not shown, chapter 2.6.2) and imaged in EM, where the TetraSpeck Fiducials can be appreciated by high electron-densities (chapter 2.6.3). Using the TetraSpeck Fiducials for light – and transmission electron micrograph correlation via Icy ec-CLEM (chapter 2.6.4), Regions of interest (boxed) can be identified in the

correlated overlay image. High magnification tilt series are acquired to image regions of interest and cytoplasmic regions to ensure the quality of ultrastructure preservation (chapter 2.6.5).

2.6.1 Light Microscopy of Thin Sections

For light microscopy, it was crucial to use a highly magnifying objective (63x) and sensitive detectors (HyD detectors). The rCPSF6wt$_{AA}$.mCh fluorescence in whole fixed cells was usually strong and required ~2% laser power for proper imaging. After embedding, thin sections required a laser power of ~25% in combination with 2-6 fold frame accumulation for mCh visualization.
The grid was oriented in the sandwich holder and eventually in the microscope in a way to visualize the coordinates readable. Acquiring light – and electron micrographs in a roughly oriented way will make the correlation step much easier.

The sandwich holder was placed into the SP8 microscope. Following the Hoechst stain allows to find nuclei in sections easily and to approximately set the focal plane (a slight focal offset can be observed between channels). The nuclei were imaged in at least two channels: 568 to image mCherry and TetraSpeck Fiducials and 647 to image the latter only. By overlaying those two channels, TetraSpecks are identified by fluorescing in both channels, whereas rCPSF6wt$_{AA}$.mCh signals will appear in the 568 channel only (compare Figure 29 & Figure 30).
Areas with a position of interest – an rCPSF6wt$_{AA}$.mCh cluster signal - were acquired at ~ 4 fold zoom, using 10% laser power in the 647 channel with a single scan and 20% laser power for the 568 laser, accumulating 2-6 scans to reliably visualize the signal of interest. ROIs too close to grid bars (<4 µM distance from rCPSF6wt$_{AA}$.mCh clusters) have not been recorded, as electron tomography would have been hampered by the proximal grid bars during tilt series acquisition.

Once the grid has been scanned, the sample sandwich was removed from the microscope and opened with a razor blade. The grid was loosened from the cover slip glass by adding another drop of water, on which the grid floats. The grid was then plotted and stored in a grid box until further processing, when not further processed directly.

2.6.2 Thin Section Postcontrasting for Electron Microscopy

All following staining and washing steps were performed in 20 µL drops on clean parafilm at RT.
For most possible accurate correlation, 15 nm PAG fiducials were added to the section surfaces. Therefore, grids were incubated first with the side not containing the sample section on 1:50 PAG in

H_2O dilution for 10 minutes, then washed 3 times for 10 seconds in H_20 and then blotted on filter paper. This was then repeated for the sample section containing side without blotting in the end.

To restore and increase contrast washed out during fiducial incubation, sections were postcontrasted using established protocols for PbCi and UAc (Hall, 1995; Reynolds, 1963).

Grids were calibrated twice for 10 seconds on 70% MeOH in H_2O, transferred onto 3% UAc in 70% MeOH solution and incubated for 5 minutes. The grids were washed twice for 5 seconds in 70% MeOH in H_2O and twice for 2 minutes in H_2O. Drops of PbCi were surrounded by 5-10 KOH pellets to prevent CO_2 from reacting with the solution and forming hardly soluble $PbCO_3$ precipitates. Grids were equilibrated for 10 seconds and then incubated for 3 minutes. 2 brief washing steps were performed in the CO_2 depleted area, then another 4 washes in H_2O were performed. Finally, the grid was blotted and stored in the grid box.

2.6.3 Low Magnification EM for Correlation

To correlate light- and electron micrographs, low magnification (4000x) electron micrographs are needed. At this magnification, we could generally image enough TetraSpeck Fiducials in one field of view (~20) to faithfully correlate LM and EM micrographs. Secondly, PAG fiducials are also well visible and can later be useful for pinpointing the position of ROIs, when higher magnification tilt series are acquired.

The sample grids were analyzed in an EM10 due to excellent contrast in acquired micrographs. Following the EM finder grid's coordinates, cell sections were found back in the electron microscope. Micrographs were acquired at positions, where rCPSF6wt_{AA}.mCh clusters have been have been identified in LM (ROI).

2.6.4 Correlation of Light - and Electron Micrographs

To overlay the light micrographs containing ROIs and electron micrographs containing ultrastructural data, the ec-CLEM plugin (Paul-Gilloteaux et al., 2017) for the image analysis software Icy (Chaumont et al., 2012) was used.

Tetraspeck Fiducials have two important properties: 1) Due to their multispectral fluorescence, Tetraspecks can be visualized in all fluorescence channels, and therefore can be discriminated from specific signals, such as DAPI (only blue channel) or rCPSF6.mCh (only red channel). 2) Tetraspeck Fiducials are very electron-dense and can therefore be well identified in electron micrographs.

Corresponding LM and EM files were loaded into the program and the data type changed to unsigned 8bit files. Once all fiducial signals (10-25) were assinged in LM and EM, the light micrograph was rotated and scaled to fit the electron micrograph, resulting in an overlay image, combining ultrastructural and fluorescence data. The single channels were extracted from Icy and overlayed in FIJI (see e.g. Figure 29).

2.6.5 High Magnification Electron Tomography and Reconstruction

In tilt series electron tomography, the 3D shape of imaged structures is reconstructed by computational backprojection of images acquired at different tilt angles.

The EM sample grid was placed and secured into a dual tilt (DT) tomography holder and inserted into the F20 electron microscope. The DT holder allows rotating the sample around the *z* axis, thereby (i) orienting the sample according to the low magnification correlation images, making it much easier to reliably identify the ROI and (ii) positioning the grid bars to allow maximum range tilt series acquisition. During acquisition, grid bars can be tilted into the imaged region and thereby end the acquisition at lower tilt angles.

SerialEM (Mastronarde, 2005) was used to control the microscope, TIA to control the in column-camera. ROIs were found back using the coordinates of the EM finder grid (rough) and the LM and EM correlated micrographs (fine).

The ROI was centered, the microscope stag's eucentricity adjusted to the ROI, focused and tilt series acquired at 19,000 fold magnification. Whenever possible, 121 consecutive tilt images, from -60° to +60° in 1° increment steps, were acquired. Exposure time and electron beam aperture were adjusted to collect ~6000 counts per one image.

To maximally omit the introduction of bias during hands-on reconstruction, the acquired tilt series (*.st files) were automatically reconstructed using batch tomogram reconstruction in eTomo (Kremer et al., 1996).

Patch tracking was used for all tomograms, with a patch size of 300x300 pixels. After reconstruction, the volume was automatically trimmed and rotated around the *x* axis.

The reconstructed tilt series (*.rec files) was loaded into 3DMOD (Kremer et al., 1996). Each apparent structure was modeled as a scatter-model in a single object (point cloud). Object points were set at positions with high electron-density within the surface of apparent structures (see Results Figure 31 & Figure 36). Models were saved as *.mod files.

2.6.6 Model Data Analysis in MatLab

The model points' coordinates were extracted out of the *.mod file and imported into MatLab. The apparent PIC structure appeared very similar in shape when compared to the cores observed in surface-bound virus particles. The cone-shape can mathematically be approximated by an ellipsoid. We therefore fit an ellipsoid function into the models and could thereby define the longest axis (= major axis) and the 2 minor axes, orthogonal to the major axis. For the envelope of the surface-bound virus particles, we approximated a ball function, instead. At this point, we corrected for the observed compression along the *z* axis as described below.

The model points were plotted along the major axis in a rotational projection: The distance of a given model point was measured and plotted against the closest position at the major axis. A trend function was calculated along the projected model points by applying a sliding average. The global maximum in this trend function was defined as the radius of the structure's widest point (half the width). The structures' length equals the length of the major axis' eigenvector.

2.6.7 Correction for *z* Compression / *xy* Stretching

In reconstructed tomograms, it was obvious that apparent PIC structures as well as surface-bound virus particles appeared compressed in *z* (or stretched in *xy*). During model evaluation, we implemented corrections to account for this. Since we do directly compare nuclear PIC structures to cell surface-bound virus particles' cores, it is irrelevant, whether the correction is applied by stretching the *z* axis or by compressing in *xy*. This was done in collaboration with Dr. Martin Schorb (EMCF at EMBL Heidelberg), who wrote the scripts and applied them to the model data.

2.6.7.1 Correction for Surface-Bound Virus Particles

Full virus particles at the cell surface not only harbor the capsid structure for reference, but are also enveloped, since they did not undergo fusion with plasma membranes. Membranes can be assumed to ideally be ball-shaped. Additionally, to the capsids, we therefore also modeled the membrane envelopes and analyzed their geometry. By comparing the diameters measured in *x*, *y*, and *z*, it was possible to directly measure the difference in length and correct for compression in *z*.

Example: The envelope measured 90.2 nm, 93 nm and 82 nm in *x*, *y* and *z*, respectively. Ideally, *x* and *y* would be equal, therefore we calculated the average: (90.2 + 93) nm / 2 = 91.6 nm. The ratio of the *xy*-average and the *z*-measurement is: 82 / 91.6 = 0.895. Meaning, the volume was compressed to 89.5% of its ideal size in *z*. The correction factor was calculated as the reciprocal of this value: 1 / 0.895 = 1.117. The volume was therefore stretched by the correction factor 1.117 in *z*.

After applying this, redone measurements are 90.2 nm, 93 nm and 91.6 nm in *x*, *y* and *z*, respectively. The compressed envelope was corrected to best match a perfect sphere. No correction was performed in other axes, as the variations were minor and more likely due to sample preparation.

2.6.7.2 Correction in Apparent PIC Structures

This correction was more difficult to implement, due to the lack of a direct reference (such as the envelope for surface-bound virus particles). Like the envelope is assumed to be a perfect sphere, we assumed the apparent PIC structure to be rotationally symmetrical along the major (longest) axis. The minor axes (orthogonal to the major axis) should in that case be of identical length. By comparing the minor axes' lengths and their orientation in respect to *z* in the volume, we can calculate the factor, by which the *z* axis was compressed and apply corrections accordingly.

Example (compare Figure 11): An apparent structure is initially analyzed (left structure, oriented in *x*). The major axis (blue) is parallel to *x* and measures 110 nm. The minor axes, being orthogonal to the major axis, are parallel to *y* (minorY, red, measuring 60 nm) and parallel to *z* (minorZ, green, measuring 52 nm). Assuming a perfect rotational symmetry in the observed structure means that the 2 minor axes minorY and minorZ would be of equal length. The structure appears compressed in *z* since minorZ is shorter than minorX. Their ratio is: 52 nm/ 60 nm = 0.867, meaning that the volume of the image is compressed to 86.7% of its original size. The correction factor is calculated as the reciprocal: 1 / 0.867 = 1.154. The volume is stretched in *z* by the correction factor. Measuring the axes again yields 110 nm for the major axis, and 60 nm each for minorY and minorZ (yielding the "actual structure" with red and green minor axes of equal length).
This example is easily calculated. When the major axis is parallel to *z*, the 2 minor axes will not be affected by the compression and would therefore not allow to correct. Therefore, the angle between the major axis and the *z* axis is important to calculate the correct correction factor.

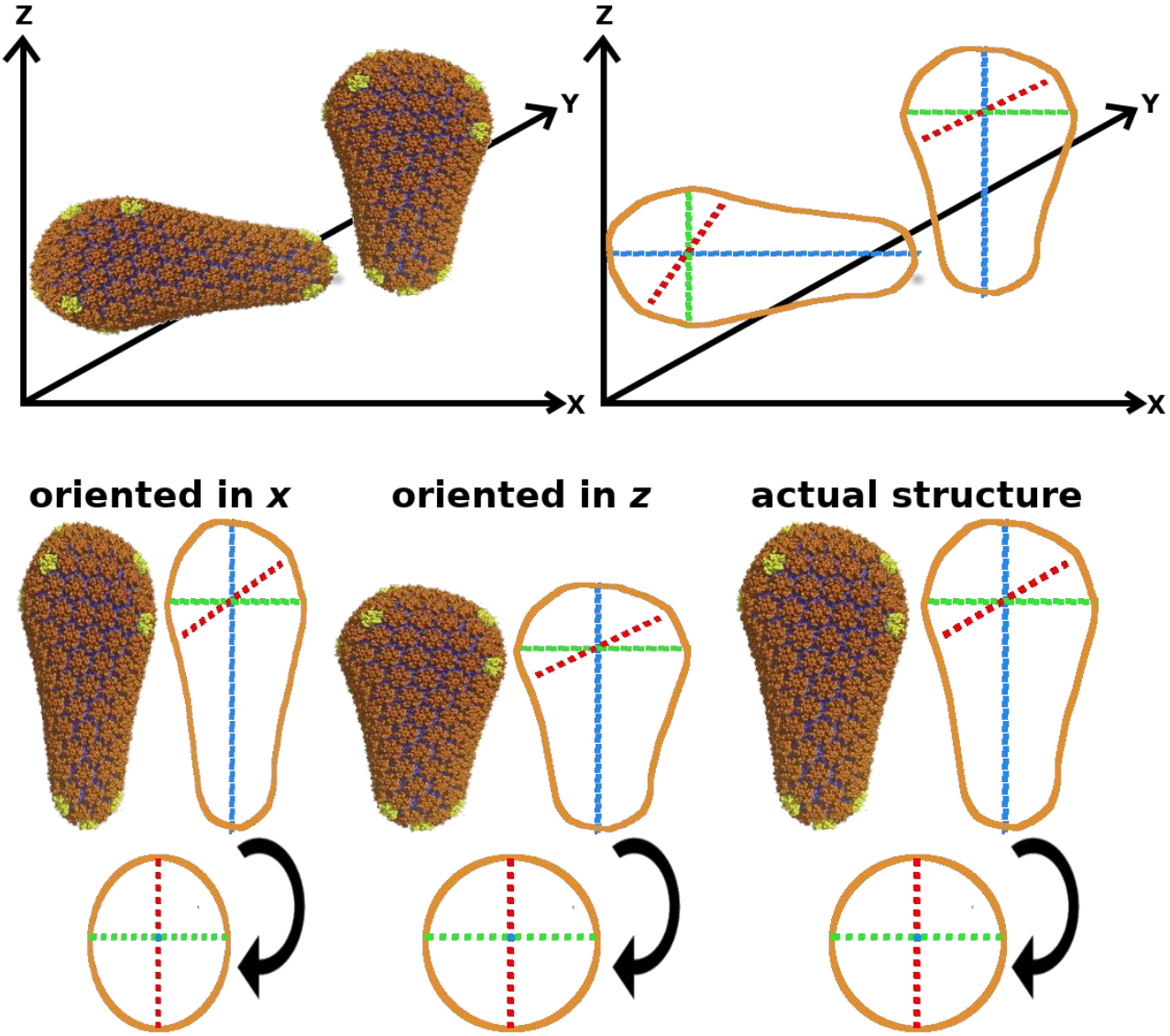

Figure 11: Schematic Representation of z-Compression

The top left panel shows 2 idealistic structures in one tomogram, the major axis oriented in z or x. The top right panel shows the extrapolated models and their fit axes (blue: major axes, green and red: minor axes). The compression in this scheme amounts to 80%. When these structures are extracted and aligned along their major axes, the structure oriented in x (lower left panel) appears compressed along the green minor axis, while the structure oriented in z (lower middle panel) appears compressed along the blue major axis. 90° rotations around the green minor axis are displayed beyond the extracted structures. The structure oriented in x can be used to calculate the compression factor by comparison of the minor axes' eigenvectors' lengths. Applying the calculated correction factor 1.25 yields a corrected tomogram, where the 2 structures will take in the actual idealistic structure (lower right panel). Idealistic structure adapted from (Pornillos et al., 2011).

3 Results

3.1 Ultrastructure Visualization of Productive Reverse Transcription Complexes (RTC)

A hallmark for productive subviral particles (RTC and PIC) is the presence of viral DNA. As earlier published by our lab (Peng et al., 2014), it is possible to detect nascent DNA by metabolic incorporation of a thymidine-analogue, called EdU, during DNA synthesis. EdU can be labeled by Cu-catalyzed click reaction, covalently binding a fluorophore to it.

Throughout establishment and testing of new and adjusted protocols, we were employing mitochondrial DNA (mtDNA) as a model for viral DNA (vDNA). They are similar in genome size (16.6 kb mtDNA, 9.7 kb vDNA, (Coffin et al., 1986; Taanman, 1999; Vogt, 1997)) and physical size (both ~100 nm in *x*, *y*, and *z* (Briggs, 2003; Brown et al., 2011)). Using mtDNA as a model also allows to work under BSL1 conditions, while experiments with infectious HIV-1 particles were performed in BSL3. Hence, we mimicked BSL3 conditions by applying BSL3 fixation protocols, which would later allow direct transfer of working protocols to infection experiments.

3.1.1 EdU Click Label Retention in HM20-Embedded Samples

Performing CLEM with high precision correlation can be achieved by retaining the fluorescence of the (surrogate) marker on EM sample thin sections (e.g. (Kukulski et al., 2011, 2012)).

The fluorescence can be retained, when samples are embedded using high pressure freezing and HM20 embedding. Importantly, such prepared samples are ultrastructurally very well retained.

We therefore tried, if we could retain EdU signals throughout EM sample preparation. U87$^{4/4}$ cells on sapphire discs were treated with EdU for 4 hours. Samples were fixed for 90 minutes in PFA, and EdU click labeled. The labeled samples were high pressure frozen, freeze substituted and embedded in HM20. 250 nm thin sections were prepared and imaged in light – and electron microscopy, homologous to the samples for nPIC correlation.

When we imaged those samples, we were able to visualize EdU signals of clearly nuclear shape and size (see Figure 12, panel A). However, extranuclear mtDNA was not visible. EM sample preparation for HM20 embedding is known to reduce the fluorescence intensity drastically. We assume that we therefore can only observe the intense nuclear DNA, but not mitochondrial DNA. Additionally, the ultrastructure was not satisfying (see Figure 12, panel B). Generally, not many cytoplasmic features were recognizable, mitochondria (Mt) appeared simply as dark tubular

structures, whereas inner mitochondrial membranes (christae) were not recognizable. Although the overall ultrastructure was suboptimal, it also needs to be mentioned that the image shows a single TEM image of a 250 nm thin section. Tomographic data would reveal more details but did not seem promising at this point.

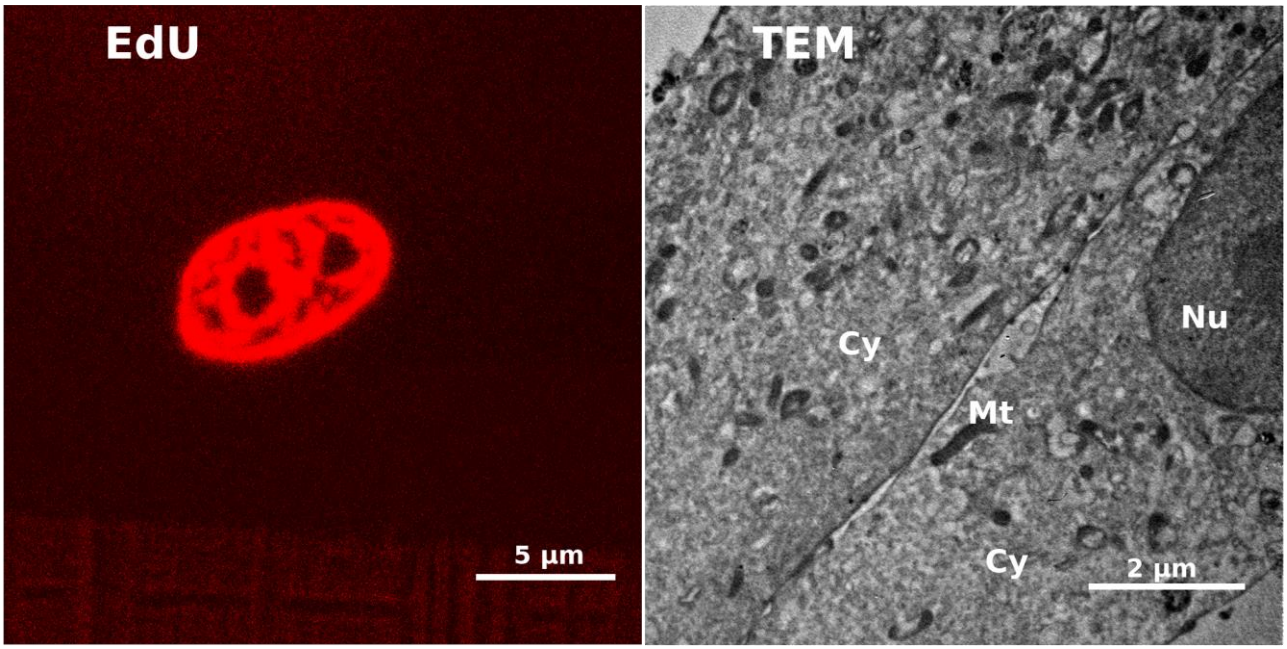

Figure 12: Light - and Electron Micrographs of Preembedding-EdU Labeled U87$^{4/4}$ Cells Thin Sections

U87$^{4/4}$ cells were allowed to incorporate EdU for 4 hours. Cells were chemically fixed and EdU labeled before high pressure freezing, freeze substitution and embedding in Lowicryl HM20. 250 nm thin sections were imaged in light (left panel, EdU signal) and transmission electron microscopy (right panel, TEM). Nuclear EdU signals (red) were visualized. Extranuclear mtDNA EdU signals were not detected. Electron micrographs of those sections were ultrastructurally damaged and partially extracted. E.g. mitochondria appear as dense, blobby structures, christae are not recognizable. Mt: Mitochondrion, Nu: Nucleus, Cy: Cytosol. Imaging performed with Leica SP2 (LM) and Zeiss EM10 (TEM).

3.1.2 EdU Click Labeling on HM20 and LR Gold Thin Sections

Since we could not retain the EdU fluorescence enough during EM sample preparation for HM20 embedding, we next tried to embed cells that had incorporated EdU before, to then click label the EdU directly on sections. Doing so, the EdU-linked fluorophores will not be bleached during sample preparation with UV light, and might therefore yield stronger EdU fluorescence signals.

HM20 and LR Gold resins have been shown earlier, to allow immunolabeling on thin sections of embedded samples (van Lookeren Campagne et al., 1991; McDonald et al., 2012). U87$^{4/4}$ cells were incubated with EdU for 4 hours before direct high pressure freezing, freeze substitution and embedding in HM20 or LR Gold resin. 250 nm thin sections were taken up on EM finder grids and incubated with the EdU click labeling mixture for 30 minutes at RT. After click labeling, the sections were also incubated with DAPI for easy identification of nuclear DNA.

Performing light microscopy, we could only detect EdU signals in LR Gold embedded samples (see Figure 13, left panel). Lowicryl HM20-embedded samples, in contrast, did not yield any fluorescence (data not shown).

Yet, like in experiments performed before, we could only visualize nuclear EdU signals. Extranuclear mtDNA remained undetected. It is sound to assume that embedding cells in solid resins limits the accessibility of EdU dramatically. We can only hypothesize about the polymer penetration of the click reaction mixture, but EdU might only be readily click labeled at the accessible surface of a section.

Additionally, the EdU click labeling procedure incurred considerable damage to the ultrastructure, as can be seen in electron micrographs of click labeled thin sections (see Figure 13, right panel). LR Gold thin sections were so much depleted of contrast, the ultrastructural retention cannot even be judged. Postcontrasting the thin sections using PbCi and UA did not improve the ultrastructural visualization.

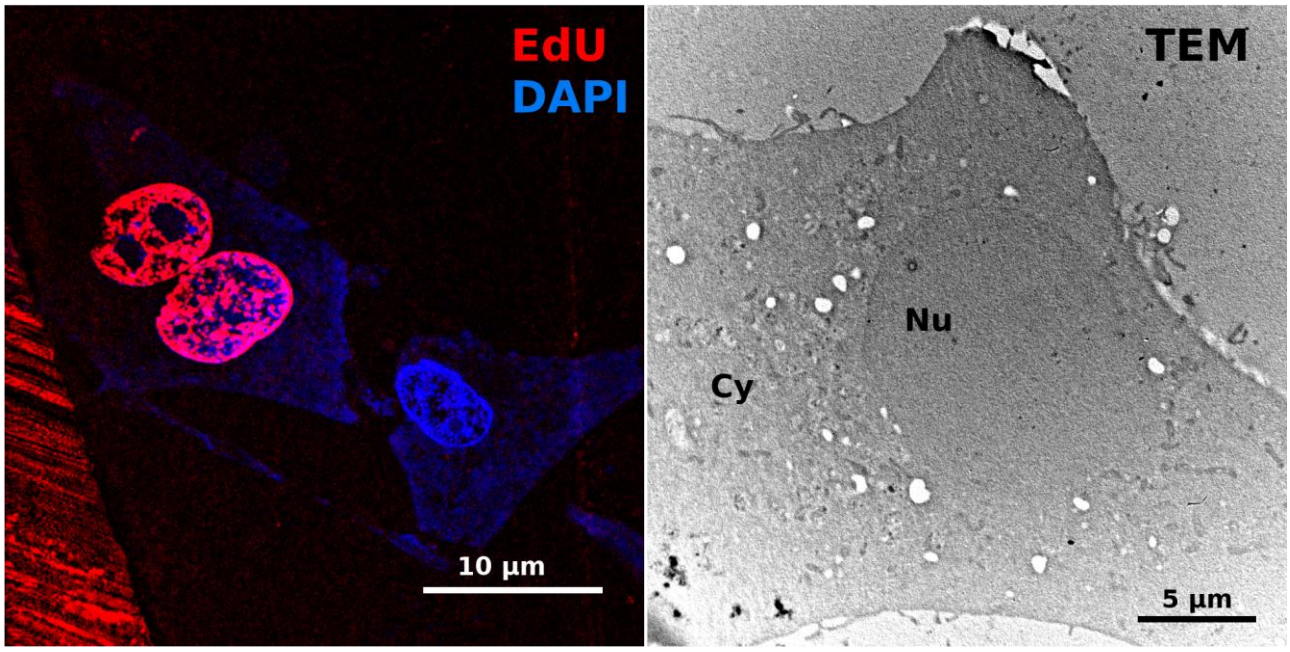

Figure 13: Light and Electron Micrographs of Embedded EdU-Treated U87$^{4/4}$ Cells Thin Sections After on-Section EdU Labeling

U87$^{4/4}$ cells were allowed to incorporate EdU for 4 hours before high pressure freezing, freeze substitution and embedding in LR Gold. 250 nm thin sections were EdU click labeled and imaged in light (left panel)- and transmission electron microscopy (right panel). Nuclear EdU signals (red) were well visualized. Extranuclear mtDNA EdU signals were not detectable. Electron micrographs of those sections were strongly reduced in contrast. Nu: Nucleus, Cy: Cytosol. Imaging performed with Leica SP2 (LM) and Zeiss EM10 (TEM).

3.1.3 Tokuyasu Cryosectioning Allows Efficient Immunolabeling

In the Tokuyasu technique (Griffiths et al., 2015; Painter et al., 1973; Tokuyasu, 1973) samples are fixed with only aldehydes and embedded in gelatin. High concentrations of sucrose prevent crystal ice formation during flash freezing in LN_2, allowing cryo-thin sectioning. The gelatin is gently removed from thin sections, which can then be processed for immunolabeling. The samples stay fully hydrated throughout the processing. This in combination with mild aldehyde-fixation generally yields good retention and high accessibility of antigen epitopes, well suited for immunolabeling. Furthermore, it is a relatively quick method that allows to image samples in LM and EM already one day after fixation and therefore allows quick evaluation of an applied protocol.
We were unable to detect mtDNA in samples that were embedded in solid resins (see Figure 13). Different from solid resin embedding techniques, the Tokuyasu sample preparation is considered and reported to provide good conditions for efficient immunolabeling. We considered that efficient immunolabeling might also increase the chances of labeling EdU, since it might be more accessible than in other EM techniques.

3.1.3.1 HIV-1 Capsid Structures can Generally be Retained in Tokuyasu Preparations

Before assessing EdU labeling itself, we tested the retainability of the capsid ultrastructure. Samples prepared following the Tokuyasu technique, in general, show well contrasted membranes, whereas proteinaceous structures are less well visualized.
We therefore prepared an HIV-1 virus particle pellet. Cell supernatant from MT4 cell cocultures are generally very rich in HIV-1 virus particles. We collected coculture supernatants, which was concentrated by ultracentrifugation in 2 steps. The yielded virus particle pellet was chemically fixed and processed according to the Tokuyasu technique. 120 nm thin sections were prepared and imaged in TEM.
We could visualize enveloped virus particles with well appreciable capsids, as well as structures that fit in size and shape to capsids, but lack an envelope (Arrow and asterisks, respectively, Figure 14). The observed apparent structures appear little clear. It has to be mentioned that these virus particles

here underwent ultracentrifugation twice, which is considered harmful to particles. However, it also has to be mentioned that there is no selection for particles that appear particularly clear, but an overall micrograph of a bulk of particles.

We conclude that (to a certain extent), the ultrastructure of HIV-1 capsids can be retained in Tokuyasu sections. This is an important prerequisite for the potential imaging of RTC structures in infected cells.

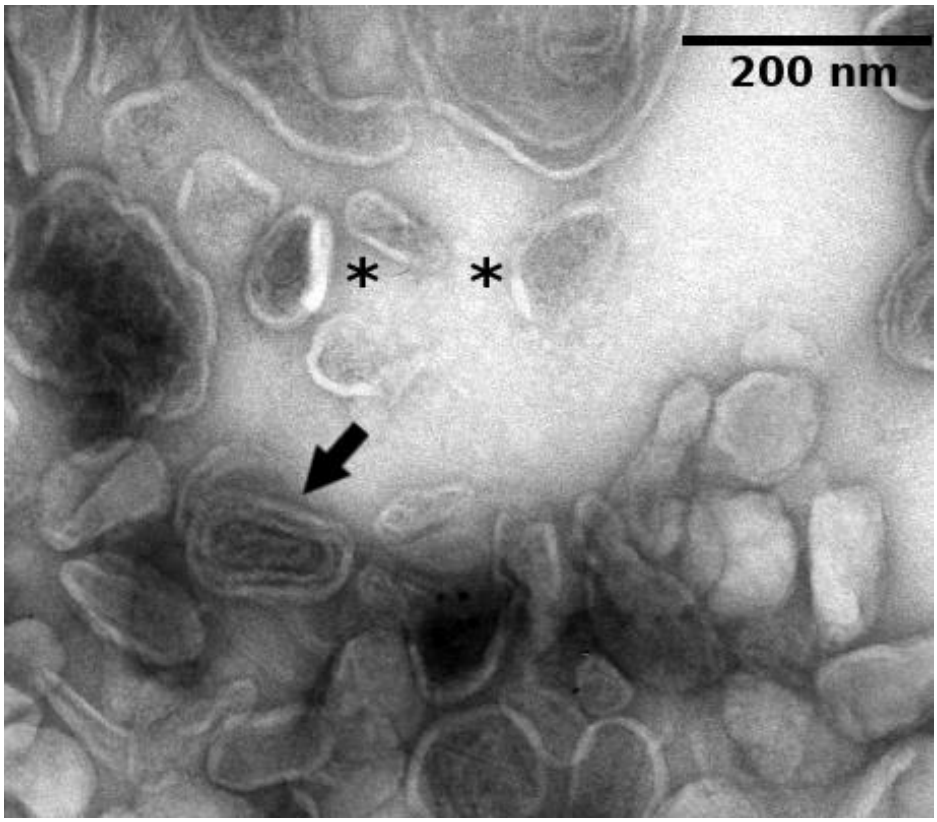

Figure 14: Electron Micrograph of a 120 nm Tokuyasu Section of a Virus Particle Pellet

HIV-1 virus particles from MT4 cocultures were concentrated by ultracentrifugation. The obtained pellet was fixed with PFA and GA and prepared following the Tokuyasu technique. 120 nm thin sections were prepared and visualized in transmission electron microscopy (Zeiss EM10). Enveloped virus particles can be appreciated (arrow), as well as multiple core-reminiscent structures (*).

3.1.3.2 High Precision Correlation of Nuclear DNA is Compatible with Tokuyasu Preparations

Next, we tested the feasibility to correlate light and electron micrographs of samples prepared according to the Tokuyasu protocol. The sample preparation, and therefore the contrast in these

sections is quite different to the solid HM20 resin embedded samples. Hence, we wanted to validate that TetraSpeck Fiducials can be recognized and used for high precision correlation.

250 nm thin sections of HeLa TZM-bl cells were prepared and on-section labeled with DAPI. LM (Wide Field Microscope) and EM (Zeiss EM10) micrographs were acquired and correlated. Using TetraSpeck Fiducials, we were able to correlate light- and electron micrographs with high precision. The TetraSpecks were well visualized in LM (multispectral fluorescence) and EM (high electron-densities). Using these signals to correlate light – and electron micrographs yielded a satisfying colocalization of the DAPI signal and the ultrastructurally identified nuclei (EM) (see Figure 15). The TetraSpeck Fiducials appear white here, which is due to particular contrasting and image acquisition in slight defocus. We could hereby prove that correlation of DNA signals is well possible in combination with the Tokuyasu technique.

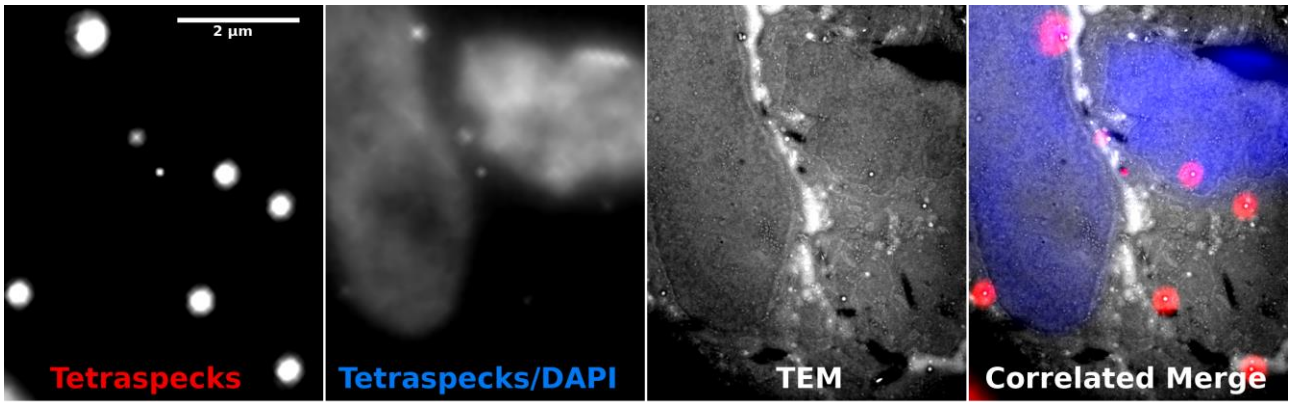

Figure 15: Correlation of HeLa TZM-bl Tokuyasu Section with DAPI Signal

HeLa TZM-bl cells were fixed and gelatin embedded, 250 nm thin sectioned and on-section DAPI labeled. A: Light microscopy of TetraSpeck Fiducials, imaged in the red channel. B: Light microscopy of DAPI and TetraSpeck Fiducial signals in the blue channel. C: Correlated transmission electron micrograph. D) Merge of fluorescence signals of (A and B) and the transmission electron micrograph (C). The scale bar in (A) is representative for all figure panels. The blue DAPI signal correlates well with nuclear sections (D), while the TetraSpeck Fiducials appear round and white with a black rim due to high electron density and imaging in slight defocus.

3.1.3.3 mtDNA Visualization in Light Microscopy

Before assessing the visualization of mitochondrial DNA EdU signals in sections, we wanted to be sure to be able to visualize them in whole cells, using the fixatives for the Tokuyasu preparation.

HeLa TZM-bl and U87$^{4/4}$ cells were allowed to incorporate EdU for 4-5 hours before fixation.

For good fixation and structural preservation, it was suggested (Bleck et al., 2010) to prepare a 2x concentrated fixative, i.e. 8% PFA, 0.4% GA in 2x PBS buffer, which is prewarmed to 37°C and added directly to culture medium in a 1:1 ratio. Such fixation supposedly avoids shocking cells due to sudden changes of buffer or temperature. When cells were fixed this way for 90 minutes and processed for immunofluorescence, we observed cytochrome c (CC) and transporter of outer mitochondrial membrane 20 (TOM20) to not efficiently colocalize (see Figure 16). This is generally interpreted as a sign of cellular stress, which was supposed to be suppressed under these fixation conditions. When hypertonic 2x fixative is mixed with cell culture medium, the mixed solution is 1.5 fold hypertonic, which may account for the observed cell stress. Furthermore, proteins in the cell culture supernatant (such as FCS) most likely sequester substantial amounts of aldehydes. The effective aldehyde concentration cannot be determined, but is certainly lower, than aimed for.

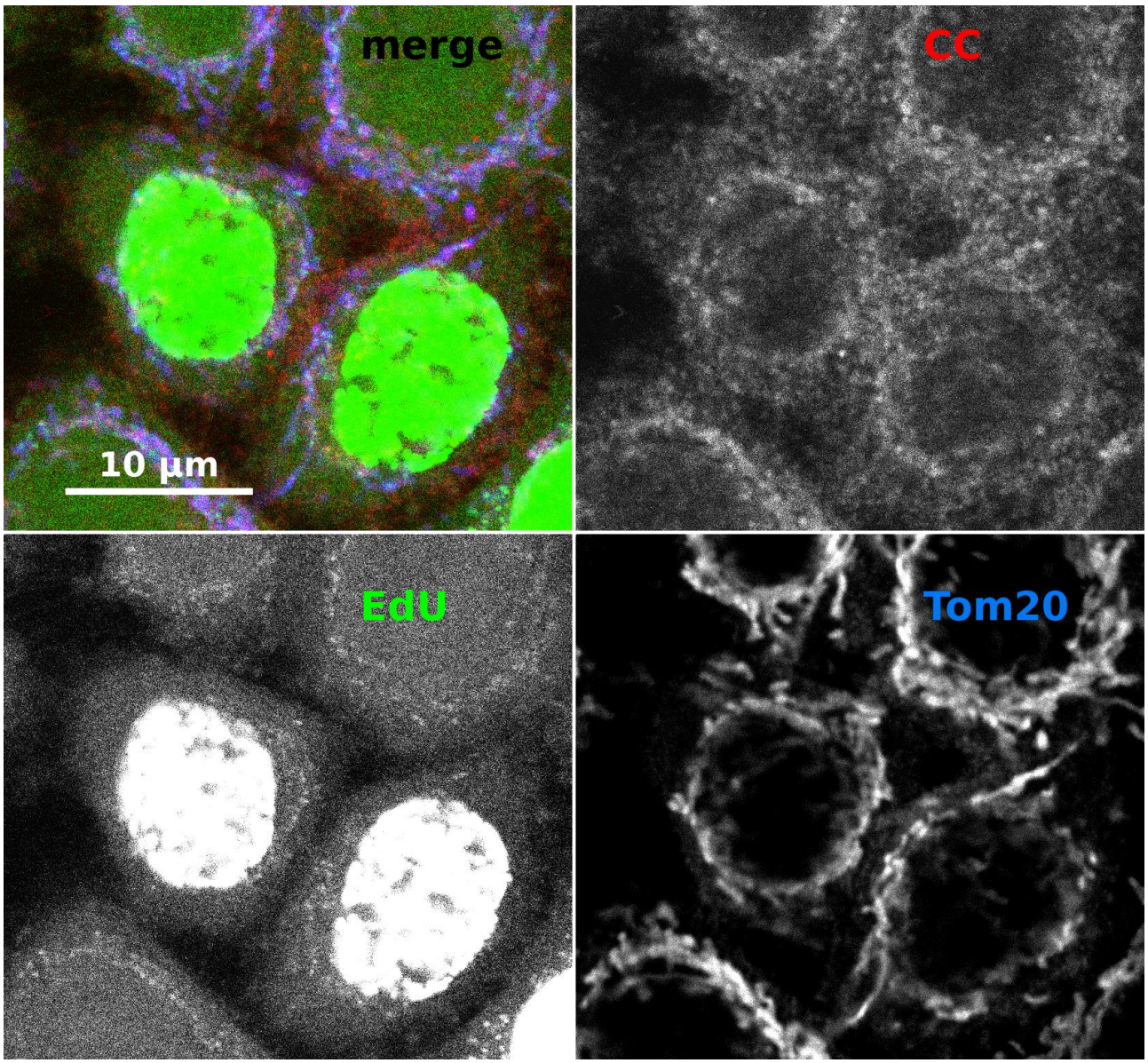

Figure 16: Light Micrographs of Hela TZM-bl Cells After 2x Fixative Fixation

HeLa TZM-bl cells were allowed to incorporate EdU for 5 hrs. Samples were fixed by diluting 2x fixative (8% PFA; 0.4% GA in 2x PBS) 1:1 in cell culture supernatant, EdU – and immunofluorescence labeled for mitochondrial markers. Within 5 hours, only a subset of HeLa cells undergo nuclear DNA synthesis and thereby incorporate EdU. Some cells therefore don't show nuclear EdU signals. While TOM20 looks as expected, CC does not colocalize efficiently with TOM20. This is understood as a sign of cellular stress. Single confocal planes, acquired with the SP2 microscope.

Fixation does not appear to happen quickly, but to leave the cells enough time to secrete CC from their mitochondria. For a satisfying ultrastructural preservation and for little introduction of artifacts, it is indispensable to fix cells quickly and efficiently. Additionally, we observed a strong background signal in the EdU channel, in which it was almost impossible to faithfully identify

mtDNA signals. GA is known to cause or increase autofluorescence, we therefore also tested different concentrations of GA in the next fixation experiments (Figure 17).

Fixing cells in 1x buffered fixative (4% PFA, 0.2% GA in 1x PBS) directly, instead of diluting 2x fixative in cell culture supernatant yielded much more satisfying results. The CC signals were not spread throughout the cells, but confined to mitochondria, as can be seen by the specific shape (also by colocalization with TOM20 (not shown). Nuclear EdU signals are always well visualized, independent of the used fixative. mtDNA, on the other hand, can only be faithfully recognized when no GA was used during fixation (see Figure 17, right lower panel). This is in line with the observation in Figure 18.

We conclude that GA either hampers EdU click labeling, or increases the background autofluorescence enough to exceed the mtDNA signals in intensity. Therefore, it is very likely to also negatively influence the detection of viral DNA in RTC. On the other hand, GA is important for proper fixation, and might well be necessary for the retention of the capsid ultrastructure.

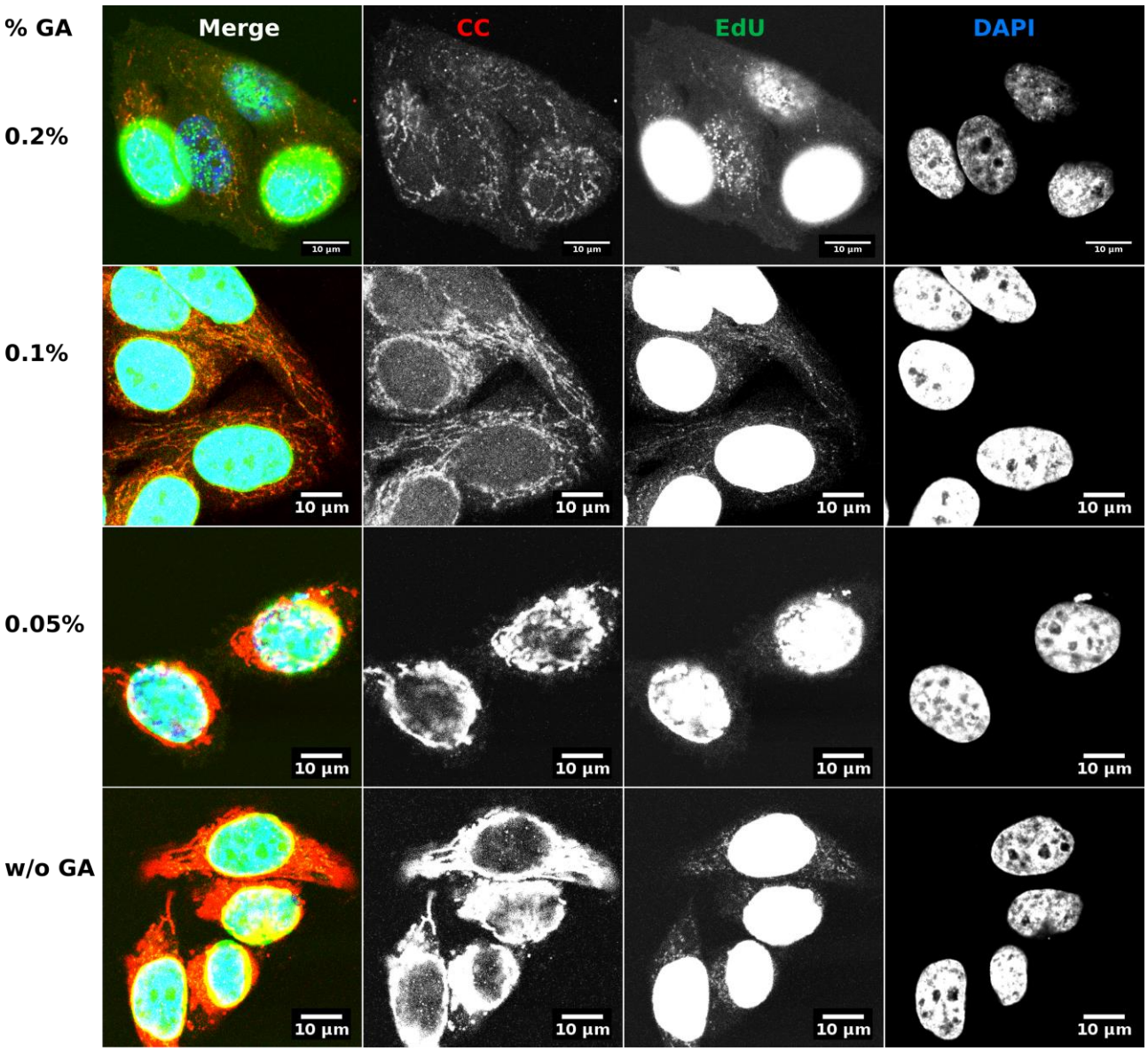

Figure 17: Visualization of mtDNA by EdU Click Labeling Under Different Fixation Conditions

HeLa TZM-bl cells were incubated with EdU for 4-5 hours, fixed in 1x PHEM buffer with 4% PFA and different concentrations of glutaraldehyde as indicated. While cells fixed with GA show strong autofluorescence in the EdU channel, this was not observed for cells fixed with PFA only (w/o GA). Only in the sample w/o GA, mtDNA (green EdU signal, extranuclear) was well colocalizing with the mitochondrial marker CC (cytochrome C, red immunostain). Confocal images have been acquired with identical laser power and acquisition settings using the SP2 confocal microscope. It is apparent that GA also reduces the immunostaining fluorescence signal for CC.

3.1.3.4 EdU Click Labeling Strongly Extracts Tokuyasu Sections

We showed before that mtDNA can only be well visualized, when no GA is used during fixation. Therefore, samples were fist fixed with only PFA, prepared according to the Tokuyasu technique, click – and immunofluorescence labeled and then postfixed with 5% GA for ultrastructural preservation. In light microscopy, TOM20 was repeatedly visualized, appearing in ring-like structures, which fit well with the 1 µm diameter of mitochondria (in cross-sections). However, only in one particular experiment, we were able to also visualize mtDNA, recognized as EdU signals within TOM20 ring structures (white arrow heads, Figure 18, left panel). Nuclear DNA (colocalizing with DAPI), on the other hand, was routinely visualized. After light microscopy, the Tokuyasu section was incubated with UA and methylcellulose, and dried. In electron microscopy, the section appears strongly extracted (Figure 18, right panel). Cytosolic structures, such as mitochondria or endosomes were not at all appreciable, and the usually dense Nucleus (Nu), also appears strongly reduced in electron-density. Whether the observed extraction was caused by insufficient fixation, when using only PFA as a fixative, or by the Cu-catalyzed click labeling, as seen in solid resin on-section labeling attempts (see Figure 13), remains unknown. Most likely, it is a combinatorial effect of both. With GA as a fixative and without EdU click labeling, the ultrastructure is much better preserved (see Figure 15).

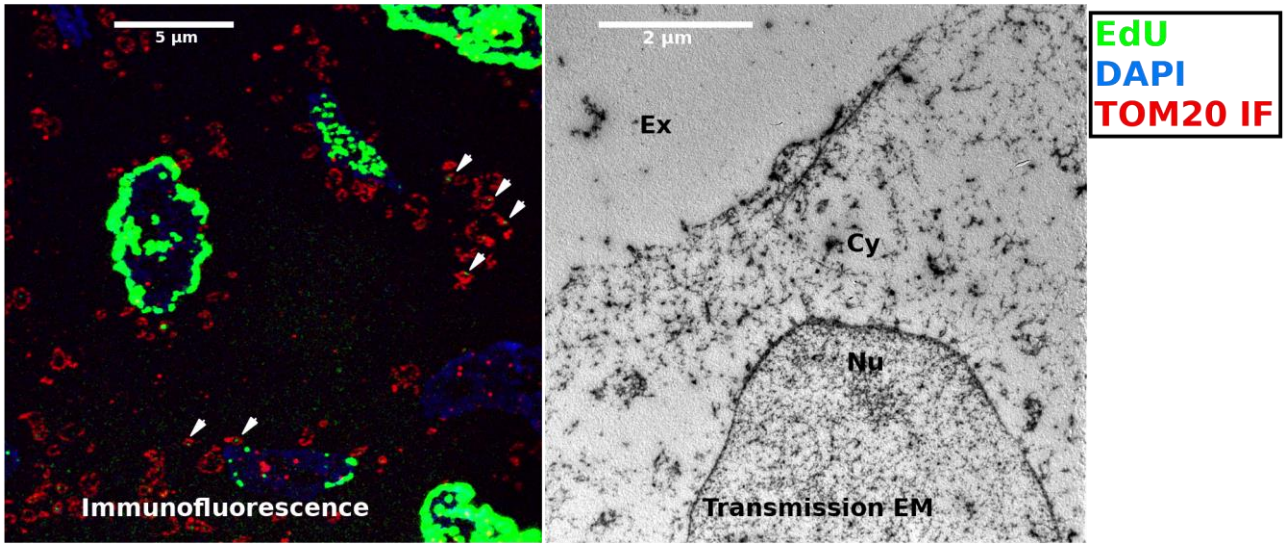

Figure 18: Light- and Electron Micrographs of Tokuyasu Sections from PFA Fixed, EdU Click Labeled and GA-Postfixed U87$^{4/4}$ Cells

U87$^{4/4}$ cells were allowed to incorporate EdU for 4-5 hours before fixation in 4% PFA in 1x PHEM buffer. After Tokuyasu preparation, 250 nm thin sections were prepared, EdU click – and immunofluorescence labeled and postfixed with GA.
In this particular case, EdU in Nuclei (see EdU and DAPI colocalization, left panel), as well as extranuclear DNA colocalizing with mitochondrial marker TOM20 was visualized (green EdU spots in TOM20 red labeled structures, examples: white arrow heads, left panel), the latter therefore most likely representing mtDNA. The right panel shows an electron micrograph of the corresponding section. The cytosol and nucleus are strongly extracted, therefore no cytosolic structures, such as vesicles or mitochondria are visible or recognizable. Ex: Extracellular Space, Cy: Cytosol, Nu: Nucleus.

3.1.4 Preembedding LM Correlation with Epon Flat Embedding

Epon embedding is a standard EM technique widely used and known to well retain cellular ultrastructure as well as the structure of the HIV-1 capsid (Bartonova et al., 2008). Retaining fluorescence in epon embedded samples, however, is not possible due to harsh fixation with GA, post-fixation and contrasting with OsO_4 and high temperature (60°C), required for resin polymerization, which results in quenching of fluorescent proteins. As mentioned above, retaining HIV-1 capsid structures requires fixation with GA. However, we have shown before that detection of mtDNA by EdU labeling is hampered when GA is used as a fixative (see Figure 17). Salic and Mitchison (Salic and Mitchison, 2008) suggest the possibility to label EdU in living cells. Although copper is toxic to cells (Gaetke et al., 2014), the limited time of exposure to Cu might still be short enough to not kill (all) cells for further analyses. The rationale for assessing Epon as a possibility

was, to counteract extraction (as observed before, see Figure 18 & Figure 13) due to the harsh fixation,

As mentioned before, fluorescence retention did not seem likely when embedding samples in epon. Therefore, we aimed to acquire LM z-stacks of labeled cells before embedding to identify ROIs (i.e. extracellular mtDNA for protocol establishment or IN.eGFP colocalizing with EdU signal for RTC detection), to find the respective cells back after embedding and to correlate the electron micrographs with LM data. The EM thin sections cannot be expected to be parallel to the single z-slices of the LM z-stack, since thin sectioning is never perfectly parallel to the block surface. Therefore, this method would require correlating the electron micrograph to a light microscopy (sub)volume of the respective cells.

3.1.4.1 EdU Live Cell Labeling is Possible, but Incurs Cellular Stress and Harms Ultrastructure

In a first experiment, we wanted to assess the compatibility of EdU labeling with living cells. U87$^{4/4}$ cells were allowed to incorporate EdU for 5 hours. They were treated live with the copper-catalyzed click reaction mixture for 30 minutes. For this purpose, we used the cell permeable TAMRA azide-dye. The cells were washed with PBS and then returned into cell medium for recovery o/n. After recovery, the cells were fixed, immunostained for CC and TOM20 and imaged (Figure 19). We were able to visualize cells that incorporated EdU and were click labeled the day before. As in earlier experiments, nuclear DNA was readily visualized. However, using this protocol, we were also able to detect extranuclear mtDNA DNA. Such fluorescence signals were partially found to colocalize with TOM20 but not with CC (see Figure 19, arrow heads), again arguing for cellular stress. Still, live labeled cells do not (all) die and the EdU signals can be well visualized even one day after labeling. The extranuclear mtDNA EdU signal was comparably weak. It must be considered that EdU dilutes during further mtDNA replication, and might therefore be not as strong as in former experiments (see Figure 17).

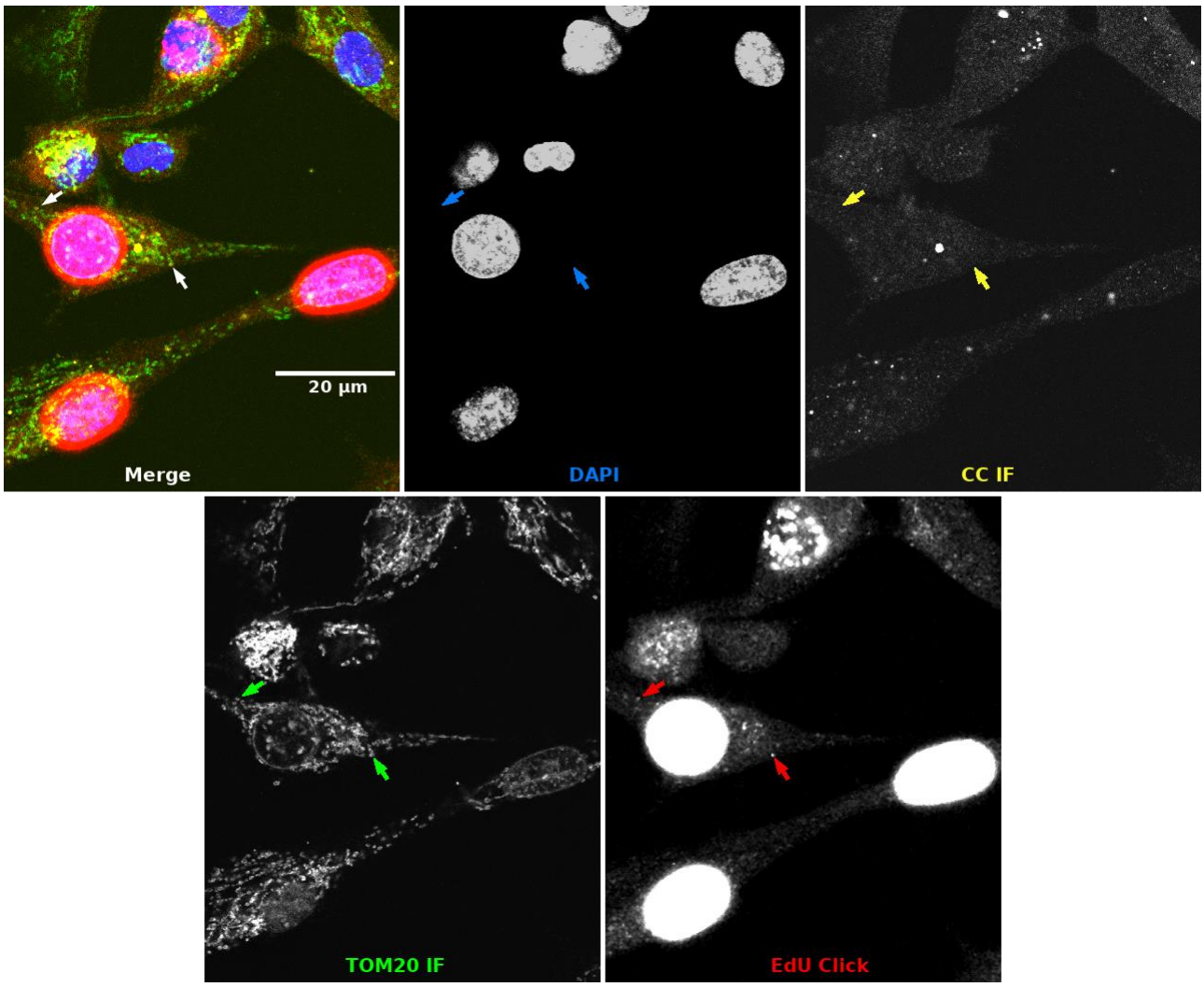

Figure 19: Immunofluorescence Micrographs of U87$^{4/4}$ Cells After Over Night Recovery From 30 Minutes Live Cell Click Labeling

U87$^{4/4}$ cells on cover glasses cells were incubated for 5 hours with EdU, then click labeled for 30 min and placed back into DMEM complete. After o/n recovery, the cells were fixed, and immunofluorescence stained for mitochondrial markers TOM20 and Cytochrome C (CC). Although cells were allowed to recover, they appear stressed, as there is no strong colocalization between TOM20 and CC observed, CC secretion from mitochondria being a hallmark for cellular stress. Nuclear as well as extranuclear EdU signals were visualized. Arrow heads point to examples, were extranuclear EdU signal colocalized with TOM20, arguing that those EdU signals most likely represent mtDNA.

To asses if live cell EdU labeling can be applied for the purpose of identifying productive RTC/PIC complexes in light microscopy and correlate that information with EM sections, we incubated living cells with click labeling mixture, subsequently fixed after different time points, and processed samples in parallel for either light microscopy (immunolabeling) or electron microscopy (epon flat embedding). To reduce cellular stress to a minimum, the aimed was to keep the time frame needed

for robust identification of extranuclear DNA to a minimum. We again used mtDNA as a model for HIV-1 RTC and PIC.

Live Cu-catalyzed click labeling of cells did yield EdU staining, the intensity and signal-to-background ratio depending greatly on the duration of click labeling of the sample (see Figure 20). While after 1 minute of click labeling (Figure 20, upper left panel), nuclear EdU signals were already apparent, longer incubation times were needed to visualize extranuclear DNA, considered to represent mtDNA: After 5 minutes incubation, the signal for extranuclear DNA was still blurry and not far over the background intensity (Figure 20, upper right panel), which improved for the 10 and 20 minutes time points (Figure 20, lower panels). We concluded that 10 minutes EdU click labeling sufficient for the detection of extranuclear DNA EdU signal. The ratio of signal-to-background was high enough and the reduced incubation time is likely to reduce the imposed cellular stress, compared to 30 minutes click label mixture incubation in our first live cell labeling experiment (see Figure 19).

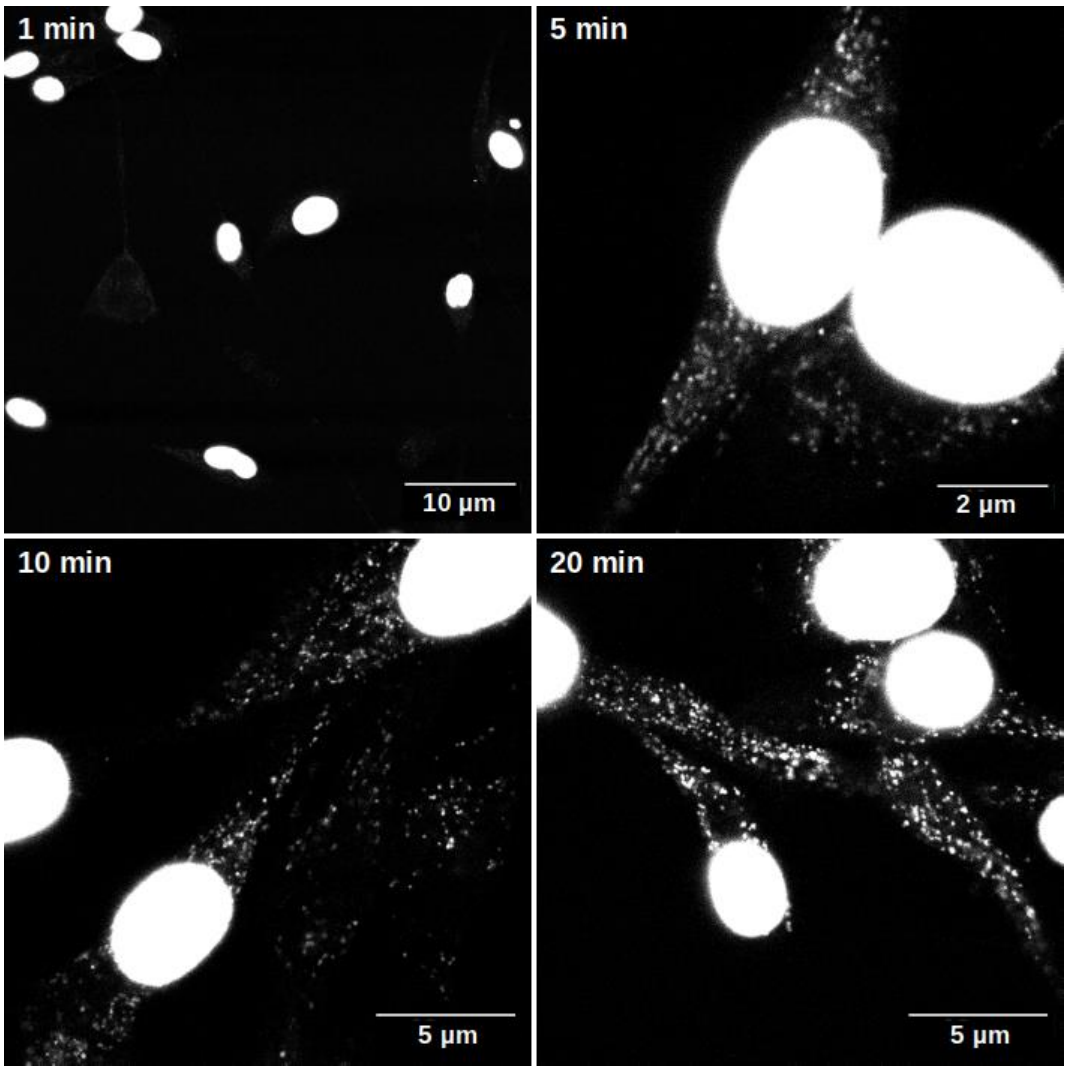

Figure 20: Fluorescence Micrographs of Live EdU Labeled U87$^{4/4}$, Fixed Cells

U87$^{4/4}$ cells were allowed to incorporate EdU for 5 hours. Living cells were EdU click labeled with TAMRA for indicated times before fixation and light microscopy imaging. Nuclear EdU signals were already well visible after only 1 minute live cell click labeling. After 5 minutes, extranuclear mitochondrial DNA (mtDNA), became visible over the background of TAMRA signal. After 10 minutes labeling, the extranuclear EdU signals developed a better signal to noise-ratio and after 20 minutes labeling, the assumed mtDNA yielded a very bright and easily distinguishable signal.

However, comparing electron micrographs of these samples, makes it obvious that already short time of Cu-containing EdU label mix exposure caused considerable damage to the cells' ultrastructure: While untreated samples appeared ultrastructurally well retained in electron micrographs (see Figure 21, upper right panel), click mix incubation for 1 minute already led to vacuolarization of mitochondrial cristae (see Figure 21, upper right panel). Incubation for 5 or 20 minutes caused strong damage to the sample cells' ultrastructure: Extracted regions in the

cytoplasm become apparent (see Figure 21, lower panels). Overall, subcellular structures apparently became extracted, e.g. the usually electron-dense nucleus became partially electron-transparent (see Figure 21, lower right panel, Nu).

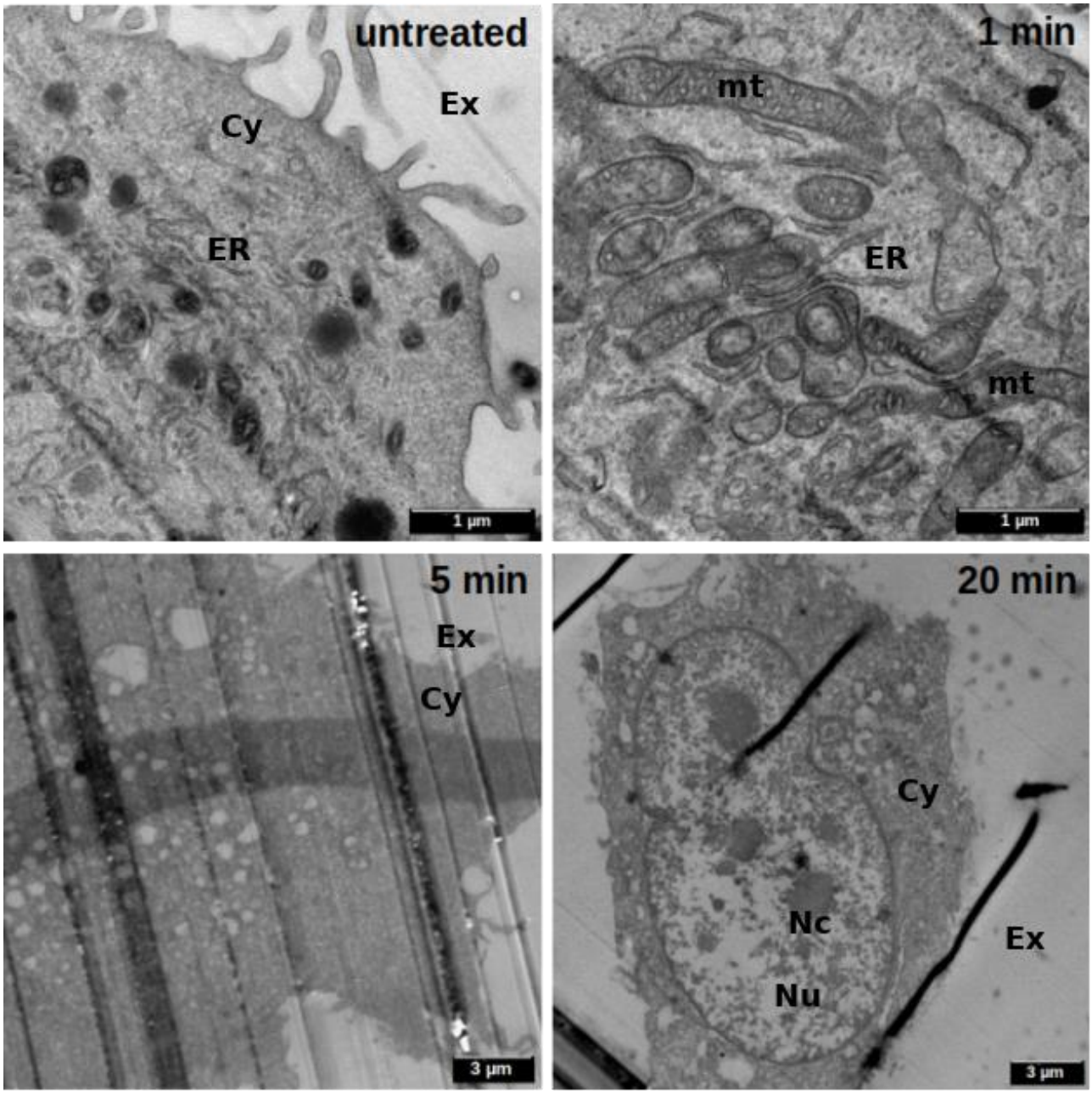

Figure 21: 100 nm Thin Sections of Epon Flat Embedded U87$^{4/4}$ Cells After Copper-Catalyzed Click Labeling

U87$^{4/4}$cells were allowed to incorporate EdU for 5 hours. Living cells were EdU click labeled with TAMRA for indicated durations before fixation and further processing for epon flat embedding. Untreated cells were ultrastructurally well retained and cellular details, such as endoplasmic reticulum were appreciable. After 1 minute click labeling, mitochondrial cristae already appeared slightly vacuolar. After 5 minutes labeling, cell

sections already appeared strongly extracted and holey, which became more pronounced after 20 minutes click labeling. Ex: Extracellular Space, Cy: Cytoplasm, Nu: Nucleus, Nc: Nucleolus, ER: Endoplasmic reticulum, mt: Mitochondrion. The parallel stripes are artifacts, caused by knife marks. TEM images acquired with Zeiss EM10.

3.1.5 Cryo-CLEM

Sample preparation for this method was similar to the methods described above: U87$^{4/4}$ cells were treated for 4-5 hours with EdU before live Cu-catalyzed EdU click labeling with TAMRA azide. Instead of chemical fixation, the cells were gently scraped and pelleted, before vitrification in metallic gold-coated Cu planchettes during high pressure freezing. 250 nm thin sections were prepared under cryo-conditions and taken up onto EM grids. In collaboration with Yura Bykov (Ph.D. student, Briggs lab, EMBL Heidelberg), samples were further analyzed by cryo-LM for retained fluorescence. These experiments did not yield satisfactory results: No EdU signal could be detected on the grids. Additionally, we were not successful in visualizing sample cells by cryo-EM. Using an easier EM method, the sample sections on grids were rapidly thawed in PHEM buffer with 4% PFA and 1% GA, and on-section contrasted with UA and PbCi. Using the EM10, we were able to identify cell-reminiscent structures (see Figure 22, lower panel). During cryo-sectioning, the block face was trimmed to ~ 150 µm in width and length. In the distance of 150 µm, we could observe similar repeating structures, pointing to serial sections of the same cells (see red boxes, Figure 21, upper panel). Also with this technique, the ultrastructural preservation was unsatisfactory (see lower panel Figure 22): There was no structure that could be reliably identified. In conclusion, circumventing dehydration and resin-infiltration by employing cryo-LM and -EM, we were not able to retain cellular ultrastructure to a useful degree, neither to visualize EdU signals.

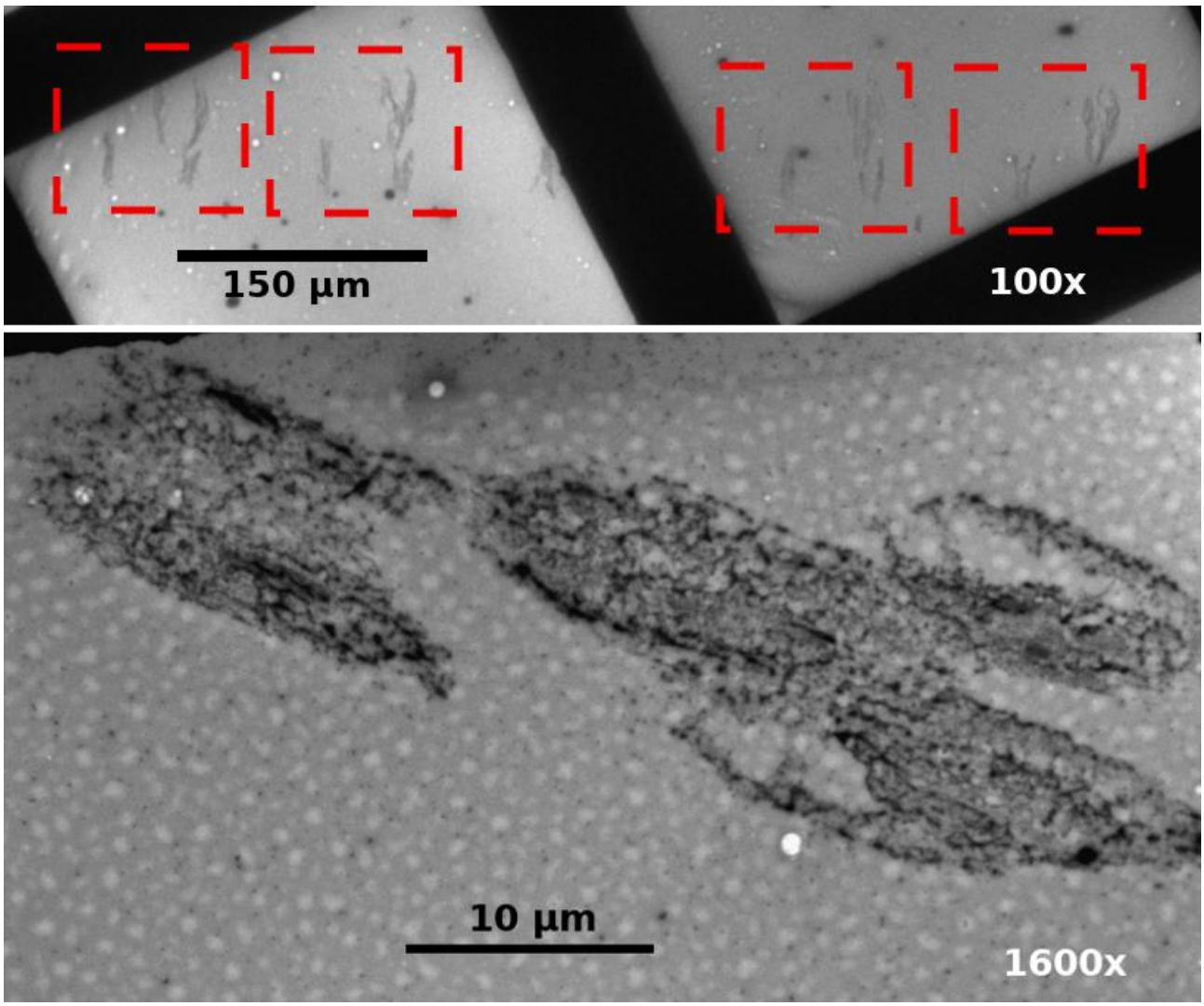

Figure 22: Electron Micrographs of Rapidly Thawed, Fixed and Contrasted Cryo-Thin Sections of Vitrified, Live EdU Click Labeled U87$^{4/4}$ Cells

Sample cells were incubated with EdU for 4 hours, live EdU click labeled, pelleted and high pressure frozen for vitrification. 250 nm thin sections were prepared and after cryo-LM and cryo-EM imaging (not shown, not successful), quickly thawed on fixative and contrasted.

The upper panel shows an overview at low magnification (100x). Repetitive structure patterns of ~ 150 µm can be observed (red outlines), fitting well to the cryo-sectioning settings (~150 µm x 150 µm block face). At higher magnification (lower panel), is also here becomes obvious that ultrastructural details (membranes, mitochondria) can't be appreciated. The dimensions of the observed structures fit well with the known U87$^{4/4}$ cell size.

In conclusion:
In several different attempts, we did not succeed to combine Cu-catalyzed EdU click labeling with electron microscopy in a way that would allow us to visualize viral DNA, while at the same time retaining a useful ultrastructure in electron microscopy. We dissected the EdU click mixture and could clearly identify the $CuSO_4$ as the detrimental agent. Using chelated copper (Tetrakis(acetonitrile)copper(I)tetrafluoroborate), is supposed to be milder or less toxic to samples. However, we could not observe any obvious improvement, when compared to $CuSO_4$. As long as other means of viral DNA labeling are unavailable, this approach to identify productive RTC and PIC most likely remains unfruitful.
We then considered alternative ways of labeling productive subviral structures.

3.2 Experimental System for Detection of HIV-1 nPICs by CLEM

An earlier study from our lab (Peng et al., 2014) found nuclear HIV-1 preintegration complexes (nPICs) to colocalize with accumulations of Cleavage and Polyadenylation Specificity Factor 6 (CPSF6). The colocalization of nPIC with CPSF6 clusters was observed in $U87^{4/4}$ cells as well as in primary human macrophages. We have designed and prepared a DNA construct to express an shRNA, targeting the endogenous CPSF6 for knockdown. In parallel, from a second promotor, a CPSF6 version is expressed, carrying silent mutations at the shRNA-targeted sequence, rendering this CPSF6 gene resistant against knockdown of the encoded shRNA (rCPSF6wt_{AA}). To allow live cell imaging, the red fluorescence protein mCherry (mCh) was fused to the carboxyterminus of the rCPSF6wt_{AA} coding region via a flexible linker (rCPSF6wt_{AA}.mCh). Downstream of the rCPSF6wt_{AA}.mCh, a 2A peptide bridge, an oligopeptide, cleaving itself during translation (Trichas et al., 2008), was added, allowing the expression of puromycin N-acetyl-transferase (PAC), an enzyme conferring resistance to eukaryotic cells against the otherwise lethal antibiotic puromycin. The PAC gene should allow us to select those $U87^{4/4}$ cells, which do express rCPSF6wt_{AA}.mCh. Like the endogenous CPSF6, the rCPSF6wt_{AA}.mCh is expected to localize to the nucleoplasm, where it should interact with CA and thereby specifically form detectable clusters at nPIC.
For our studies, HeLa TZM-bl and $U87^{4/4}$ cells were used. As these cell lines are routinely used in HIV-1 research, they are well suited for establishing new methods and techniques and to gain preliminary data before expanding protocols on more relevant cell types, such as primary human macrophages or $CD4^+$ T-cells. Based on our previous research (Peng et al., 2014), $U87^{4/4}$ cells are also considered as a good starting point for the analysis of nuclear preintegration complexes (nPIC).

3.2.1 Cell Line Generation and Sorting

The DNA construct was cloned into the pLENTICRIPSR vector, yielding the pLENTICRISPR-rCPSF6wt$_{AA}$.mCh plasmid (see Figure 5). In 293T cells, the pLENTICRISPR-rCPSF6wt$_{AA}$.mCh construct was packaged into the lentiviral transduction vector psPAX2, using VSV-G as an envelope glycoprotein for efficient transduction. U87$^{4/4}$ cells were transduced with lentivirus particle-containing cell supernatant. 4-5 days after transduction, red nuclear signals were detectable in transduced cells. This was the starting point for treating the cells with puromycin to select for transduced cells, expressing the rCPSF6wt$_{AA}$.mCh-2APB-PAC cassette.

Dead cells were washed off and the selection medium replaced daily. During the first selection process, the number of viable cells was steadily declining. Also, cells with nuclear mCh expression, were dying gradually. We hypothesized this might be an effect of very low cell density. To circumvent the death of rCPSF6wt$_{AA}$.mCh.2APB.PAC-expressing cells, we selected cells in Sort$_{50}$ medium (50%FCS, 50% DMEM, Pen/Strep and puromycin). Higher percentages of FCS have been observed to increase cell survival and overcome effects caused by low cell density (Thorsten Müller, personal communication). Doing so, we were able to obtain sufficient numbers of cells. Once cells were grown to confluency, the FCS was reduced to regular 10% again. Puromycin was used continuously while passaging the transduced U87$^{4/4}$ rCPSF6wt$_{AA}$.mCh cells. Even though the rCPSF6wt$_{AA}$.mCh.2APB.PAC cassette should be stably integrated, we observed a loss of nuclear red signal within ~3 passages, after puromycin was withdrawn.

To exclude the possibility of mixing phenotypes of lentiviral transduction and lentiviral HIV-1 infection, the cells were allowed to grow for 3 weeks before performing further experiments.

3.2.2 Transduced Cells express rCPSF6wt$_{AA}$.mCh Fusion Protein

After observing a nuclear signal in the red channel, we started validating the expression and functionality of rCPSF6wt$_{AA}$.mCh by Western Blot and confocal microscopy. U87$^{4/4}$ wt and rCPSF6wt$_{AA}$.mCh cells were analyzed by western blot and confocal microscopy.

In light microscopy, the nuclei (as identified in the DAPI channel) also displayed a signal in the mCh channel, while the U87$^{4/4}$ wt cells did not show mCh fluorescence. The mCh fluorescence in U87$^{4/4}$ rCPSF6wt$_{AA}$.mCh was largely restricted to the nucleus, as it is expected for a CPSF6 fusion protein. The mCh fluorescence was variable, which was observed throughout all experiments (see Figure 23, panel B). Higher expression levels might be a consequence of multiple lentiviral vector integration or might be cell cycle-dependent. Overall, more than 90% of cells kept under constant selection pressure by puromycin showed a well detectable mCh signal.

To confirm that the observed mCh fluorescence is no consequence of mere mCh expression, but due to the rCPSF6wt$_{AA}$.mCh fusion protein, we also performed WB.

The house keeping protein α-tubulin was immunolabeled as a marker for the total amount of protein, loaded onto the gel. Using a second antibody against CPSF6, A specific band at ~70kDa in wt and rCPSF6wt$_{AA}$.mCh cells was visible (molecular mass of CPSF6: 68 kDa). A second specific band at ~37 kDa can be observed, potentially due to residual GAPDH antibodies in the incubation vessels from former experiments.

2 bands between the 100 and 130 kDa marker bands are visible in U87$^{4/4}$ rCPSF6wt$_{AA}$.mCh samples only. The upper and lower bands might account for rCPSF6wt$_{AA}$.mCh.2APB.PAC (~130 kDa) and cleaved rCPSF6wt$_{AA}$.mCh fusion proteins (~110 kDa, including the flexible linker and parts of the 2APB), respectively. While the tubulin band is more intense in U87$^{4/4}$ rCPSF6wt$_{AA}$.mCh lysates (indicating more total protein loading), the intensity of the endogenous CPSF6 at ~70 kDa is less intense, in comparison to wt cells, clearly speaking for a partial downregulation due to the expressed shRNA, targeting CPSF6.

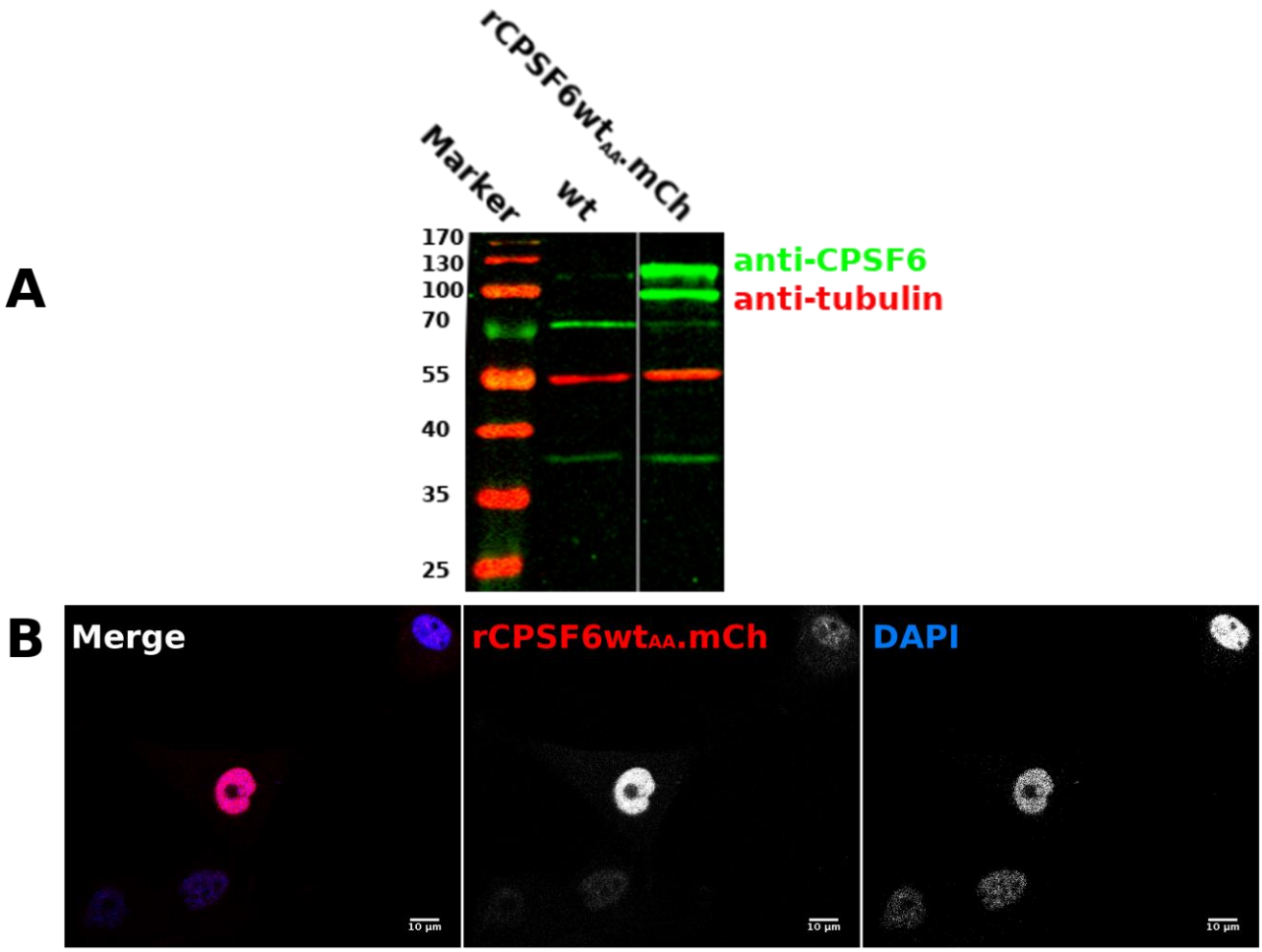

Figure 23: Confirmation of rCPSF6wt$_{AA}$.mCh Expression in Transduced U87$^{4/4}$ Cells by Western Blot and Light Microscopy

A) U87$^{4/4}$ wt and rCPSF6wt$_{AA}$.mCh cells were lysed in WB sample buffer, 5 days after transduction. Proteins were separated by SDS-gel electrophoresis, transferred onto a PVDF membrane, blocked and incubated with antibodies against CPSF6 and the house-keeping protein α-tubulin. Marker size is given in kDa. A CPSF6 band of ~70 kDa is recognizable in both samples, while only the rCPSF6wt$_{AA}$.mCh cells show additional bands at ~130 kDa and ~110 kDa, size-wise fitting to different rCPSF6wt$_{AA}$.mCh fusion proteins. The reduced intensity of the 70kDa band in the U87$^{4/4}$ rCPSF6wt$_{AA}$.mCh cell sample indicates downregulation of endogenous CPSF6 due to the encoded shRNA$_{CPSF6}$.

B) U87$^{4/4}$ rCPSF6wt$_{AA}$.mCh cells were, one day after seeding, stained for DAPI and imaged in a confocal microscope (single confocal z-slice. Leica SP8). In nuclei (DAPI, represented in blue), red signals, variable in their intensities were recorded, most likely derived from rCPSF6wt$_{AA}$.mCh fusion protein expression.

3.2.3 HIV-1 Infection Causes CPSF6 Clustering in Nuclei of Infected Cells

After confirming the expression of the rCPSF6wt$_{AA}$.mCh fusion protein, by light microscopy and Western Blot, we next tested, whether rCPSF6wt$_{AA}$.mCh coclusters with nPIC in HIV-1 infected

U87$^{4/4}$ rCPSF6wt$_{AA}$.mCh cells, as it was reported for wild type CPSF6 (Peng et al., 2014). For this, U87$^{4/4}$ rCPSF6.mCh cells were infected with IN.eGFP labeled HIV-1 virus particles for 4 hours before fixation and immunolabeling for CPSF6. In infected cells, we were able to observe nuclear mCh clusters, exceeding the basal nuclear mCh signal in intensity, which was not observed in uninfected control cells.

To characterize the observed rCPSF6wt$_{AA}$.mCh clusters, we performed immunofluorescence labeling against CPSF6 in infected U87$^{4/4}$ rCPSF6wt$_{AA}$.mCh cells. We found the mCh signal clusters in infected cells' nuclei to efficiently colocalize with the fluorescence signal for CPSF6. We therefore assumed the observed mCh signals to truly represent CPSF6wt$_{AA}$.mCh autofluorescence (AF) signals.

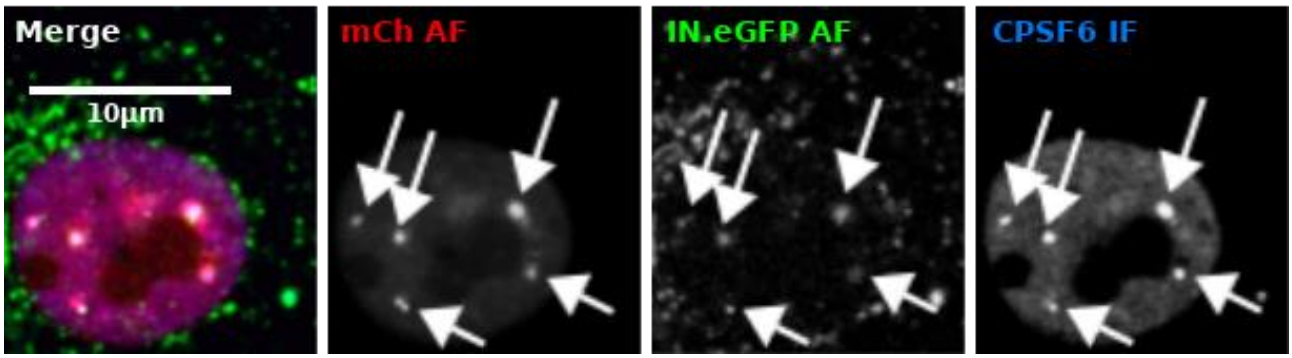

Figure 24: Colocalization of Nuclear rCPSF6wt$_{AA}$.mCh Clusters with IN.eGFP and CPSF6 Immunofluorescence Signal

U87$^{4/4}$ rCPSF6wt$_{AA}$.mCh cells were infected with IN.eGFP NL4-3 virus particles for 4 hours, fixed and immunostained for CPSF6. In the mch channel (mCh AF), a background signal and intense clusters are visible, colocalizing well with the CPSF6 immunofluorescence signal (CPSF6 IF), indicating that the observed mCh autofluorescence (mCh AF) truly represents rCPSF6wt$_{AA}$.mCh molecules. The observed clusters colocalize with IN.eGFP signals, indicating that the CPSF6 clustering is being caused by viral particles. Single confocal z-slice, Leica SP2.

3.2.4 The HIV-1 Surrogate Marker IN.eGFP Colocalizes Efficiently With CPSF6 Clusters in the Nuclei of Infected Cells, While CA Signal Detection Varies

To verify that mCh signal clusters are truly caused by and localized to subviral particles, we made use of a fluorescence surrogate marker, IN.eGFP. The integrase enzyme is thought to stay attached to the viral genome until vDNA integration into the host cell genome (Albanese et al., 2008). It has been shown by our lab that subviral IN.eGFP-positive particles in infected cells' nuclei partially

(~50%) colocalize with CA immunofluorescence signals. Here, we aimed to reproduce the colocalization of CA in rCPSF6wt$_{AA}$.mCh clusters. For this, U87$^{4/4}$ wt and rCPSF6wt$_{AA}$.mCh cells were infected with NL4-3 IN.eGPF virus preparation (as shown before in Figure 24) and additionally immunostained against CA.

We found the vast majority (>90%) of nuclear IN.eGFP signals to colocalize with mCh cluster signals, letting us deduce that using rCPSF6wt$_{AA}$.mCh as a surrogate marker does not (strongly) bias for a subpopulation of IN.eGFP positive subviral particles, but can be used to identify nuclear subviral particles in general. However, positions positive for rCPSF6wt$_{AA}$.mCh clusters and IN.eGFP signals, were not found to colocalize with CA immunofluorescence signals under these conditions. As no colocalization was observed for the transduced, as well as for the parental U87$^{4/4}$ cell line, we assume this not to be an artifact introduced by lentiviral transduction or puromycin selection. Not detecting any nuclear CA immunofluorescence signal, but only cytoplasmic ones, is in disagreement with U87$^{4/4}$ data obtained earlier in our lab (Peng et al., 2014).

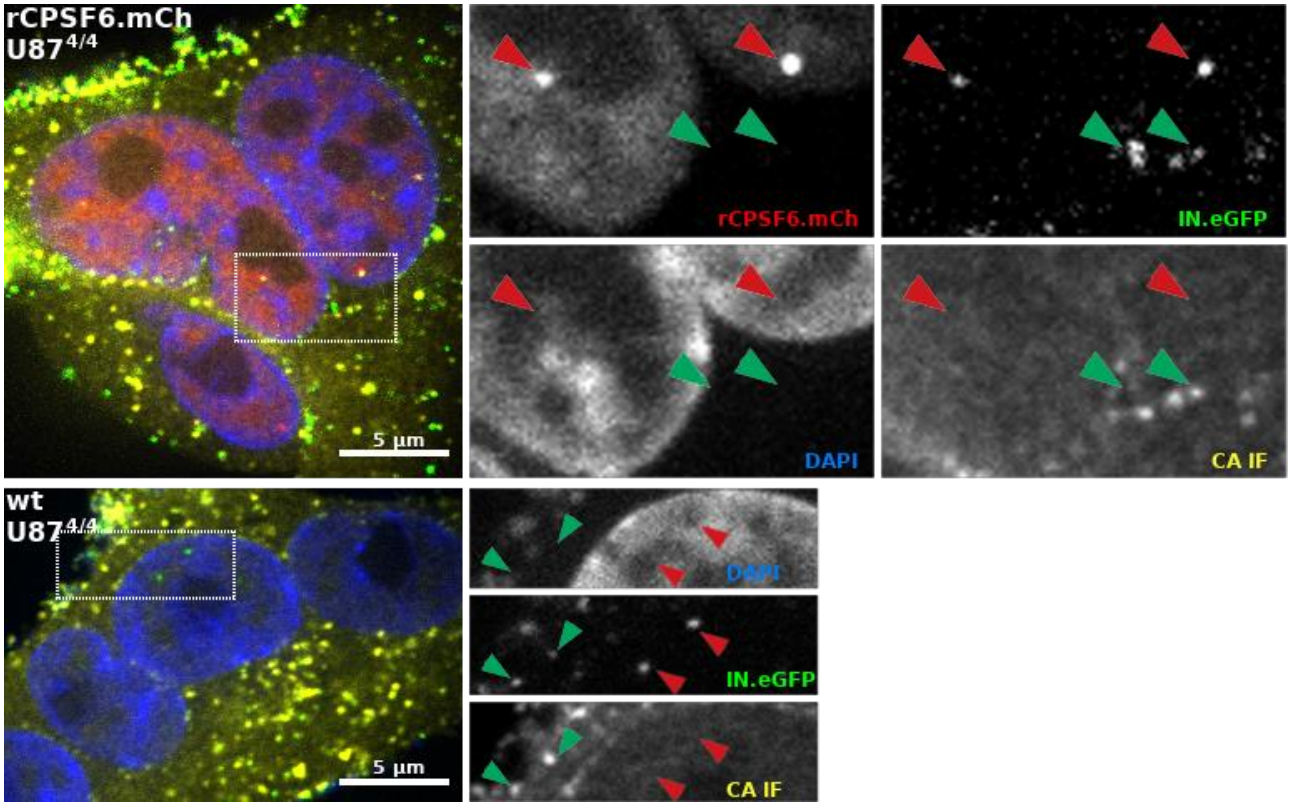

Figure 25: IN.eGFP-Positive Subviral Particles Colocalize With CA in the Cytoplasm But not in the Nuclei of Infected Cells

rCPSF6wt$_{AA}$.mCh (upper panel) and parental wildytpe (lower panel) U87$^{4/4}$ cells were infected with IN.eGFP labeled NL4-3 virus particles, fixed and immunostained. In both cell lines, it can be observed that cytoplasmic IN.eGFP signals efficiently colocalize with CA immunofluorescence (CA IF) signals (green

arrow heads), whereas nuclear IN.eGFP signals are devoid of colocalizing CA staining signals (red arrow heads). IN.eGFP signals being nuclear or cytoplasmic was defined by colocalization with DAPI. In U87$^{4/4}$ rCPSF6wt$_{AA}$.mCh cells, nuclear IN.eGFP signals colocalize with intense rCPSF6wt$_{AA}$.mCh cluster signals, as observed before (see Figure 24). Single confocal Z slices, Leica SP8.

3.2.5 rCPSF6.mCh Clusters Colocalize With IN.eGFP, CA and EdU Signals

To assess, whether the observed nuclear subviral particles can be considered productive preintegration complexes, we performed EdU click labeling experiments in U87$^{4/4}$ rCPSF6wt$_{AA}$.mCh cells to potentially visualize the presence of viral DNA. 1 hour before infection, cells were treated w/ or w/o aphidicolin (APC) to block synthesis of cellular nuclear DNA (APC does not impair viral and mitochondrial DNA synthesis). The thymidine analogue EdU was present throughout infection to become integrated into nascent DNA during reverse transcription. Infected cells were fixed and processed for EdU click labeling as described in Materials and Methods. LM images were acquired using the Leica SP8 microscope.

We observed nuclear mCh clusters, colocalizing with IN.eGFP (~ 85%) and EdU click signal (> 90%).Different from the experiment before (see Figure 25), in these samples, we were able to detect CA immunofluorescence signals colocalizing with nuclear rCPSF6wt$_{AA}$.mCh clusters and IN.eGFP signals (colocalization ~ 80%). After click labeling in this experiment, the CA immunostaining appeared generally different: In comparison to Figure 25, the background in the click labeled samples is much more evenly distributed over the whole cell and does not appear reduced in the nucleus. In follow up experiments, we could only detect nuclear CA, when samples were extensively click labeled (for 30 minutes or more) or extracted o/n in 70% EtOH (experiments performed by Dr. Vojtech Zila).

Detecting the viral hallmarks IN.eGFP, CA and viral DNA (identified by EdU signal) in rCPSF6wt$_{AA}$.mCh clusters clearly shows that rCPSF6wt$_{AA}$.mCh can be used as a reliable surrogate marker for the detection on nuclear PIC.

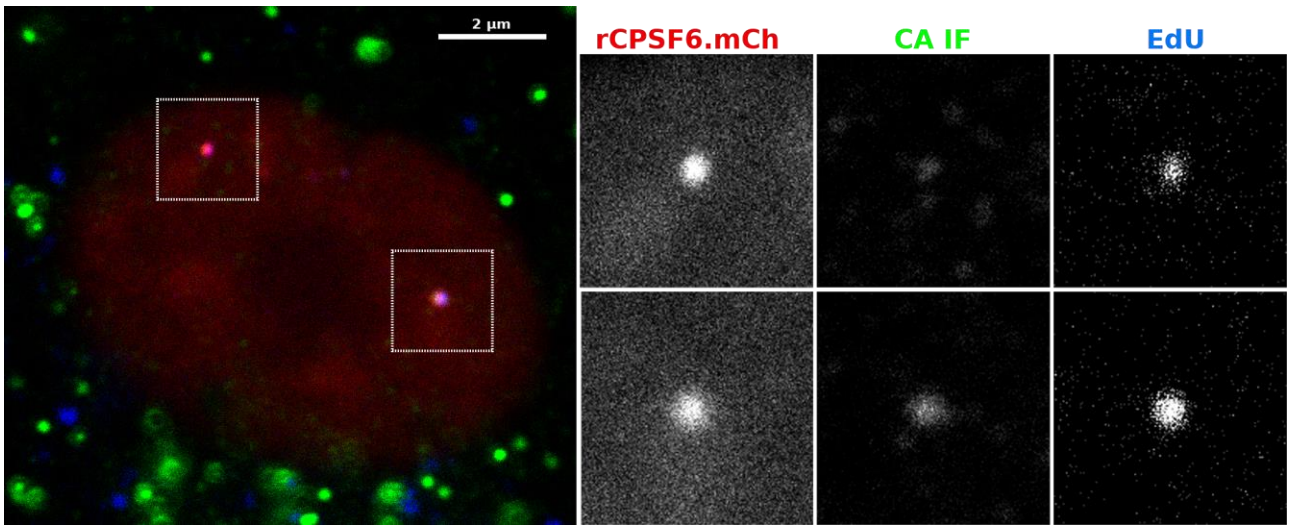

Figure 26: Confocal Fluorescence Microscopy of EdU-Treated, IN.eGFP-Labeled Virus Particles Infected U87$^{4/4}$ Cells Show PIC Colocalization With rCPSF6wt$_{AA}$.mCh Cluster Signals

U87$^{4/4}$ rCPSF6wt$_{AA}$.mCh cells were infected with IN.eGFP labeled NL4-3 virus particles in the presence of EdU. Cells were fixed, EdU click labeled and immunostained against CA (CA IF). rCPSF6wt$_{AA}$.mCh signal clusters colocalize with IN.eGFP (not shown), EdU signals and, under these circumstances, also with CA immunofluorescence signals. The two zoom-ins show that the CA signal was variable in intensity, but specifically colocalizing with the other signals. rCPSF6wt$_{AA}$.mCh cluster signals therefore serve as a reliable surrogate marker for productive PIC. Single confocal z-slice, Leica SP8.

3.2.6 Infectivity of wt and Transduced U87$^{4/4}$ Cells is Comparable

We have observed before that nuclear mCh cluster signals colocalize with IN.eGFP and EdU, representing productive preintegration complexes. Such complexes are thought to lead to integration of vDNA into the host cell genome, further leading to expression of viral proteins.

We did not assess so far, whether expression of the rCPSF6wt$_{AA}$.mCh fusion protein might affect viral gene expression. Nuclear CPSF6 does only affect steps starting from nuclear entry on and therefore does not affect entry of viral DNA synthesis. Therefore, observed alterations in viral gene expression would hint towards an effect on nuclear entry or provirus integration, where CPSF6 has been shown to play major roles.

To assess viral gene expression of infected cells, wt and rCPSF6wt$_{AA}$.mCh U87$^{4/4}$ cells were infected in parallel with serial dilutions of NL4-3 wt virus preparations. At 4 hours after infection, the inoculum was removed and replaced by fresh medium with the entry inhibitor T20 to block second-round infections. The samples were fixed 2 days after infection and immunostained for CA. Performing wide-field microscopy, we could quantify infection. No dramatic difference was

observed between wt and transduced U87$^{4/4}$ cells. Inoculating 0.125 µL virus preparation yielded 7.3% infected cells for wt cells and 3.9% for transduced cells. Inoculating 0.5 µL, lead to ~16.5% infection in both cell lines. Inoculating 2 µL of virus particle preparation yielded 38.6% and 31.2% infected wt and transduced cells, respectively (images not shown).

We conclude that neither lentiviral transduction and the associated rCPSF6wt$_{AA}$.mCh expression, nor puromycin selection of transduced cells had major effects on virus infectivity, measured by CA expression.

The same virus particle preparation has been used throughout all experiments. Since we seeded 20,000 cells in this experiment, the virus particle titer for U87$^{4/4}$ cells can be calculated to ~ 6400 infectious units per µL.

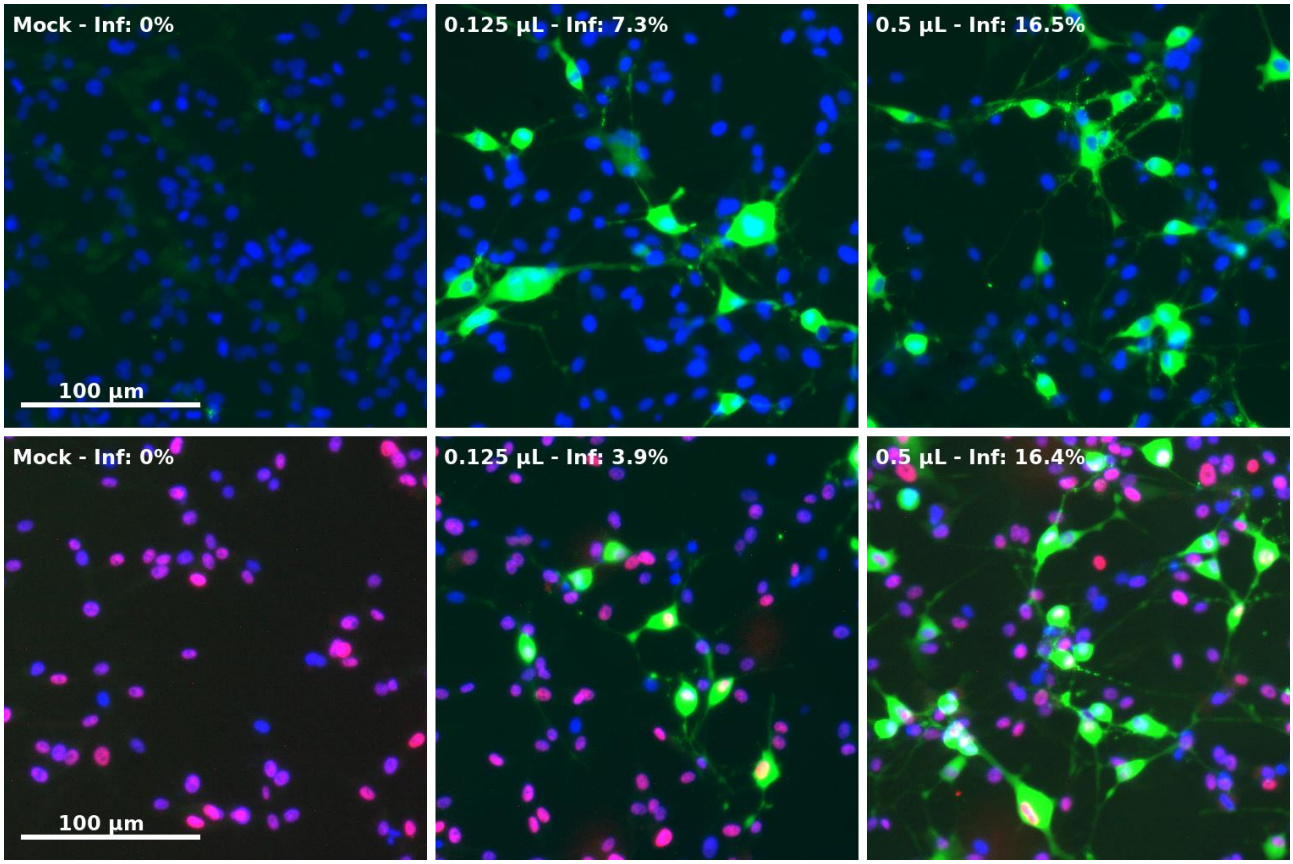

Figure 27: Representative Wide Field Fluorescence Micrographs Used for Infectivity Quantification in U87$^{4/4}$ wt and rCPSF6wt$_{AA}$.mCh Cells

U87$^{4/4}$ wt (upper panel) and rCPSF6wt$_{AA}$.mCh (lower panel) cells were infected with serial virus particle dilutions in parallel, fixed and immunostained for newly produced CA, which was used as marker of viral gene expression. Infectivity was quantified using FIJI's particle analyzer, counting all cells (DAPI) and infected cells (CA). The volume of particle preparation and infectivity quantification are displayed at the upper edge of each image. While 0.125 µL virus preparation lead to minor differences in infectivity between

wt and transduced cells, this was not observed for 0.5 µL virus preparation. Infection with 2 µL virus preparation lead to 38.6% (wt) and 31.2% (transduced) cells (not shown). Green: CA IF, blue: DAPI, red: rCPSF6wt$_{AA}$.mCh.

3.2.7 The Applied CLEM Protocol Yields Good Ultrastructural Preservation

While developing protocols for fluorescence retention during EM sample preparation, we also needed to ensure that the ultrastructure can be preserved well by the used techniques. Therefore, we acquired several tomograms of non-ROI regions, where more subcellular ultrastructure would be visible, than in the nucleus.

The reconstructed tilt-series clearly show that the ultrastructure is indeed very well retained (see Figure 28). Rough endoplasmic reticulum (rER) can be easily identified by the tubular appearance, decorated with electron-dense ribosomes. Distinct cytoskeletal filaments are well recognizable. Membranes always serve as a good indicator for successful EM sample preparation. We could see that e.g. the nuclear envelope can clearly be appreciated as 4 distinguished membrane leaflets (double-membrane with 2 leaflets, each. Figure 28 see NE). NPC were harder to appreciate in single computational slices, but recognizable in tomograms (Tomograms are included as supplementary data on the attached DVD). This well retained ultrastructure provides the basis for the recognition of a potential PIC structure.

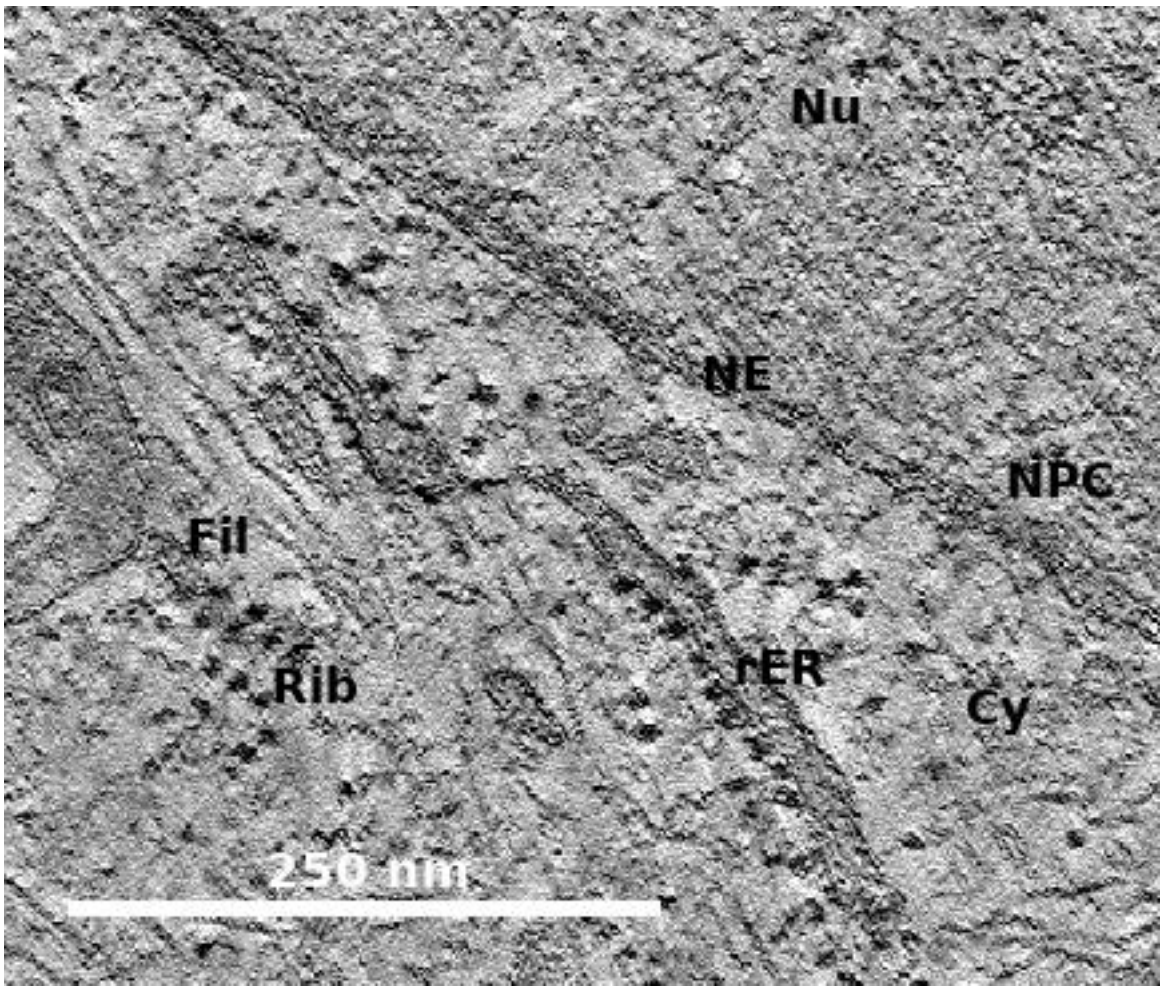

Figure 28: Electron Micrograph Showing Good Ultrastructure Preservation of CLEM Sample Sections

U87$^{4/4}$ rCPSF6wt$_{AA}$.mCh cells were infected for 4 hours with NL4-3 virus preparation before chemical fixation. The sample was high pressure frozen, freeze substituted and embedded in Lowicryl HM20. 250 nm thin sections were prepared.

This micrograph is one extracted computational slice of a reconstructed tilt series tomogram. The tilt series was acquired in an area, where ROI have been detected to validate the good ultrastructural preservation. Fine ultrastructural details can be appreciated: Free ribosomes (Rib) as well as ribosomes at rough endoplasmic reticulum (rER). Lengthy cytoskeletal filaments are visible (Fil) in the cytoplasm (Cy). The nuclear envelope (NE) can partially be appreciated as a stack of 4 membrane leaflets (2 leaflets per membrane). At some positions, the NE is interrupted by nuclear pore complexes (NPC). An additional tomogram is available in the supplementary data on the enclosed DVD.

3.2.8 CLEM of U87$^{4/4}$ rCPSF6wt$_{AA}$.mCh Cells

So far, we were able to prove that HIV-1 infection causes rCPSF6wt$_{AA}$.mCh clustering (see Figure 25), which represent true rCPSF6wt$_{AA}$.mCh signals (see Figure 24). The observed clusters colocalize with IN.eGFP efficiently and are positive for vDNA and CA under certain circumstances (see Figure 26). Therefore, these rCPSF6wt$_{AA}$.mCh clusters represent productive preintegration complexes, leading to viral gene expression. In conclusion, nuclear viral preintegration complexes can be faithfully identified by rCPSF6wt$_{AA}$.mCh cluster signals.

To examine the ultrastructure of preintegration complexes, we aimed to perform correlative light and electron microscopy. The size of viral particles being ~120-140 in size (e.g. (Briggs, 2003)), the resolution limit of conventional (~300 nm) and superresolution (~20 nm) fluorescence microscopy would not allow to visualize potential subviral structures, but only the identification of regions of interest (ROIs), by e.g. nuclear CPSF6wt$_{AA}$.mCh cluster signals. Visualizing these ROIs in EM would yield much higher resolution and information about the underlying putative ultrastructure and subcellular environment.

3.2.8.1 CLEM Sample Preparation

U87$^{4/4}$ rCPSF6wt$_{AA}$.mCh cells were seeded on carbon-coated sapphire discs and infected with NL4-3 virus particles for 4 hours. These BSL-3 samples were fixed for 90 minutes with aldehydes to meet the requirements for high pressure freezing, operated under BSL-1 conditions. PHEM buffer was used instead of the more commonly used PBS, as the latter is believed to extract more cellular content (Dr. Krijnse-Locker, personal communication) and might therefore deplete valuable information. Furthermore, PHEM, in contrast to PBS, does not contain phosphates, which form insoluble, electron-dense precipitates with uranyl.

During high pressure freezing, the sample cells are vitrified under high pressure (~2100 bars) in a minimal timeframe of ~20 ms. The cooling rate (>15,000 K/s) does not allow crystal ice formation, which would otherwise result in cell membrane damage and suboptimal preservation of the cellular ultrastructure. In a process called freeze substitution (FS), the sample's frozen water is first replaced by a polar solvent (here: acetone), which is in turn replaced by an electron transparent EM sample resin (here: Lowicryl methacrylate type HM20). HM20 will infiltrate the sample, polymerize and harden, and eventually allow thin sectioning of sample cells. Similar protocols have been applied successfully in the past for CLEM (e.g. (Kukulski et al., 2011)).

250 nm thin sections were prepared from HM20-embedded samples and taken up on EM finder grids. This special kind of grids has alphanumerical coordinates at the grid bars. Imaging the same position in light – and electron microscopy is facilitated by simply following the coordinates.

Additionally, we also used TetraSpeck Fiducials, which can be visualized in both, LM and EM. Using such fiducials allows to correlate light – and electron micrographs with high precision. The rCPSF6wt$_{AA}$.mCh fluorescence signal can then be used to identify regions of interest (ROI) in the subcellular environment.

We found the number of TetraSpeck Fiducials on a sample to strongly depend on the used diluent: When diluted in PHEM buffer instead of water, much more Fiducials were bound to the thin section (data not shown). Hoechst or DAPI was added to the fiducial dilution to easily identify nuclei and the focal plane during LM.

It is critical to keep the thin section in water or buffer, as exposure to air reduces the retained fluorescence signal dramatically.

To prevent sample bleaching, HM20 blocks were stored dark, in the sample processing holder, until sectioning and imaging. Excess material and sapphire discs were only removed directly before thin sectioning and subsequent LM imaging. Once a block has been processed, the fluorescence faded within one week.

3.2.8.2 CLEM Micrograph Acquisition

The sample grid was imaged in a sample holder, sandwiched between 2 cover glasses, to meet the LM objective's (63x oil immersion) requirements. During fixation and FS processing, the fluorescence signal intensity is strongly reduced. Using the Leica SP8 microscope, rCPSF6wt$_{AA}$.mCh in whole cells can well be visualized with ~3 % intense lasers, while thin sections require a laser power of 25-30% and 2-6 fold frame accumulation, to properly identify rCPSF6wt$_{AA}$.mCh-positive nuclear clusters.

After LM, the sample contrast was enhanced for EM, using heavy metals. Regions of interest, as identified in LM, were then imaged in an EM10 transmission electron microscope. Light and electron micrographs were correlated, allowing the identification of regions of interest within the ultrastructure of the thin sections.

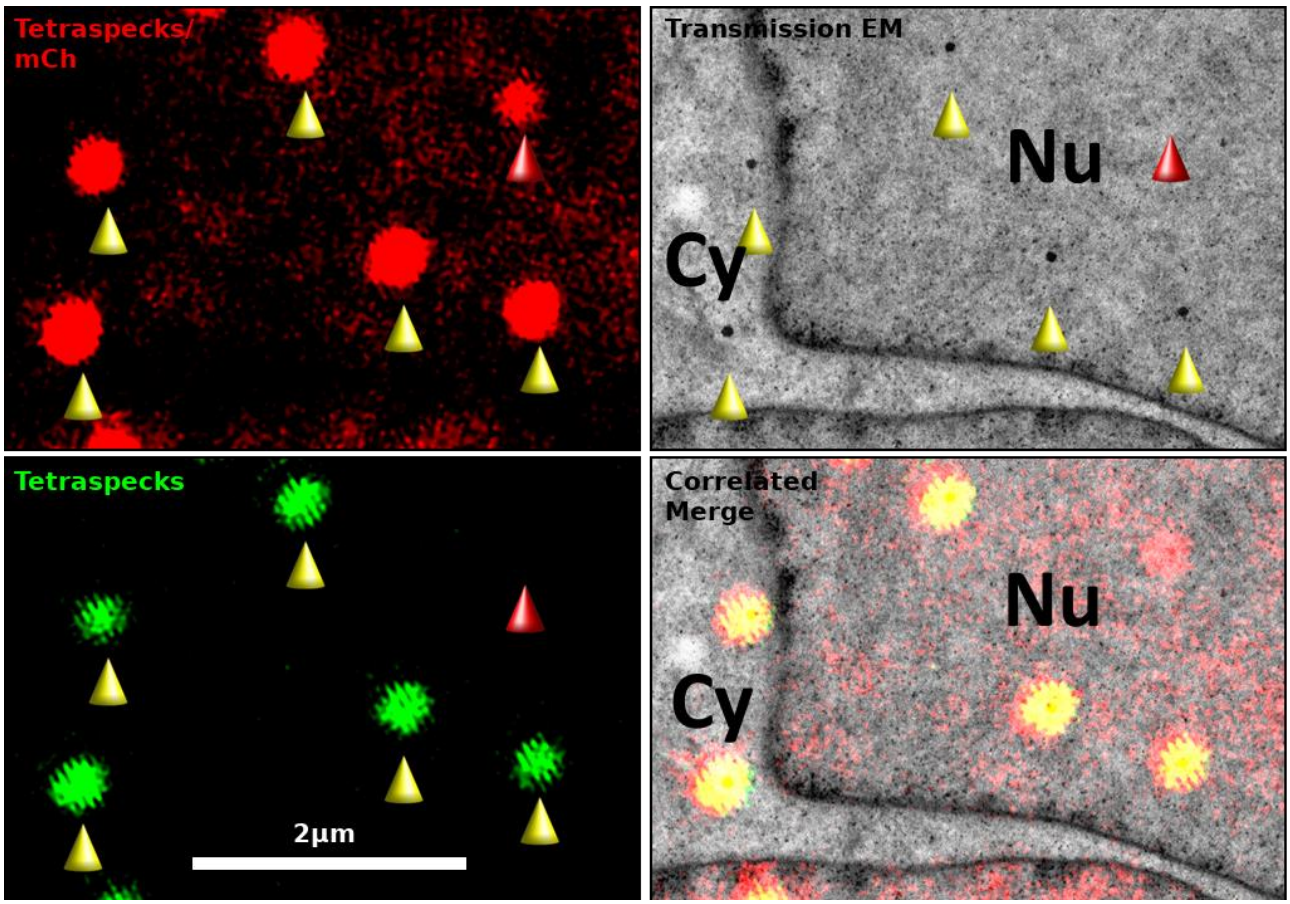

Figure 29: Representative Example of Light – and Electron Micrograph Correlation

U87$^{4/4}$ rCPSF6wt$_{AA}$.mCh cells were infected with NL4-3 virus preparation on sapphire discs for 4 hours, followed by chemical fixation, vitrification, freeze substitution and embedding in HM20 resin. 250 nm thin sections were prepared and incubated with TetraSpeck Fiducials.
Light micrographs in the mCh channel (upper left) and far-red channel (lower left) are shown in red and green respectively. TetraSpeck Fiducials are visible in both images (yellow arrowheads), while mCh nuclear background and cluster signals appear in the mCh channel only (red arrowhead). In a TEM image (upper right) of the corresponding region, Tetraspeck Fiducials can be identified by high electron-densities (yellow arrowheads). Correlating the light- and electron micrographs yield the correlated merge image (lower right), where the rCPSF6wt$_{AA}$.mCh cluster signal can be visualized merged into the subnuclear environment. Scale bar is consistent among all images. Cy = Cytosol, Nu= Nucleus.

Tilt series tomograms were then acquired, using a Tecnai F20 microscope, operated at 200 kV, at 19,000 fold magnification. After 3D tomogram reconstruction, the exact positions of the CPSF6wt$_{AA}$.mCh clusters were determined and the region visually screened for potential structures. We could indeed identify structures reminiscent of HIV-1 capsid structures that were modeled by hand and analyzed together with Dr. Martin Schorb using custom MatLab scripts (see below).

RESULTS

We acquired tomograms at a total of 57 regions of interest, i.e. nuclear rCPSF6wt$_{AA}$.mCh cluster signals. Only 3 tomograms did not reveal any apparent structure, another 3 tomograms showed aberrant fiducials that were recognized as false-positive signals. In these 3 instances, we found perfectly round structure of ~ 100 nm. We hypothesize that the greens fluorophores were not present at their surface. These particular fiducials were fluorescent in only the mCh channel and therefore mistaken as rCPSF6wt$_{AA}$.mCh cluster signals.

In the remaining 51 regions of interest, we could visualize a total of 63 conical structures. In 42 tomograms, we could only appreciate a single conical structure, while in 9 tomograms, >1 structures were apparent. It is worth mentioning that the number of regions of interest with multiple structures most likely is and underestimate, since potential additional structures may be physically cut off during sectioning. The 21 conical structures that were not analyzed were either only contained partially, of too low contrast and / or could not be reliably segmented. We could also image 2 nuclear PIC in very close proximity to NPC, potentially still interacting with it (Figure 33). It appears as I those structures were caught just entering the nucleus. However, this cannot be judged do to the static nature of these data.

The complete set of correlated positions is available in Figure 34 & Table 1. Cropped tomograms of all positions and single images are available in the supplementary data on the enclosed DVD.

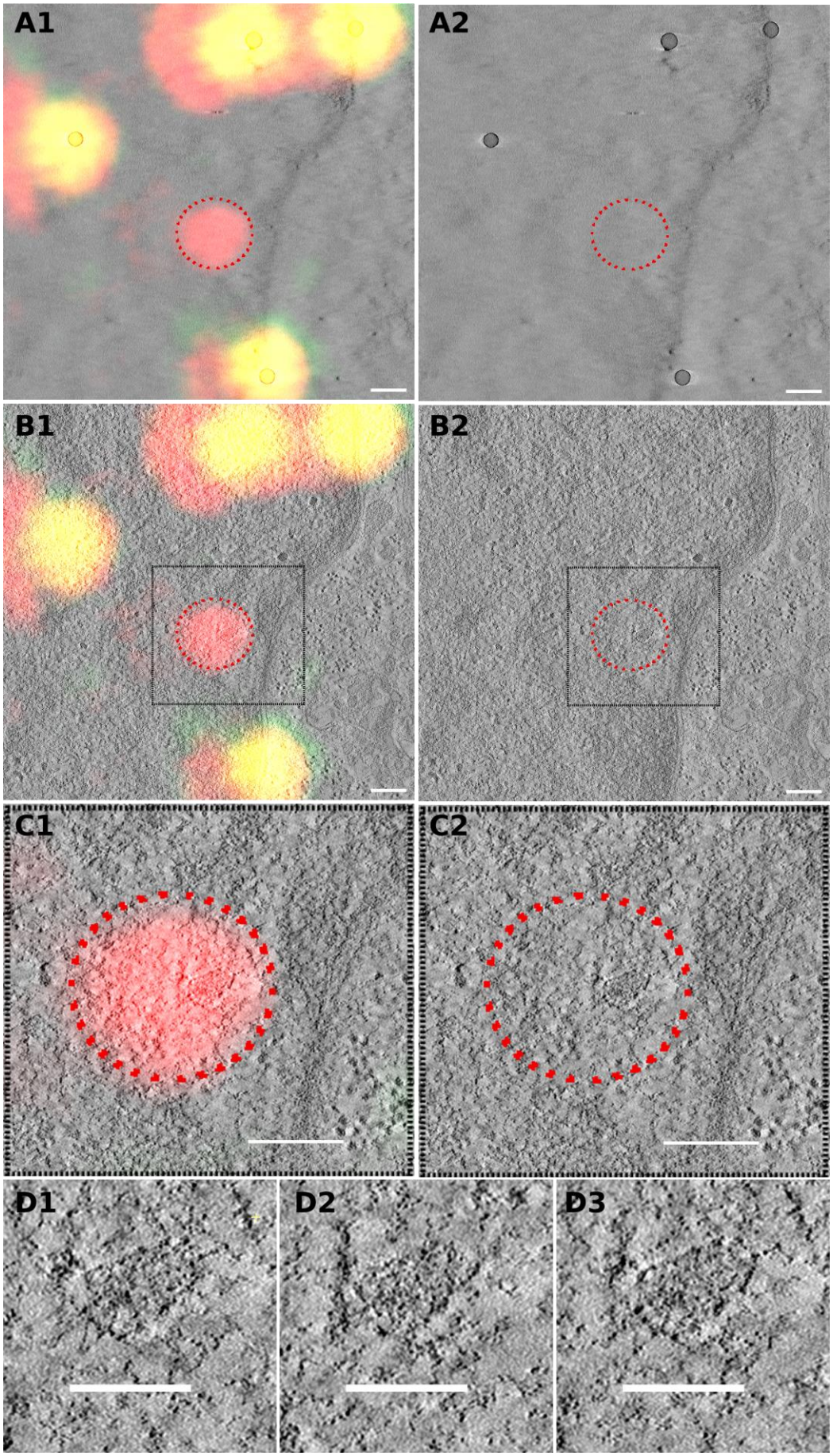
A1
A2
B1
B2
C1
C2
D1
D2
D3

Figure 30: Representative Example of a High Magnification Correlation With High Precision

Samples were processed as described for Figure 29. All images are extracted computational z slices of a reconstructed tilt series tomogram. Left panels are merged with the correlating fluorescence signals (red and green = yellow: TetraSpeck Fiducials, red only: CPSF6wtAA.mCh). The dashed red line outlines the CPSF6.mCh cluster signal for better visualization in the left and right panels. Panels A show the top computational section of the sample with the electron-dense TetraSpeck Fiducials. Panels B show the center of the sample containing a capsid-reminiscent structure within the CPSF6.mCh cluster signal. Panels C show zooms of the boxed regions in panels B. Panels D show 3 different extracted computational slices of the tomogram of the correlated nuclear PIC structure. A cone-shaped architecture is clearly recognizable. Structure 66 (as in Table 1 & Figure 31, panels C-E & Figure 34).
Scale bars panels A-C: 200 nm, panel D: 100 nm.

3.2.9 PIC Model Generation and Structure Evaluation

The apparent nPIC structures were situated in the very electron-dense nucleus and were therefore not easily 3D rendered. In a similar project, according to Dr. Martin Schorb, the best way to generate models in 3D structure of such objects was by hand, taking into account the modeler's possible bias. The modeling was done in 3DMOD by manually adding model points to electron-dense (apparent dark points) positions at the surface of the observed apparent structures (see Figure 31). Exemplary models are shown in Figure 32.

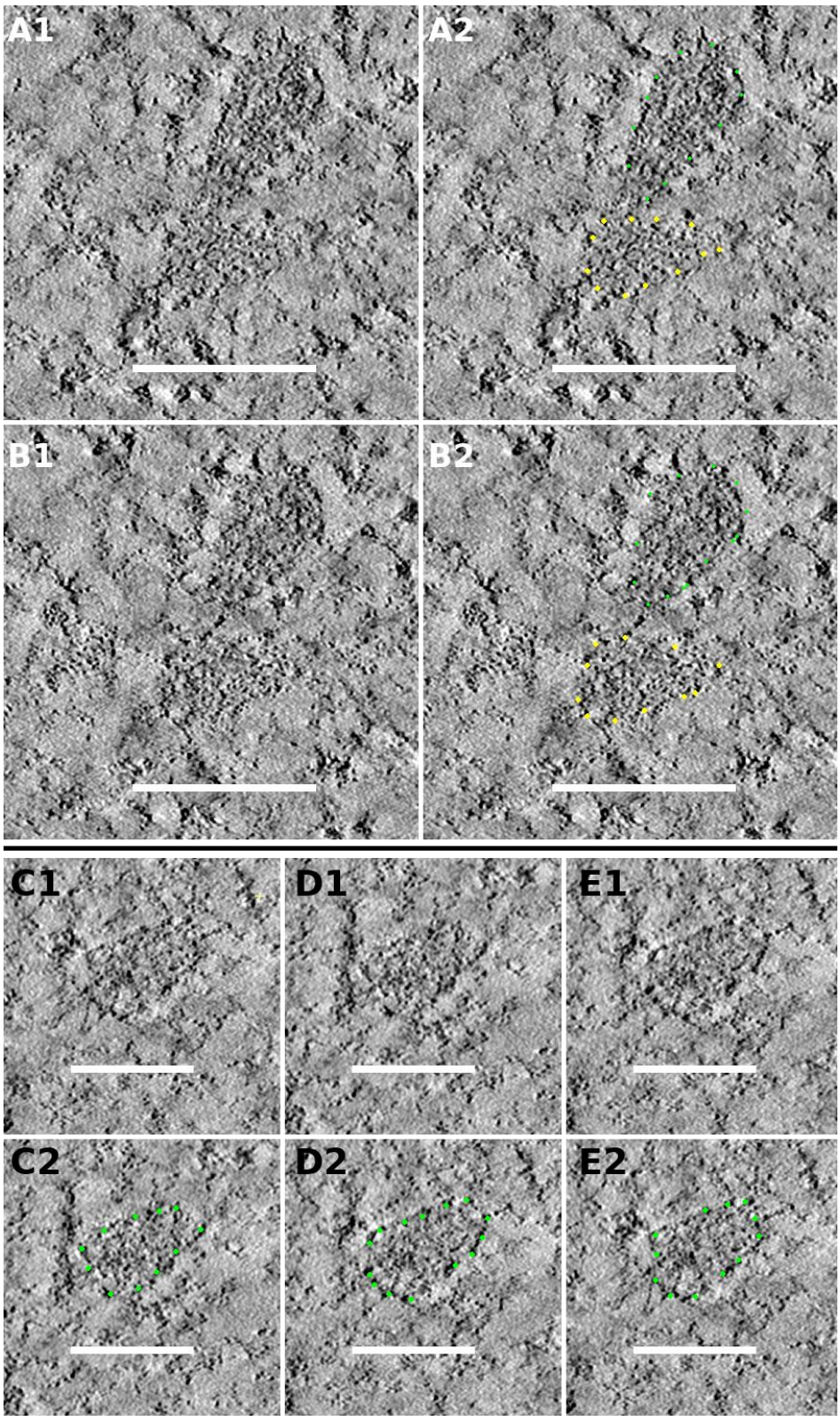

Figure 31: Representative Examples of Modeling Nuclear PIC Structures

U87$^{4/4}$ rCPSF6wt$_{AA}$.mCh cells were infected for 4 hours with NL4-3 virus particles. Samples were chemically fixed, vitrified, freeze substituted and 250 nm thin sectioned. Nuclear PIC were identified by CPSF6.mCh signal clusters in LM.

Panels A and B show an example of 2 apparent nPIC structures in direct proximity, contained in a single region of interest. The structure numbers are 52 and 53 (see Figure 34 & Table 1). Panel C shows structure 66 (same as in Figure 30, also see Table 1 & Figure 34). Panels X1 show the structure as observed in reconstructed tilt series, panels X2 additionally show the model points that were added by hand.

All images are extracted computational slices from reconstructed tilt series tomograms. Scale bars: 150 nm (AB) & 100 nm (C-E).

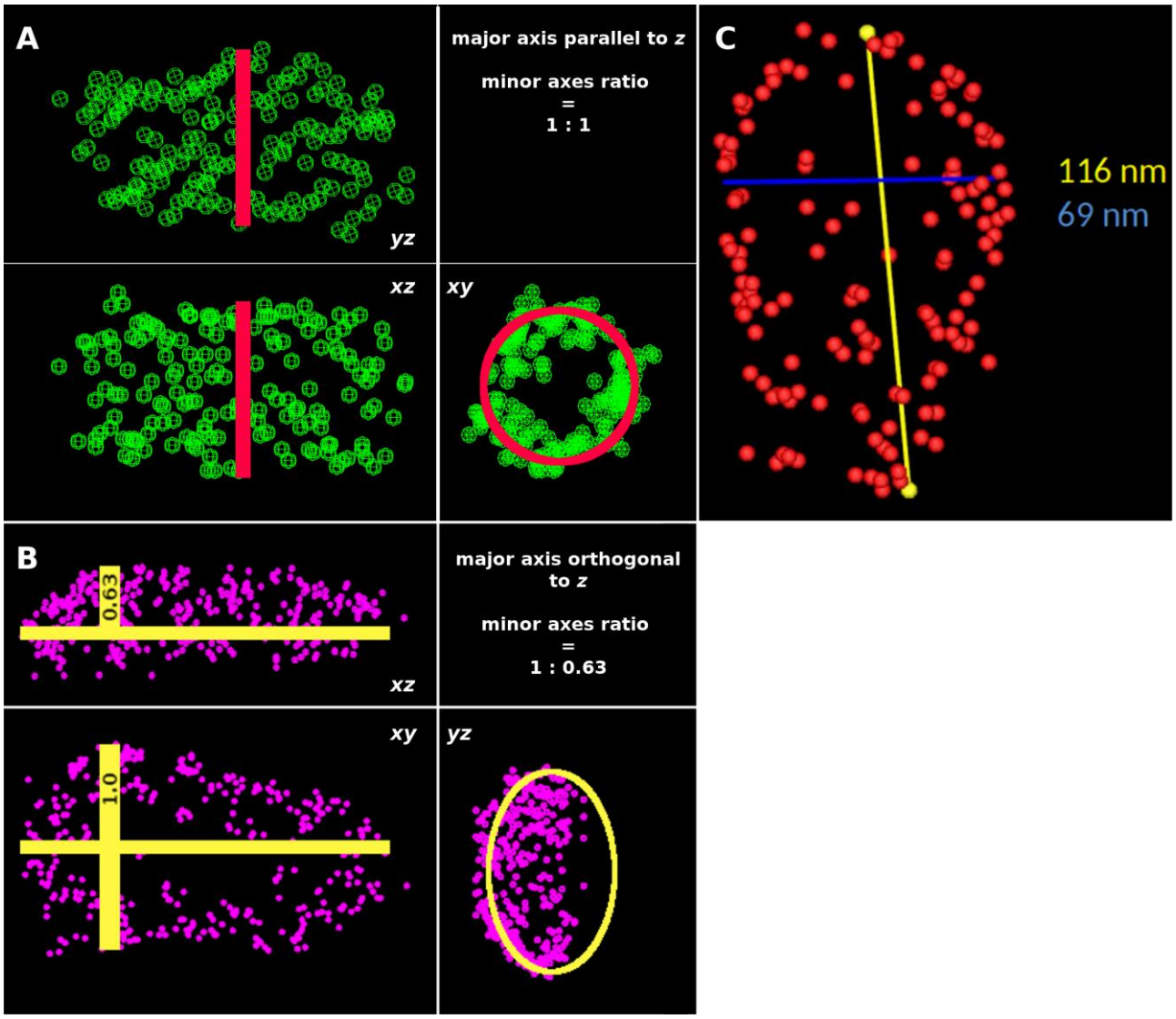

Figure 32: Exemplary Models with Major and Minor Axes and Exemplary z-Compression

This image shows 3 different models of different orientations in the tomogram volume. Indicated structures according to Figure 34 & Table 1).

Panel A shows the model (green points) of structure 4, where the major axis was almost parallel to z. During z compression, the minor axes (shown in red bars) were not affected. The apparent structure therefore appears almost ideally rotational symmetrically, as can be appreciated in the top (xy) view. Panel B shows the model (pink points) of structure 29, where the major axis was orthogonal to z. Due to z compression, the

minor axes (yellow vertical bars in xz and xy views) are of different length. This can also be appreciated in the top (yz) view, where the yellow ellipse indicates the imperfect rotational symmetry. The ratio of the minor axes was ~ 1 : 0.63.

Panel C shows the model (red points) of structure 12. The major axis (yellow) and one minor axis (blue) were modeled by hand) and measured in 3DMOD and therefore are not identical to the measures in Table 1 & Figure 34, measuring 116 nm in length and 69 nm in width.

Videos of these models are available in the supplementary data on the enclosed DVD.

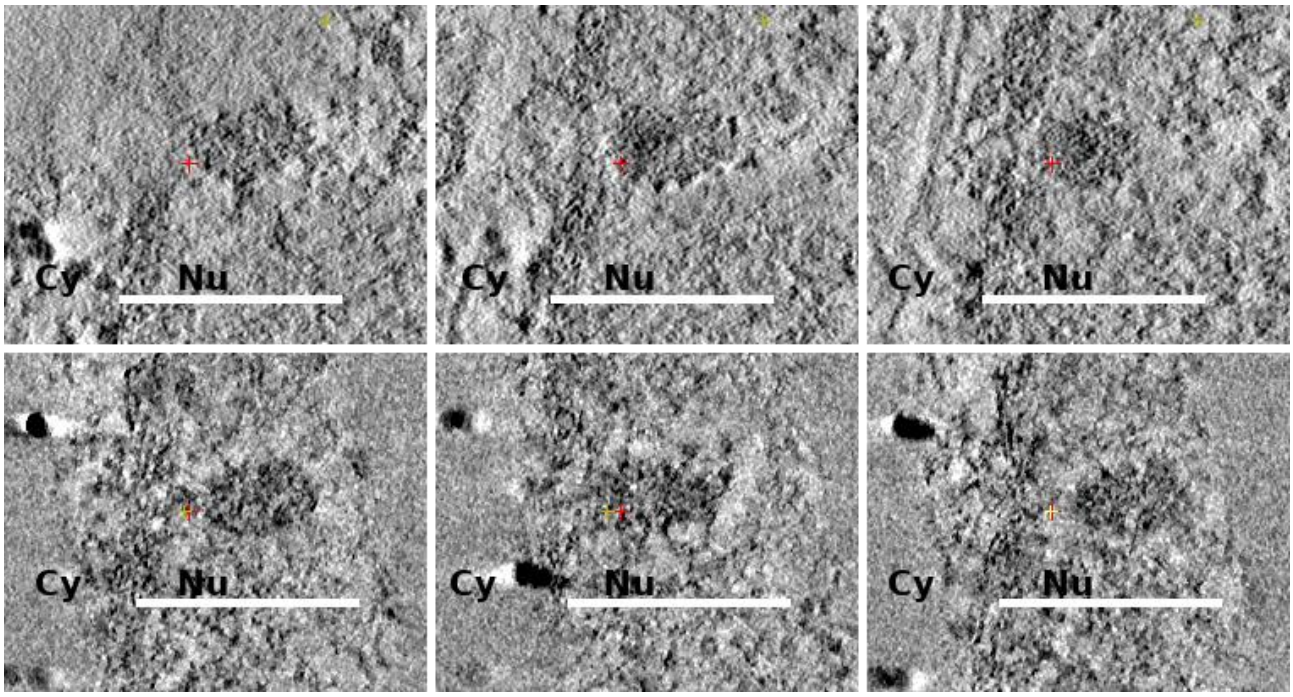

Figure 33: Nuclear PIC Structures in Close Proximity to Nuclear Pore Complexes

U87$^{4/4}$ rCPSF6wt$_{AA}$.mCh cells were infected for 4 hours with NL4-3 virus particles. Cells were chemically fixed, vitrified, freeze substituted and embedded in HM20 resin. The shown regions have been identified by CPSF6.mCh cluster signals in light microscopy and correlated with electron micrographs.

The upper and lower panels show 1 PIC structure each in different computational planes of a reconstructed tomogram. Both are very close to -, or still partially within nuclear pore complexes. At those positions, the nuclear double membrane envelope, dividing the cytosol (Cy) from the nucleoplasm (Nu) is interrupted by NPC (left of the red marks). Obviously, the methodology does not allow to draw conclusions about the mode of entry, but NPC clearly seem to be involved. Scale bar: 150 nm.

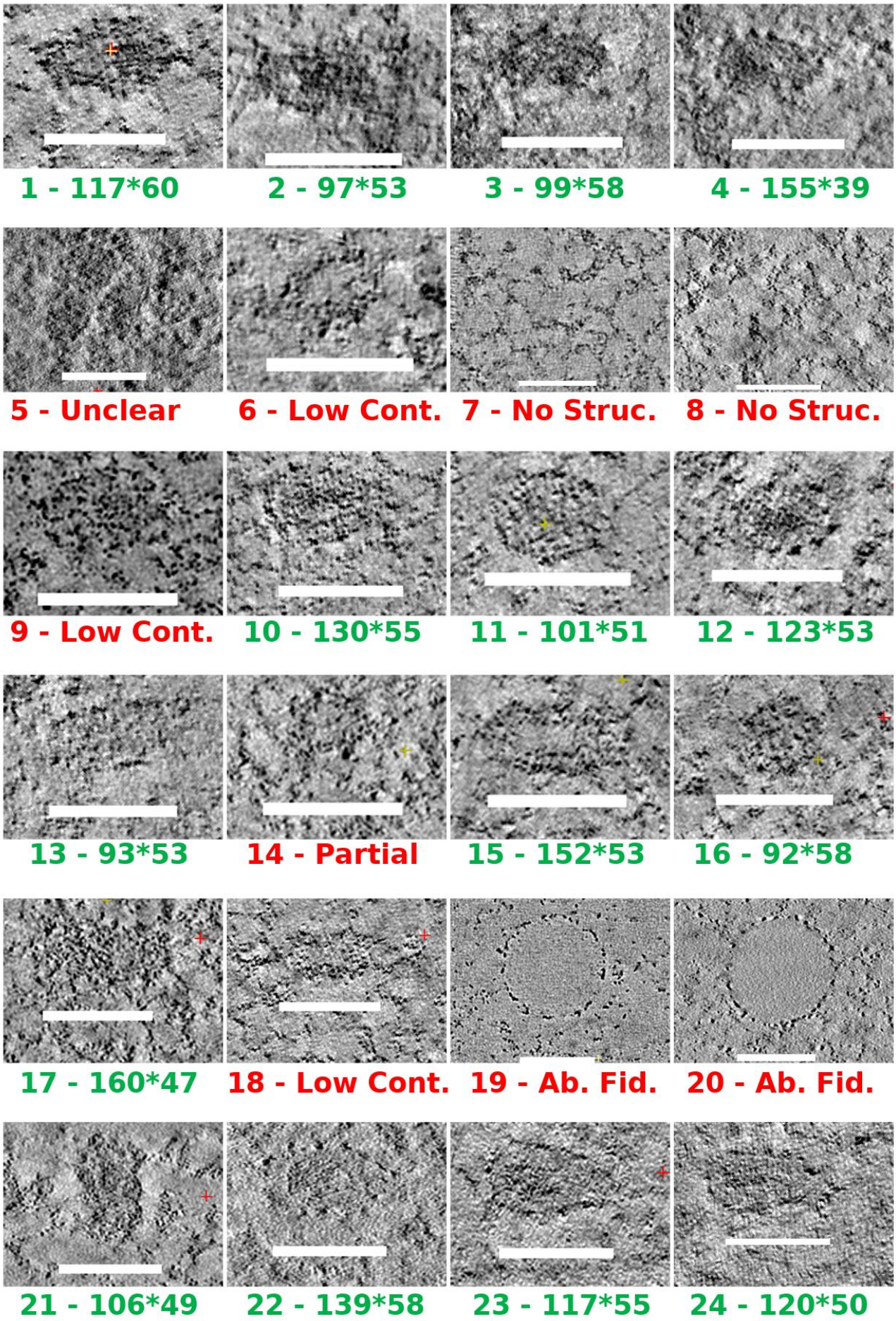
1 - 117*60
2 - 97*53
3 - 99*58
4 - 155*39
5 - Unclear
6 - Low Cont.
7 - No Struc.
8 - No Struc.
9 - Low Cont.
10 - 130*55
11 - 101*51
12 - 123*53
13 - 93*53
14 - Partial
15 - 152*53
16 - 92*58
17 - 160*47
18 - Low Cont.
19 - Ab. Fid.
20 - Ab. Fid.
21 - 106*49
22 - 139*58
23 - 117*55
24 - 120*50

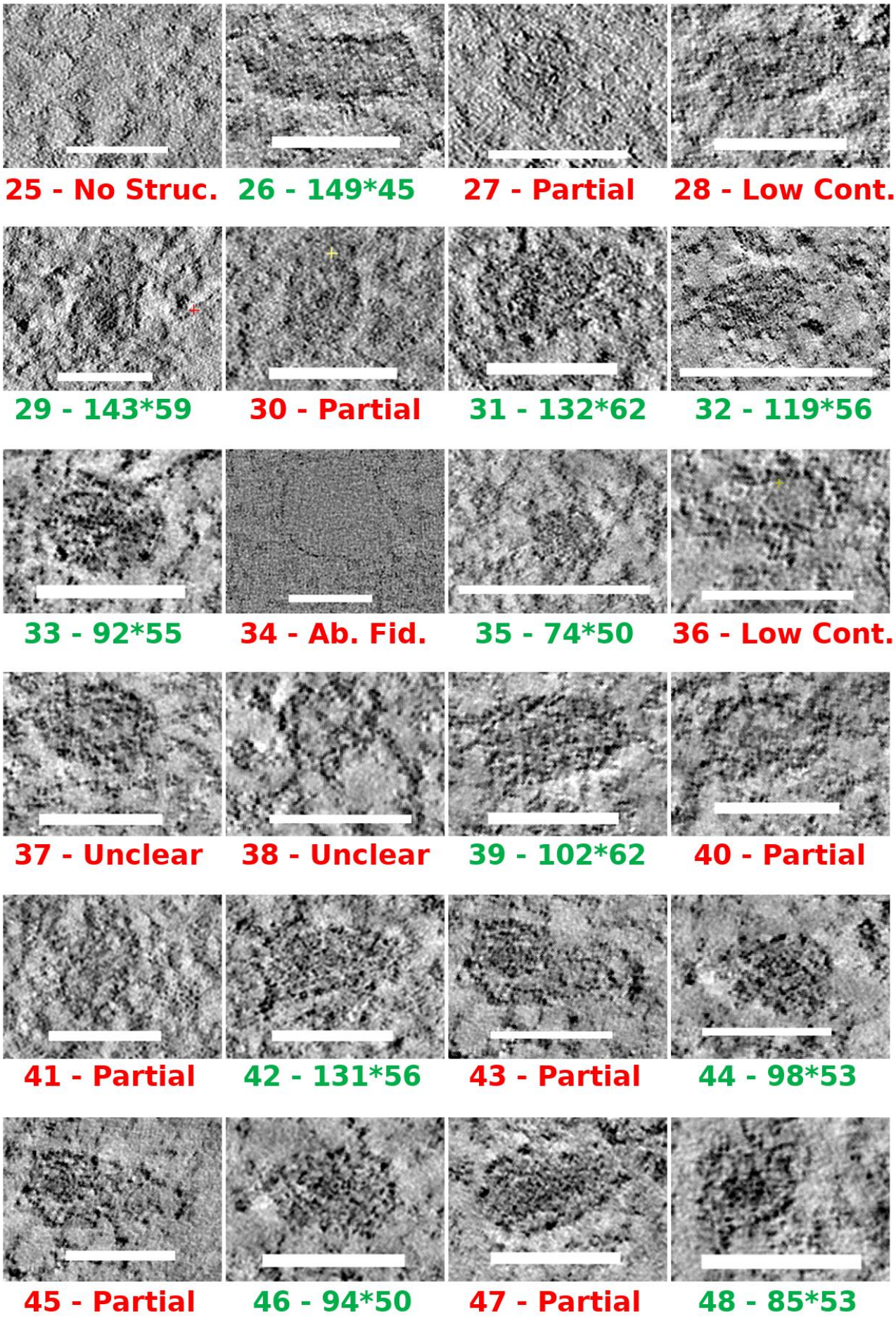
25 - No Struc.
26 - 149*45
27 - Partial
28 - Low Cont.
29 - 143*59
30 - Partial
31 - 132*62
32 - 119*56
33 - 92*55
34 - Ab. Fid.
35 - 74*50
36 - Low Cont.
37 - Unclear
38 - Unclear
39 - 102*62
40 - Partial
41 - Partial
42 - 131*56
43 - Partial
44 - 98*53
45 - Partial
46 - 94*50
47 - Partial
48 - 85*53

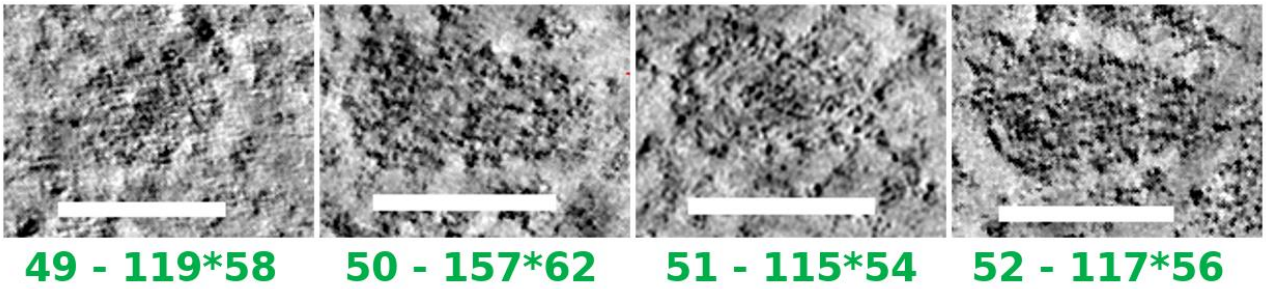

49 - 119*58 50 - 157*62 51 - 115*54 52 - 117*56

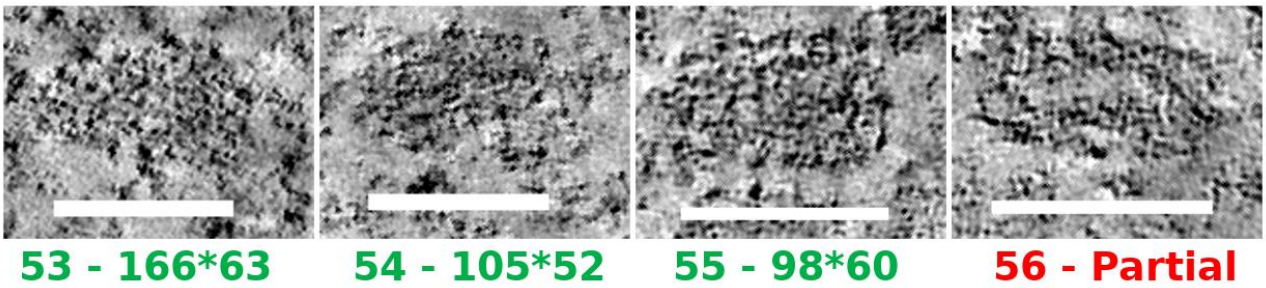

53 - 166*63 54 - 105*52 55 - 98*60 56 - Partial

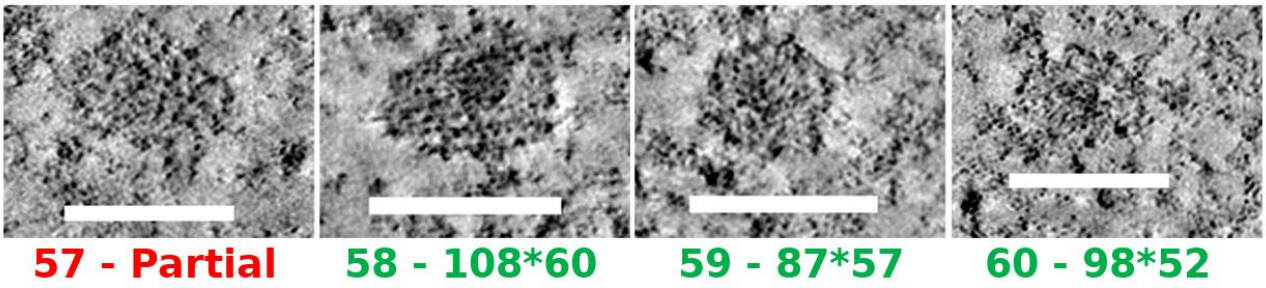

57 - Partial 58 - 108*60 59 - 87*57 60 - 98*52

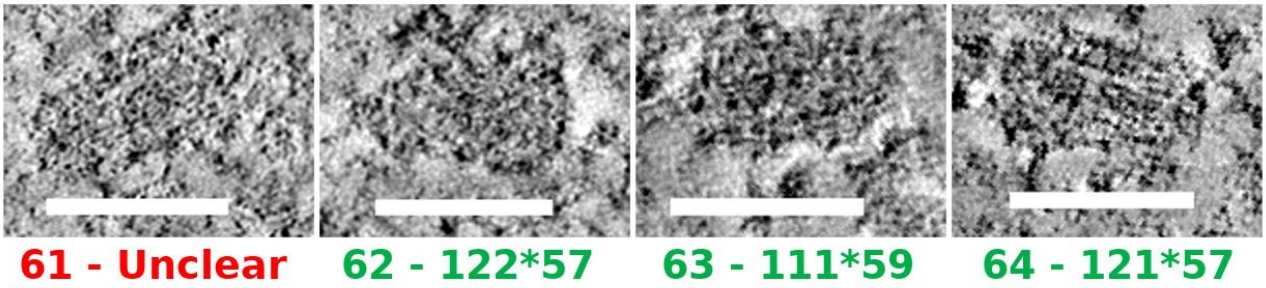

61 - Unclear 62 - 122*57 63 - 111*59 64 - 121*57

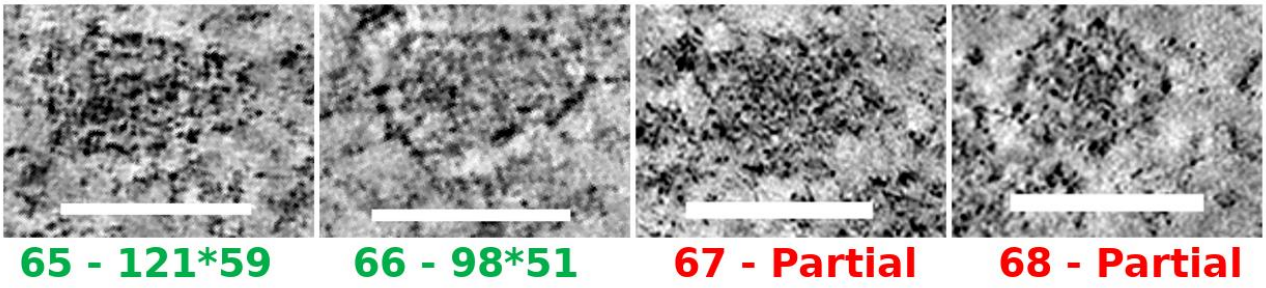

65 - 121*59 66 - 98*51 67 - Partial 68 - Partial

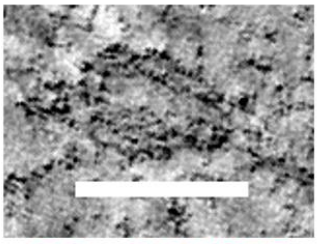

69 - 143*57

Figure 34: Gallery of all Correlated rCPSF6wt$_{AA}$.mCh Cluster Signals

U87$^{4/4}$ rCPSF6wt$_{AA}$.mCh cells were infected for 4 hours with NL4-3 virus particles. Samples were chemically fixed, vitrified, freeze substituted and 250 nm thin sectioned. Nuclear PICs were identified by CPSF6.mCh signal clusters in LM.

Each single image shows the structure (if recognizable) of an rCPSF6wt$_{AA}$.mCh cluster signal. The images were prepared with 3DMOD using the Slicer tool and attempted to align in xy. The structures are numbered (first number as identifier). Green labeled text indicates that the structure was analyzed and measured and includes the measurements in nm. Structures that were hard to recognize, not completely contained in the volume, not apparent or identified as aberrant fiducials are labeled in red and have not been analyzed and measured. The enumeration is consistent with Table 1. Occasional red and yellow crosses are added by 3DMOD. Scale bars: 100 nm.

Images and cropped tomograms for each structure are available in the supplementary data on the enclosed DVD.

Table 1: Complete Summary of all Correlated rCPSF6wt$_{AA}$.mCh Cluster Signals

This table summarizes relevant information about all correlated rCPSF6wt$_{AA}$.mCh cluster signals. An overall summary can be found at the very end of the table. Column 1 (Correlated Position #) is consistent with the enumeration in Figure 34. ST: single tilt tomogram, DT: dual tilt tomogram, Axis A or B: tomogram was acquired in 2 tilts, but only the indicated axis (A or B) axis was used for modeling. ROI: regions of interest. Green labeled structures have been modeled and analyzed, red indicated correlated positions have not been analyzed due to incomplete or nonapparent structures, aberrant fiducials, or low contrast, as indicated.

Correlated Position #	Acquisition Date [yyyy/mm/dd]	Grid	Coordinates	Axis Used	# of ROIs	# of Structures (Complete or Partial)	Model Dimensions [nm]	Remarks
1	20170111	Q4	C3RU	ST	1	1 Complete	117 * 60	
2		P4	E4U_Oben_1	ST	1	1 Complete	97 * 53	
			E4U_Oben_2	ST	2			
3					- A	1 Complete	99 * 58	
4					- B	1 Complete	155 * 39	
5			E4U_Oben_3	ST	1	1		Structure Unclear
6	20170307	T2	E3_1	Axis B	1	1		Low Contrast
7			E3_2	DT	1	0		No Structure Visible
8			E3_3	Axis A	1	0		No Structure Visible
9			E3U_1A	DT	1	1		Low Contrast
10			E3U_1B	Axis B	1	1 Complete	130 * 55	
			E3U_2	Axis B	1	4		
11						A – 1 Complete	101 * 51	
12						B – 1 Complete	123 * 53	
13						C – 1 Complete	93 * 53	
14						D – 1 Partial		
			E3U_3	Axis A	2			
15					- A	1 Complete	152 * 41	
16					- B	1 Complete	92 * 58	
17			E3U_4	Axis B	1	1 Complete	160 * 47	
18			E4R_1	Axis B	1	1		Low Contrast
19			E4R_3	DT	1	Aberrant Fiducial		
20			E4R_4	Axis A	1	Aberrant Fiducial		
21			E4R_5	Axis A	1	1 Complete	106 * 49	
22	20170207	T3	D2RU_1	ST	1	1 Complete	139 * 58	
23			D2RU_2	ST	1	1 Complete	117 * 55	
24			D2RU_3	ST	1	1 Complete	120 * 50	
25			D2RU_4	ST	1	0		No Structure Visible
26			D2RU_5	ST	1	1 Complete	149 * 45	
27			D4L_1	ST	1	1 Partial		Low contrast
28			D4L_2	ST	1	1 Complete		Low contrast

Correlated Position #	Acquisition Date [yyyy/mm/dd]	Grid	Coordinates	Axis Used	# of ROIs	# of Structures (Complete or Partial)	Model Dimensions [nm]	Remarks
	20170212	T4	F4_2-3	ST	2			
					- A	2		
29						- A: 1 Complete	143 * 59	
30						- B: 1 Partial		
31					- B	1 Complete	132 * 62	
32			F4_4	Axis A	1	1 Complete	119 * 56	
33			F4_5	DT	1	1 Complete	92 * 55	
34			F4U_2	DT	1	Aberrant Fiducial		
35	20170330	A1	D1R_1	ST	1	1 Complete	74 * 50	
36			D1R_2	ST	1	1 Complete		Low contrast
37			D1R_4	ST	1	1 Complete		Unclear Structure
38			D2L_1	ST	1	1 Complete		Unclear Structure
			D2L_2	ST	2			
39					- A	1 Complete	102 * 62	
					- B	2		
40						- A: 1 Partial		
41						- B: 1 Partial		
42	20180105-08	P1	F5RU	ST	1	1 Complete	131 * 56	
			D2LU_1	ST	1	2		
43						- A: 1 Partial		
44						- B: 1 Complete	98 * 53	
			D2LU_2	ST	1	3		
45						- A: 1 Partial		
46						- B: 1 Complete	94 * 50	
47						- C: 1 Partial		
48			C4LU	ST	1	1 Complete	85 * 53	
49			B2LU	ST	1	1 Complete	119 * 58	
		P2	G4R	ST	1	2		
50						- A: 1 Complete	157 * 62	
51						- B: 1 Complete	115 * 54	

Correlated Position #	Acquisition Date [yyyy/mm/dd]	Grid	Coordinates	Axis Used	# of ROIs	# of Structures (Complete or Partial)	Model Dimensions [nm]	Remarks
	20180105-08	P2	F4LU_2	ST	1	2		
52						- A: 1 Complete	117 * 56	
53						- B: 1 Complete	166 * 63	
54			F4LU_1	ST	1	1 Complete	105 * 52	
			F3RU	ST	1	2		
55						- A: 1 Complete	98 * 60	
56						- B: 1 Partial		
57			F3	ST	1	1 Partial		
58			F2RU	ST	1	1 Complete	108 * 60	
59			E3	ST	1	1 Complete	87 * 57	
60			E2R	ST	1	1 Complete	98 * 52	
61			E2	ST	1	1		Unclear Structure
62			D4L	ST	1	1 Complete	122 * 57	
63			D2LU	ST	1	1 Complete	111 * 59	
64			C3R	ST	1	1 Complete	121 * 57	
65			C2R	ST	1	1 Complete	121 * 59	
66			B2RU	ST	1	1 Complete	98 * 51	
		P3	D2R	ST	1	2		
67						- A: 1 Partial		
68						- B: 1 Partial		
69			C3O	ST	1	1 Complete	143 * 57	

Total Number of ROIs	57
Without apparent Structure	3
With Aberrant Fiducials	3
With 1 Structure	42
With >1 Structure	9

Total Number of Conical Structures	63
Analyzed	42
Not Analyzed	21

3.2.10 Intact Viral Particle Cores as Reference Structures, Analysis and Comparison of Models

By visual examination, the apparent nPIC structures are intriguingly reminiscent of the HIV-1 capsid and could represent just this: Full HIV-1 capsids or remnants thereof. As a most direct reference structure, we next analyzed intact viral particles cores under largely identical conditions. Cells on sapphire discs were incubated with NL4-3 virus particles, of the same preparation as used for infection experiments, at 16°C overnight. At this temperature, neither virus-cell membrane fusion, nor endocytosis can take place (Doms and Moore, 2000; Frey et al., 1995; Weigel and Oka, 1981). Therefore, virus particles were bound to specific receptors (CD4) and nonspecific attachment factors at the cell surface (Wilen et al., 2012). HeLa TZM-bl cells were used in this experiment, as this cell line binds more virus particles at the cell surface, possibly due to higher expression levels of unspecific attachment factors, in comparison to U87$^{4/4}$ cells (see Figure 35). These samples were identically processed as the samples for CLEM of nuclear PICs described above, except for that no light microscopy was performed here.

Virus particles at the cell surface were identified based on their unique morphology (compare Figure 1, Figure 36 & Figure 37). Tilt series tomograms were acquired and reconstructed, of a total of 22 viral cores of cell surface-bound viral particles. Their cores and envelopes were modeled in analogy to the nuclear PIC modeling (see Figure 36). A complete gallery (Figure 37) and Table 2 summarize the measurements of the cell surface-bound virus particles. The measurements of intact viral particles' cores and the correlated nPIC structures are summarized in Figure 38.

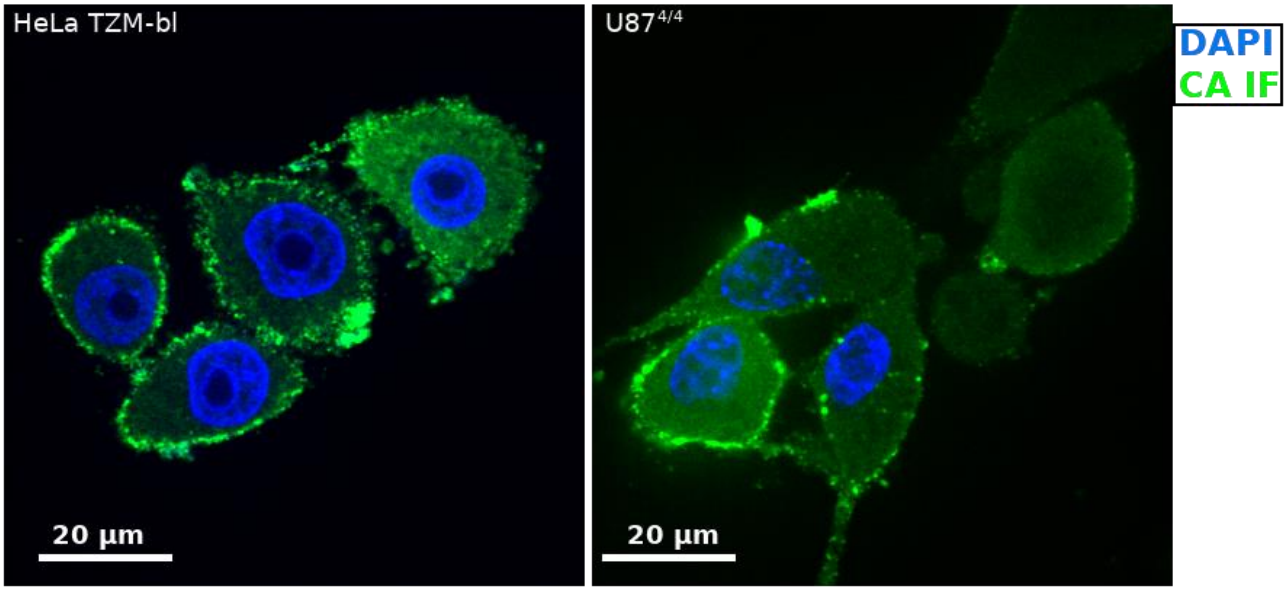

Figure 35: Hela TZM-bl Cells Bind NL4-3 Virus Particles More Efficiently Than U87$^{4/4}$ Cells

HeLa TZM-bl and U87$^{4/4}$ wt cells were incubated with NL4-3 virus particle preparation o/n at 16°C, not allowing entry or endocytosis. Samples were fixed and immunostained for CA. Visually, it is obvious that

HeLa TZM-bl cells bind virus particles much more efficient than U87$^{4/4}$ cells. Since the cells in this experiment merely serve as a virus particle binding platform, we assume the choice of cell line negligible. Single confocal z-slice, Leica SP8.

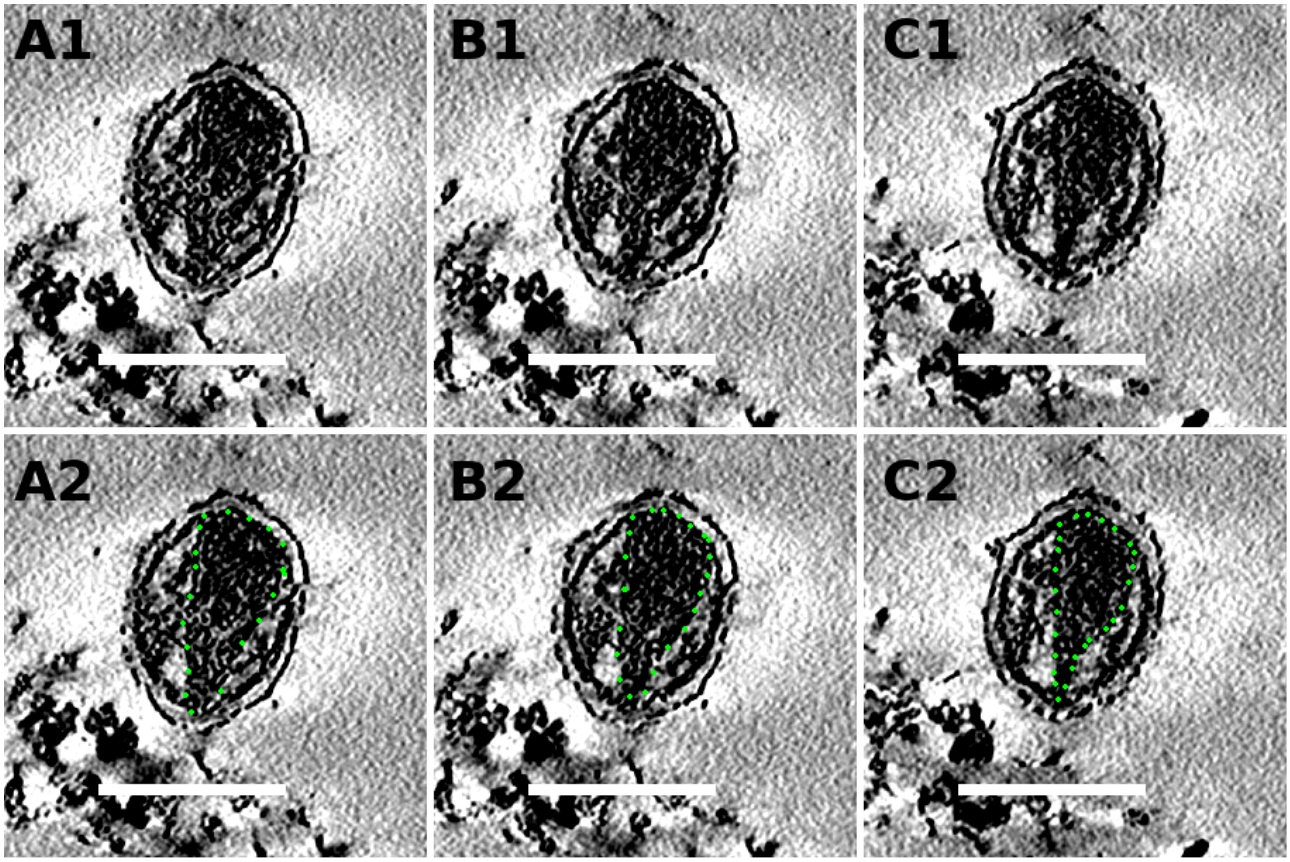

Figure 36: Exemplary Modeling of Cell Surface-Bound Virus Particle

HeLa TZM-bl cells were incubated with virus particle preparations at 16°C before chemical fixation, high pressure freezing, freeze substitution and HM20 embedding. 250 nm thin sections were prepared and visually analyzed for bona-fide HIV-1 virus particles, which were then imaged by electron tilt series tomography.
Panels A-C show 3 different extracted computational z slices from a reconstructed tilt series tomogram. The conical capsid is clearly recognizable. X2 panels are identical to X1 models, except for the addition of modeled points in X2. Those were added manually to the apparent edge of the structure. Scale bars: 100 nm. Tomograms of all analyzed cell surface-bound virus particles are available in the supplementary data on the enclosed DVD.

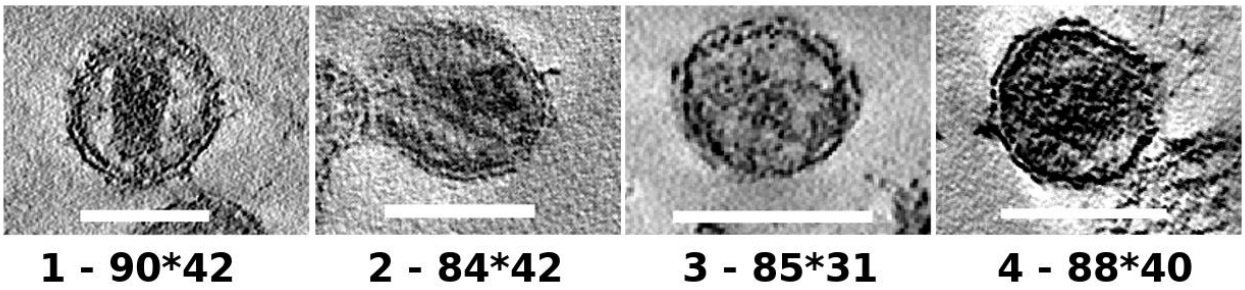

1 - 90*42 2 - 84*42 3 - 85*31 4 - 88*40

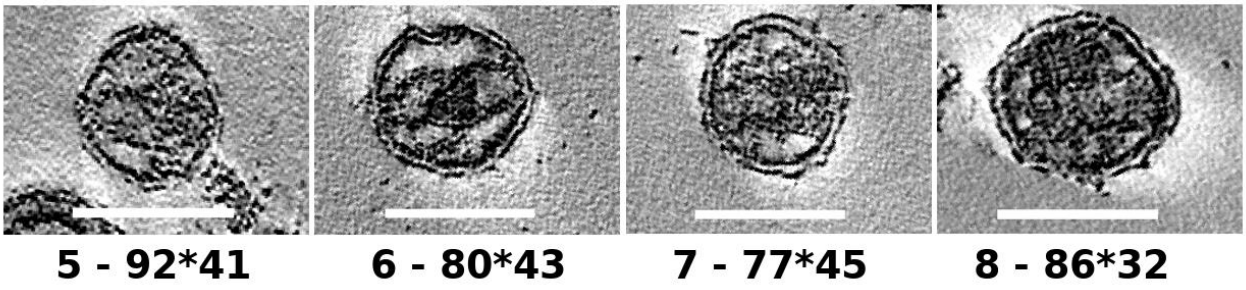

5 - 92*41 6 - 80*43 7 - 77*45 8 - 86*32

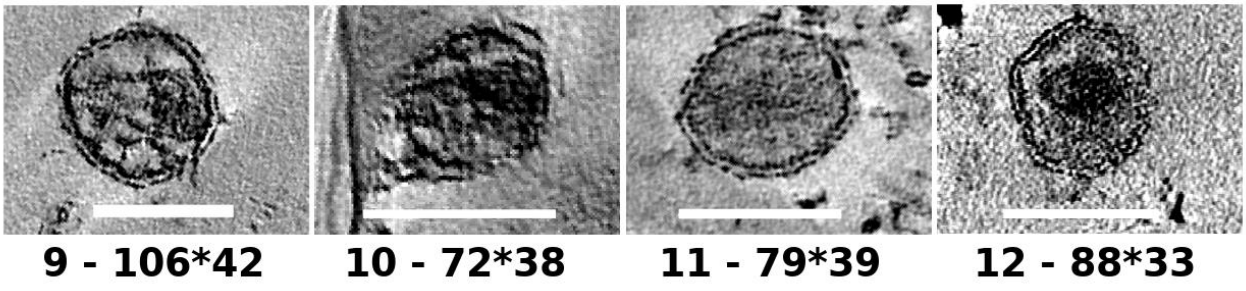

9 - 106*42 10 - 72*38 11 - 79*39 12 - 88*33

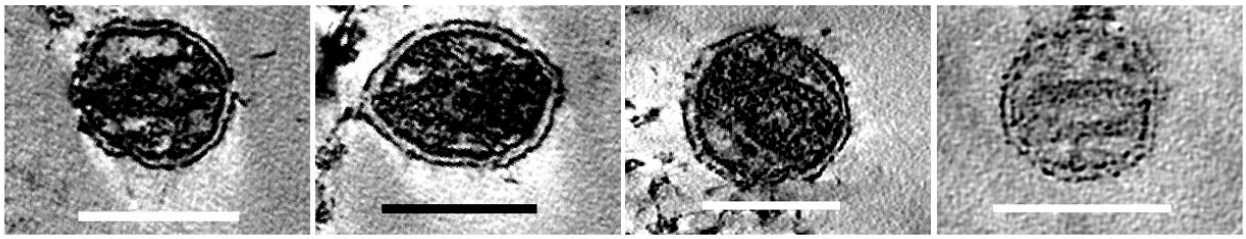

13 - 98*40 14 - 125*45 15 - 155*56 16 - 71*35

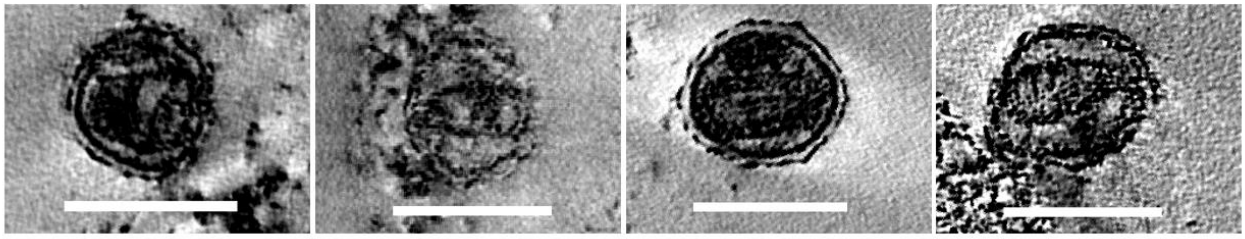

17 - 78*45 18 - 73*35 19 - 86*43 20 - 81*38

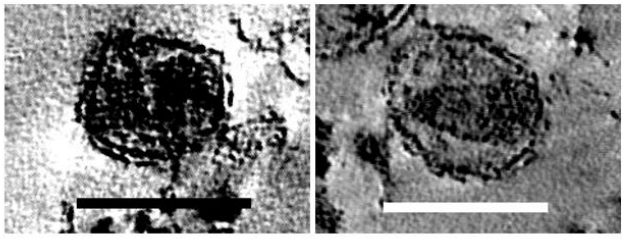

21 - 77*42 22 - 89*35

Figure 37: Gallery of all Analyzed Cell Surface-Bound Virus Particles

Each single image a single cell surface-bound virus particle. The images were prepared with 3DMOD using the Slicer tool and attempted to align in xy. The structures are numbered (first number as identifier) and the measurements of length and width are indicated in nm.
The enumeration is consistent with Table 2. Occasional red and yellow crosses are added by 3DMOD. Scale bars: 100 nm.
Images and cropped tomograms for each structure are available in the supplementary data on the enclosed DVD.

Table 2: Complete Summary of all Analyzed Cell Surface-Bound Virus Particles

This table summarizes the relevant information of all analyzed cell surface-bound virus particles. The enumeration is consistent with the one in Figure 37. The model dimensions indicate the length and width of a given core structure. The measurements are graphically represented in Figure 38. Images and cropped tomograms for each structure are available in the supplementary data on the enclosed DVD.

Viral Particle Core Structure #	Acquisition Date [yyyy/mm/dd]	Grid	Position	# of Structures	Model Dimensions [nm]
1	20170704	S2G1	D2RU	1	90 * 42
2	20170725	A1	Pos_1	1	84 * 42
3		A2	Pos_1	1	85 * 31
4		A2	Pos_4	1	88 * 40
5	20170815	G1	E2R	1	92 * 41
6	20170925	R1	F4RU	1	80 * 43
7			G3RO_2	1	77 * 45
8		R2	Pos_11	1	86 * 32
9			Pos_12	1	106 * 42
	20171128	1128	Pos_1	2	
10				A – 1	72 * 38
11				B – 1	79 * 39
12	20171130	B3	2_0	1	88 * 33
13			2_1	1	98 * 40
			2_2	3	
14				A	125 * 45
15				B	155 * 56
16				C	71 * 35
			2_3	3	
17				A – 1	78 * 45
18				B – 1	73 * 35
19				C – 1	86 * 43
	20180110	0110	2	2	
20				A – 1	81 * 38
21				B – 1	77 * 42
22			5	1	89 * 35

The model analysis was purely based on the created models, the actual tomograms were not further taken into account. This was done in collaboration with Dr. Martin Schorb (EMCF, EMBL, Heidelberg). For all data processing, we developed and applied MatLab scripts. As a conical structure was observed for the vast majority of structures (see Figure 34 & Table 2), an ellipsoid function was fit to the model as an approximation. The longest model axis was defined as the major axis. An ellipsoid function has 2 minor axes, which in the case of a rotational symmetry would be of equal length. In the observed models, a compression along the *z* axis was observed, as structures seemed flattened in *z (*or stretched in *xy)*. A perfect rotational symmetry is never reached in biological samples, but, in the sense of lowest energy, fair to assume, and therefore used as an approximation. This means, the length of the minor axes, is assumed to be practically equal, not appearing so in the tomograms. In the case of the major axis being parallel to *z*, the minor axes would not differ from each other, unless the compression being so strong, an actual minor axis would be identified as the major axis (see Figure 11), as the minor axes would both be orthogonal to

z. When the observed structure's major axis is not parallel to z, comparing the 2 minor axes can be used as quantification for the compression and allows calculation of the correction factor.

The overall compression was calculated and amounts ~89 % on average and in median (meaning the apparent, measured z thickness was compressed to 89% of the original thickness). To compensate for this, all tomograms and models were computationally stretched in z by a factor of ~ 1.12 (=100/89). After compression correction, the major axis was plotted as length, and the minor axes average was plotted as width of the observed core-like nuclear structures, or viral particles' cores (see Figure 38). Exemplary models and z compression are shown in Figure 32.

For the reference structures (cores of cell surface-bound virus particles), instead of using minor axes to calculate the z compression, we used the viral envelope. Ideally, the envelope would have the shape of a perfect sphere, as this is energetically favorable. Therefore, the viral envelope was modeled and fit to a perfect sphere function. The tomograms were stretched in *z* until all 3 axes of the approximated ball were mostly equal. The cores were then analyzed as described above, by fitting an ellipsoid function and measuring the length and width. See all analyzed viral particles in Figure 37 & Table 2. Eventually, the apparent nuclear PIC structures (Table 1 & Figure 34) were compared to the reference cell surface-bound virus particle reference structures (Table 2 & Figure 37) were compared (see Figure 38).

PIC structures were 119 nm long and 55 nm wide, on average. The reference capsids from cell surface-bound virus particles, on the other hand, merely were measured 89 nm long and 40 nm wide, which is considerably smaller (see Figure 38). However, the structures appear very similar in shape. The ratio of width to length accounts to 0.45 and 0.49 for viral cores and nPIC structures, respectively. When compared to previously published cryo-ET data, viral cores have been measured 119 nm in length and 60 nm in width, accounting to a width to length-ratio of 0.5 (Briggs, 2003; Briggs et al., 2006). These measurements are very similar, yet incomparable due to different EM techniques.

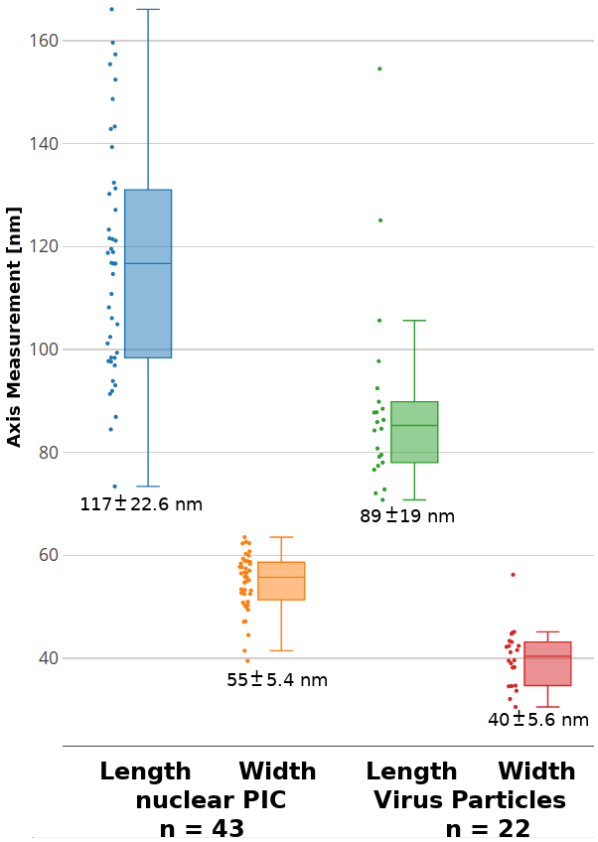

Figure 38: PIC Structure and Virus Particle Core Model Measurements

The models created for nuclear PIC (left) and the virus particle cores as a reference (right) were analyzed and measured in length and width using custom MatLab scripts together with Dr. Martin Schorb. Every point represents one model, the box plots show the median (solid line) and the inner 2 quartiles (colored box), and the biggest and smallest measurements (upper and lower whisker, excluding outliers). Depicted below each box is the average measurement and standard deviation.

3.3 rCPSF6wtAA.mCh Expression in Primary Human Macrophages

We have successfully visualized the structure of nuclear preintegration complexes in U87$^{4/4}$ model cells. Since they are no natural target cells, they were engineered susceptible to HIV-1 infection by transducing CD4 and CXCR4. Also, it is an immortal cell line. Therefore, the observations we made can not necessarily be extrapolated to natural primary target cells.

For this reason, we tried to express the rCPSF6wt$_{AA}$.mCh cassette also in primary monocyte-derived macrophages macrophages (MDM), derived from healthy blood donors, isolated and differentiated by technical assistant Anke-Mareil Heuser. Lentiviral transduction was to be omitted, since observations, when infecting with another lentivirus (HIV-1) shortly after transduction, could

not be clearly assigned to the infection or transduction. We therefore chose adeno-associated virus particles for gene-delivery. These have been shown before to successfully transduce primary human macrophages. Especially well performed the capsids AAV6 and AAVDJP2 (Dr. Kathleen Börner). We produced AAV particles in 293T cells, packaging the rCPSF6wt$_{AA}$.mCh cassette and a double stranded vector encoding YFP as a positive control. Before harvesting, the cells were visually checked for fluorescence protein expression, which was clearly visible 2 days after proviral plasmid transfection. Yet, when we transduced primary MDM, we repeatedly could not detect any mCh fluorescence (see Figure 39). Neither one of the 2 tested capsids lead to detectable expression of the mCh fusion protein. Further experiments for CPSF6.mCh fusion protein expression in primary macrophages are being planned.

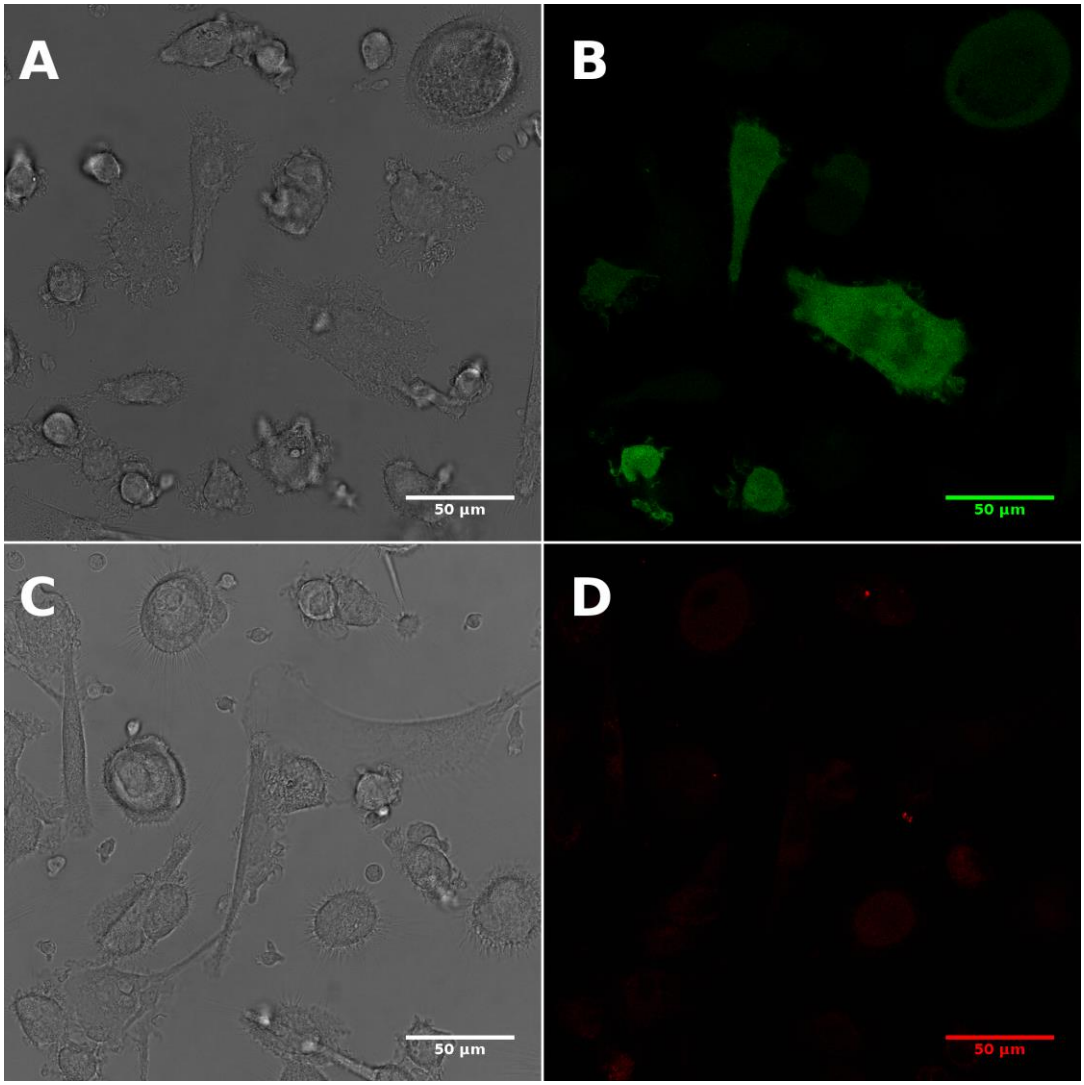

Figure 39: Fluorescence Images of AAV-Transduced MDM

RESULTS

AAV virus particles were produced in 293T cells, using the AAVDJP2 capsid to package the rCPSF6wt$_{AA}$.mCh or YFP expression sequences. MDM were transduced with crude lysates and 1 week after transduction subjected to fluorescence microscopy, to check the transduction efficiency.

Panel A and B show bright field and YFP fluorescence images, respectively. YFP expression can readily appreciated in B. Panel C and D show bright field and mCh fluorescence images, respectively. In contrast to B, D does not display considerable fluorescence signals.

4 Discussion

CPSF6 colocalizes as intense clusters with infectious nuclear preintegration complexes. We could clearly show that the surrogate marker rCPSF6wt$_{AA}$.mCh, is very well suited to minimal invasively label these complexes. We could not detect any particular changes in terms of infectivity or cellular phenotype due to the expression of rCPSF6wt$_{AA}$.mCh and/or the downregulation of the endogenous CPSF6.

In CLEM experiments, we could clearly show that correlating rCPSF6wt$_{AA}$.mCh clusters yields capsid-reminiscent structures. Finding these structures has implications for further HIV-1 research.

Here, we want to discuss limitations and considerations concerning the employed technique and the obtained results.

4.1 Implications of Using rCPSF6wt$_{AA}$.mCh as a Surrogate Marker

1) The rCPSF6wt$_{AA}$.mCh expression is mediated by lentiviral transduction. Using a lentiviral transduction vector might lead to overlapping phenotypes when infecting with HIV-1 (a lentivirus) afterwards. In fact, during the first 2 weeks following lentiviral transduction, we could observe mCh signal clusters in cells without additional infection. During further passaging, this phenotype disappeared. This shows the importance of our colocalization studies, to prove, what the CPSF6 fusion protein really detects (see chapter 3.2.3). In principle, rCPSF6wt$_{AA}$.mCh cluster signals can be caused also by lentiviral vectors, or remnants thereof. In primary macrophages, CPSF6 cluster signals are observed several weeks after infection (David Bejarano, data not shown).

2) CPSF6 is a key factor in integration site targeting (Lusic and Siliciano, 2017; Sowd et al., 2016). We could show that the rCPSF6wt$_{AA}$.mCh fusion protein is functional in binding nuclear CA (see Figure 26). Whether the integration site targeting might be altered, due to the mCh fusion or CPSF6 overexpression was not address. We could prove that the infectivity in U87$^{4/4}$ rCPSF6wt$_{AA}$.mCh is not different from wildtype cells. If proviruses were to integrate differently in transduced cells, e.g. into loci with low gene expression, this would likely affect viral gene expression, and thereby the infectivity score. Analyzing this in detail would require deep integration site analysis. Since here we merely CPSF6 here as a surrogate marker for nPIC detection and did only analyze postentry events up to nuclear localization, it did not appear necessary to investigate viral integration sites.

3) CPSF6 predominantly localizes to the nucleus. Therefore, using CPSF6 as an identifier marker also means that experiments were limited to only nuclear subviral structures, nuclear PIC. CPSF6 can also be targeted to the cytoplasm e.g. by expressing truncated versions (e.g. murine mCPSF6-

358 (Lee et al., 2010), or human hCPSF6-375 (Hori et al., 2013)). Downregulation of the CPSF6 nuclear import factor TNPO3 is reported to also localize full length endogenous CPSF6 to the cytoplasm (De Iaco et al., 2013; Gallay et al., 1997; Logue et al., 2011).

In both cases, the cytoplasmic CPSF6 is able to interact with theoretically all CA-positive subviral particles.

CPSF6-positive nuclear PIC are considered likely to contribute to infection, since they contain viral DNA and already overcame the nuclear envelope barrier by translocating into the nucleus.

We do not know about the correlation of CPSF6 colocalization and infectivity of subviral particles in the cytoplasm, when expressing truncated CPSF6 versions or knocking down TNPO3. CPSF6 has been shown to bind CA hexamers with high affinity (Price et al., 2014). Therefore, specific binding to productively infectious RTC seems unlikely. The expectation is rather that cytoplasmic CPSF6 would bind any CA-positive complex. Furthermore, CPSF6 relocation to the cytoplasm would be highly artificial. hCPSF6-375 and mCPSF6-358 have been reported to negatively affect reverse transcription and to restrict viral infection (Ning et al., 2018).

For these reasons, using CPSF6 as a surrogate marker for cytoplasmic complexes does not appear to be an obvious alternative. Visualization of viral DNA, as we have tried in this study, would still be the superior method of choice.

4.1.1 rCPSF6wt$_{AA}$.mCh Colocalizes with Immunofluorescence Staining against CPSF6

The functionality of fusion proteins can be greatly influenced by different factors: Position and size of the fusion tag / protein (Hanne et al., 2016b; Sakin et al., 2016) as well as choice of linkers between the actual protein and the fluorescence protein (Chen et al., 2013).

In first experiments, we were able to show that the autofluorescence signal of rCPSF6wt$_{AA}$.mCh colocalizes efficiently with the CPSF6 immunofluorescence signal (see Figure 24).

Fusion proteins often degrade to some extent in cells. Those degradation products could potentially form clusters similar to the expected infection phenotype. However, mCh cluster signals were only detected in infected cells, uninfected cells only displayed basic nuclear CPSF6wt$_{AA}$.mCh signals. We therefore conclude that the observed phenotype is truly caused by infection and not an artifact.

4.1.2 IN.eGFP-Labeled Subviral Particles Colocalize With rCPSF6wt$_{AA}$.mCh Clusters

To further prove that the observed rCPSF6wt$_{AA}$.mCh cluster phenotype is caused by HIV subviral particles, we next infected transduced cells with IN.eGFP-containing virus particles. IN.eGFP fusion proteins have been demonstrated as efficient virus particle labels (Albanese et al., 2008). The IN protein must stay attached to the viral genome until integration and is therefore used as a subviral particle marker throughout infection events until integration is completed. The nucleus is no perfect sphere but is of unregular shape and contains invaginations. It is therefore not always clear whether an IN.eGFP positive structure is really in the nucleus, at the nuclear envelope or close but yet cytoplasmic. All IN.eGFP signals we considered truly nuclear were colocalizing with mCh cluster signals. On the other hand, we were also able to detect few rCPSF6wt$_{AA}$.mCh cluster signals that did not show any IN.eGFP signal. This can be explained by the labeling efficiency of IN.eGFP. The Vpr.IN.eGFP and a proviral plasmid were cotransfected for virus particle production, a 100% labeling efficiency is never reached, as there will always be cells transfected with the proviral plasmid only. As described before, the observed phenotype was only observed in nuclei of infected - but not in uninfected cells. In combination, these results indicate an efficient labeling of subviral particles by the rCPSF6wtAA.mCh fusion protein in the nuclei of infected cells. The possibility to bias our CLEM experiments to subviral particles colocalizing with mCh cluster signals can be mostly ruled out, as we could not observe nuclear IN.eGFP signals without mCh cluster signal colocalization.

4.1.3 Ambiguous Results on Nuclear CA Signal Detection

To show the presence of further viral hallmarks, we performed immunofluorescence staining experiments to detect the CA protein and Cu-catalyzed click labeling to detect EdU signals (i.e. nascent viral DNA). I was never able to detect a CA signal in the nuclei of infected cells, neither in wt nor in transduced cells. Cytoplasmic subviral particles, on the other hand, always yielded easily detectable CA immunofluorescence signals. This is dissonant with the experimental outcome of David Bejarano and Dr. Ke Peng in our laboratory. Both have been able to detect nuclear CA signals in their experiments, also without Cu-catalyzed click labeling (observing pronounced variation in CA signal intensity and colocalization efficiency). This is still under investigation. Protocols have been compared and reagents shared. So far, the cause for this dissonance could not be pinpointed. We are still working on the reproducibility. As we are trying to shed light on the CA detection, we ordered two additional antibodies used by other groups, who are able to detect nuclear

CA signals efficiently in nuclei of infected cells ((Francis et al., 2016), KewalRamani, personal communication). We have assumed that our polyclonal rabbit serum against CA used in our studies should be superior in detection, compared to the monoclonal antibodies we ordered.

In single experiment, however, when EdU click labeling was performed, I was able to detect CA signals colocalizing with both, IN.eGFP and rCPSF6wt$_{AA}$.mCh signal clusters. As shown in the experiments aiming to combine EdU click labeling and electron microscopy, the labeled cells appeared heavily extracted, which was dependent on the duration of the click reaction mixture incubation (see Figure 21). When the click reaction mixture was applied for 60 minutes, nuclear CA signals were readily visualized, whereas 20 minutes labeling did not suffice. We hypothesize that extraction of nuclear (and cellular) content during the click procedure seems a prerequisite for the accessibility of nuclear CA. Potentially, CPSF6 and other nuclear host factors shield the nuclear CA from antibody detection. CA detection in the cytoplasm worked efficiently under all tested conditions, as assessed by colocalization with IN.eGFP. Experiments in monocyte-derived macrophages, performed by Dr. Vojtech Zila in our laboratory, showed that also incubation with 70% EtOH o/n, which is also known to extract cellular contents, enabled nuclear CA detection.

To show the presence of further viral hallmarks, we performed immunofluorescence staining experiments to detect the CA protein and Cu-catalyzed click labeling to detect EdU signals (i.e. nascent viral DNA). CA signals could not reliably be detected inside nuclei of infected wt or rCPSF6wt$_{AA}$.mCherry transduced cells. Cytoplasmic subviral particles, on the other hand, showed easily detectable CA immunofluorescence signals. While it was thought for many years that capsid uncoating happens in the cytoplasm because most labs could not detect any nuclear CA signals (which appears to be strongly cell line-dependent), some more recent studies indicate that CA can still be detected inside nuclei ((Francis et al., 2016; Peng et al., 2014), David Bejarano, unpublished). This apparent contradiction might be explained by the fact that staining and fixation conditions, as well as the choice of antibody appear to be a major factor influencing the ability to detect nuclear CA. Similar to extraction, allowing nuclear CA detection, different fixatives are also thought to affect the accessibility of epitopes. e.g. GA fixation, leading to crosslinking, would be expected to stabilize the shielding factors around the CA-positive structure, thereby lowering the antibody accessibility and hampering CA detection.

We do not fully understand the circumstances of the dissonance in nuclear immunofluorescence CA detection, but actively investigating it.

4.1.4 rCPSF6wtAA.mCh Overexpression Does not (Greatly) Affect Postentry Events

Overexpression of the rCPSF6wt$_{AA}$.mCh fusion protein and constant puromycin selection could influence postentry events and cause artifacts. To assess this, infectious virus particle preparation was titrated on wt and rCPSF6wt$_{AA}$.mCh U87$^{4/4}$ cells, and the percentage of CA expressing cells was scored 48 hours after infection. We did not observe differences in the percentage of CA-expressing cells, which could not be accounted for by biological variation. It therefore seems to us that there was no apparent influence on postentry events by the overexpression of the fusion protein (unless positive and negative effects compensate for each other). Whether there are effects on downstream processes, such as integration site specificity, virus particle budding, release, etc., we did no assess, since the purpose of the fusion protein expression was to label incoming nuclear PIC. Overall, we did not observe any negative aspects by transduction or puromycin treatment. Based on this basic readout, we assume our surrogate marker system to not cause considerable artifacts in the processes we analyze (i.e. postentry events).

4.2 Structure Visualization and Processing

4.2.1 Modeling

DNA, lipids and phosphorylated proteins are rich in phosphate groups, which are stained with uranyl (acetate) during EM sample preparations. The nuclear chromatin (histones and DNA) therefore appear electron dense in electron micrographs. In the already electron dense nuclear background, it was not sure, whether it would be possible to detect potential nuclear subviral structures. This concern held true: It was very challenging to visually identify these structures in electron tomograms, even for experienced EM users. The nuclear electron-dense background impeded the recognition and modeling of intranuclear structures. This was additionally complicated by considerable variations in contrast, which varied not only between different samples and block, but even within the same section. Lastly, the apparent structures were oriented in random angles in the section volume, which plays a certain role during tomography acquisition, considering the missing wedge, a part of the tilt-series volume, which is comparably low in information (Baumeister et al., 1999).

Under these circumstances, we could not identify distinct traits or characteristics that would allow an automated program to reliably identify and segment the apparent structures. Together with Dr.

Martin Schorb (EMCF EMBL Heidelberg), we agreed to model the structures by hand (Figure 31 & Figure 36).

This was unproblematic for obvious apparent structures (see Figure 31), but likewise challenging in samples with low contrast, or when the observed structure was close to the top or bottom of the thin section and only parts thereof contained. The ends of the structures (top and bottom edges, narrow ends) were challenging to model, as there is a very limited amount of protein and therefore also low information and contrast.

To circumvent the introduction of a bias during by-hand modeling, it would be favorable to render the apparent structures in 3D computationally. At the moment, Dr. Vibor Laketa (IDIP, CIID Heidelberg) is assessing the possibility to 3D render the apparent structures using the ILASTIK software (Sommer et al., 2011). The software is based on pattern recognition and requires minimal input to define background and structure. First results look promising and will provide additional support for the study at hand. Once the automated segmentation works well and a workflow is set up to measure the single structures, the measurements can be compared with the models prepared by hand, to yield more reliable numbers. Exact measurements will be interesting and helpful for comparing PIC structures to the viral particle core reference. Yet, the repeated visualization of the apparent structures is a highly interesting result by itself. This will be elaborated on in chapter 4.2.4.

4.2.2 Tetraspeck Fiducials Allow High Precision Correlation

The only surrogate marker we were using in this study is the signal of the rCPSF6wt$_{AA}$.mCh fusion protein, which is mainly localized to the nucleus. While the cytoplasm provides a number of subcellular structures, useful for correlation between lower and higher magnification (such as mitochondria or vesicles), the nucleus is, except for nucleoli, rather uniformly electron-dense. Nuclei of U87$^{4/4}$ are rather big (~10 µm in diameter), while the area acquired in a tomogram is comparably small (~ 4 µm²). In first attempts, we were fitting the nuclear background rCPSF6wt$_{AA}$.mCh fluorescence signal by hand into the ultrastructurally identified nucleus. This was already good enough to eventually identify first apparent PIC structures but was not reliable enough. Addition of TetraSpeck Fiducials allowed much higher correlation precision, by enabling an almost exact overlay of light and electron micrographs. In general, resins tend to shrink when exposed to the electron microscope's electron beam. When imaging close to an end of a section or close to a hole (due to incomplete resin infiltration), the EM thin section can shrink to some extent unidirectionally. In that case, scaling and rotating the light micrograph does not yield a perfect overlay, but requires a nonlinear transformation. Depending on the number and positioning of the

TetraSpeck Fiducials in respect to the shrinking area, also nonlinear transformation reaches its limitations.

Yet, the correlation worked stably well, so that the vast majority of apparent structures was identified within a distance of <300 nm from the center of the fluorescence cluster signal (see Figure 29).

In some cases, the mCh cluster signal was correlated to autofluorescent dust particles or aberrant fiducials, fluorescing in the mCh channel only. These were considered false-positives and neglected for further analysis. As dust particles were readily identified as false negatives, no tomograms were acquired at these positions. Aberrant fiducials were only apparent after tilt-series reconstruction and are therefore included in the full list of tomograms (Table 1 & Figure 34).

4.2.3 Loss of Fluorescence Intensity During EM Sample Preparation Poses a Risk for Introducing Bias

Unless performing cryo-CLEM, the mCh fluorescence is greatly reduced during sample preparation. mCh signal clusters as well as the nuclear mCh background were considerably reduced (estimate >90%) in fluorescence intensity. The selection of regions of interest starts with a visual examination through the microscope's oculars. Areas that seemed promising, were then imaged by confocal laser scanning. Imaging the complete sample grid would be too time-consuming and potentially lead to drying of the thin section.

This procedure involves the possibility of introducing a bias depending on the fluorescence intensity: Structures of low mCh cluster intensities are more likely to be overseen than such of strong signal intensities. Automated imaging and ROI identification of the whole sample could rule out this potential bias. However, thin sections mostly are not perfectly flat on the sample grid. The samples overall fluorescence could be bleached already during automated focal plane identification. For this study, we considered this potential bias acceptable, while keeping the implications on the apparent structures in mind (discussed below). The acquisition of the Leica SP8 microscope in early 2016 was a huge advancement. Its HyD detectors are much more sensitive, than the formerly used Leica SP2's PMT. A laser power of ~25% and 2-8 times frame accumulation was still necessary, using HyD sensors (SP8).

4.2.4 Apparent Structures

So far, the only truly convincing electron micrographs of intracellular HIV-1 subviral particles was presented in (Jun et al., 2011). They made use of the CA E45A mutation, which renders the capsid more stable (Forshey et al., 2002). Cone-shaped structures could only be detected for hyperstable mutant -, but not for wildtype intracellular subviral particles. The study at hand is the first to report a structure associated with wildtype HIV-1 nuclear PIC.

The apparent structures were clearly cone-shaped, reminiscent of the HIV-1 capsid. Whether the modeled electron-densities represent a particular CA (i.e. a capsid lattice), cannot be judged due to the limited resolution, resulting from extensive sample processing (chemical fixation, vitrification, infiltration and embedding). Higher resolution imaging by e.g. cryo- ET and data processing such as subtomogram-averaging might in the future resolve this question. The detection of nuclear CA signal colocalizing with the surrogate marker rCPSF6wt$_{AA}$.mCh supports the possibility that the apparent structure indeed is particular capsid CA. On the other hand, in earlier experiments, CA protein was only detected in ~50% of nPIC in U87$^{4/4}$ cells (David Bejarano, unpublished data). As discussed above, nuclear CA immunofluorescence detection is still being investigated. Assumed our hypothesis of restricted antigen accessibility held true, the 50% colocalization of CA with nuclear PIC might simply be an underestimate.
Genetically engineered CA, incorporating noncanonical aminoacids by Amber-suppression, which can be click labeled with small fluorophores instead of fusion proteins, could offer an alternative for CA immunofluorescence detection in infected cells.
Eventually, it can’t be ruled out that the observed electron-densities represent a coat of host factors, such as CPSF6.

To get a better understanding of what these structures represent, we acquired tomograms of intact virus particles bound to the cell surface as a reference under almost identical conditions (Figure 37, Figure 36 & Table 2). Cores of these cell surface-bound virus particles were modeled analogous to the apparent nuclear PIC structures. We observed a considerable difference in size (cell surface-bound particle cores are ~30% smaller), in comparison to the PIC structures (Figure 38). Their shapes, on the other hand, are very similar. For the time being, we can’t provide an experimentally based explanation for this observation. However, there are some possible explanations.

1) As mentioned before, embedding resins tend to shrink when exposed to the electron beam. The composition of the direct environment is very different between nuclear PIC and extracellular virus

particles. Nuclear PIC are surrounded by high amounts of host factors, histones and dense chromatin, while surface-bound particles are mainly surrounded by plain HM20 resin, also meaning that the absolute amount of HM20 resin is much higher for extracellular particles. It appears logic that more resin can shrink to a higher extent. Furthermore, the chromatin and proteins in the PIC's direct environment might serve as an interlinked scaffold, potentially being much sturdier and less likely to shrink. This assumption could be experimentally addressed and validated by vitrifying cells with surface-bound viral particles in protein solution, which might then prevent shrinkage of the particles. Alternatively, Env^- virus particles can be pseudotyped with VSV-G, bound to the cell surface and incubated additionally with NH_4Cl. Virus particles would then be taken up into endosomes, but could not fuse due to the NH_4Cl. Trapped in endosomes, the virus particles would then be surrounded by scaffolding material, proteins and membranes that might also prevent shrinkage. The latter option was tried in one experiment but did not yield enough data for a comparison. Searching for – and identifying virus particles in endosomes throughout the cytoplasm is much more laborious and less efficient. Also, we were concerned about using NH_4Cl, as it alters the pH value in endosomes and might thereby also influence the structural appearance, thereby potentially being a worse reference than surface-bound virus particles.

2) As described above, the applied method requires extensive processing of samples, and does therefore not allow to retain the apparent structure to a degree, where substructures (hexamers, pentamers) could be observed, or computationally rendered using subtomogram-averaging. We assume the apparent structure to represent capsid, or remnants thereof, due to the similarity in shape. The observation of the strong CPSF6 clustering at nuclear PIC could also mean that the incoming capsid serves as a scaffold for CPSF6, which multimerizes around it. This would create an additional protein layer that would increase the dimensions of the apparent structure. On the other hand, the additional CPSF6 layer would then rather be assumed to increase the length and width of the apparent structure by a given, consistent layer thickness. As an example: The length of viral particles' cores and nuclear PIC structures in average measures ~89 nm and 117 nm, respectively. If an additional CPSF6 (or also other factors) coat would account for the observed difference in size, one would assume a coat thickness of 14 nm at the wide and the narrow end, each (89 nm + 2*14 nm = 119 nm). Assuming the coat thickness would be of consistent thicknes all over the structure, one would also add 28 nm to the width of the viral particle cores (40 nm). This would add up to a total width of 68 nm, whereas we merely measured an average width of 56 nm for nuclear PIC structures.

Therefore, if an additional protein coat would account for the difference in size measurements, it would have to be considerably thinner (~ 50%) at the sides, in comparison to the ends. The first explanation therefore appears more likely.

3) A size distribution is always observed in particle preparations, just like in our model measurements (see Figure 38). Theoretically, structures that are bigger to begin with, might recruit more host factors, or only those might be big enough for reverse transcription within the capsid shelter, while smaller capsid might break due to DNA-synthesis induced increase of pressure frim within. As a consequence, bigger structures would be less likely to be sensed and degraded by cellular sensors, and more likely to complete reverse transcription and to enter the nucleus. This hypothesis would then argue against considerable resin shrinkage, but for a big capsid being a quality feature for successful infection.

To prove these speculations right or wrong, higher resolution imaging is crucial. Ideally, chemical fixation would be circumvented by using S1 or S2 lentiviruses as models, which should behave similarly in early postentry events. Samples would then be directly vitrified and imaged in cryo-EM. Hexamers and pentamers could potentially be visualized and counted, in nuclear structures as well as in surface-bound particles' cores, and directly compared. These experiments are currently in planning.

4.2.5 When do Virus Particles Uncoat?

The visualization of the apparent structure in the nuclei of infected cells raises the question: When do virus particles uncoat, when such a structure is apparent within the nucleus? Recent studies from other groups also indicated the presence of (residual) CA in infected cells' nuclei (Francis et al., 2016; Mamede and Hope, 2016). However, the authors interpret these observations as gradual uncoating in the cytoplasm and at the NPC, which leaves nuclear PIC with only small amounts of CA. As discussed above, the CA staining procedure is not trivial and needs close examination.
Nuclear CA detection strongly suggests that the fate of capsid bulk analysis assay cannot reflect the behavior of infectious subviral infectious particles (Yang et al., 2014). The presence of CA can also not directly be extrapolated towards the retention of the capsid as such in its structure. The results presented in this study, however, strongly suggest this capsid structure retention. This has considerable implications towards the understanding of how these big macromolecule complexes employ nuclear pore complexes of limited size for nuclear entry.

4.2.6 How do These Structures Enter the Nucleus?

While most of the regions of interest contained single apparent nuclear PIC structures, we also found several apparent structures in close proximity (a few 100 nm) underlying single ROIs (see Table 1). Considering the size of the apparent structure and the nucleus itself, and the number of nuclear pores, the likelihood of several structures being found within a few hundred nanomenters seems small. Subviral particles do not freely diffuse in the cytoplasm but are actively transported towards the nucleus (Balasubramaniam and Freed, 2011). At this stage, clustering of structures could already be primed. Following transport into the nucleus, these already close structures could be imported through nuclear pores in close temporal and spatial proximity and be coclustered with host factors, such as CPSF6. Furthermore, taking into account the vast number of Nups, there might be heterogeneity among nuclear pore complexes (Kane et al., 2018). Different subsets might be involved in export and import of different cargo (macro)molecules. Assuming there were specialized NPC for HIV-1 subviral particle import, this would be another promoter for structure clustering: If the number of available entrance points was limited, the likelihood of structures appearing in close proximity would dramatically increase. A combination of both hypotheses is also possible. To date, we have no experimental data supporting either idea. However, live imaging of rCPSF6wt$_{AA}$.mCh enrichment at subviral particles upon nuclear entry, as well as minimally invasive click labeling might in the future allow to shed light onto this question: Are there specialized points of entry at the nuclear envelope? Do subviral particles cluster during early postentry? A publication from 2002 already showed clustering of subviral particles at the MTOC (microtubule organizing center), which might be one starting point for RTC/PIC clustering at one location (McDonald et al., 2002).

Irrespective of potentially specialized NPC and clustering of structures, it is questionable how exactly these structures enter the nucleus, considering their comparably huge size.

(Macro)molecules bigger than 5- 9 nm in diameter cannot diffuse over the nuclear envelope but require active transport (Kabachinski and Schwartz, 2015; Knockenhauer and Schwartz, 2016; Paine et al., 1975). Hepatitis B Virus Particle cores are reported to be transported into the nuclear basket of nuclear pore complexes, having a diameter of ~40 nm (Kann et al., 1999; Panté and Kann, 2002). This is very close to measurements of the central pore in NPC, measuring ~ 41 nm. The overall NPC has a diameter of ~ 82 nm. The space in between is taken in by nuclear pore proteins (Nup). Further to the inside, mostly intrinsically unstructured protein chains leave an opening of 27 nm which is then mostly unoccupied (Bui et al., 2013). Our lab's current working model suggests the CA-Nup153 interaction to be competed for by nuclear CPSF6, allowing the Nup153 to bind other CA molecules more towards the cytoplasmic side, thereby "dragging" the core-reminiscent

structure into the nucleoplasm (David Bejarano, manuscript under review). Yet, fitting a structure of ~60 nm in width through the nuclear pore with a central channel of 41 nm is hard to envision. It is reported that during viral DNA synthesis, some stress force is incurred to the viral core, which might lead to leakage of the fluid core-content marker (Mamede and Hope, 2016; Rankovic et al., 2017). One can imagine that the sturdy nascent DNA cracks the core from within, potentially leading to a partial loss of structural CA. Similar observation have been made for HBV, where reverse transcribed DNA from within provides energy to "explode" the viral core structure. Rupturing the capsid might lead to a partial loss of structural CA elements. This, in turn, most likely lead to an increase in HIV-1 capsid structure flexibility. Would this allow "squeezing" the capsid(-remnant) through the comparably narrow NPC? As described above, only higher resolution imaging of the apparent structure in combination with computational modeling of forces and flexibility would possibly provide the answer to this question. We were lucky to image 2 structures that seem to be just entering the nucleoplasm through NPC. Conclusions to the mode of entry with this resolution and sample size cannot be drawn. Rendering the structure itself against the also electron-dense nuclear envelope is too error-prone.

4.2.7 Comparison to Cytoplasmic RTC

Additional to the nuclear PIC, we also wanted to visualize cytoplasmic structures. Since not only the structure itself, but also the surrounding environment can provide further insght into the HIV-1 structure and trafficking. The main interest thereby lies within the truly productive RTC, recognizable by the presence of viral DNA.

Due to the great loss of fluorescence signals upon sample preparation, the retention of EdU signals, which were very weak to begin with, during sample preparation was highly unlikely. Instead, we tried to click label EdU on embedded sections or to visualize EdU signals retained during EM sample preparation. While this worked well for nuclear EdU signals, it was not successful for mtDNA (see Figure 12 & Figure 13), which we used as a model for viral DNA (to circumvent BSL3 work during protocol establishment). The EdU accessibility upon embedding cells in solid resins was most likely considerably reduced. Nuclear EdU signals were already weak, compared to cells prepared directly for light microscopy.

The Tokuyasu technique is known for high accessibility of antigens and was therefore thought to most likely also yield efficient EdU labeling. In a first experiment, we addressed the ultrastructural

retainability of virus particle cores. While only a subset of cores was clearly recognizable, those retained ones might represent the productively infectious ones.

Efficient EdU click labeling was only possible without GA (see Figure 17). Henceforth, PFA only was used to fix samples before EdU click labeling, reducing the likelihood to retain viral cores.

Labeling extranuclear mtDNA with EdU on Tokuyasu sections was cumbersome and eventually not reproducible. Furthermore, Cu-catalyzed EdU click labeling was incurring considerable damage to the observed ultrastructure, rendering electron micrographs mostly useless (see Figure 21). To limit ultrastructural extraction of sections, we considered embedding into solid resins more promising.

Epon-embedded samples usually yield superb contrast and ultrastructural core preservation. GA plays an important role to retain the capsid structure. Since we experienced before that click labeling does not work efficiently after GA fixation, we first identified the necessary duration for proper EdU click labeling of extranuclear mtDNA. Even though we could prove that cells were stressed by - but survived the toxic Cu-treatment, already short times of labeling strongly reduced the ultrastructure quality in electron micrographs. Since cells were surviving the live labeling, we considered the ultrastructural damage and extraction to be due to the combination of dehydration and resin-embedding. We therefore assessed cryo-CLEM as a possible alternative. Live labeled cells were pelleted and vitrified, followed by cryo-sectioning. Although we could eventually visualize cell sections, we did not retain any fluorescence signal (see Figure 22).

After all, visualizing viral DNA by EdU incorporation and subsequent labeling was not compatible with any of the electron microscopy methods we tried.

We could pinpoint the Cu to negatively influence the ultrastructure. However, Cu can so far not be omitted in this labeling technique. Cu-independent techniques for viral DNA labeling are at the moment developed but are to date not at the stage of application. While direct effects of copper on cells are known (e.g. reactive oxygen species-formation), how exactly the ultrastructure is harmed, remains elusive. Copper can cause DNA fragmentation, which might be more easily extracted during sample preparation. Yet, this study is the first one directly showing the negative influence of Cu-catalyzed click labeling on the ultrastructural preservation of samples.

5 Summary and Outlook

In conclusion, we were able to create a stable U87$^{4/4}$ cell line by lentiviral expression of rCPSF6wt$_{AA}$.mCh, where the expressed fusion protein shows very similar behavior to the wildtype cell line's endogenous CPSF6. rCPSF6wt$_{AA}$.mCh cluster signals can be detected upon HIV-1 infection. We prove these clusters to colocalize with CA, IN.eGFP and viral DNA. Whether these exact nuclear PICs would have led to productive infection cannot be reliably stated. Yet, these structures seem highly relevant, as they have the potential to be productively infectious, judged by the presence of viral DNA, and successfully entered the nucleus.

The observed clusters therefore represent truly infectious subviral particles, or nPIC. On this basis, we were further able to develop a protocol allowing us to retain the cluster signal fluorescence phenotype throughout EM sample preparation. Light - and electron micrographs were successfully correlated, defining the regions of interest within the ultrastructure. By electron tomography, we could gain high resolution electron tomograms, in which core-reminiscent structures were observed. As a reference structure, we imaged intact virus particles bound to the cell surface. Both, viral cores and nPIC structures were modeled by hand and compared. The nPIC structure and the reference are very similar in shape, but quite different in size. What the observed structure is composed of and how it enters the nucleus can only be hypothesized about. The used method in this study does not allow defining the composition or integrity of the apparent PIC structure.

In the future, it will be interesting to shed light onto the pathway of entry and the composition and integrity of the observed structure. The U87$^{4/4}$ rCPSF6wt$_{AA}$.mCh cell line might serve as a good starting point for time-lapse imaging of subviral particles while entering the nucleus. Will there be distinct access points for subviral particles, potentially due to subsets of specialized nuclear pore complexes? Would this explain the clustering of apparent structures in close proximity within the nuclei of infected cells?

Cryo-EM would most likely allow gathering higher resolution images of the observed structures. Applying subtomogram-averaging on such cryo-EM data would then allow pinpointing the molecular nature of the apparent structure. Is it made up of CA protein, or do we observe a structural CPSF6 coat, or some other protein, yet to be defined? Thorsten Müller (Ph.D. student, AG Kräusslich) developed an HIV-1 NL4-3 derivative, capable of reverse transcription, but impaired in integrating proviruses into the host cell genome. This construct is considered BSL1 (also due to a partial *tat* deletion) and could therefore be used in experiments without chemical fixation, which is known to negatively affect the ultrastructural preservation. U87$^{4/4}$ rCPSF6wt$_{AA}$.mCh cells were

infected with the described construct and directly vitrified. It is in progress to perform cryo-CLEM on these samples, i.e. cryo-LM to identify the regions of interest, followed by cryo-ET. With much higher effort, but the circumvention of artifact-introduction by cryo-thin sectioning, we are also assessing to grow, infect and freeze sample cells on grids and use focused ion beam milling to create lamella in cell nuclei. These nuclei lamella would then be fed into the cryo-LM workflow to identify regions of interest within the lamella. Technical advances in cryo-light microscopy may reduce the necessary effort for this tremendously: Sample cells could be imaged before lamella milling and the position of ROI predefined, making the lamella milling not random, but targeted. Cryo-electron tomograms acquired this way would yield much higher resolution of the observed structure. It would allow to define the integrity and organization, and therefore potentially also allow conclusions towards the mode of entry into the nucleus via NPC.

The study at hand is limited to the glioblastoma cell line $U87^{4/4}$, which is widely used in HIV-1 research but yet represents an artificial system. Following up on the acquired data in this study, the next logical step will be to expand these experiments to primary cells, i.e. macrophages, being much more relevant for the HIV-1 biology. We did try to transduce the rCPSF6wt_{AA}.mCh fusion protein into macrophages by adeno-associated virus gene delivery or microinjection, but so far did not succeed in expressing it. To not introduce artificial phenotypes, we omitted the use of lentiviral transduction vectors.

The study at hand employs precisely correlated light - and electron microscopy. We could visualize nuclear PIC structures repeatedly. This opens the question of how this big structure enters the nucleus. We can now be sure that (complete) uncoating does not take place soon after infection, but only after nuclear entry of PIC. The developed method allows to analyze single, infectious particles, and thereby overcomes the limitations of bulk analyses. It will be interesting to see in the future, whether this new insight can be reproduced in more relevant primary cells, and if it lays the foundation for the targeted design of drugs targeting the capsid and influencing its stability.

6 References

Abbe, E. (1873). Beiträge zur Theorie des Mikroskops und der mikroskopischen Wahrnehmung. Arch. Für Mikrosk. Anat. *9*, 413–418.

Adachi, A., Gendelman, H.E., Koenig, S., Folks, T., Willey, R., Rabson, A., and Martin, M.A. (1986). Production of acquired immunodeficiency syndrome-associated retrovirus in human and nonhuman cells transfected with an infectious molecular clone. J. Virol. *59*, 284–291.

Albanese, A., Arosio, D., Terreni, M., and Cereseto, A. (2008). HIV-1 Pre-Integration Complexes Selectively Target Decondensed Chromatin in the Nuclear Periphery. PLOS ONE *3*, e2413.

Arhel, N. (2010). Revisiting HIV-1 uncoating. Retrovirology *7*, 96.

Arhel, N.J., Souquere-Besse, S., Munier, S., Souque, P., Guadagnini, S., Rutherford, S., Prévost, M.-C., Allen, T.D., and Charneau, P. (2007). HIV-1 DNA Flap formation promotes uncoating of the pre-integration complex at the nuclear pore. EMBO J. *26*, 3025–3037.

Balasubramaniam, M., and Freed, E.O. (2011). New Insights into HIV Assembly and Trafficking. Physiology *26*, 236–251.

Barre-Sinoussi, F., Chermann, J., Rey, F., Nugeyre, M., Chamaret, S., Gruest, J., Dauguet, C., Axler-Blin, C., Vezinet-Brun, F., Rouzioux, C., et al. (1983). Isolation of a T-lymphotropic retrovirus from a patient at risk for acquired immune deficiency syndrome (AIDS). Science *220*, 868–871.

Bartonova, V., Igonet, S., Sticht, J., Glass, B., Habermann, A., Vaney, M.-C., Sehr, P., Lewis, J., Rey, F.A., and Kraüsslich, H.-G. (2008). Residues in the HIV-1 Capsid Assembly Inhibitor Binding Site Are Essential for Maintaining the Assembly-competent Quaternary Structure of the Capsid Protein. J. Biol. Chem. *283*, 32024–32033.

Baumeister, W., Grimm, R., and Walz, J. (1999). Electron tomography of molecules and cells. Trends Cell Biol. *9*, 81–85.

Berger, E.A. (1997). HIV entry and tropism: the chemokine receptor connection. AIDS Lond. Engl. *11 Suppl A*, S3-16.

Bhargava, A., Lahaye, X., and Manel, N. (2018). Let me in: Control of HIV nuclear entry at the nuclear envelope. Cytokine Growth Factor Rev. *40*, 59–67.

Bleck, C.K.E., Merz, A., Gutierrez, M.G., Walther, P., Dubochet, J., Zuber, B., and Griffiths, G. (2010). Comparison of different methods for thin section EM analysis of Mycobacterium smegmatis. J. Microsc. *237*, 23–38.

Blumenthal, R., Durell, S., and Viard, M. (2012). HIV Entry and Envelope Glycoprotein-mediated Fusion. J. Biol. Chem. *287*, 40841–40849.

de Boer, P., Hoogenboom, J.P., and Giepmans, B.N.G. (2015). Correlated light and electron microscopy: ultrastructure lights up! Nat. Methods *12*, 503–513.

Bouyac-Bertoia, M., Dvorin, J.D., Fouchier, R.A., Jenkins, Y., Meyer, B.E., Wu, L.I., Emerman, M., and Malim, M.H. (2001). HIV-1 infection requires a functional integrase NLS. Mol. Cell *7*, 1025–1035.

Brass, A.L., Dykxhoorn, D.M., Benita, Y., Yan, N., Engelman, A., Xavier, R.J., Lieberman, J., and Elledge, S.J. (2008). Identification of host proteins required for HIV infection through a functional genomic screen. Science *319*, 921–926.

Briggs, J.A.G. (2003). Structural organization of authentic, mature HIV-1 virions and cores. EMBO J. *22*, 1707–1715.

Briggs, J.A.G., Grünewald, K., Glass, B., Förster, F., Kräusslich, H.-G., and Fuller, S.D. (2006). The Mechanism of HIV-1 Core Assembly: Insights from Three-Dimensional Reconstructions of Authentic Virions. Structure *14*, 15–20.

Brown, T.A., Tkachuk, A.N., Shtengel, G., Kopek, B.G., Bogenhagen, D.F., Hess, H.F., and Clayton, D.A. (2011). Superresolution Fluorescence Imaging of Mitochondrial Nucleoids Reveals Their Spatial Range, Limits, and Membrane Interaction. Mol. Cell. Biol. *31*, 4994–5010.

Brügger, B., Glass, B., Haberkant, P., Leibrecht, I., Wieland, F.T., and Kräusslich, H.-G. (2006). The HIV lipidome: a raft with an unusual composition. Proc. Natl. Acad. Sci. U. S. A. *103*, 2641–2646.

Bryant, M., and Ratner, L. (1990). Myristoylation-dependent replication and assembly of human immunodeficiency virus 1. Proc. Natl. Acad. Sci. U. S. A. *87*, 523–527.

Bui, K.H., von Appen, A., DiGuilio, A.L., Ori, A., Sparks, L., Mackmull, M.-T., Bock, T., Hagen, W., Andrés-Pons, A., Glavy, J.S., et al. (2013). Integrated Structural Analysis of the Human Nuclear Pore Complex Scaffold. Cell *155*, 1233–1243.

Bukrinsky, M.I., Sharova, N., McDonald, T.L., Pushkarskaya, T., Tarpley, W.G., and Stevenson, M. (1993). Association of integrase, matrix, and reverse transcriptase antigens of human immunodeficiency virus type 1 with viral nucleic acids following acute infection. Proc. Natl. Acad. Sci. *90*, 6125–6129.

Buzon, V., Natrajan, G., Schibli, D., Campelo, F., Kozlov, M.M., and Weissenhorn, W. (2010). Crystal structure of HIV-1 gp41 including both fusion peptide and membrane proximal external regions. PLoS Pathog. *6*, e1000880.

Bykov, Y.S., Cortese, M., Briggs, J.A.G., and Bartenschlager, R. (2016). Correlative light and electron microscopy methods for the study of virus-cell interactions. FEBS Lett. *590*, 1877–1895.

Bykov, Y.S., Schaffer, M., Dodonova, S.O., Albert, S., Plitzko, J.M., Baumeister, W., Engel, B.D., and Briggs, J.A. (2017). The structure of the COPI coat determined within the cell. ELife *6*.

REFERENCES

Caffrey, M. (2001). Model for the structure of the HIV gp41 ectodomain: insight into the intermolecular interactions of the gp41 loop. Biochim. Biophys. Acta *1536*, 116–122.

Campbell, E.M., and Hope, T.J. (2015). HIV-1 capsid: the multifaceted key player in HIV-1 infection. Nat. Rev. Microbiol. *13*, 471–483.

Chalfie, M., Tu, Y., Euskirchen, G., Ward, W.W., and Prasher, D.C. (1994). Green fluorescent protein as a marker for gene expression. Science *263*, 802–805.

Chan, D.C., Fass, D., Berger, J.M., and Kim, P.S. (1997). Core structure of gp41 from the HIV envelope glycoprotein. Cell *89*, 263–273.

Chaumont, F. de, Coura, R.D.-S., Serreau, P., Cressant, A., Chabout, J., Granon, S., and Olivo-Marin, J.-C. (2012). Computerized video analysis of social interactions in mice. Nat. Methods *9*, 410–417.

Chen, X., Zaro, J.L., and Shen, W.-C. (2013). Fusion protein linkers: property, design and functionality. Adv. Drug Deliv. Rev. *65*, 1357–1369.

Chertova, E., Bess, J.W., Crise, B.J., Sowder II, R.C., Schaden, T.M., Hilburn, J.M., Hoxie, J.A., Benveniste, R.E., Lifson, J.D., Henderson, L.E., et al. (2002). Envelope glycoprotein incorporation, not shedding of surface envelope glycoprotein (gp120/SU), Is the primary determinant of SU content of purified human immunodeficiency virus type 1 and simian immunodeficiency virus. J. Virol. *76*, 5315–5325.

Coffin, J., Haase, A., Levy, J.A., Montagnier, L., Oroszlan, S., Teich, N., Temin, H., Toyoshima, K., Varmus, H., and Vogt, P. (1986). Human immunodeficiency viruses. Science *232*, 697.

Coffin, J.M., Hughes, S.H., and Varmus, H.E. (1997). Retroviruses (Cold Spring Harbor (NY): Cold Spring Harbor Laboratory Press).

Coons, A.H., Creech, H.J., and Jones, R.N. (1941). Immunological Properties of an Antibody Containing a Fluorescent Group. Exp. Biol. Med. *47*, 200–202.

Daecke, J., Fackler, O.T., Dittmar, M.T., and Kräusslich, H.-G. (2005). Involvement of clathrin-mediated endocytosis in human immunodeficiency virus type 1 entry. J. Virol. *79*, 1581–1594.

Dale, B.M., McNerney, G.P., Thompson, D.L., Hubner, W., de Los Reyes, K., Chuang, F.Y.S., Huser, T., and Chen, B.K. (2011). Cell-to-cell transfer of HIV-1 via virological synapses leads to endosomal virion maturation that activates viral membrane fusion. Cell Host Microbe *10*, 551–562.

Day, R.N., and Davidson, M.W. (2009). The fluorescent protein palette: tools for cellular imaging. Chem. Soc. Rev. *38*, 2887–2921.

De Iaco, A., Santoni, F., Vannier, A., Guipponi, M., Antonarakis, S., and Luban, J. (2013). TNPO3 protects HIV-1 replication from CPSF6-mediated capsid stabilization in the host cell cytoplasm. Retrovirology *10*, 20.

REFERENCES

De Leys, R., Vanderborght, B., Vanden Haesevelde, M., Heyndrickx, L., van Geel, A., Wauters, C., Bernaerts, R., Saman, E., Nijs, P., and Willems, B. (1990). Isolation and partial characterization of an unusual human immunodeficiency retrovirus from two persons of west-central African origin. J. Virol. *64*, 1207–1216.

Debyser, Z., Christ, F., De Rijck, J., and Gijsbers, R. (2015). Host factors for retroviral integration site selection. Trends Biochem. Sci. *40*, 108–116.

Di Nunzio, F. (2013). New insights in the role of nucleoporins: A bridge leading to concerted steps from HIV-1 nuclear entry until integration. Virus Res. *178*, 187–196.

Di Nunzio, F., Danckaert, A., Fricke, T., Perez, P., Fernandez, J., Perret, E., Roux, P., Shorte, S., Charneau, P., Diaz-Griffero, F., et al. (2012). Human Nucleoporins Promote HIV-1 Docking at the Nuclear Pore, Nuclear Import and Integration. PLOS ONE *7*, e46037.

Ding, X., Zhang, X., Chong, H., Zhu, Y., Wei, H., Wu, X., He, J., Wang, X., and He, Y. (2017). Enfuvirtide (T20)-Based Lipopeptide Is a Potent HIV-1 Cell Fusion Inhibitor: Implications for Viral Entry and Inhibition. J. Virol. *91*.

Doms, R.W., and Moore, J.P. (2000). HIV-1 Membrane Fusion. J. Cell Biol. *151*, f9–f14.

Eckhardt, M. (2010). Quantitative analysis of the early steps of virus host cell interaction of human immunodeficiency virus type 1 and hepatitis C virus.

Eckhardt, M., Anders, M., Muranyi, W., Heilemann, M., Krijnse-Locker, J., and Müller, B. (2011). A SNAP-Tagged Derivative of HIV-1—A Versatile Tool to Study Virus-Cell Interactions. PLoS ONE *6*, e22007.

Ekouevi, D.K., Balestre, E., Coffie, P.A., Minta, D., Messou, E., Sawadogo, A., Minga, A., Sow, P.S., Bissagnene, E., Eholie, S.P., et al. (2013). Characteristics of HIV-2 and HIV-1/HIV-2 Dually Seropositive Adults in West Africa Presenting for Care and Antiretroviral Therapy: The IeDEA-West Africa HIV-2 Cohort Study. PLOS ONE *8*, e66135.

Emerman, M., Bukrinsky, M., and Stevenson, M. (1994). HIV-1 infection of non-dividing cells. Nature *369*, 108.

Fassati, A. (2012). Multiple roles of the capsid protein in the early steps of HIV-1 infection. Virus Res. *170*, 15–24.

Felli, C., Vincentini, O., Silano, M., and Masotti, A. (2017). HIV-1 Nef Signaling in Intestinal Mucosa Epithelium Suggests the Existence of an Active Inter-kingdom Crosstalk Mediated by Exosomes. Front. Microbiol. *8*.

Felts, R.L., Narayan, K., Estes, J.D., Shi, D., Trubey, C.M., Fu, J., Hartnell, L.M., Ruthel, G.T., Schneider, D.K., Nagashima, K., et al. (2010). 3D visualization of HIV transfer at the virological synapse between dendritic cells and T cells. Proc. Natl. Acad. Sci. *107*, 13336–13341.

Forshey, B.M., von Schwedler, U., Sundquist, W.I., and Aiken, C. (2002). Formation of a Human Immunodeficiency Virus Type 1 Core of Optimal Stability Is Crucial for Viral Replication. J. Virol. *76*, 5667–5677.

Francis, A.C., Marin, M., Shi, J., Aiken, C., and Melikyan, G.B. (2016). Time-Resolved Imaging of Single HIV-1 Uncoating In Vitro and in Living Cells. PLOS Pathog. *12*, e1005709.

Freed, E.O. (2015). HIV-1 assembly, release and maturation. Nat. Rev. Microbiol. *13*, 484–496.

Frey, S., Marsh, M., Günther, S., Pelchen-Matthews, A., Stephens, P., Ortlepp, S., and Stegmann, T. (1995). Temperature dependence of cell-cell fusion induced by the envelope glycoprotein of human immunodeficiency virus type 1. J. Virol. *69*, 1462–1472.

Fuller, S.D., Wilk, T., Gowen, B.E., Kräusslich, H.G., and Vogt, V.M. (1997). Cryo-electron microscopy reveals ordered domains in the immature HIV-1 particle. Curr. Biol. CB *7*, 729–738.

Gaetke, L.M., Chow-Johnson, H.S., and Chow, C.K. (2014). Copper: toxicological relevance and mechanisms. Arch. Toxicol. *88*, 1929–1938.

Gallay, P., Hope, T., Chin, D., and Trono, D. (1997). HIV-1 infection of nondividing cells through the recognition of integrase by the importin/karyopherin pathway. Proc. Natl. Acad. Sci. *94*, 9825–9830.

Ganser, B.K., Li, S., Klishko, V.Y., Finch, J.T., and Sundquist, W.I. (1999). Assembly and analysis of conical models for the HIV-1 core. Science *283*, 80–83.

Gao, F., Bailes, E., Robertson, D.L., Chen, Y., Rodenburg, C.M., Michael, S.F., Cummins, L.B., Arthur, L.O., Peeters, M., Shaw, G.M., et al. (1999). Pan troglodytes troglodytes. *397*, 6.

Gaudin, R., Alencar, B.C. de, Arhel, N., and Benaroch, P. (2013). HIV trafficking in host cells: motors wanted! Trends Cell Biol. *23*, 652–662.

Gottlieb, M.S., Schroff, R., Schanker, H.M., Weisman, J.D., Fan, P.T., Wolf, R.A., and Saxon, A. (1981). Pneumocystis carinii pneumonia and mucosal candidiasis in previously healthy homosexual men: evidence of a new acquired cellular immunodeficiency. N. Engl. J. Med. *305*, 1425–1431.

Griffiths, G., Slot, J.-W., and Webster, P. (2015). Kiyoteru Tokuyasu: a pioneer of cryo-ultramicrotomy. J. Microsc. *260*, 235–237.

Grimm, D., Lee, J.S., Wang, L., Desai, T., Akache, B., Storm, T.A., and Kay, M.A. (2008). In Vitro and In Vivo Gene Therapy Vector Evolution via Multispecies Interbreeding and Retargeting of Adeno-Associated Viruses. J. Virol. *82*, 5887–5911.

Grosse, S., Penaud-Budloo, M., Herrmann, A.-K., Börner, K., Fakhiri, J., Laketa, V., Krämer, C., Wiedtke, E., Gunkel, M., Ménard, L., et al. (2017). Relevance of Assembly-Activating Protein for Adeno-associated Virus Vector Production and Capsid Protein Stability in Mammalian and Insect Cells. J. Virol. *91*.

Grotjohann, T., Testa, I., Reuss, M., Brakemann, T., Eggeling, C., Hell, S.W., and Jakobs, S. (2012). rsEGFP2 enables fast RESOLFT nanoscopy of living cells. ELife *1*.

Gürtler, L.G., Hauser, P.H., Eberle, J., von Brunn, A., Knapp, S., Zekeng, L., Tsague, J.M., and Kaptue, L. (1994). A new subtype of human immunodeficiency virus type 1 (MVP-5180) from Cameroon. J. Virol. *68*, 1581–1585.

Hall, D.H. (1995). Chapter 17 Electron Microscopy and Three-Dimensional Image Reconstruction. In Methods in Cell Biology, (Elsevier), pp. 395–436.

Hanne, J., Göttfert, F., Schimer, J., Anders-Össwein, M., Konvalinka, J., Engelhardt, J., Müller, B., Hell, S.W., and Kräusslich, H.-G. (2016a). Stimulated Emission Depletion Nanoscopy Reveals Time-Course of Human Immunodeficiency Virus Proteolytic Maturation. ACS Nano *10*, 8215–8222.

Hanne, J., Zila, V., Heilemann, M., Müller, B., and Kräusslich, H.-G. (2016b). Super-resolved insights into human immunodeficiency virus biology. FEBS Lett. *590*, 1858–1876.

Harada, S., Koyanagi, Y., and Yamamoto, N. (1985). Infection of HTLV-III/LAV in HTLV-I-carrying cells MT-2 and MT-4 and application in a plaque assay. Science *229*, 563–566.

Hare, S., Gupta, S.S., Valkov, E., Engelman, A., and Cherepanov, P. (2010). Retroviral intasome assembly and inhibition of DNA strand transfer. Nature *464*, 232–236.

Hartwig, J.H., and Yin, H.L. (1988). The organization and regulation of the macrophage actin skeleton. Cell Motil. Cytoskeleton *10*, 117–125.

Herold, N., Anders-Osswein, M., Glass, B., Eckhardt, M., Muller, B., and Krausslich, H.-G. (2014). HIV-1 Entry in SupT1-R5, CEM-ss, and Primary CD4+ T Cells Occurs at the Plasma Membrane and Does Not Require Endocytosis. J. Virol. *88*, 13956–13970.

Hori, T., Takeuchi, H., Saito, H., Sakuma, R., Inagaki, Y., and Yamaoka, S. (2013). A Carboxy-Terminally Truncated Human CPSF6 Lacking Residues Encoded by Exon 6 Inhibits HIV-1 cDNA Synthesis and Promotes Capsid Disassembly. J. Virol. *87*, 7726–7736.

Hu, W., and Temin, H. (1990). Retroviral recombination and reverse transcription. Science *250*, 1227–1233.

Huang, C., Tang, M., Zhang, M.-Y., Majeed, S., Montabana, E., Stanfield, R.L., Dimitrov, D.S., Korber, B., Sodroski, J., Wilson, I.A., et al. (2005). Structure of a V3-containing HIV-1 gp120 core. Science *310*, 1025–1028.

Hulme, A.E., Perez, O., and Hope, T.J. (2011). Complementary assays reveal a relationship between HIV-1 uncoating and reverse transcription. Proc. Natl. Acad. Sci. *108*, 9975–9980.

Hulme, A.E., Kelley, Z., Okocha, E.A., and Hope, T.J. (2015). Identification of Capsid Mutations That Alter the Rate of HIV-1 Uncoating in Infected Cells. J. Virol. *89*, 643–651.

Hung, M., Patel, P., Davis, S., and Green, S.R. (1998). Importance of ribosomal frameshifting for human immunodeficiency virus type 1 particle assembly and replication. J. Virol. *72*, 4819–4824.

Inoue, H., Nojima, H., and Okayama, H. (1990). High efficiency transformation of Escherichia coli with plasmids. Gene *96*, 23–28.

Jacks, T., Power, M.D., Masiarz, F.R., Luciw, P.A., Barr, P.J., and Varmus, H.E. (1988). Characterization of ribosomal frameshifting in HIV-1 gag-pol expression. Nature *331*, 280–283.

Jin, M.J., Rogers, J., Phillips-Conroy, J.E., Allan, J.S., Desrosiers, R.C., Shaw, G.M., Sharp, P.M., and Hahn, B.H. (1994). Infection of a yellow baboon with simian immunodeficiency virus from African green monkeys: evidence for cross-species transmission in the wild. J. Virol. *68*, 8454–8460.

Jun, S., Ke, D., Debiec, K., Zhao, G., Meng, X., Ambrose, Z., Gibson, G.A., Watkins, S.C., and Zhang, P. (2011). Direct Visualization of HIV-1 with Correlative Live-Cell Microscopy and Cryo-Electron Tomography. Structure *19*, 1573–1581.

Kabachinski, G., and Schwartz, T.U. (2015). The nuclear pore complex - structure and function at a glance. J. Cell Sci. *128*, 423–429.

Kane, M., Rebensburg, S.V., Takata, M.A., Zang, T.M., Yamashita, M., Kvaratskhelia, M., and Bieniasz, P.D. (2018). Nuclear pore heterogeneity influences HIV-1 infection and the antiviral activity of MX2. ELife *7*.

Kann, M., Sodeik, B., Vlachou, A., Gerlich, W.H., and Helenius, A. (1999). Phosphorylation-dependent Binding of Hepatitis B Virus Core Particles to the Nuclear Pore Complex. J. Cell Biol. *145*, 45–55.

Karageorgos, L., Li, P., and Burrell, C. (1993). Characterization of HIV Replication Complexes Early after Cell-to-Cell Infection. AIDS Res. Hum. Retroviruses *9*, 817–823.

Keele, B.F. (2006). Chimpanzee Reservoirs of Pandemic and Nonpandemic HIV-1. Science *313*, 523–526.

Khattab, A.D.S. (1995). Dances with microscopes: antoni van leeuwenhoek (1632–1723). Cytopathology *6*, 215–218.

Kiernan, R.E., Ono, A., and Freed, E.O. (1999). Reversion of a Human Immunodeficiency Virus Type 1 Matrix Mutation Affecting Gag Membrane Binding, Endogenous Reverse Transcriptase Activity, and Virus Infectivity. J. Virol. *73*, 4728–4737.

Klymchenko, A.S., and Kreder, R. (2014). Fluorescent probes for lipid rafts: from model membranes to living cells. Chem. Biol. *21*, 97–113.

Knockenhauer, K.E., and Schwartz, T.U. (2016). The Nuclear Pore Complex as a Flexible and Dynamic Gate. Cell *164*, 1162–1171.

Knoll, M., and Ruska, E. (1932). Das Elektronenmikroskop. Z. Für Phys. *78*, 318–339.

Koistinen, K., Blancett, C., and Sun, M. (2016). A Review of Correlative Light and Electron Microscopy (CLEM) Methods, Markers, and Instrument Set Ups to Study Infectious Disease. 14.

König, R., Zhou, Y., Elleder, D., Diamond, T.L., Bonamy, G.M.C., Irelan, J.T., Chiang, C., Tu, B.P., De Jesus, P.D., Lilley, C.E., et al. (2008). Global Analysis of Host-Pathogen Interactions that Regulate Early-Stage HIV-1 Replication. Cell *135*, 49–60.

Korber, B., Muldoon, M., Theiler, J., Gao, F., Gupta, R., Lapedes, A., Hahn, B.H., Wolinsky, S., and Bhattacharya, T. (2000). Timing the ancestor of the HIV-1 pandemic strains. Science *288*, 1789–1796.

Kremer, J.R., Mastronarde, D.N., and McIntosh, J.R. (1996). Computer visualization of three-dimensional image data using IMOD. J. Struct. Biol. *116*, 71–76.

Krishnan, L., Li, X., Naraharisetty, H.L., Hare, S., Cherepanov, P., and Engelman, A. (2010). Structure-based modeling of the functional HIV-1 intasome and its inhibition. Proc. Natl. Acad. Sci. *107*, 15910–15915.

Kruger, D.H., Schneck, P., and Gelderblom, H.R. (2000). Helmut Ruska and the visualisation of viruses. The Lancet *355*, 1713–1717.

Kuhn, J.H., and Jahrling, P.B. (2010). Clarification and guidance on the proper usage of virus and virus species names. Arch. Virol. *155*, 445–453.

Kuhn, J.H., Radoshitzky, S.R., Bavari, S., and Jahrling, P.B. (2013). The International Code of Virus Classification and Nomenclature (ICVCN): proposal for text changes for improved differentiation of viral taxa and viruses. Arch. Virol. *158*, 1621–1629.

Kukulski, W., Schorb, M., Welsch, S., Picco, A., Kaksonen, M., and Briggs, J.A.G. (2011). Correlated fluorescence and 3D electron microscopy with high sensitivity and spatial precision. J. Cell Biol. *192*, 111–119.

Kukulski, W., Schorb, M., Welsch, S., Picco, A., Kaksonen, M., and Briggs, J.A.G. (2012). Precise, Correlated Fluorescence Microscopy and Electron Tomography of Lowicryl Sections Using Fluorescent Fiducial Markers. In Methods in Cell Biology, (Elsevier), pp. 235–257.

Lahaye, X., Satoh, T., Gentili, M., Cerboni, S., Conrad, C., Hurbain, I., El Marjou, A., Lacabaratz, C., Lelièvre, J.-D., and Manel, N. (2013). The Capsids of HIV-1 and HIV-2 Determine Immune Detection of the Viral cDNA by the Innate Sensor cGAS in Dendritic Cells. Immunity *39*, 1132–1142.

Lampe, M., Briggs, J.A.G., Endress, T., Glass, B., Riegelsberger, S., Kräusslich, H.-G., Lamb, D.C., Bräuchle, C., and Müller, B. (2007). Double-labelled HIV-1 particles for study of virus-cell interaction. Virology *360*, 92–104.

REFERENCES

Lee, K., Ambrose, Z., Martin, T.D., Oztop, I., Mulky, A., Julias, J.G., Vandegraaff, N., Baumann, J.G., Wang, R., Yuen, W., et al. (2010). Flexible Use of Nuclear Import Pathways by HIV-1. Cell Host Microbe *7*, 221–233.

Lemey, P., Pybus, O.G., Rambaut, A., Drummond, A.J., Robertson, D.L., Roques, P., Worobey, M., and Vandamme, A.-M. (2004). The molecular population genetics of HIV-1 group O. Genetics *167*, 1059–1068.

Liu, J., Bartesaghi, A., Borgnia, M.J., Sapiro, G., and Subramaniam, S. (2008). Molecular architecture of native HIV-1 gp120 trimers. Nature *455*, 109–113.

Logue, E.C., Taylor, K.T., Goff, P.H., and Landau, N.R. (2011). The Cargo-Binding Domain of Transportin 3 Is Required for Lentivirus Nuclear Import. J. Virol. *85*, 12950–12961.

van Lookeren Campagne, M., Oestreicher, A.B., van der Krift, T.P., Gispen, W.H., and Verkleij, A.J. (1991). Freeze-substitution and Lowicryl HM20 embedding of fixed rat brain: suitability for immunogold ultrastructural localization of neural antigens. J. Histochem. Cytochem. Off. J. Histochem. Soc. *39*, 1267–1279.

Lu, Z., Berson, J.F., Chen, Y., Turner, J.D., Zhang, T., Sharron, M., Jenks, M.H., Wang, Z., Kim, J., Rucker, J., et al. (1997). Evolution of HIV-1 coreceptor usage through interactions with distinct CCR5 and CXCR4 domains. Proc. Natl. Acad. Sci. U. S. A. *94*, 6426–6431.

Lusic, M., and Siliciano, R.F. (2017). Nuclear landscape of HIV-1 infection and integration. Nat. Rev. Microbiol. *15*, 69–82.

Maelfait, J., Seiradake, E., and Rehwinkel, J. (2014). Keeping your armour intact: How HIV-1 evades detection by the innate immune system: HIV-1 capsid controls detection of reverse transcription products by the cytosolic DNA sensor cGAS. BioEssays *36*, 649–657.

Maertens, G.N., Hare, S., and Cherepanov, P. (2010). The mechanism of retroviral integration from X-ray structures of its key intermediates. Nature *468*, 326–329.

Mamede, J.I., and Hope, T.J. (2016). Detection and tracking of dual-labeled HIV particles using wide-field live cell imaging to follow viral core integrity. Methods Mol. Biol. Clifton NJ *1354*, 49–59.

Marozsan, A.J., Fraundorf, E., Abraha, A., Baird, H., Moore, D., Troyer, R., Nankja, I., and Arts, E.J. (2004). Relationships between Infectious Titer, Capsid Protein Levels, and Reverse Transcriptase Activities of Diverse Human Immunodeficiency Virus Type 1 Isolates. J. Virol. *78*, 11130–11141.

Mastronarde, D.N. (2005). Automated electron microscope tomography using robust prediction of specimen movements. J. Struct. Biol. *152*, 36–51.

REFERENCES

Matreyek, K., and Engelman, A. (2013). Viral and Cellular Requirements for the Nuclear Entry of Retroviral Preintegration Nucleoprotein Complexes. Viruses *5*, 2483–2511.

Matreyek, K.A., Yücel, S.S., Li, X., and Engelman, A. (2013). Nucleoporin NUP153 Phenylalanine-Glycine Motifs Engage a Common Binding Pocket within the HIV-1 Capsid Protein to Mediate Lentiviral Infectivity. PLoS Pathog. *9*, e1003693.

Matsushita, T., Elliger, S., Elliger, C., Podsakoff, G., Villarreal, L., Kurtzman, G.J., Iwaki, Y., and Colosi, P. (1998). Adeno-associated virus vectors can be efficiently produced without helper virus. Gene Ther. *5*, 938–945.

Mattei, S., Glass, B., Hagen, W.J.H., Kräusslich, H.-G., and Briggs, J.A.G. (2016). The structure and flexibility of conical HIV-1 capsids determined within intact virions. Science *354*, 1434–1437.

McDonald, K.L. (2009). A review of high-pressure freezing preparation techniques for correlative light and electron microscopy of the same cells and tissues. J. Microsc. *235*, 273–281.

McDonald, D., Vodicka, M.A., Lucero, G., Svitkina, T.M., Borisy, G.G., Emerman, M., and Hope, T.J. (2002). Visualization of the intracellular behavior of HIV in living cells. J. Cell Biol. *159*, 441–452.

McDonald, K.L., Sharp, D.J., and Rickoll, W. (2012). Postembedding Immunolabeling of Thin Sections of Drosophila Tissues for Transmission Electron Microscopy. Cold Spring Harb. Protoc. *2012*, pdb.prot068437.

McNicholl, J.M., Smith, D.K., Qari, S.H., and Hodge, T. (1997). Host genes and HIV: the role of the chemokine receptor gene CCR5 and its allele. Emerg. Infect. Dis. *3*, 261–271.

Miller, M.D., Farnet, C.M., and Bushman, F.D. (1997). Human immunodeficiency virus type 1 preintegration complexes: studies of organization and composition. J. Virol. *71*, 5382–5390.

Miyauchi, K., Kim, Y., Latinovic, O., Morozov, V., and Melikyan, G.B. (2009). HIV enters cells via endocytosis and dynamin-dependent fusion with endosomes. Cell *137*, 433–444.

Miyawaki, A. (2011). Proteins on the move: insights gained from fluorescent protein technologies. Nat. Rev. Mol. Cell Biol. *12*, 656–668.

Ning, J., Zhong, Z., Fischer, D.K., Harris, G., Watkins, S.C., Ambrose, Z., and Zhang, P. (2018). Truncated CPSF6 Forms Higher-Order Complexes That Bind and Disrupt HIV-1 Capsid. J. Virol. *92*.

Paillart, J.-C., and Göttlinger, H.G. (1999). Opposing Effects of Human Immunodeficiency Virus Type 1 Matrix Mutations Support a Myristyl Switch Model of Gag Membrane Targeting. J. Virol. *73*, 2604–2612.

Paine, P.L., Moore, L.C., and Horowitz, S.B. (1975). Nuclear envelope permeability. Nature *254*, 109–114.

Painter, R.G., Tokuyasu, K.T., and Singer, S.J. (1973). Immunoferritin Localization of Intracellular Antigens: The Use of Ultracryotomy to Obtain Ultrathin Sections Suitable for Direct Immunoferritin Staining. Proc. Natl. Acad. Sci. U. S. A. *70*, 1649–1653.

Panté, N., and Kann, M. (2002). Nuclear Pore Complex Is Able to Transport Macromolecules with Diameters of ~39 nm. Mol. Biol. Cell *13*, 425–434.

Paul-Gilloteaux, P., Heiligenstein, X., Belle, M., Domart, M.-C., Larijani, B., Collinson, L., Raposo, G., and Salamero, J. (2017). eC-CLEM: flexible multidimensional registration software for correlative microscopies. Nat. Methods *14*, 102–103.

Peeters, M., Gueye, A., Mboup, S., Bibollet-Ruche, F., Ekaza, E., Mulanga, C., Ouedrago, R., Gandji, R., Mpele, P., Dibanga, G., et al. (1997). Geographical distribution of HIV-1 group O viruses in Africa. AIDS Lond. Engl. *11*, 493–498.

Peng, K., Muranyi, W., Glass, B., Laketa, V., Yant, S.R., Tsai, L., Cihlar, T., Müller, B., and Kräusslich, H.-G. (2014). Quantitative microscopy of functional HIV post-entry complexes reveals association of replication with the viral capsid. ELife *3*.

Perilla, J.R., and Schulten, K. (2017). Physical properties of the HIV-1 capsid from all-atom molecular dynamics simulations. Nat. Commun. *8*, 15959.

Petropoulos, C. (1997). Retroviral Taxonomy, Protein Structures, Sequences, and Genetic Maps (Cold Spring Harbor Laboratory Press).

Pieribone, V., and Gruber, D.F. (2005). Aglow in the Dark: The Revolutionary Science of Biofluorescence (Harvard University Press).

Plantier, J.-C., Leoz, M., Dickerson, J.E., De Oliveira, F., Cordonnier, F., Lemée, V., Damond, F., Robertson, D.L., and Simon, F. (2009). A new human immunodeficiency virus derived from gorillas. Nat. Med. *15*, 871–872.

Pornillos, O., Ganser-Pornillos, B.K., and Yeager, M. (2011). Atomic-level modelling of the HIV capsid. Nature *469*, 424–427.

Prasher, D.C., Eckenrode, V.K., Ward, W.W., Prendergast, F.G., and Cormier, M.J. (1992). Primary structure of the Aequorea victoria green-fluorescent protein. Gene *111*, 229–233.

Price, A.J., Jacques, D.A., McEwan, W.A., Fletcher, A.J., Essig, S., Chin, J.W., Halambage, U.D., Aiken, C., and James, L.C. (2014). Host Cofactors and Pharmacologic Ligands Share an Essential Interface in HIV-1 Capsid That Is Lost upon Disassembly. PLOS Pathog. *10*, e1004459.

Rankovic, S., Varadarajan, J., Ramalho, R., Aiken, C., and Rousso, I. (2017). Reverse Transcription Mechanically Initiates HIV-1 Capsid Disassembly. J. Virol. *91*.

Reynolds, E.S. (1963). The use of lead citrate at high pH as an electron-opaque stain in electron microscopy. J. Cell Biol. *17*, 208–212.

Rijnsoever, C. van, Oorschot, V., and Klumperman, J. (2008). Correlative light-electron microscopy (CLEM) combining live-cell imaging and immunolabeling of ultrathin cryosections. Nat. Methods *5*, 973–980.

Riquelme, P., and Hutchinson, J.A. (2018). Standard Protocols for Generation of Monocyte-derived Cell Types.

Sahl, S.J., Hell, S.W., and Jakobs, S. (2017). Fluorescence nanoscopy in cell biology. Nat. Rev. Mol. Cell Biol. *18*, 685–701.

Sakin, V., Paci, G., Lemke, E.A., and Müller, B. (2016). Labeling of virus components for advanced, quantitative imaging analyses. FEBS Lett. *590*, 1896–1914.

Salbreux, G., Charras, G., and Paluch, E. (2012). Actin cortex mechanics and cellular morphogenesis. Trends Cell Biol. *22*, 536–545.

Salic, A., and Mitchison, T.J. (2008). A chemical method for fast and sensitive detection of DNA synthesis in vivo. Proc. Natl. Acad. Sci. *105*, 2415–2420.

Santos, C.D.S., Tartour, K., and Cimarelli, A. (2016). A Novel Entry/Uncoating Assay Reveals the Presence of at Least Two Species of Viral Capsids During Synchronized HIV-1 Infection. PLOS Pathog. *12*, e1005897.

Schorb, M., Gaechter, L., Avinoam, O., Sieckmann, F., Clarke, M., Bebeacua, C., Bykov, Y.S., Sonnen, A.F.-P., Lihl, R., and Briggs, J.A.G. (2017). New hardware and workflows for semi-automated correlative cryo-fluorescence and cryo-electron microscopy/tomography. J. Struct. Biol. *197*, 83–93.

Schur, F.K.M., Obr, M., Hagen, W.J.H., Wan, W., Jakobi, A.J., Kirkpatrick, J.M., Sachse, C., Kräusslich, H.-G., and Briggs, J.A.G. (2016). An atomic model of HIV-1 capsid-SP1 reveals structures regulating assembly and maturation. Science *353*, 506–508.

Sena-Esteves, M., Saeki, Y., Camp, S.M., Chiocca, E.A., and Breakefield, X.O. (1999). Single-step conversion of cells to retrovirus vector producers with herpes simplex virus-Epstein-Barr virus hybrid amplicons. J. Virol. *73*, 10426–10439.

Sharp, P.M., and Hahn, B.H. (2011). Origins of HIV and the AIDS Pandemic. Cold Spring Harb. Perspect. Med. *1*, a006841–a006841.

Shimomura, O., Johnson, F.H., and Saiga, Y. (1962). Extraction, Purification and Properties of Aequorin, a Bioluminescent Protein from the Luminous Hydromedusan,Aequorea. J. Cell. Comp. Physiol. *59*, 223–239.

Simon, F., Mauclère, P., Roques, P., Loussert-Ajaka, I., Müller-Trutwin, M.C., Saragosti, S., Georges-Courbot, M.C., Barré-Sinoussi, F., and Brun-Vézinet, F. (1998). Identification of a new

human immunodeficiency virus type 1 distinct from group M and group O. Nat. Med. *4*, 1032–1037.

Singh, P.K., Plumb, M.R., Ferris, A.L., Iben, J.R., Wu, X., Fadel, H.J., Luke, B.T., Esnault, C., Poeschla, E.M., Hughes, S.H., et al. (2015). LEDGF/p75 interacts with mRNA splicing factors and targets HIV-1 integration to highly spliced genes. Genes Dev. *29*, 2287–2297.

Sirven, A., Pflumio, F., Zennou, V., Titeux, M., Vainchenker, W., Coulombel, L., Dubart-Kupperschmitt, A., and Charneau, P. (2000). The human immunodeficiency virus type-1 central DNA flap is a crucial determinant for lentiviral vector nuclear import and gene transduction of human hematopoietic stem cells. Blood *96*, 4103–4110.

Slot, J.W., and Geuze, H.J. (2007). Cryosectioning and immunolabeling. Nat. Protoc. *2*, 2480–2491.

Sommer, C., Straehle, C., Köthe, U., and Hamprecht, F.A. (2011). Ilastik: Interactive learning and segmentation toolkit. In 2011 IEEE International Symposium on Biomedical Imaging: From Nano to Macro, pp. 230–233.

Sowd, G.A., Serrao, E., Wang, H., Wang, W., Fadel, H.J., Poeschla, E.M., and Engelman, A.N. (2016). A critical role for alternative polyadenylation factor CPSF6 in targeting HIV-1 integration to transcriptionally active chromatin. Proc. Natl. Acad. Sci. *113*, E1054–E1063.

Spear, M., Guo, J., and Wu, Y. (2012). The trinity of the cortical actin in the initiation of HIV-1 infection. Retrovirology *9*, 45.

Sundquist, W.I., and Kräusslich, H.-G. (2012). HIV-1 assembly, budding, and maturation. Cold Spring Harb. Perspect. Med. *2*, a006924.

Suzuki, Y., and Craigie, R. (2007). The road to chromatin — nuclear entry of retroviruses. Nat. Rev. Microbiol. *5*, 187–196.

Swanstrom, R., and Coffin, J. (2012). HIV-1 pathogenesis: the virus. Cold Spring Harb. Perspect. Med. *2*, a007443.

Sydor, A.M., Czymmek, K.J., Puchner, E.M., and Mennella, V. (2015). Super-Resolution Microscopy: From Single Molecules to Supramolecular Assemblies. Trends Cell Biol. *25*, 730–748.

Taanman, J.W. (1999). The mitochondrial genome: structure, transcription, translation and replication. Biochim. Biophys. Acta *1410*, 103–123.

Thomas, J.A., Ott, D.E., and Gorelick, R.J. (2007). Efficiency of Human Immunodeficiency Virus Type 1 Postentry Infection Processes: Evidence against Disproportionate Numbers of Defective Virions. J. Virol. *81*, 4367–4370.

Tokuyasu, K.T. (1973). A technique for ultracryotomy of cell suspensions and tissues. J. Cell Biol. *57*, 551–565.

Trichas, G., Begbie, J., and Srinivas, S. (2008). Use of the viral 2A peptide for bicistronic expression in transgenic mice. BMC Biol. *6*, 40.

Trkola, A., Dragic, T., Arthos, J., Binley, J.M., Olson, W.C., Allaway, G.P., Cheng-Mayer, C., Robinson, J., Maddon, P.J., and Moore, J.P. (1996). CD4-dependent, antibody-sensitive interactions between HIV-1 and its co-receptor CCR-5. Nature *384*, 184–187.

Valle-Casuso, J.C., Di Nunzio, F., Yang, Y., Reszka, N., Lienlaf, M., Arhel, N., Perez, P., Brass, A.L., and Diaz-Griffero, F. (2012). TNPO3 Is Required for HIV-1 Replication after Nuclear Import but prior to Integration and Binds the HIV-1 Core. J. Virol. *86*, 5931–5936.

Vicidomini, G., Bianchini, P., and Diaspro, A. (2018). STED super-resolved microscopy. Nat. Methods *15*, 173–182.

Vink, C., Groenink, M., Elgersma, Y., Fouchier, R.A., Tersmette, M., and Plasterk, R.H. (1990). Analysis of the junctions between human immunodeficiency virus type 1 proviral DNA and human DNA. J. Virol. *64*, 5626–5627.

Vogt, P.K. (1997). Historical Introduction to the General Properties of Retroviruses. In Retroviruses, J.M. Coffin, S.H. Hughes, and H.E. Varmus, eds. (Cold Spring Harbor (NY): Cold Spring Harbor Laboratory Press), p.

Vorster, P.J., Guo, J., Yoder, A., Wang, W., Zheng, Y., Xu, X., Yu, D., Spear, M., and Wu, Y. (2011). LIM Kinase 1 Modulates Cortical Actin and CXCR4 Cycling and Is Activated by HIV-1 to Initiate Viral Infection. J. Biol. Chem. *286*, 12554–12564.

Wei, X., Decker, J.M., Liu, H., Zhang, Z., Arani, R.B., Kilby, J.M., Saag, M.S., Wu, X., Shaw, G.M., and Kappes, J.C. (2002). Emergence of resistant human immunodeficiency virus type 1 in patients receiving fusion inhibitor (T-20) monotherapy. Antimicrob. Agents Chemother. *46*, 1896–1905.

Weigel, P.H., and Oka, J.A. (1981). Temperature dependence of endocytosis mediated by the asialoglycoprotein receptor in isolated rat hepatocytes. Evidence for two potentially rate-limiting steps. J. Biol. Chem. *256*, 2615–2617.

Weissenhorn, W., Dessen, A., Harrison, S.C., Skehel, J.J., and Wiley, D.C. (1997). Atomic structure of the ectodomain from HIV-1 gp41. Nature *387*, 426–430.

Whittaker, G.R. (2003). Virus nuclear import. Adv. Drug Deliv. Rev. *55*, 733–747.

Wilen, C.B., Tilton, J.C., and Doms, R.W. (2012). HIV: Cell Binding and Entry. Cold Spring Harb. Perspect. Med. *2*, a006866–a006866.

Wilk, T., Gross, I., Gowen, B.E., Rutten, T., Haas, F. de, Welker, R., Kräusslich, H.-G., Boulanger, P., and Fuller, S.D. (2001). Organization of Immature Human Immunodeficiency Virus Type 1. J. Virol. *75*, 759–771.

REFERENCES

Woodward, C.L., Prakobwanakit, S., Mosessian, S., and Chow, S.A. (2009). Integrase interacts with nucleoporin NUP153 to mediate the nuclear import of human immunodeficiency virus type 1. J. Virol. *83*, 6522–6533.

Worobey, M., Gemmel, M., Teuwen, D.E., Haselkorn, T., Kunstman, K., Bunce, M., Muyembe, J.-J., Kabongo, J.-M.M., Kalengayi, R.M., Van Marck, E., et al. (2008). Direct evidence of extensive diversity of HIV-1 in Kinshasa by 1960. Nature *455*, 661–664.

Yamashita, M., and Emerman, M. (2004). Capsid Is a Dominant Determinant of Retrovirus Infectivity in Nondividing Cells. J. Virol. *78*, 5670–5678.

Yang, Y., Luban, J., and Diaz-Griffero, F. (2014). The fate of HIV-1 capsid: a biochemical assay for HIV-1 uncoating. Methods Mol. Biol. Clifton NJ *1087*, 29–36.

Yoder, A., Yu, D., Dong, L., Iyer, S.R., Xu, X., Kelly, J., Liu, J., Wang, W., Vorster, P.J., Agulto, L., et al. (2008). HIV envelope-CXCR4 signaling activates cofilin to overcome cortical actin restriction in resting CD4 T cells. Cell *134*, 782–792.

Zennou, V., Petit, C., Guetard, D., Nerhbass, U., Montagnier, L., and Charneau, P. (2000). HIV-1 genome nuclear import is mediated by a central DNA flap. Cell *101*, 173–185.

Zhang, R., Mehla, R., and Chauhan, A. (2010). Perturbation of Host Nuclear Membrane Component RanBP2 Impairs the Nuclear Import of Human Immunodeficiency Virus -1 Preintegration Complex (DNA). PLoS ONE *5*, e15620.

Zhu, P., Chertova, E., Bess, J., Lifson, J.D., Arthur, L.O., Liu, J., Taylor, K.A., and Roux, K.H. (2003). Electron tomography analysis of envelope glycoprotein trimers on HIV and simian immunodeficiency virus virions. Proc. Natl. Acad. Sci. U. S. A. *100*, 15812–15817.